Tesis Doctoral

MODELADO COMPACTO DE MECANISMOS FÍSICOS EN CÉLULAS SOLARES ORGÁNICAS.

Autora:

PILAR LÓPEZ VARO

Directores:
Juan Antonio Jiménez Tejada
M. Jamal Deen

Programa de Doctorado en Física y Ciencias del Espacio

Dept. Electrónica y Tecnología de Computadores

Universidad de Granada

2016

Editor: Universidad de Granada. Tesis Doctorales
Autora: Pilar López Varo
ISBN: 978-84-9163-068-5
URI: http://hdl.handle.net/10481/44589

A Thesis for the Degree of Doctor of philosophy

COMPACT MODELING OF PHYSICAL MECHANISMS IN ORGANIC SOLAR CELLS.

Author:

PILAR LÓPEZ VARO

Supervisors:
Juan Antonio Jiménez Tejada
M. Jamal Deen

Doctorate program on Physics and Space Science

Dept. Electrónica y Tecnología de Computadores

University of Granada

2016

La doctoranda/ *The doctoral candidate* PILAR LÓPEZ VARO y los directores de la tesis/ *and the thesis supervisors* JUAN ANTONIO JIMÉNEZ TEJADA y M. JAMAL DEEN garantizamos, al firmar esta tesis doctoral, que el trabajo ha sido realizado por la doctoranda bajo la tutela de los directores de la tesis, y hasta donde nuestro conocimiento alcanza, en la realización del trabajo, se han respetado los derechos de otros autores a ser citados, cuando se han utilizado sus resultados o publicaciones. / *Guarantee, by signing this doctoral thesis, that the work has been done by the doctoral candidate under the direction of the thesis supervisors and, as far as our knowledge reaches, in the performance of the work, the rights of the authors to be cited (when their results or publications have been used) have been respected.*

Granada, 28 de octubre de 2016

Directores de la Tesis		Doctoranda
Thesis supervisors;		*Doctoral Candidate*:
J. A. Jiménez Tejada	M. J. Deen	P. López Varo

The research was carried out within the framework of a scholarship supported financially by Ministerio de Educación y Ciencia under research Grant FPU12/02712 and MINECO under research Project TEC2013-47283-R.

Acknowledgements

This thesis has been possible thanks to the contribution of many people who gave me the support necessary at each moment. I want to show all my gratitude to all those people who have meant a lot to me.

I would like to make a special gratitude to my director, Prof. Juan Antonio Jiménez Tejada, for his invaluable help, for all the time that he has invested in me, his constant support, for his patience and for sharing with me his scientific knowledge. He is an exceptional researcher in the modeling of semiconductor devices, especially, he possesses an outstanding insight in the field of transistors. His guidance helped me during the time of research and writing of this thesis. Everything started with an Initiation Research Grant and the Final Project in the Degree in Electronic Engineering. It was followed by the Project Master in Physics and finally with these four years of the thesis with the FPU contract from the MECD. There are countless number of hours we have spent working together these years. Along this thesis, there have been a lot of moments that I will keep in my memory forever: those days working as a work team and our scientific discussions. Without his guidance and constant help this thesis would not have been possible. From all my heart, I will always be grateful to you.

I would also like to express my deep thankful to my co-director Prof. Jamal Deen for his guidance and his insightful comments throughout this thesis. I remember the congress in Tarragona, ICOE 2012, in which I saw him giving an extraordinary conference, full of contents, and how he transmitted everything that he wanted to say. At that moment, I realized the brilliant researcher that he is. It is an honor and a challenge for me, being your PhD student. I would also thank him for giving me the opportunity to stay six months in Canada. I learned a lot and these six months have been decisive in the development of the thesis. From all of that, I feel that I am very lucky to have you as directors: Prof. Juan Antonio Jiménez Tejada and Prof. Jamal Deen.

I am especially grateful to Prof. Juan Bisquert, from whom I have learned a lot in these intense last two years. I really admire you as an incredible scientist. Thanks for all those "Skypes"sharing with me your opinions in scientific discussions. I am grateful for the encouragement and faith you have had in me.

I would also like to express my special gratitude to Dr. Ognian Marinov, who was always working hand in hand with me during the six months in Canada, giving me faith to believe in myself. I really enjoyed working with him. He always was with me, even when he did not have to. Thanks for helping me with the building of the code. The truth is that I am grateful to you.

I would like to thank to Ministerio de Educación y Ciencia for the research Grant FPU12/02712 and the funding to short stays in Canada. My short stays in Canada during six months and in Castellón during three months allow me to meet and work with a lot of kind people. In Canada, I would like to thank Prof. Chen who showed me, among other values, the importance of how to explain and present a scientific research. I also want to mention Dra. Ana Mari and Lauranne who gave me all the strength and the support that I needed and Prof. Luis Marsal for the 'coffee times'. In Castellón, I would like to thank Dr. Luca Bertoluzzi who I had a lot of nice scientific discussions with, and Nuria Vicente who make my stay there easier.

Another special thankful is for my friend-workmates, brilliant minds and hard workers, in the office 19. They have been with me all these years and I feel them like a second family: Trini, Celso, Karam, Cristina, Enrique, Biba, Ernesto and José María. I will remember our coffee times and our fun scientific discussions in the blackboard about electronic devices. Trini was a huge help at the beginning of my thesis, not only at the scientific level but also at the personal one, which has been very important for me. I thank Celso for his advices on the thesis and his help in the simulation problems. Cristina has been with me, a lot of days, from dawn to sunset, and she has always been encouraging me. Ernesto and José María have been with me during my last year of the thesis, time enough to help me in any thing I needed.

In the Departmento de Electrónica y Tecnología de Computadores in the University of Granada, I would like to thank for their constant support: Salvador Rodríguez Bolívar, Juan Enrique Carceller, Juan Antonio López Villanueva, Toñi and José Miguel. I appreciate the opportunity and the funding that Salvador and Juan Enrique have given me to attend scientific conferences.

Me gustaría agradecer a todos mis amigos que han estado ahí siempre que lo he necesitado (espero no olvidar a nadie): Laura Rejón, María Isabel, Cabel, Soledad, Laura V., Paula, Patricia, Gloria, José Manuel, Nani, Ana, Ruth, Eunice, Irene and Mari Cruz.

Finalmente, quiero expresar mis más sinceros agradecimientos a todos mis familiares, en particular, a mis padres Rosa y Manuel, a mis hermanos: Emilio y Manuel, a mi hermana Rosa por todo su amor, paciencia y por haber estado siempre que lo he necesitado. No hubiera llegado a donde estoy sin vosotros.

Thanks to all of you,

Pilar

Abstract

Organic solar cells (OSCs) are promising devices in the field of solar energy. Their many advantages are intrinsic of the organic/polymeric technology, such as light weight, flexibility and low manufacturing costs. However, the degradation of OSCs hinders a predictable and a stable performance. In order to improve the device performance, accurate physics-based models, including boundary conditions, are needed. In this thesis, a model that relates the charge carrier density at the metal-organic boundaries with the current density in OSCs is considered for simulation and modeling purposes. The model is proposed after initial studies on single-carrier and bipolar organic diodes in darkness.

The work begins with the proposal of a model for the current-voltage characteristics of organic and polymeric single-carrier diodes. The model unifies two different mechanisms in the structure, the injection and transport of charge, and includes a proper boundary condition for the free charge density at the metal-organic interface and a temperature and electric-field dependent mobility model. The results of the model highlight the importance of the boundary condition at the interface, which is used to explain different trends and their transitions in experimental current–voltage characteristics: linear, quadratic and a higher than quadratic trend at high electric fields.

The importance of this boundary condition leads to a model that relates the boundary values of the charge concentration at the interface with the current density. This relation follows a power-law function with the current in drift-dominated transport. In diffusion-dominated transport, at low bias close to the diode's built-in voltage, the charge density at the contact is almost constant with the current. This boundary condition, initially proposed in single carrier diodes, is tested positively in bipolar devices. Then, the model is adapted to OSCs, where the power law relation is valid not only in darkness but under illumination. The model is verified by comparing experimental current-voltage characteristics with numerical simulation. The numerical simulations of the current-voltage characteristics of OSCs consider well-established models for the main physical and optical processes which take place in the device: light absorption, generation of excitons, dissociation into free charge carriers, charge transport, recombination and injection-extraction of free carriers. Our analysis provides a general picture of the influence of the metal-organic interfaces in the global performance of OSCs.

In an effort to extend the applicability of our study to other devices and physical mechanisms, the work includes a study of the contact effects in organic thin film transistors (OTFTs) and the study of ferroelectric aspects in solar cells. In the first case, we propose a compact model for the current-voltage characteristics of OTFTs. This model includes the effects of the contact regions in which the current-

voltage model developed in organic diodes is incorporated. The model explains successfully two trends observed in current-voltage curves of the contacts of different OTFTs (linear and non linear) which so far were explained with different models. A characterization technique to determine the value of the parameters of the model from experimental data is also developed.

The second case is the inclusion of ferroelectricity to the study of solar cells. Ferroelectricity assists a permanent electrical polarization which may enhance the charge transport and may modify the electrical behavior of interfaces improving the efficiency of solar cells. Theoretically, the ferroelectric polarization affects the transport in semiconductors by means of shifts in the band bending. The control the polarization with an external field allows to electrically tuning charge transport and hence reaching unidirectional electric conduction. We have included ferroelectric effects in the physical model of a solar cell. Our analyses provide a general picture of the influence of ferroelectric effects on the power conversion efficiency of the solar cell device, and we are able to assess whether these effects or their combinations are beneficial or counterproductive.

Contents

1

Introduction and background

1.1. Motivation

Currently, our daily needs of energy are mainly provided by fossil fuels. However, fossil fuels have a limited supply and are the main source of environmental contamination. Based on the world's population growth trend and the increment of technology devices, the worldwide energy demand will continue increasing every year. Under this scenario, we need to look for a clean and long lasting renewable source of energy.

Solar energy has been the most promising alternative for decades. The earth receives approximately 1.74×10^{17} W power from the sun whereas the current worldwide electric energy consumption is approximately 18 TW, which is 10.000 times smaller. That means that the earth receives from the sun more energy in one hour than the world's energy demand for a whole year[1]. Among the different methods to extract and convert the solar energy in electrical energy, the solar cells or photovoltaic cells are in the spotlight of all researchers.

There is a wide variety of solar cells which are typically classified based on the absorber semiconductor layer. They are grouped into the so called: first, second and third generation cells. The efficiencies of these solar cells are also different as is reported by the National Renewable Energy Laboratory (NREL) [2] (Fig. 1.1). Currently, the most efficient solar cells are the multijunction cells with almost a fifty percent. The first generation cells are made of crystalline and polycristalline silicon (c-Si, p-Si). The second generation cells are thin film solar cells, that include amorphous silicon (a-Si), Cadmium Telluride (CdTe) and Gallium Arsenide (GaAs) cells. Finally, the third generation cells include emerging photovoltaic devices. Most of them have not yet been commercially applied and are still under research or development. This category includes solar cells based on organic dyes, dye sensitized materials, organic or polymeric materials, quantum dots and perovskite materials.

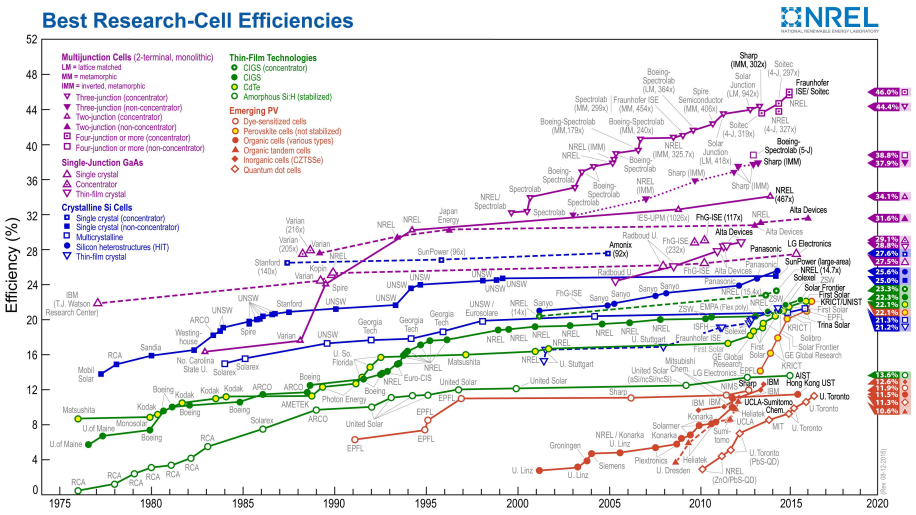

Figure 1.1: Best research-cell efficiencies reported by [2]

Silicon-based solar cells dominate the photovoltaic market. Silicon is abundant in the nature and has

a broad absorption spectrum. However, the main problem of silicon solar cells is the production costs due to the requirements of the clean-room and the high temperature processes. For this reason, the prices of electricity produced by photovoltaic silicon devices are still very high compared to electricity produced by the conventional power industry [3]. Cheaper photovoltaic-electricity is possible by a trade-off between efficiency and cost. In this regard, organic-polymeric solar cells (OSCs) are suitable in the future of photovoltaic-market as they can achieve higher power conversion efficiencies for large-scale manufacture with low fabrication costs [3, 4].

Organic solar cells have the intrinsic advantages of the organic technology, such as simplicity of the production processes, low processing temperatures, affinity for chemical modification, flexibility, large area printing, low weight, and low environmental impact. OSCs are also compatible with other applications such as clothing, flexible screens, or recharging cell phones. This opens a whole new range of possibilities which traditional solar cells cannot offer. Nevertheless, their efficiency levels are still below the ones provided by standard solar cells. Another drawback is the degradation of OSCs due to air and light exposure that decrease their operational lifetimes [5]. In order to commercialize this technology, research and development efforts to enhance the efficiency and to achieve long-life devices are thus necessary [4, 5].

Sensitive regions of the OSCs are the contacts between the metal electrodes and the organic material. On the one side, the contacts control the flux of the current. The carriers that are photogenerated inside the semiconductor must be extracted at the metal-organic interfaces. On the other side, the contact region is sensitive to degradation. The formation of an insulating layer close to the metal-organic interface or the decrease of recombination velocity at the contact are detrimental effects that can reduce the efficiency of the OSCs [6, 7]. In order to optimize the performance of these devices, a detailed physical description and proper modeling and simulation of the metal-organic structure are necessary.

The modeling of organic solar cells is supported by a previous long-standing experience of our group in the field of simulation and modeling of inorganic and organic electronic devices. It is worth mentioning previous works in the development of a unified model for injection and charge transport in organic diodes, which is the basis of the present work [8–11]. The main feature of this model is that it incorporates together drift, diffusion, thermionic and tunnel injection, and oxidation-reduction mechanisms in the study of a metal-organic interface. This model allows relating the charge density at the interface with the applied voltage and current density. Later, this analytic model was successfully introduced in a compact model for organic thin film transistors with the objective of characterizing the contact regions of these transistors [12–15].

1.2. Objectives and methodology

This thesis is focused on the modeling and simulation of organic solar cells. The transport equations in semiconductors combined with opto-electrical models have been used extensively in the literature to model the generation and transport of charge carriers in OSCs. However, there are particular aspects that differ among different researchers, such as the models used for the charge-carrier generation and

recombination, the mobility, or the boundary values for the free charge density, the last one being the main objective of this work.

For this purpose, a proper model that defines the free charge density at the contact will be proposed and later integrated with the optical and electrical models in the simulation. The way to achieve this objective is through several steps or secondary objectives with increasing difficulty.

1. The boundary values of the free charge density at a metal-organic interface are determined in the first place in metal-organic-metal structures with the following features: single carrier transport in the organic material in order to avoid the complexity of bipolar transport; symmetric and ohmic contacts in order to avoid injection limited current regime and to reduce the transport to drift processes; and darkness in order to neglect optical phenomena.

2. In a second step, the boundary values of the free charge density at the interfaces are determined in symmetric single-carrier metal-organic-metal structures with high barriers. The effect of the injection through the barriers on the boundary values is analyzed. The injection limited current (ILC), space-charge limited current (SCLC), and diffusion regimes are compared and their effects integrated in the boundary condition model.

3. Asymmetric single-carrier organic diodes in dark are studied in the third place.

4. A new step in complexity is added with the study of bipolar conduction in organic diodes and OSCs in darkness. The model for the the charge carrier density at the metal-organic interfaces is adapted to this new situation.

5. Finally, the model is completed for organic solar cells under illumination. A characterization procedure is also given to determine the value of the model parameters from the comparison of experimental data with numerical results.

6. The model developed in metal-organic-metal structures is applied in the modeling and simulation of organic thin film transistors (OTFT). The idea is to extend the validity of the boundary condition model to other organic devices.

7. A different type of solar cells is studied: a ferroelectric solar cell. Different physical mechanisms and materials are incorporated in the simulation and the results checked with experimental data.

The main tool to develop these steps is a computational program. The transport equations, the opto-electrical models, the proposed boundary condition model and the procedures to characterize the parameters of the model are implemented in this program. The particular aspects related with the aforementioned steps are detailed in each chapter of the work.

1.3. Structure of the Thesis

Throughout this memory, we focus on the modeling of physical mechanisms of organic solar cells, although we pay special attention to the modeling of the contact regions of these devices.

This work is divided in seven main chapters that follow this introduction (Chapters 2-8). Although they are written in sequence order, each one can be read independently from the others. For this reason, the terminology can change among them and notation is always defined in each chapter.

The first four chapters are focused on the study of injection and transport mechanisms in metal-organic-metal structures. They lead in sequence to the modeling of OSCs, which is the main purpose of the thesis and is treated in Chapter 6. Chapter 7 focuses on compact modeling of TFTs. Although the topic may seem different, the problem of the contact is common in both devices. We make use of the studies of the contacts in organic diodes to propose a compact model for TFTs including the contact effects. Finally, in Chapter 8, the numerical simulator is tested in other kind of solar cell: the ferroelectric solar cell.

In Chapter 2, a model for the charge transport in organic diodes is proposed. It provides a physical explanation of the transition from ohmic to space-charge limited current (SCLC) regimes. It also explains internal transitions in the SCLC regime when high electric fields are applied. The model is based on two established models: a unified model for the injection and transport of charge in organic diodes, including a proper boundary condition for the free charge density at the metal–organic interface; and a temperature and electric-field dependent mobility model. Organic diodes with low energy barriers at the interfaces are studied over a wide range of applied voltages, or electric fields.

Chapters 3 and 4 combine the study of the injection-limited-current (ILC) and SCLC regimes. Different energy-barrier heights at the interfaces are analyzed and the resulting current density is modeled. A model that relates the charge density at the interface with the current density is proposed unifying both SCLC and ILC regimes. At high current densities, the model is described with a power-law function between the charge density at the interface and the current flowing through the metal-organic contacts. The unified model allows characterizing metal–organic contacts subjected to controlled technological treatments or unintentional degradation processes. This boundary condition model is the first step to introduce the contact effects in the simulation of organic devices.

Chapter 5, studies the boundary conditions for the charge density at the metal-organic contacts of symmetric and asymmetric organic diodes with unipolar and bipolar conduction. From the analysis of experimental current-voltage curves, an analytical model that relates the value of the charge density at the contacts with the current density is proposed. The relation between charge and current for injecting electrodes, extracted from the analysis of single-carrier diodes, can be used as boundary condition in bipolar devices.

In Chapter 6, the boundary condition model, initially developed for single-carrier and bipolar diodes, is finally adapted to OSCs. The model captures both the optical and electrical effects in the OSC. The verification of this model is done by comparing experimental results with numerical results. The numerical simulator is developed which combines the transfer matrix method to study the optical propagation, the Onsager-Braun theory to describe the exciton disociation and the drift-diffusion transport equations with the boundary condition model, which is the main achievement of this thesis.

In Chapter 7, we apply a current-voltage model, initially proposed in organic single-carrier diodes, in the modeling of organic thin film transistors (OTFT). The model that relates the current in the transistor with the voltage drop at the contacts is introduced in a generic analytical model for the current–voltage of

OTFTs. The resulting compact model can describe anomalies produced by the contacts on experimental current–voltage curves of OTFTs.

In Chapter 8, we have included ferroelectric effects in the physical model of a solar cell. The idea is to extend the validity of the simulator to other type of solar cells as in this case, a ferroelectric solar cell. Different physical mechanisms and materials are incorporated in the simulation and the results checked with experimental data. The simulator includes effects associated to both the ferroelectric polarization surface polarization charges and the spatial dependent polarization, which are necessary in order to interpret experimental current-voltage curves obtained so far.

The memory is ended with concluding remarks and recommendations for future work.

1.4. Background

In this last section of the introductory chapter, we present basic concepts that will be treated throughout this work. They are related to the electric conduction in organic semiconductors and will help in the understanding of the transport mechanisms in OSCs.

1.4.1. Organic Semiconductor

Organic electronics is a very promising complement to silicon-based technology, providing the opportunity of using flexible and low-cost substrates for large-area applications by simple and low-temperature fabrication. The main disadvantage of the organic materials is the low value of the charge carrier mobility. Organic semiconductors are carbon-based semiconductors with a certain number of functional groups that are attached to it. Conductivity in organic semiconductors is due to conjugation, the alternation of single and double bonds between the carbon atoms that leads to delocalization of the charges which allows the free movement of the electrons in such region. Based on the conjugation length, the organic semiconductors can be classified in two groups: the small molecule, or organic semiconductor and the polymeric semiconductor. Polymeric semiconductors are constituted by a long chain of similar smaller molecules, and therefore, they tend to have a long conjugation length, while small molecules, have a shorter one. Both types present very similar electrical characteristics.

In spite of the good conduction within the molecule, the organic semiconductors (hereafter, we use organic to mean both organic and polymeric) are formed by a system of molecules and the macroscopic conduction depends not only on the motion of the charge within the molecule but also on the transfer of charge between molecules. The organic molecules are held together by a weak bonding Van der Waals interaction, and therefore the transfer of charges between molecules is not as easy as in a covalent crystal.

Transport in Organic Semiconductor

In general, the organic semiconductor is assumed to be constituted by two delocalized “energy bands” commonly characterized by the highest occupied molecular orbital (HOMO) and the lowest unoccupied molecular orbital (LUMO). By analogy with inorganic semiconductor, the HOMO and LUMO are associated with the valence and conduction bands, respectively. HOMO and LUMO are separated by a

"bandgap" in the order of typically two to three electron volts. The transition between these two levels can be excited by light in the visible spectrum. This makes conjugated organics a very interesting choice for photovoltaic applications.

The validity of a band theory (Figure 1.2 (b)) is open to debate [16]. A better approach for the conduction in organic semiconductors is the charge transport via hopping over the barriers between molecules from one localized state to the next[17] (Figure 1.2 (a)). The percolation or hopping theory is used to describe the electronic behavior of devices [16]. Evidence for hopping transport mostly relies on the fact that the field effect mobility of organic semiconductor is thermally activated and electric field dependent. This will be treated in Chapter 2.

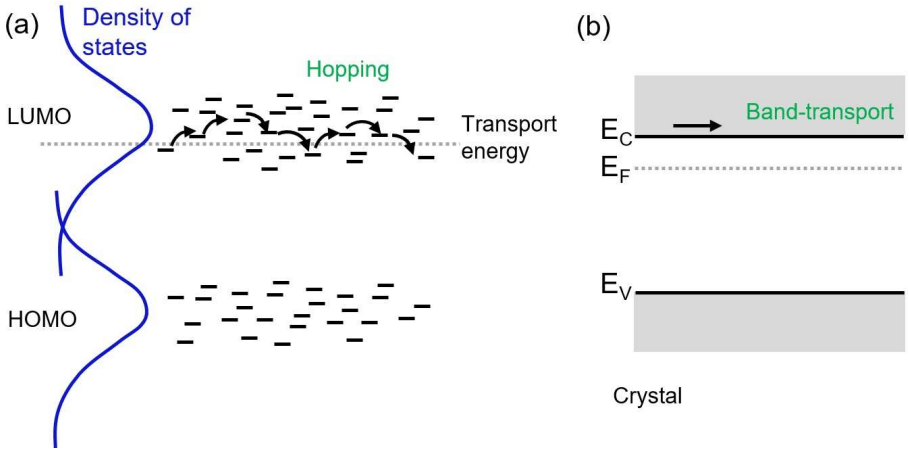

Figure 1.2: (N-type) transport models. a) Hopping/percolation conduction which consists of jumps from one localized state to another in the Gaussian energy distribution of the LUMO for electrons and of the HOMO for holes. The injected (or photogenerated) charge carriers can be generated at higher energies, followed by a relaxation of the charge carriers to a quasi-equilibrium transport energy. The steady-state charge transport takes place around the effective transport energy, which depends mainly on temperature and disorder. At low temperature, the charge carriers relax to the deepest states where they remain trapped. b) Crystal/band theory. Conduction occurs in the conduction band, E_C, (for electrons) and in the valence band, E_V, (for holes). The dashed line is the Fermi level E_F.

Injection and Extraction of charge

The injection and extraction of charge through metal-organic interfaces are present in any organic devices and the OSCs are no exception. The current that flows through this interface is the result of different factors such as the height of the injection barrier, the applied electric field, the temperature, chemical reactions leading to interface dipoles, and band bending or Fermi level pinning (Chapter 3). For a small energy barrier, the contact imposes no restriction to the flow of charges. The performance of the device is limited by the transport in the organic semiconductor bulk. In this case, the current is space charge limited and follows the usual quadratic dependence with the voltage, the well known Mott-Gurney model [8, 18]. In the opposite case, that correspond to a high energy barrier, the performance of the device is mainly limited by the injection through this barrier. The current is said to be limited

by injection mechanisms. The typical injection models are the thermionic emission model employed for lower barriers and low electric fields and the Fowler-Nordheim tunneling injection model for higher barriers.

1.4.2. Organic Solar Cells

A typical organic solar cell is a multilayer structure with a transparent and conductive electrode (usually an ITO anode), a transparent substrate, an hole transport layer HTL or electron blocking layer (such as PEDOT: PSS), an active organic polymer layer (monolayer, bilayer or bulk heterojunction) and a cathode (typically Al or Ca/Al). The general performance of OSCs is the following (Fig. 1.3). Light (1), coming through the transparent substrate, propagates in the OSC structure, and the absorbed energy generates excitons (2) (optically excited electron-hole bound pairs). The stored potential energy is not enough to dissociate immediately the excitons into electron-hole pairs. Some excitons are lost by recombination and others diffuse (3) until they reach a dissociation site (usually a region with high electric field or the interface between two different materials). There, free electrons and holes are separated (4). These separated charges are transported in opposite directions towards their respective electrodes (5) where they are extracted (6).

Organic Solar Cells Architectures

The first generation of OSCs was based on a single active layer. This type of solar cell is constituted by an organic semiconductor layer between two metals with different work functions. Fig. 1.3 (a) shows the energy diagram and the different mechanisms that take place in a single-layer solar cell. In this configuration, one of the contacts is ohmic and the other one is a Schottky contact. The Schottky barrier creates a strong electric field close to the contact, which is able to dissociate excitons. In this device, the power conversion efficiency is very poor. This fact gave rise to the second generation of OSCs based on a bilayer structure (Fig. 1.3 (b)). The concept behind a bilayer OSC is to create an interface between two different materials (called donor and acceptor) at which exciton dissociation takes place more efficiently. The efficiency of the bilayer OSCs is still low due to the high exciton recombination rate, which is attributed to the short exciton diffusion length in organic semiconductors (around 10 nm). The efficiency was enhanced with the introduction of the bulk heterojunction (BHJ) architecture (Fig. 1.3 (c)), in which the donor and acceptor phases are intermixed on the nanometer scale to form a much larger interface area throughout the photoactive layer. These distributed interfaces help excitons to be dissociated before recombination events occur. Figure 1.3 shows the energy diagram and the main physical mechanisms that appear in (a) single-layer, (b) bilayer and (c) bulk-heterojunction solar cells.

All these architectures established the ground for the design of new structures, such as the pseudo-bilayer solar cells [19] or the test of different morphologies. Several works analyze different textures and geometries to improve the optical properties of the device [20, 21]. In the search for an optimal morphology in BHJ solar cells, these authors focused on different ways of intermixing donor and acceptor materials, such as the creation of “islands” of one material surrounded by the other. These inclusions can act as charge traps and may influence the local charge densities and charge transport.

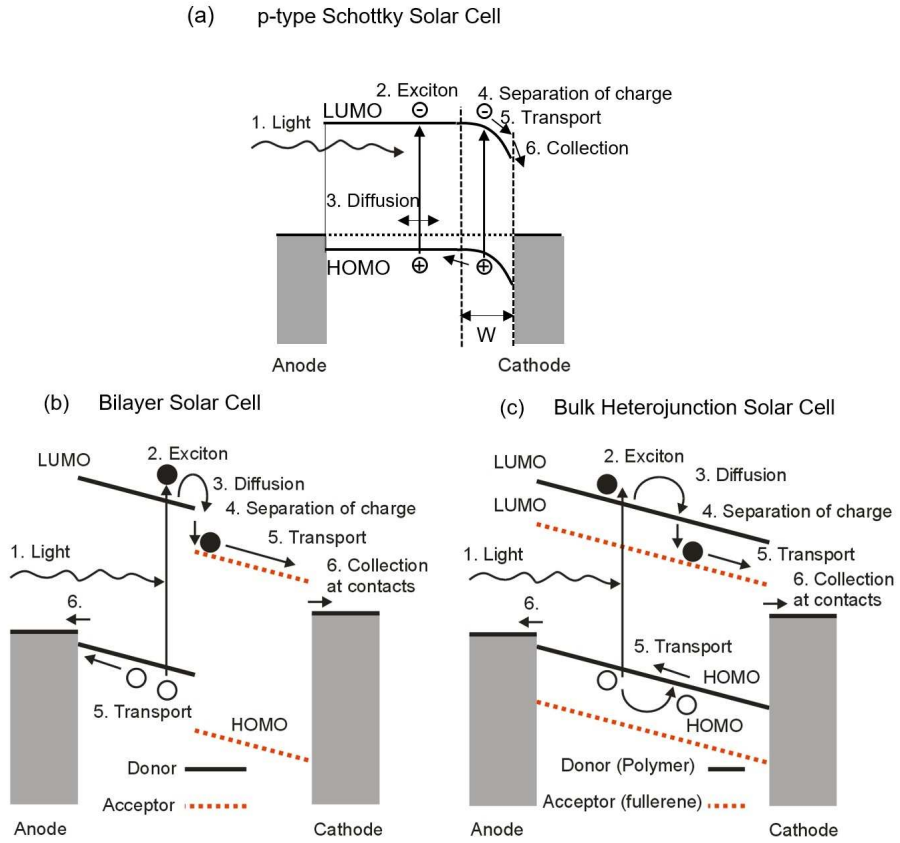

Figure 1.3: The energy diagram and the main physical mechanisms that appear in (a) a single layer, (b) bilayer and (c) bulk heterojunction solar cell.

Numerical Models

In order to describe the performance of OSCs, different physical models have been proposed. The numerical simulations of OSCs consider the main physical-chemical mechanisms which govern OSC performance. Several excellent works pay attention to the understanding of each mechanism and to the interactions between them. These mechanisms can be classified in three groups: optical, electrical and opto-electrical.

The optical mechanisms treat the light as an electromagnetic wave and consider the reflection, refraction and interference effects in a multilayer structure. They are commonly modeled using the Transfer Matrix Method (TMM) [22–26], which provides a low computational cost and their results agree quite well with experimental data. Other works use finite element method (FEM) simulations [21, 27] to solve the electromagnetic wave equation on the whole estructure. TMM and FEM, coupled with the drift-diffusion equations, allow to estimate the optimum thickness of the active layer [21, 24–27]. The optical models provide the exciton generation rate, which is used as input in opto-electrical models.

The opto-electrical models take into account the processes that take place from the creation until the dissociation of the exciton at the donor-acceptor interface of OSCs [28, 29]. They include the exciton

formation and dissociation and the geminate and nongeminate recombination. In general, the models are based on Onsager-Brown theory [30],[31] which may partly be due to the availability of an analytic expression. These models determine the value of the free charge that appears after the dissociation of the excitons which is incorporated in the electrical model.

The electrical models complete the set of models necessary for simulation of OSCs. With them, current-voltage characteristic curves can be calculated. In the literature, two different computational models are found: drift-diffusion (DD) and Monte Carlo (MC) models [32]. The main difference is that drift-diffusion equations focus on the macroscopic quantities, while the Monte Carlo model focuses on the behavior of a microscopic particle [33], or to study realistic blend morphologies [34].

The drift-diffusion model is a common technique for semi-classical modeling of semiconductor devices over a generic geometry in 1, 2 or 3 dimensions. A large number of publications have studied the charge transport in organic solar cells, using the DD model. They apply this method to simulate the organic photovoltaic devices and study the influence of doping levels [35, 36], temperature [37], type of recombination, traps [38], space charge, lifetime and/or mobility [39, 40] in the performance of OSCs. Modifications of the DD model are also proposed in order to investigate the impact of the interface morphology and of exciton dissociation on device performance [41].

DD model comprises the differential equation system of Poisson, drift-diffusion and continuity equations. In this work, DD equations are used. Their computational requirements are low, their numerical results provide a good agreement with experimental data, and offer strategies for further improving the device efficiency. The use of the DD model in OSCs is combined with a common approximation called the effective medium approach, in which the blend of donor and acceptor materials is treated as one effective material [42, 43].

Compact Models

To speed up the simulation the use of compacts models is recommended. The compact models can be easily integrated in more complex circuits. A compact model is defined by three important parts: an analytical expression to describe the current-voltage characteristic, an extraction parameter procedure with a defined range of physical-meaningful parameter values and a final step of verification of the proposed model. There are two kind of compact models, models that are described with an equivalent circuit model [44], and the ones extracted from the analytical solution of the drift-diffusion equations using specific approximations [45, 46]. In this last group, there are different analytical studies that describe the $J - V$ characteristics of BHJ solar cells [42, 47, 48]. The way to distinguish one from the other is by their specific assumptions, such as the spatial generation profile [47, 49], the recombination model [45, 48, 50], the dissociation efficiency model for bound electron-hole pairs, or a particular carrier trapping model. In general, they are a powerful tool to design and optimize OSCs without dealing with numerical computational complexities [48, 50].

2

Modeling the ohmic-SCLC transition in organic semiconductors

2.1. Introduction

Devices based on organic and polymeric materials are being researched by many groups because of the advantages associated to these materials, such as flexibility, low fabrication costs and weight [51, 52]. These researches are motivated by the promise of low-cost, easy-to-fabricate or flexible consumer products that include light-emitting diodes, flexible integrated electronics, sensors or displays. For these and other applications, it is vital to understand and model the key mechanisms that determine the current–voltage (j—V) characteristics of a given device structure [53–56], in order to improve the performance of organic devices (OLEDs, OFETs, and organic solar cells), to design and synthesize appropriate materials, and to improve the efficiency and lifetime of devices.

The current–voltage characteristics of metal–organic–metal devices are mainly controlled by two basic processes: injection of charge carriers, and transport of charge in the organic bulk. In both these processes, the connection between the metallic contact and the polymer is of crucial importance. Injection barriers can be difficult to estimate using only the metal work-function and the energy levels of the semiconductor. The atmosphere in which the samples are fabricated also affects the interfacial electronic structure [57]. The actual injection barrier height is attributed to chemical reactions between the metal and the organic semiconductor leading to interface dipoles [56, 58], band bending [59] or Fermi pinning [60–62].

It has been shown [63–65] that if the barrier at a metal–organic interface is greater than 0.3 eV at zero electric field, then the current is limited by injection (injection-limited current, ILC). If the barrier is less than 0.3 eV, the injection barrier is small and charges can be injected efficiently into the device. Thus, the limiting factor to the flow of charge through the device is imposed by the transport of charge through the bulk. In this chapter, we pay special attention to the charge transport. Many investigations have addressed the mobility μ of charge carriers in order to optimize the device performance, for example [54, 66, 67], and to explain different trends that are observed in the current–voltage characteristics. Three regions can be distinguished in a typical current–voltage curve:

(a) a linear or ohmic region at low voltages,

(b) a quadratic region when the voltage is increased, and

(c) a region showing a higher than quadratic relation at high voltages.

The ohmic region is observed when the amount of injected carriers is low compared to the existing thermally generated carriers and impurities. Regions (b) and (c) correspond to the so-called space charge limited current (SCLC) where the electrode injects more carriers than the material can transport.

The study of transport and mobility in organic devices is often performed using different models and sometimes even different physical descriptions, despite the fact that similar (or even identical) materials are being used [54][68]. There exist simple models that can be used to explain the ohmic and quadratic regions [69–72], and also some discussions on contact effects [12, 73, 74]. However, they cannot explain the transition from one region to the other. More complex models have been suggested in order to interpret the high voltage region. They include dependences with the temperature T, the electric field

E, and the free charge density p. However, these models also fail to connect the SCLC regime with the linear region [75, 76]. In spite of this progress, a model that links all the different regions in a current-voltage curve is lacking. The objective of this chapter is to propose such a model.

In order to tackle the issue of different regions in the current–voltage characteristics, we use a unified model, developed previously in our research group [8–10], which considers all the key phenomena that occur inside the organic diodes: carrier injection, redox mechanisms and charge transport. This model was initially developed for a temperature-dependent mobility. It is the aim of the current chapter to incorporate the dependence on the electric field in order to extend the validity of the model to high voltages, as well as to explain the low voltage region including the transition from ohmic to quadratic regimes.

The proposed model assumes a finite boundary condition for the free charge density at the metal–organic interface that is controlled by redox reactions[8]. There are researchers that question the use of an infinite charge density at the contact [56–62, 77]. An overestimation of the charge density in diodes might lead to an underestimation of the value of the mobility extracted from experimental current–voltage curves. This would explain different values extracted for the mobility in the same material by different authors [78–82].

With this in mind, Sec. 2.2 reviews the progress in mobility models. It also includes a summary of our unified model. In Sec. 2.3, we propose a model that links our unified model with an electric-field and temperature dependent mobility model. In Sec. 2.4, the model is applied to published current-voltage characteristics measured at different temperatures in organic diodes with different lengths. We interpret the transitions among different regions in a current-voltage curve: linear, quadratic at low injection, and a higher than quadratic region at high injection. The parameters employed in the mobility are analyzed and compared with those obtained in previous works. In Sec. 2.5, we provide an expression that relates the free charge density at the metal-organic interface in the SCLC regime. The main conclusions are provided in Chapter 9.

2.2. Theory

In this section, we focus on transport in organic diodes with Gaussian disorder. We review mobility models and analize their advantages and disadvantages, including some aspects of our unified model for injection and transport of charge [8] that are important for a better understanding of this work.

2.2.1. Mobility models

Charge transport in a disordered organic film is regarded as a hopping or thermally-assisted tunneling process between two molecular localized sites through the Gaussian density-of-states $GDOS = g(\varepsilon) = (2\pi\sigma^2)^{-1/2}\exp[-\varepsilon^2/(2\sigma^2)]$, where σ is the width of the distribution and ε is the site-energy. The hopping transport in disordered organic semiconductors is electric-field dependent and thermally activated. The dependence of mobility on temperature T and electric field E has been studied extensively by different authors, for example, [83–86]. The electric field dependence of mobility described by Eq. (2.1) stems

from the reduction of barriers by charge transport in the field direction by the applied electrostatic potential. The well-known Poole-Frenkel (PF) relation includes such dependences [84]:

$$\mu(E,T) = \mu(0,T)exp(\gamma(T)\sqrt{E}) \tag{2.1}$$

where $\mu(0,T)$ and $\gamma(T)$ are the temperature dependent zero field mobility, and the field activation of the mobility, respectively. Expressions for $\mu(0,T)$ and $\gamma(T)$ have evolved in the course of time. From time-of-flight (TOF) experiments, Gill proposed : $\gamma(T) = B[1/(k_BT) - 1/(k_BT_0)]$ and an Arrhenius temperature dependence for the mobility $\mu(0,T) = \mu_\infty \exp[-\Delta/(k_BT)]$ [83]. In these expressions, k_B is the Boltzmann constant, μ_∞ is the mobility in the limit $T \to \infty$ and Δ is the activation energy. Also, T_0 and B are fitting parameters that depend on the molecular dopant density [78]. Later, Monte-Carlo simulations of hopping transport in Gaussian site energies were performed by Bässler et al. [87], rendering the Gaussian disorder model (GDM). This model exhibits a non-Arrhenius temperature dependence and a Poole–Frenkel behavior. An important limitation of this model is that it only reproduces the experimental currents in a rather limited range of electric field values. However, a Poole–Frenkel behavior occurs in a broad range of electric-fields, as observed in TOF measurements. In [88] and [89] the applicability of a PF relation over a wide range of electric fields was shown to require a spatial correlation among hopping sites, leading to what is now known as the correlated Gaussian disorder model (CGDM also so-called CDM) [85] that is given by:

$$\begin{aligned}\mu_{CGDM}(T,E) = \mu_\infty \exp\Bigg\{ &- \left(\frac{3\sigma}{5k_BT}\right)^2 \\ &+0.78\left[\left(\frac{\sigma}{k_BT}\right)^{3/2} - 2\right]\left(\frac{qaE}{\sigma}\right)^{1/2}\Bigg\}\end{aligned} \tag{2.2}$$

where a is the intersite spacing (natural measure for the length scale involved in the charge transport process) and q is the unit of electric charge. Also, Kreouzis et al. [90] found that CGDM is more successful than the GDM in explaining experimental data.

Recently, different authors have studied the dependence of the mobility with the free charge-carrier density p, for example [91]. Such studies have been motivated, on the one hand, by experiments in diodes and FETs with the same organic semiconductor as active material, where μ can differ up to 3 orders of magnitude between devices [92]. On the other hand, models that include a free carrier density dependent mobility have been used to explain the dependence of j–V curves with the device length. At room temperature, mobility models depending only on the free charge density have been proposed [91]. However, such models fail to reproduce experimental j–V curves at low temperatures and high voltages, and it is necessary to introduce a dependence with the electric field [93].

In order to describe the dependence of the mobility on the electric field and charge carrier density, extended disorder models were introduced. Schuster et al. [94] commented that the extended Gaussian disorder model (EGDM) is applicable to polymeric systems [93, 95], while the extended correlated disorder model (ECDM) can also be used for molecular materials [54]. In this regard, it is worth mentioning

the proposed models by van Mensfoort et al. (a combination of EGDM plus diffusion) [75, 76] and by Torricelli et al. [96].

In this chapter, we want to stress the importance of the charge density as a boundary condition when solving the Poisson and drift equations, instead of enhancing the importance of this variable in the mobility. In fact, the mobility in (2.2) depends on the electric field, which at the same time is related to the charge density by the Poisson equation (see (2.3) below). In this regard, we exclude the dependence of the free charge density from the mobility model by using the CGDM (2.2). Apart from cited above advantages of this model, it maintains the simplicity needed for compact modeling, not found in other more complex models.

2.2.2. Transport equations

The $j - V$ curve of a hole-only device without charged impurities is characterized by the transport equations (2.3)-(2.5) given below. The Poisson equation, which describes the relationship between the electric-field E and the local charge density $p(x)$, is given by:

$$\frac{dE}{dx} = \frac{q}{\epsilon_0 \epsilon_r} p(x) \tag{2.3}$$

where ϵ_r and ϵ_0 are the relative permittivity and the permittivity of free space, respectively, q is the magnitude of the electron charge, and x is the distance from the injected electrode. Charges injected from the electrode into the organic region move through it due to the electric field. The drift current density is given by:

$$j = q\mu(T, p(x), E(x))p(x)E(x). \tag{2.4}$$

In general, $\mu(T, p(x), E(x))$ can be one of the mobility models previously described. The dependence of the mobility with position through $E(x)$ or $p(x)$ requires the numerical solution for (2.3) and (2.4) for a given hole current density j and a boundary condition for the electric field in the metal-organic interface, $E(x = 0)$. The related voltage for this current is given by:

$$V = \int_0^L E(x)dx \tag{2.5}$$

where L is the length of the organic material.

2.2.3. Unified model for the injection and transport of charge

In a previous work, we proposed a unified model for injection and transport of charge in organic diodes [8]. Specifically, our model assumes that three phenomena take place in a generic metal–organic–metal structure:

1. injection from the metal electrode towards the organic material,

2. redox mechanisms at the interface and

3. charge transport in the organic bulk.

Associated with these three physical mechanisms, we consider that the applied voltage V is shared by the respective voltages: $V_{injection}$, V_{redox} and $V_{transport}$. Therefore:

$$V = V_{transport}(j) + V_{redox}(j) + V_{injection}(j) \tag{2.6}$$

In that former work [8], we detailed regions where any of these mechanisms are dominant. In this chapter, we pay main attention to the charge transport. For this reason, the barrier height in studied organic devices is considered low, which results in small injection voltages ($V \approx V_{transport}(j) + V_{redox}(j)$)[10]. The redox voltage is usually small and is related to the charge density at the interface $p(0)$ by using the Nernst equation:

$$V_{redox} = \phi + V_t(T)\ln(p(0)/\rho_m) \tag{2.7}$$

where ϕ is a constant which depends on the material involved in a given redox reaction, ρ_m is the molecular density of the organic material, and $V_t(T) \equiv k_B T/q$ is the thermal voltage.

The redox voltage is usually smaller than the transport voltage. However, both terms can be comparable at very low voltages. If $V_{redox}(j)$ is assumed constant ($V_{redox}(j) = V_{redox0}$), then the $j - V$ curve given by $V = V_{transport}(j) + V_{redox0}$, would not cross the origin $(j, V) = (0, 0)$ but the point $(j, V) = (0, V_{redox0})$. The redox voltage can be estimated if the j–V curve in the low voltage regime is extended by a straight line towards the V-axis. The crossing of this extrapolated line with the x-axis gives an estimation of the redox voltage. Except for this consideration at low voltages, the applied voltage can be approximated by the drift voltage ($V \approx V_{transport}(j)$). The voltage required for the transport across the contact region is calculated assuming that the charge transport is due to the drift of positive charges with a charge density at the interface $p(0)$. This condition at the interface is equivalent to expressing the electric field at this point as:

$$E(0) = \frac{j}{q\mu p(0)} \tag{2.8}$$

In the formulation of this model, we initially considered a constant mobility at a given temperature, $\mu = \mu(T)$ [8]. This leads to the following analytical solution for the set of equations (2.3)-(2.5):

$$V_{transport}(j) = \frac{2}{3}\left(\frac{2j}{\epsilon_r \epsilon_o \mu}\right)^{1/2} \times \left\{[L + x_c(j, p(0))]^{3/2} - [x_c(j, p(0))]^{3/2}\right\} \tag{2.9}$$

$$x_c(j, p(0)) = \frac{j\epsilon_r \epsilon_o}{2q^2\mu\,(p(0))^2} \tag{2.10}$$

$$E(x)^2 = E(0)^2 + 2jx/(\epsilon_r \epsilon_o \mu) \tag{2.11}$$

where the characteristic length x_c is defined as the point from the contact interface towards the organic film, at which the charge density $p(x_c)$ decays to $p(0)/\sqrt{2}$. In our model, we assume that finite values for $p(0)$ or non-zero values for the electric field at the interface are reasonably valid. This characteristic differs from other assumptions that necessarily impose $E(0) = 0$ or $p(0) = \infty$. By extending the possible range of values for the charge density at the interface, our model is able to reproduce linear and quadratic j–V relations (ohmic and SCLC regimes, respectively). One of these situations is found when the characteristic length is much smaller than the length of device. In other words, it is represented by a large $p(0)$ where the contact delivers a large amount of charge into the bulk. In this case, (2.9) is reduced to the Mott-Gurney's equation:

$$j = \frac{9}{8}\mu\epsilon_r\epsilon_0\frac{V^2}{L^3} \tag{2.12}$$

The other limit is found when a relatively small amount of charge exists in the device. In this case, the characteristic length is larger than the length of device $x_c \gg L$, and expanding (2.9) in Taylor series [10], this reduces to Ohm's law:

$$j_{ohmic} = q\mu p\frac{V}{L} \tag{2.13}$$

Therefore, it is noted that an electric-field dependent mobility such as (2.2) does not lead to the analytical solutions (2.9)-(2.11). Instead, a numerical solution should be used to solve (2.2)-(2.5). Our main objective is to demonstrate that Eqs. (2.9)-(2.11) are still a good alternative to interpret the $j-V$ curves, even in the high electric field region.

2.3. Determination of the free charge density at the metal-organic interface

An analytical $j-V$ curve can be deduced from (2.9)-(2.11) when both $p(0)$ and μ can be expressed as a function of the applied voltage or the current density. As mentioned above, models that link the mobility with the electric field exist. Therefore, a first step forward is already achieved in relation to the mobility. However, so far, a relation of the free charge density at the metal–organic interface is not known. Our goal is to extract this relation from experimental data. Fundamental parameters that appear in a mobility model are extracted as well.

The free charge density is determined from experimental $j-V$ curves following an iterative scheme with three steps. First, an initial guess value for the mobility at zero electric field is proposed by analyzing the ohmic region. Second, we use an analytical approach. The electric field is assumed to be uniform with distance, and the charge density at the metal–organic interface and the parameters of the mobility model are determined by minimizing the differences between the experimental $j-V$ curves and predictions using (2.9)-(2.11). Third, we use a numerical approach. Now, the value of $p(0)$ obtained in step two is used as a boundary condition to solve numerically the transport Eqs. (2.2)-(2.5). The values of the variables obtained from the numerical approach are compared with the ones obtained in the analytical approach in step two. If they are different, a new iteration is performed. The full details are given below.

The final solution provides a distribution of the free charge density at the metal–organic interface as a function of the current density.

2.3.1. Analysis of the ohmic region. Defining the initial guess value.

The ohmic region is analyzed in order to establish an initial value for the mobility at zero electric field. At low fields, the mobility can be assumed constant $\mu = \mu(E,T) \approx \mu(0,T)$ [86, 97, 98] and $E(x) = V/L$ gives the average value of spatial electric field distribution. Therefore, the slope of the drift Eq. (2.4) (that in this case reduces to (2.13)) is proportional to the product of the free charge density and the mobility ($\mu \times p \approx \mu \times p(0)$). The value of $p(0)$ can be obtained from (2.7) and the estimation of V_{redox0} proposed in the previous section is used, whenever experimental data are measured in a low enough voltage range. In the case $V \gg V_{redox}$, we have seen that the condition $x_c \gg L$ must be fulfilled in the linear region of the $j - V$ curve. Combining this inequality with (2.10) and (2.13), we obtain:

$$p(0,V) \ll \frac{\varepsilon V}{2qL^2}, \qquad V \gg V_{redox} \tag{2.14}$$

The condition in (2.14) imposes an upper limit for the free charge density at the metal–organic interface in the ohmic regime.

This maximum also limits the range of possible values that the mobility can take. The slope k measured from an experimental $j-V$ curve in the ohmic region defines this range ($j = k \times V$; $k \equiv qp\mu/L$):

$$\mu(E \cong 0,T) \gg \frac{L^3}{\varepsilon_0 \varepsilon_r V} \times k \tag{2.15}$$

This result indicates that if the slope of the $j - V$ curve in the ohmic region is known, then a lower limit for the mobility can be established. This expression also provides a way to limit the possible range of realistic mobility values. In some cases, a broad range of experimental values of the mobility for the same material and temperature can be found in the literature. This is the case of poly(pphenylene vynilene) (PPV) where values of the mobility are found in the range $10^{-7} - 10^{-5}$ cm^2/Vs [78–81].

2.3.2. Analytical solution

Once limits for the mobility at low electric fields $\mu(0,T)$ and the free charge density $p(0)$ are established in the low voltage regime, a second approach to the solution is performed. In this step, the dependence of the mobility on the electric field is considered. For the reasons mentioned above, the CGDM model (2.2) is considered in this chapter. For the sake of simplicity, it can be expressed as a function of its fundamental parameters as $\mu = \mu(\mu(0,T), a, \sigma)$.

Initially, a uniform electric field $E(x) \approx E_0 = V/L$ is incorporated in (2.2). Neglecting the dependence of the electric field with the distance allows for the use of the analytical expression (2.9). This assumption is later examined. A value for $\mu(0,T)$ between one and ten times the value imposed by condition (2.15) in the ohmic region is introduced in (2.2). Values for parameters a and σ must also be introduced in (2.2). Some authors [99] find that σ should be in the range between 50 and 150 meV by the central limit

theorem in typical molecular doped polymers. Other authors [92, 100] confirm values for σ inside this range. The value of a is typically of the order of 1 nm [75]. However, some other authors [54, 65, 93] have found values for a in the range 0.3-2 nm.

This resulting mobility is introduced in (2.9), and a relation $V = V(j, p(0))$ is established. Then, pairs of experimental data $j_{exp} - V_{exp}$ are introduced in this relation, and the following set of equations is obtained: $V_{exp} = V(j_{exp}, p(0))$. From this set of equations, $p(0)$ is extracted as a function of the current density j_{exp} or applied voltage V_{exp}. The values for $p(0)$ must fulfill different physical criteria.

I A uniform distribution of $p(0)$ with the applied voltage should be expected in the ohmic region, and it must fulfill condition (2.14).

II In the transition from the ohmic to the SCLC regime, once space charge starts being created in the organic material, an increment of $p(0)$ with the applied voltage should be expected.

III If $p(0)$ is determined from $j - V$ curves measured at different temperatures, an increment of $p(0)$ with temperature should also be expected.

IV The values of $p(0)$ at low voltages should be consistent with the value estimated from the redox voltage V_{redox} (2.7).

V Organic diodes fabricated in the same conditions but with different lengths should show similar $p(0) - j$ relations.

VI Finally, the electric field obtained from (2.8) and (2.11) is checked and compared with the initial assumptions. The electric field is then averaged along the organic material and the result must be consistent with the uniform value considered initially.

Failure to comply any of these criteria leads to a modification of parameters a and σ or the mobility at low electric fields; a new iteration is repeated and a new distribution of $p(0)$ with the current density is provided.

2.3.3. Numerical solution.

Once convergence is achieved in the analytical step, the transport Eqs. (2.2)-(2.5) are solved numerically. For a given value of j, the values of parameters a and σ and the boundary condition $p(0)$, or $E(0)$, obtained in the previous step are introduced in these equations. The numerical solution provides a value for the applied voltage. The process is repeated until a current–voltage curve is completed and can be compared to the experimental data. In this step, parameters a and σ are varied until a good fitting is obtained. The convergence is fast as the values of the parameters obtained in the previous step are close to the final solution. In any case, a new examination of the initial hypothesis is done.

The solution for $p(0)$ as a function of j, obtained in the analytical step, comes from the initial consideration of a uniform with distance electric field. Thus, the average value of the electric field obtained in the numerical solution should be consistent with this assumption. If they are not the same, then the numerical average value of the electric field should be used in the analytical step and the process

is repeated until convergence is achieved. No iteration was necessary with any of the experimental data analyzed in this work, showing that the analytical procedure gives a very close solution to the final one.

2.4. Results and discussions

In this section, we apply our proposed model to hole-only organic diodes. We extract the values of the free charge density at the metal–organic interface from experimental data and perform a detailed quantitative analysis of the dependence of the current density with voltage, temperature and length of the organic-layer. We use current voltage characteristics taken from literature. Fig. 2.1 shows a comparison between experimental data (circles) [76] and our numerical results (solid line). The experimental $j - V$ curve depicted in this figure corresponds to a glass/ITO/PEDOT:PSS/LEP/Pd organic diode. The result of such a fitting is a finite value for the free charge density at the anode-organic interface. It is represented as a function of the current density in the inset of Fig. 2.1. Parameters $\sigma = 50$ meV and $a = 1.2$ nm are used in the mobility model (2.2). Both are within acceptable physical ranges defined above [54, 65, 75, 92, 93, 99, 100].

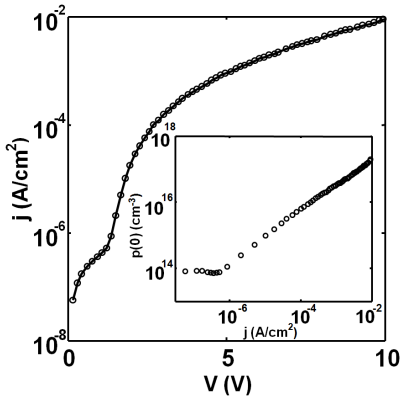

Figure 2.1: Experimental current–voltage characteristics for a glass/ITO/PEDOT:PSS/LEP/Pd organic diode taken from [76] at 295 K (open circles) ($L = 122$ nm and $\varepsilon_r = 3.2$). Our numerical results are shown in solid line using the parameters $\sigma = 50$ meV, $a = 1.2$ nm and $\mu_\infty = 1.28 \times 10^{-6}$ cm^2/Vs. Inset: free charge density at the metal–organic interface extracted with our analytical procedure and employed as a boundary condition in the numerical analysis.

The experimental data in Fig. 2.1 shows a transition from linear to quadratic regions. Our model explains this transition by means of the finite charge density at the metal– organic interface (inset in Fig. 2.1). At low voltages, the amount of injected carriers is low, compared to the existing thermally generated carriers; for this reason, the charge at the contact is constant. When the voltage is increased, the charge density increases, the electrode injects more holes than those that the material can transport and a space charge region is formed, limiting the current.

As mentioned in Section 2.2.1, different models have been proposed to interpret the quadratic region in the j—V curves of organic diodes and its transition at high voltages towards a $I - V^n$ relation ($n > 2$). However, these models pay less attention to the linear-quadratic transition. The simplest way to treat

this transition is by considering two expressions with constant mobility as in [69]: use (2.13) for the linear regime and (2.12) for the SCLC regime. Both expressions intercept at the inflection point:

$$V_x = \frac{qp_0L^2}{\varepsilon_0\varepsilon_r} \tag{2.16}$$

where p_0 is the background concentration of thermal free carriers. This inflection point can be defined as the voltage at which the average concentration of the injected charge is equal to the concentration of the thermally generated carriers [101, 102]. In Fig. 2.1, this inflection point is $V_x = 1.21$ V, and $p_0 = 1.44 \times 10^{16}$ cm^{-3} and it is deduced from (2.16). Such a value contradicts the initial hypothesis from which (2.12) is deduced, i.e. a zero electric field at the interface, which is equivalent to an infinite charge density at this point [18]. Our model solves this contradiction as it considers a finite boundary condition at the interface for the free charge density. Our model imposes a limit for the free charge density at the interface for the ohmic region depicted in Fig. 2.1: $p(0) << 10^{15}$ cm^{-3}. Values for the free charge density around or lower than 10^{14} cm^{-3} have been proposed previously [96]. The analysis of the experimental data in Fig. 2.1 with our model provides a value for the free charge density at the interface in the linear region around 10^{14} cm^{-3}.

In order to check the value of the free charge density, it is also determined from an estimation of the redox voltage. In the previous section, we have proposed how to estimate this voltage by determining the intercept of the linear region with the voltage axis and equating this to the redox voltage. For the data in Fig. 2.1, $V_{redox} = 0.02 \pm 0.01$ V. Introducing this value in (2.7), and assuming typical values for $\phi = 0.35$ V [8] and $\rho_m = 1.8 \times 10^{20}$ cm^{-3} [76], we find $p(0) = (4 \pm 2) \times 10^{14}$ cm^{-3}. Thus, the order of magnitude of the free charge density calculated by extrapolation of the $j - V$ curve to zero current agrees with the one obtained at low voltages (inset of Fig. 2.1).

At high voltages, a transition from a quadratic $j - V^2$ relation to a $j - V^n$ (with $n > 2$) relation is observed in Fig. 2.1. This transition has been observed previously and reproduced with electric-field dependent mobility models [76]. We reproduce this region with our calculations using a mobility at low electric fields $\mu(0, 295K)$=3.2×10^{-7} cm^2/Vs and a finite value of the free charge density at the interface. This value of the mobility is larger than the one obtained in [76]. A problem associated with an overestimation of the free charge density is an underestimation of the mobility. Different values of the mobility extracted in diodes and transistors with the same material are usually reported in the literature. One reason of this difference might be attributed to this overestimation of the free charge density in organic diodes. Our main contribution is to provide a plausible link between the free charge density at the interface with bias and that is valid over the entire applied voltage range.

2.4.1. Length of organic-material

An additional test for our method is to apply it to $j - V$ curves measured in organic diodes with the same material, but with different lengths. The $j - V$ curves measured with different lengths are reproduced with our model. These curves are depicted in Fig. 2.2. The symbols represent the experimental data from [76] and the solid lines show our calculations. The experimental data correspond to the same

diodes analyzed in Fig. 2.1. The values of the parameters used in our calculations are also the same. Fig. 2.3 shows the free charge density at the interface obtained in our calculations as a function of the current density. The results for the three lengths converge, showing no dependence with the length.

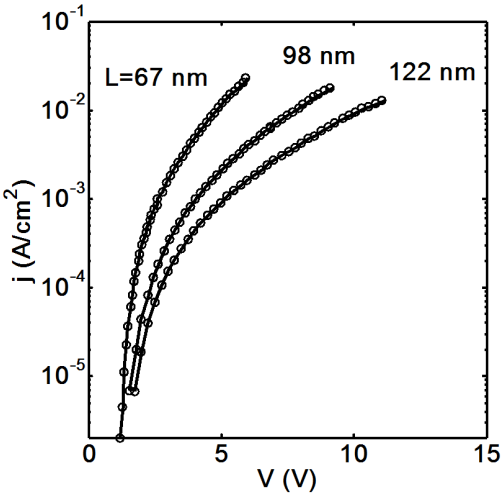

Figure 2.2: Comparison between experimental current–voltage curves [76] (symbols), measured at temperature of 295 K in glass/ITO/PEDOT:PSS/LEP/Pd diodes with different length (67, 98 and 122 nm), and our calculations. The parameters employed in the calculations are the same as in Fig. 2.1.

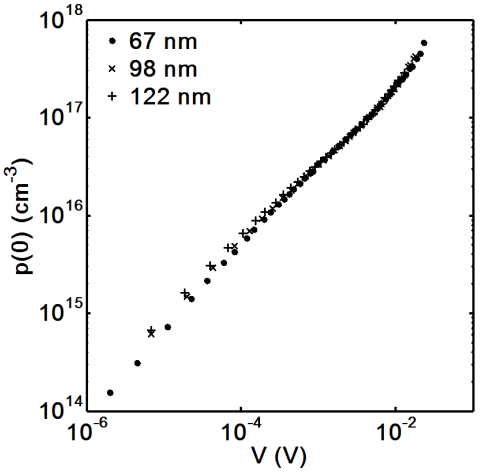

Figure 2.3: Free charge density at the interface as a function of the current density employed in the fitting of Fig. 2.2.

Fig. 2.4 shows a comparison between another set of experimental data measured in ITO/CuPc/Al diodes at 320 K [85] and our results. The curves correspond to devices with different lengths. In the simulation, $\sigma = 50$ meV and $a = 2$ nm are used for all devices. Both are within acceptable physical

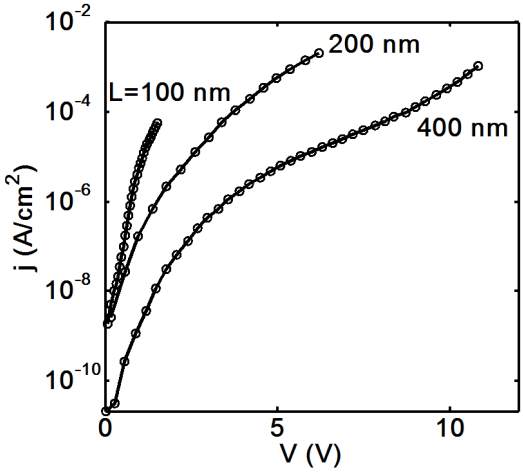

Figure 2.4: Experimental current–voltage characteristics (symbols) measured at 320 K in ITO/CuPc/Al diodes with different lengths: 100, 200 and 400 nm [85]. Our fitting results are represented with solid lines. Parameters μ(0,T = 320 K) =2×10^{-6} cm^2/Vs, $\sigma = 55$ meV and $a = 2$ nm are used in our calculations for all the curves.

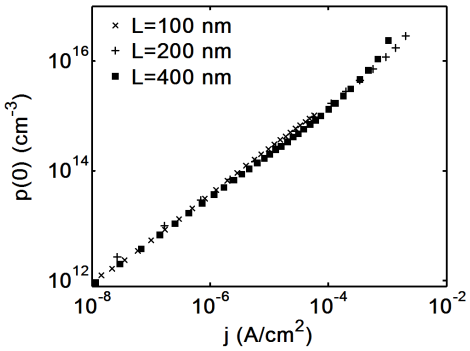

Figure 2.5: Free carrier charge density at the metal organic interface as a function of the current density used as a boundary condition in our calculations in order to fit the experimental data of Fig. 2.4.

ranges defined above [54, 65, 75, 92, 93, 99, 100].

In Fig. 2.5, the values of the free charge density at the interface $p(0)$ that are used in our calculations, are represented as a function of the current density. The three curves superimpose on each other, eliminating any dependence with the length of the organic material. In Figs. 2.3 and 2.5, we can observe a strong dependence of the free charge carrier density at the contact with the current. More specifically, a linear relation between $log(p(0))$ and $log(j)$ is found.

2.4.2. Temperature effects.

Fig. 2.6a shows another comparison between experimental data (symbols) of the same diodes analyzed in Fig. 2.1 and our calculated results (solid lines). Fig. 2.6b shows the free charge density at the

interface as a function of the current density used in this fitting. In this case, a linear behavior was not reported in [76], since the SCLC regime was the only one under test. Although the ohmic regime is not shown, the curves of the free charge density at different temperatures tend to converge at low injection, meaning that the ohmic regime is close to these values. It is interesting to observe that during the fitting procedure, different values of σ and a inside the range mentioned above are tested. Good fittings are also observed between the experimental data and our calculations with these different values. However, anomalous dependences of the free charge density curves with the temperature are observed. Therefore, non-physical solutions are ignored until a solution with physical meaning, such as the one observed in Fig. 2.6 is obtained.

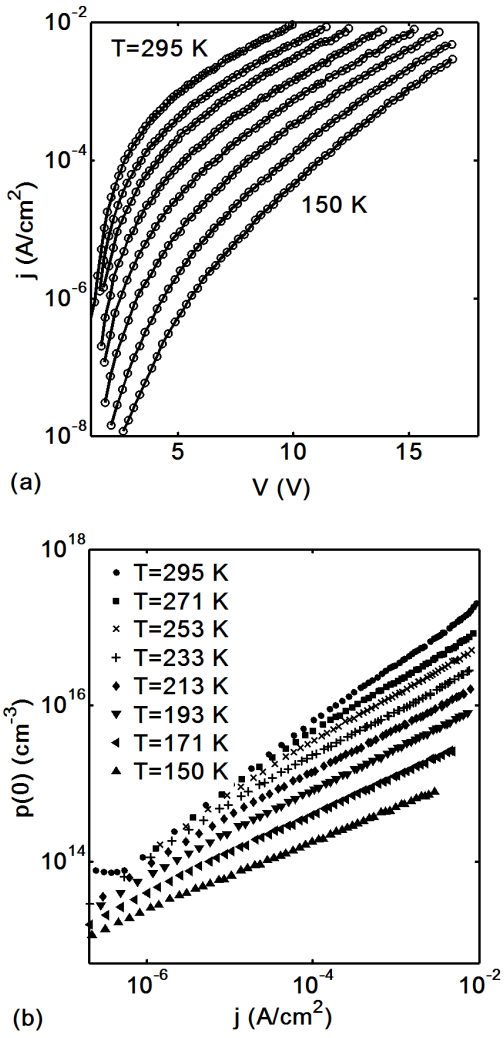

Figure 2.6: (a) Comparison between experimental current–voltage characteristics for a glass/ITO/PEDOT:PSS/LEP/Pd organic diode measured at T = 150, 171, 193, 213, 233, 253, 271 and 295 K from bottom to top (symbols) [76], and our numerical results (solid lines). $L = 122$ nm. (b) Free charge density at the metal organic interface as a function of the current density used in the fitting of (a).

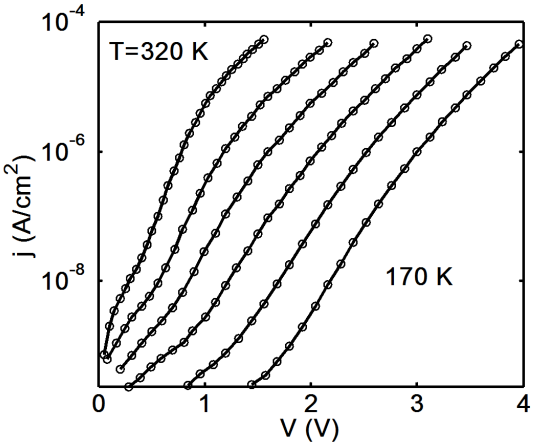

Figure 2.7: Comparison between experimental current–voltage characteristics (symbols) measured at different temperatures in ITO/CuPc/Al diodes (from 170 to 320 K in 30 K steps) [85] and our fitting results (solid lines). Parameters $\sigma = 55$ meV, $a = 2$ nm and $\mu(0, 320K) = 2 \times 10^{-6}\ cm^2/Vs$ are used in our calculations.

Fig. 2.7 shows another comparison between experimental current–voltage characteristics (symbols) measured at different temperatures in ITO/CuPc/Al diodes [85] and our numerical results (solid lines). Using parameters $\sigma = 50$ meV, $a = 2$ nm and $\mu(0, 320K) = 2 \times 10^{-6}\ cm^2/Vs$ in our calculations, we obtain an excellent agreement with the experimental data. Fig. 2.8 shows the free carrier charge density at the metal organic interface as a function of the current density extracted from our analytical procedure to fit the experimental data of Fig. 2.7. In Fig. 2.7, a small region at low voltages shows a linear behavior. This is reflected in Fig. 2.8 with an also small region of constant free charge density. The charge that is injected into the organic material is smaller than the existing thermally generated carriers and impurities. Due to the reduced range where the linear behavior is observed, the determination of the redox voltage produces a large error and the value of the charge density extracted by this method is not significant. Nevertheless, the transition from ohmic to SCLC regime can be observed in Fig. 2.8. We observe an increment of the whole $p(0)$ curve with temperature, meaning that more carriers are available when the temperature increases.

Another interesting remark is the fact that $log(p(0))$ is a linear function of $log(j)$ once space charge effects dominate. This behavior is also observed in Figs. 2.3 and 2.5.

2.5. Model for the space charge limited conduction - SCLC

In Figs. 2.3, 2.5 and 2.8, a linear relation between the logarithm of the free charge density and the logarithm of the current density is observed in the SCLC regime. This linear relation between logarithms is equivalent to writing:

$$p\,(0) = \left(\frac{j}{m}\right)^{\frac{1}{n}} \tag{2.17}$$

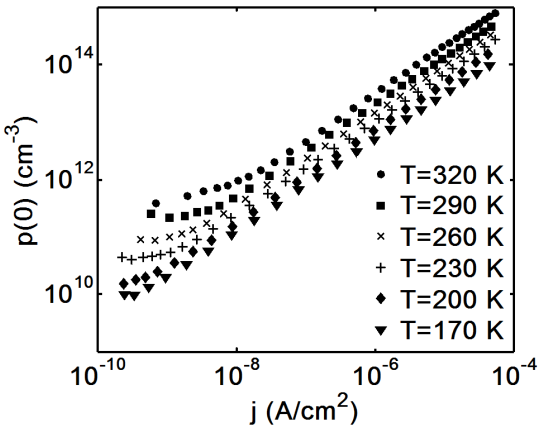

Figure 2.8: Free carrier charge density at the metal organic interface as a function of the current density used in our calculations to fit the experimental data of Fig. 2.7.

where m and n are empirical fitting parameters. When these two parameters were known, the initial estimation of $p(0)$ by our numerical procedure could be avoided and an analytical expression could be used instead by combining (2.2), (2.9) and (2.17).

By way of illustration, we have extracted m and n in (2.17) from the experimental data of Fig. 2.7. The result is $n = -2.269 \times 10^{-4}T + 1.329$ and $m = -1.739 \times 10^{-25}T + 6.786 \times 10^{-23}$. If we introduce these values in (2.17), combine the result with (2.9), and assume $E \approx V/L$ in (2.2), analytical $j - V$ curves are obtained. The resulting curves are represented in Fig. 2.9 in solid lines and compared with the experimental data (symbols). The result of this model is valid only in the SCLC regime, where an excellent fitting is obtained. However, this is a promising result as an analytical model can reproduce experimental $j-V$ curves. A complete model that reproduces the complete curve is desirable and is under research. This model could help to incorporate the effects of the metal–organic contact in previously developed compact models of other organic devices, such as organic thin film transistors [12, 72, 73]. Further work is also necessary in order to determine whether this result can be extended to other devices employing the same organic material and whether it can be generalized to other materials, defining a link between m and n and the organic material.

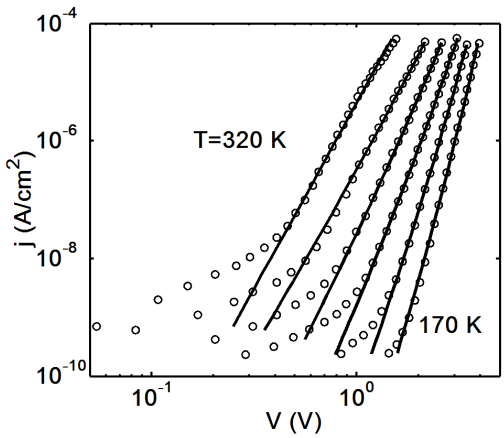

Figure 2.9: Comparison between experimental current–voltage characteristics (symbols) measured at different temperatures in ITO/CuPc(100 nm)/ Al diodes (from 170 to 320 K in 30 K steps) [85] and our results (solid lines) from (2.9), (2.10) and (2.17). The mobility model (2.2) is used assuming $E = V/L$ and $\mu(V/L, T)$; the model (2.17) is used with $n = -2.269 \times 10^{-4}T + 1.329$ and $m = -1.739 \times 10^{-25}T + 6.786 \times 10^{-23}$.

3

Space-charge and injection limited current in organic diodes: A unified model

3.1. Introduction

Research and technology development of organic/polymeric devices (hereafter the term organic is used for both) is now evolving rapidly due to some key advantages for niche applications [4, 51]. These advantages stem from the features of the organic materials and their low-cost manufacturing technology [4]. Some niche applications include low-cost, large-area, flexible and/or light weight electronics, displays or e-paper [98, 103]. However, more technological effort is required to improve the stability, reliability and performance of the organic semiconductor systems. In order to achieve this goal, a proper theoretical understanding of the electrical conduction mechanism in these materials and interfaces is needed. With this understanding, further improvements using better and more stable organic materials, interfacial layers and technological innovations become feasible.

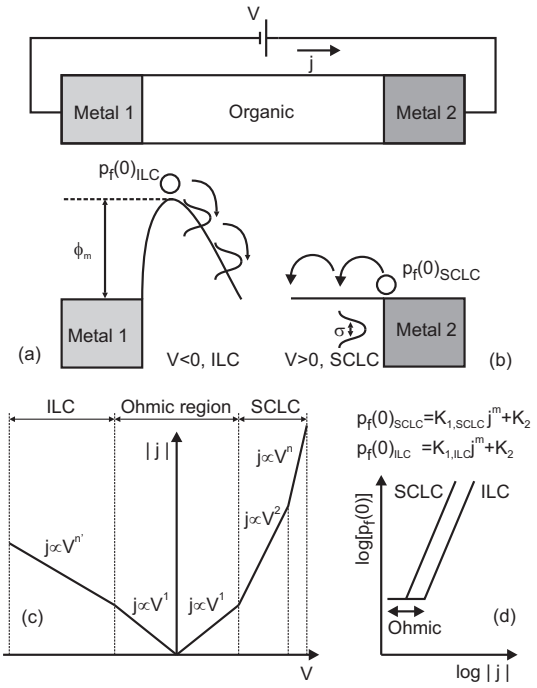

Figure 3.1: Sandwich-type device with two different metal-organic contacts. a) Contacts with a high energy barrier at the interface (ILC regime, $V < 0$). b) Contacts with low energy barriers (SCLC regime, $V > 0$) c) Typical current density vs. voltage curve for this structure. d) Our proposed unified relation between the current density and the free charge density at the interface. The physical meaning of parameters m, K_1 and K_2 is defined in the text.

For many organic devices, the metal-organic interfaces and contacts limit charge injection and transport [12, 104, 105]. Here, the injection of charge depends on different factors such as the height of the injection barrier, the applied electric field, the temperature, chemical reactions leading to interface dipoles, and band bending or Fermi level pinning [57, 61, 106, 107]. Devices operating under such a limitation are said to work in the injection-limited current (ILC) regime (Fig. 1(a) with $V < 0$). In other cases, the performance of the devices is not controlled by the injection barrier, but rather by the transport

of charge through the organic semiconductor [55, 68, 108]. The resulting current of this mechanism is referred as space-charge-limited current (SCLC) (Fig. 3.1b with $V > 0$).

In the past, ILC and SCLC regimes have been analyzed and modeled separately. There are models that study charge injection through a metal-organic interface [64, 109, 110] and models that treat the transport of charge along the organic material, basically by means of mobility models [67, 76, 85]. These models interpret the dependence of current density-voltage ($j - V$) curves on the electric field, the temperature and the kind of contact. Each model is able to reproduce current-voltage curves in the device while one of these mechanisms is dominant over the other [85, 110]. What is missing is a procedure that models the transition between these regimes. Moreover, even in situations where SCLC or ILC regimes are well established, the respective models fail to reproduce the low-voltage regime in the current-voltage curves, where an Ohmic relation is usually found [76, 111].

In the previous chapter, we proposed a single model to interpret the whole range of current-voltage curves in organic diodes operating under the SCLC regime [112]. This whole range includes the following regions and their respective transitions (Fig. 3.1c for $V > 0$):

- an Ohmic region observed at low voltages and usually described by Ohm's law [69];
- a quadratic relation at moderate electric fields usually described by Child's law [18]; and
- a higher than quadratic regime, usually described with mobility models where the dependences with temperature, electric field and/or charge carrier concentration are introduced.

Our model solves the transport equations in the semiconductor by considering a finite and unique value for the free charge density at the metal-organic interface (named $qp_f(0)_{SCLC}$ in Fig. 3.1b). It establishes a relation between the current-density j and the value of this boundary condition.

In this chapter, we extend this SCLC model to the ILC regime (Fig. 3.1c for $V < 0$), providing a unified treatment of all the different conduction modes that take place in the transport of charge in organic diodes. Our first objective is to reduce all the physical mechanisms included in the injection through the metal-organic interface to a specific value of the free charge density at the interface (named $qp_f(0)_{ILC}$ in Fig. 3.1a). Our second goal is to propose a relation between the current density and the free charge density similar to the one obtained for the SCLC mechanism. The only difference should be the value of a parameter associated to the height of the energy barrier at the interface. The model we are developing in this chapter is depicted in Fig. 3.1d. The meaning of the model parameters are described throughout the work.

In the past, injection models have been developed by considering the essential physical mechanisms that take part during the charge injection from a metal into a random hopping system [17, 55, 64, 106, 109, 110]. One attractive model was proposed by Arkhipov and collaborators [17, 106, 110]. They succeeded in interpreting the weak temperature dependence of the injection current, observed in experimental data and not explained by the classical thermionic injection model. This model has been used to interpret the field and temperature dependence of charge injection in organic diodes [68, 111, 113]. Despite its success with researchers, the model shows certain limitations. Its developers showed that it failed to reproduce current-voltage curves in organic diodes with lower than 0.2 eV

energy barriers [110]. Other authors have failed to apply it to the low voltage range of current-voltage curves [74, 85, 111]. In circuit simulation, a much more compact model with less number of parameters would also be preferable. It would also reduce the computing time necessary to extract the value of these parameters from sets of experimental data. In this chapter, we present such a model.

3.2. Modeling the SCLC and ILC regimes

The transition from SCLC to ILC regimes has been studied in the past by combining models for injection with the transport equations. An example of this can be found in [106], where the authors propose a two-step procedure to reproduce $j - V$ curves in an organic diode. In one step, the model relates the injection current and the parameters associated with the injection mechanisms to a boundary value for the electric field at the interface, $F(0)$. In the second step, this value is used as boundary condition in order to solve the transport equations, which provide a value for the voltage drop along the device. The pair of values thus obtained with this model -injection current and voltage drop, should match experimental $j - V$ data. The evaluation of the electric field at the interface requires that the charge injection process is described as thermally-assisted tunneling from the delocalized states of the metal into the localized states of the organic semiconductor. The injection process depends on the mean barrier height, the image potential, the energetic disorder and the applied electric field.

In this chapter, we make use of the transport equations exclusively, independent of the value of the energy barrier at the interface, even in the cases where the conduction mechanisms are dominated by charge injection. This, in turn, will affect the value of the electric field at the interface [106]. In our case, we aim to find a relation between the free charge density at the interface and the experimental current. We study this relation in devices with different organic materials, different metal contacts and at different operating temperatures. We analyze how this boundary value for the free charge density evolves with these variables.

Our model emerges from the main ideas developed in a previous work [8]. In order to reproduce current voltage curves measured in organic diodes, we demonstrated the importance of considering a finite value for the free charge density at the metal-organic interface, instead of an infinite value as assumed in Child's law. Initially, this value was considered constant throughout an entire $j - V$ curve. Later, we demonstrated that this value should vary with the current density [112]. Otherwise, the widely observed transition from ohmic to SCLC regimes in $j - V$ curves could not be explained.

The idea of considering different mechanisms that contribute to the flow of charge through the diode, such as injection, transport of charge and redox reactions at the interface, also comes from our earlier publication [8]. Originally, we estimated the relative contribution of all of them from the analysis of $j - V$ curves. In the present chapter, we derive a more robust model in which the information of all these mechanisms is encapsulated in the value of the free charge density at the metal-organic interface. The advantage is that it provides a continuity between the different regimes observed in a current-voltage curve.

We also incorporate other improvements to the first idea, such as an electric field dependent mobility model, which allows for the interpretation of the SCLC regime at high electric fields [112]. Finally, the

comparison with the thermionic injection model is not necessary. In addition, we compare our results with Arkhipov's model allowing for the interpretation of $j-V$ curves at much lower temperatures [106].

With this in mind, we consider the transport of charge from the interface into the bulk of the organic material. The origin of the free charge density at the interface can be diverse: injected from the metal, generated thermally from doping impurities (natural or introduced), or created by redox mechanisms [8]. The volume density of free charges is termed $p_f(x)$ (holes in a hole-only device) and its value at the interface is $p_f(0)$. These free charges are transported through the organic material mainly by the action of an electric field $F(x)$. The drift current density is given by:

$$j = q\mu[T, F(x), p_f(x)]p_f(x)F(x) \tag{3.1}$$

where q is the absolute value of the electron charge, x is the distance from the injecting electrode and $\mu[T, F(x), p_f(x)]$ is a mobility model with a generic dependence on the temperature, electric field and charge concentration. Due to the lack of long-range order in the organic semiconductors, the electrical transport mostly takes place by hopping from one localized state to the next. A correlated Gaussian disordered model (CGDM) was proposed to explain the electrical transport [89], where spatial and energy disorders depend on each other, with the idea that a changing environment for a given molecule will have an influence on its energetic position [89, 114]. This model, given in the expression below, has been widely used because it includes the effects of varying temperatures and electric fields [85, 89]:

$$\begin{aligned} \mu_{CGDM}(T,F) &= \mu(T,0)\exp(\gamma\sqrt{F}) \\ \mu(T,0) &= \mu_\infty \exp\{-[3\sigma/(5k_BT)]^2\} \\ \gamma &= 0.78\{[\sigma/(k_BT)]^{3/2} - \Gamma\}[qa/\sigma]^{1/2} \end{aligned} \tag{3.2}$$

where a is the intersite spacing, k_B is the Boltzmann's constant, T is the temperature, σ is the width of the Gaussian density of states (GDOS) caused by the electrostatic coupling of a charged site to neighboring dipoles, Γ is related to the positional disorder, and usually $\Gamma \approx 2$. Recently, several authors have studied the dependence of the mobility with the carrier concentration, which they termed the enhanced Gaussian disordered model (EGDM) [76, 96]. In this chapter, we consider the CGDM, neglecting the explicit dependence of the carrier concentration on the mobility. Nevertheless, we stress the importance of the carrier concentration as a boundary condition when solving the Poisson's equation, which relates this variable with the electric field:

$$\frac{dF}{dx} = \frac{q}{\varepsilon_0\varepsilon_r}p(x) \tag{3.3}$$

where ε_r and ε_0 are the relative permittivity and the permittivity of the free space, respectively. The free charge density is a fraction θ of the total charge density: $qp_f = \theta qp(x)$. The free carriers hop around the so called transport energy. Charge carriers below this energy mostly do not contribute to the conductivity. Thus, the total carrier concentration $p(x)$ can be described as the sum of mobile, free charge carriers $p_f(x)$ and immobile charge carriers pt trapped in the tails of the Gaussian or exponential density of states or other traps present in the semiconductor [115]. With the parameter θ, we implicitly

incorporate the concept associated to the carrier concentration dependent mobility found in the EGDM: the filling of the Gaussian density of states, where lower states act as charge traps.

The set of transport equations is completed with the integral of the electric field to find the voltage along the device:

$$V = \int_0^L F(x)dx \tag{3.4}$$

3.2.1. Extraction of $p_f(0)$ from experimental $j - V$ curves

Here, we propose a procedure to extract the values of $p_f(0)$ as a function of the current density j and the parameters of the mobility model (3.2) from experimental $j - V$ curves. It is an iterative procedure that is applied to all the experimental data (j, V) in the curve. In the first place, (3.1) and (3.3) are combined into the integral:

$$\int_{F(0)}^{F(x)} \frac{\mu\theta\varepsilon_r\varepsilon_0 F dF}{j} = \int_0^x dx \tag{3.5}$$

with $F(0) = j/[q\mu p_f(0)]$. If the values of the parameters of the mobility model are known or initial guessed values are provided, the determination of $p_f(0)$ or $F(0)$ as a function of j or V can be obtained easily with a typical root-finding method. The experimental values of V and j are introduced in (3.4) and (3.5), respectively. An initial guessed value $F^*(0)$ is introduced in (3.5) to obtain a distribution of the electric field $F^*(x)$:

$$\int_{F^*(0)}^{F^*(x)} F\exp(\gamma\sqrt{F})dF = jx/(\mu(T,0)\theta\varepsilon_r\varepsilon_0) \tag{3.6}$$

The resulting distribution is introduced in (3.4) to obtain the value of the voltage V^*,

$$V^* = \int_0^L F^*[F^*(0), x)]dx \tag{3.7}$$

The value of $F^*(0)$ is iteratively modified until the relative difference is less than a certain tolerance. In our calculations, we have considered a tolerance of 0.1 %.

The solution $p_f(0)$ as a function of j depends on the values of the parameters of the mobility model (3.2) [$\mu(T,0)$, a and σ] and the free to total charge ratio θ. Thus, different solutions can be obtained, but only physically-based ones are acceptable. In order to optimize these parameters we used the following criteria.

Except in situations where instabilities are present, the value of θ can be considered as a constant. The initial guess value is $\theta = 1$. The final value for θ is obtained by the comparison of the total charge density $qp(0) = qp_f(0)/\theta$ determined with the above iterative procedure with the value qp, where p is determined from the density of localized carriers [17, 106]:

$$p(x) = \int_{-\infty}^{E_{tr}} dE \frac{g(E)}{1 + (q\mu N_t F/j)\exp(E/k_B T)} \tag{3.8}$$

with $F = F(0)$ and j is substituted with the experimental current density. The integral in (3.8) is

evaluated up to the transport energy, which can be estimated as $E_{tr} = 1.2k_BT[6\gamma'^3/(\pi N_t)]^{1/3}$ [17], for typical values for the volume density of sites $N_t = 10^{19} - 10^{21}$ cm^{-3}, and the inverse localization radius $\gamma' = 4$ nm^{-1}; $g(E)$ is the Gaussian density of states. The value of θ is iteratively modified until $|[p(0) - p^*(0)]/p(0)|$, evaluated for the entire $j - V$ curve, is less than a certain tolerance.

The value of the parameters of the mobility model must fulfill some conditions. In the case of the CGDM, σ and a must be in the range between 40-150 meV [92, 99] and in the range 0.3-2 nm [54, 75, 100], respectively. The values of $\mu(T, 0)$ must be consistent with the ones found in the literature. The convergence procedure is very sensitive to the parameters a and σ because they affect the value of the integral in (3.6), mainly in the high electric field region. It is convenient to split the $j - V$ curve into two regions to accelerate the fitting. At low electric fields, we can neglect the effect of parameter a. Thus, $\mu(T, 0)$ and σ can be found. Then, the high electric field region is analyzed to determine a. Even in these conditions, different $p_f(0) - j$ relations can be found, being necessary the next step.

The value of $p_f(0)$ is studied as a function of current density, temperature, and/or energy barrier height. The study of the evolution of $p_f(0)$ vs. j curves with the temperature for the same metal contact or the evolution of these curves extracted for the same organic material with different metal contacts helps in finding a physically acceptable solution. Erroneous values for these parameters can lead to anomalous behaviors of the free charge density, such as a decrease of the free charge density when temperature increases or when the energy barrier height decreases, or anomalous non-constant values of the free charge density in the Ohmic region. In these cases, the values of the mobility model parameters are varied and the process of finding a different $p_f(0) - j$ relation is repeated.

The objective of this study is to apply this procedure to $j - V$ curves measured in different organic diodes, in order to establish a correlation between the different $p_f(0) - j$ relations with the organic material, the height of the energy barrier and doping impurities in the material. Then, a model for the current density as a function of the free charge density at the interface, in which the parameters depend on the organic material, the height of the energy barrier and doping impurities in the material, is proposed. Finally, in order to validate our model, we compare the extracted values of the free, $p_f(0)$, and total, $p_f(0)/\theta$, charge density with well-established and widely used models [17, 106, 110].

3.2.2. Validation with injection models

In Arkhipov's model, given a current density $j = j_{inj}$, a boundary condition for the electric field $F_o = F(0)$ is estimated from the charge injection rate [110]:

$$j_{inj} = q\nu_0 \int_{a'}^{\infty} dx_0 exp\left(-2\gamma' x_0\right) w_{esc}(x_0) \times \tag{3.9}$$
$$\int_{-\infty}^{\infty} dE' Bol(E') g[\Delta - qF_o x_o - q^2/(16\pi\varepsilon_0\varepsilon_r x_o) - E']$$

where ν_0 is the frequency of a hop, a' is the distance from the electrode to nearest hopping sites (~ 1 nm), γ' is the inverse localization radius, N_t the volume-density of sites, σ is the width of the Gaussian distribution, Bol(E') is the Boltzmann's function, $g(E)$ is the Gaussian distribution, Δ the height of

barrier and E is the energy. This model considers the injection of the charge from the electrode's Fermi level into localized states of the Gaussian distribution of hopping sites of the organic semiconductor. To apply this equation, the condition of weak injection must be fulfilled. It requires the potential energy next to the contact to be positive relative to the Fermi level of the metal, yielding $\Delta > 0.2$ eV, and imposing a limit in the application of this model [110].

The value of F_o, extracted from (3.9), is introduced in the transport equations (3.1), (3.3) and (3.4) to find the voltage drop in the device. In the formulation in [17, 106], the total carrier density, $p(x)$, introduced in the Poisson's equation (3.3) is practically equal to the density of localized carriers (3.8). This expression is frequently used with a constant mobility, although these authors recognized that this is an approximation that is not valid for a strong dependence of the mobility on the electric field [106]. In order to be consistent, throughout this chapter, we employ the CGDM for the mobility in (3.8), $\mu = \mu_{CGDM}(T, F)$.

In the following section, we compare the values of the total charge-carrier density and the free or mobile charge-carrier density at the interface, $p(0)$ and $p_f(0)$, respectively, extracted with our unified treatment and this injection model. To do this, published experimental $j - V$ curves of organic diodes with different energy barriers at the interface, under the ILC regime, are considered.

3.3. Results

In this section, our procedure is applied to experimental $j - V$ curves operating in the ILC regime. The results of our procedure are compared with Arkhipov's injection model. A compact relation between the charge-carrier density at the metal-organic interface and the current density is proposed after this validation. Then, this compact model is verified with a study of organic semiconductors with different barriers. SCLC and ILC are analyzed under our unified treatment. Finally, a study of the static electrical characteristics with the temperature is given.

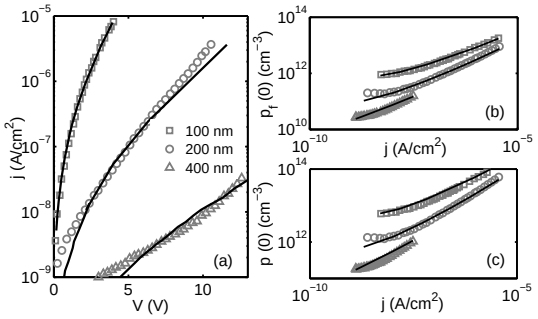

Figure 3.2: a) Comparison between experimental current density vs. voltage curves (symbols), measured at 320 K in ITO/CuPc/Al diodes [85] with different lengths, and Arkhipov's model (solid lines) (the injection is from Al). Our model fits the experimental data within the 0.1 % (not shown). b) Free and c) total charge-carrier density at the metal-organic interface as a function of the current density extracted from the experimental data of Fig. 3.2a with Arkhipov's model (solid lines) and with our model (symbols).

3.3.1. Validation of the procedure

We apply our procedure to the experimental $j-V$ curves shown with symbols in Fig. 3.2a. They were measured in ITO/Copper phthalocyanine(CuPc)/Al diodes with different lengths ($L = 100$, 200 and 400 nm), and with Al as the injecting contact [85]. The height of the injection barrier is 0.6 eV. Our model [(3.2),(3.4) and (3.5)] is used to determine the values of $p_f(0)$ and $p(0)$ (symbols in Fig. 3.2b and Fig. 3.2c, respectively) to exactly reproduce the experimental $j-V$ curves. When we say exactly throughout the chapter, we mean that the relative difference between our calculations and the experimental data is less than a certain tolerance (0.1 % in this work). To avoid cluttering the graphs, we do not superimpose our calculations over the experimental data. The values of the parameters of the mobility model employed in our calculation are $\sigma = 55$ meV, $a = 2$ nm and $\mu(320\text{ K}, 0) = 2 \times 10^{-6}$ cm^2/Vs. The experimental curves in Fig. 3.2a are also treated with Arkhipov's model [106] (solid lines in Fig. 3.2a). The fit to the data at small currents is not too good due to the reduced accuracy of the measurements [85]. The values of $p_f(0)$ and $p(0)$ extracted from (3.8) and (3.9) are shown with solid lines in Fig. 3.2b and Fig. 3.2c. The parameters employed in this model are: $\sigma = 55$ meV, $\mu(320\text{ K}, 0) = 2 \times 10^{-6}$ cm^2/Vs, $a = 2$ nm, $\nu_0 = 10^{12}$ Hz, $T = 320$ K, $\varepsilon_r = 2.1$, $\Delta = 0.6$ eV, $N_t = 10^{19}$ cm^{-3}, $\gamma' = 4$ nm^{-1}, $E_{tr} = 0.8$ eV, $a' = 0.5$ nm for $L = 100$ nm, and $a' = 0.9$ nm for $L = 200$ and 400 nm. These parameters are consistent with values reported in the literature [17, 52, 106, 110, 113]. An excellent agreement is observed between our model and Arkhipov's model. The advantages of our method are the reduced computational time, it is around 600 times faster than Arkhipov's model, and the reduced number of parameters employed, basically the ones associated to the mobility model and the free to total charge ratio θ, that in this case is $\theta = 0.3$. In Arkhipov's model, the total charge-carrier density $p(0)$ is evaluated from (3.8) and additional parameters to model the transitions from the metal to the organic material are needed (see eq. (3.9) above). Our model does not intend to substitute this or other injection models that has, on many occasions, successfully linked experimental data with the physical mechanisms that take part during injection [55, 64, 109, 110]. Our objective is to provide a more compact and less computing-time alternative to previously developed injection models. At the same time, we aim to interpret the transitions among the three cases - SCLC, ILC and Ohmic regimes.

3.3.2. Barrier height effects

In Fig. 3.3a, we analyze again experimental data measured in the ITO/CuPc/Al diodes with different lengths [85]. In this case, we study the effect of the injecting contact. The $j-V$ curves represented with open symbols correspond to Al as the injecting contact. The curves measured by injecting from the ITO are represented with crosses. In this last case, the height of the barrier is low, 0.05 eV. Injection models are not valid for a typical SCLC regime like this. Our procedure extracts the free charge-carrier density in both regimes using the same set of parameters for the fitting in Fig. 3.2. The result is seen in Fig. 3.3b. The open symbols correspond to the high barrier contact (Al) and the crosses to the low barrier contact (ITO). As expected, the amount of free charges at the interface is higher for the lower-barrier case.

All the curves in Fig. 3.3b show a flat region at low current densities, corresponding to the existing

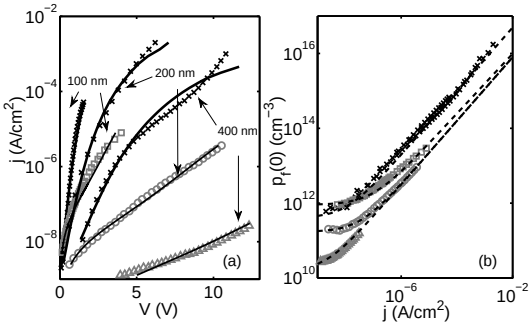

Figure 3.3: a) Comparison between experimental current-voltage curves (symbols), measured at 320 K in ITO/CuPc/Al diodes with different lengths [85], and our model (3.10) with parameters in Table 3.1 (solid lines). b) Free charge-carrier density at the metal-organic interface (symbols) extracted with our procedure to reproduce *exactly* the experimental data of Fig. 3.3a. The dashed lines follow the empirical model (3.10) with the parameters of Table 3.1. The injection from the Al and ITO electrodes is represented with open symbols and crosses, respectively.

Table 3.1: Fitting parameters used in (3.10), (3.4) and (3.5) to reproduce the experimental data in Fig. 3.3a.

Electrode	K_1 (cm^{2m-3}/A^m)	m (-)	K_2 (cm^{-3})
ITO(100 nm)	1.7×10^{18}	0.8	4.0×10^{11}
ITO(200 nm)	1.7×10^{18}	0.8	4.0×10^{11}
ITO(400 nm)	1.7×10^{18}	0.8	2.0×10^{11}
Al(100 nm)	3.9×10^{17}	0.8	9.0×10^{11}
Al(200 nm)	2.4×10^{17}	0.8	1.5×10^{11}
Al(400 nm)	2.4×10^{17}	0.8	1.0×10^{10}

thermally generated carriers in the semiconductor. The effect of these charges is seen as a linear or Ohmic trend on the $j - V$ curves. At higher current densities, the amount of injected charges surpasses this threshold, making a transition from Ohmic to ILC or SCLC (Al or ITO cases, respectively). In the SCLC case, the relation $p_f(0) - j$ is independent of the length of the organic material. In the ILC case, the curves diverge at low current densities, but tend to converge at high current densities to the dashed line drawn in Fig. 3.3b. The reason of this divergence is due to one of the mechanisms that control the injection regime: the reduction of the energy barrier due to the Poole-Frenkel effect, being more important for short lengths, thus increasing the injected charge.

At high current densities, the $p_f(0) - j$ relations in both regimes are linear and parallel, when plotted on a logarithmic scale (Fig. 3.2b). We propose to model the complete relation as (Fig. 3.1d):

$$p_f(0) = K_1 j^m + K_2 \tag{3.10}$$

where m is the slope in the logarithmic scale of the $p_f(0) - j$ relation at high currents, the parameter K_1 controls the parallel displacement of the $p_f(0) - j$ relation and K_2 controls the flat region at low

currents. In Fig. 3.3b, the model (3.10) with the values of the parameters of Table 3.1 is represented in dashed lines. The parameter K_1 is greater for the low barrier case. It depends on an effective barrier seen by the carriers at the metal-organic interface. The parameter m is the same for the different curves represented in Fig. 3.3b. This slope is unaffected by the energy barrier at the interface or the thermal carriers, which can be detected at low current densities and do affect the parameter K_2. Thus, only intrinsic properties of the organic material may alter parameter m. Combining this model (3.10) and the parameters of Table 3.1, with (3.4) and (3.5), the solid lines in Fig. 3.3a are obtained, showing very good agreement with the experimental data. Only, for the low barrier case and length greater than 200 nm is the fitting not so good. One reason may be the large sensitivity of the current density to the value of the free carrier density at the interface. The relative difference between the free carrier density shown as symbols in Fig. 3.3b), which correspond to the exact fitting to the experimental data in Fig. 3.3a, and the model (3.10) (dashed lines) is no greater than 10 % for all the points. However, the relative difference between the experimental and theoretical $j - V$ curves in Fig. 3.3a can increase to 30 % in some cases. This means that an uncontrolled modification of the free charge density at the interface can greatly affect the value of the current density along the device.

In order to check whether our proposed $p_f(0) - j$ relation (3.10) can be applied to other materials and contacts, we analyze the experimental $j - V$ curves (symbols) in Fig. 3.4a [116]. The experimental data were measured at 300 K and correspond to dendrimer-based diodes with different contacts: ITO, Pt and Au. In this case, all the diodes have the same length, $L = 100$ nm. Dendrimers are novel forms of organic molecules. Their properties of solubility and light emission color can be tuned separately due to the spatial separation of their functional properties. The dendrimer core controls the color of light emission and the electron affinity and the surface groups control the solubility. The studied dendrimer has cores of fac-tris(2-phenylpyridine) iridium, [(Irppy)3], with phenylene dendrons covalently bonded to it [116].

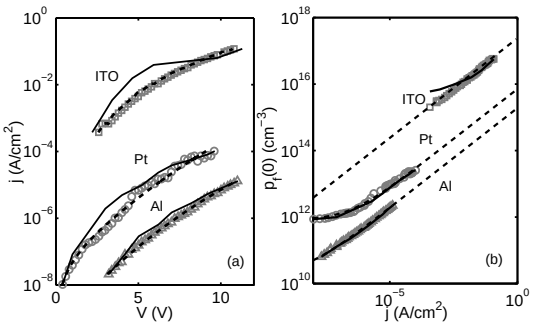

Figure 3.4: a) Comparison of experimental $j - V$ curves in dendrimer-based diodes with different contacts (ITO, Pt and Au) [116] (symbols) with Arkhipov's model (solid lines) and our calculation (dashed lines) using (3.10) and the parameters of Table 3.2. b) Free charge-carrier density at the metal-organic interface to reproduce exactly the experimental data of Fig. 3.4a (symbols); determined from Arkhipov's model (solid lines); and from our empirical model (3.10) (dashed lines) with the parameters of Table 3.2.

As the energy barrier is high in the three cases, we again compare our procedure to determine the boundary value $p_f(0)$ (symbols in Fig. 3.4b) with Arkhipov's model (solid lines). Our $p_f(0)$ (symbols),

Table 3.2: Fitting parameters used in (3.10), (3.4) and (3.5) to reproduce the experimental data in Fig. 3.4a.

Electrode	Δ (eV)	K_1 (cm^{2m-3}/A^m)	m (-)	K_2 (cm^{-3})
ITO	0.40	2.4×10^{17}	0.6	-
Pt	0.61	7.1×10^{15}	0.6	8×10^{11}
Au	0.69	1.9×10^{15}	0.6	2×10^{10}

extracted from the transport equations (3.4) and (3.5) to exactly fit the experimental data of Fig. 3.4a, was obtained with $\gamma(300\ \mathrm{K}) = 3.4 \times 10^{-3}\ \mathrm{V}^{-1/2}\ \mathrm{cm}^{-1/2}$ and the mobility at low electric field $\mu(300\ \mathrm{K}, 0) = 9.3 \times 10^{-7}\ \mathrm{cm}^2/\mathrm{Vs}$. These values of the mobility coincide with the ones obtained from time-of-flight (TOF) measurements [117]. The parameters used in Arkhipov's model are: $\mu(300\ \mathrm{K}, 0) = 9.3 \times 10^{-7}\ \mathrm{cm}^2/\mathrm{Vs}$, $\nu_0 = 10^{13}$ Hz, $\varepsilon_r = 3$, $a' = 0.7$ nm, $N_t = 10^{19}\ \mathrm{cm}^{-3}$, $\sigma = 50$ meV, $\gamma' = 4\ \mathrm{nm}^{-1}$ and $E_{tr} = 0.71$ eV. The height of the energy barriers Δ is shown in Table 3.2 [116]. The $p_f(0) - j$ relations, extracted with both procedures (symbols and solid lines in Fig. 3.4b, respectively), are in good agreement. In addition, the dashed lines in Fig. 3.4b correspond to our model (3.10) with the parameters of Table 3.2. Introducing this relation in (3.4) and (3.5), the dashed lines in Fig. 3.4a are derived. This excellent agreement with the experimental data is controlled with the three parameters of (3.10). The dependence with the electrode or the energy barrier at the interface is controlled with the parameter K_1. K_1 reflects the fact that the lower the height of the energy barrier is, the greater the value of $p_f(0)$ is obtained. The parameter K_2 controls the region of low voltages, where the thermal carriers dominate over the injected charge. Thus, we can establish a correlation between K_2 and the sources of these thermal carriers, such as doping impurities, traps or defects. Finally, the parameter m is constant for the three cases represented in the figure. In this case, a correlation can be assumed between the kind of organic semiconductor and this parameter m.

3.3.3. Temperature effects

In this section, we check our procedure with experimental data taken at different temperatures. We also show how our procedure can be adapted to other mobility models necessary to interpret the transport of charge in certain organic semiconductors. This is the case of pentacene, in which the mobility of charge carriers shows a dual behavior. Increasing mobilities around room temperature and decreasing mobilities at low temperatures, when the temperature increases, have been detected in different experimental results [118]. Hopping and band theory models, [119–121] respectively, have been employed to interpret these two different trends. In this regard, other authors proposed to model the mobility as the sum of two contributions, $\mu = \mu_{hop} + \mu_{band}$, [118, 122, 123] where μ_{band} is related to the coherent electron transfer that dominates at low temperatures and μ_{hop} is related to hopping transport (incoherent electron transfer) that dominates at higher temperatures. Different experimental measurements show that below a fixed temperature, the mobility follows a power-law and decreases with temperature [124].

Combining these ideas, we propose to model the mobility for these kinds of material as:

$$\mu = \mu_{CGDM}(T, F) + \mu_0 T^{-n} \tag{3.11}$$

in which we consider the CGDM model for the mobility as the hopping model. We introduce this idea in our procedure to determine the evolution with temperature of the $p_f(0) - j$ relation from the $j - V$ curves shown in Fig. 3.5a. If we used only the CGDM as in the other experimental data of the chapter, we would obtain an increment of the concentration of free charges when the temperature decreases, which lacks any physical meaning. These measurements on Ag/Pentacene(Pn)($L = 100$ nm)/Ag diodes at different temperatures were measured in both forward and reverse modes [125]. An asymmetry in the curves was detected, despite using the same contact material. This asymmetry was attributed to interfacial differences during the fabrication process. The authors distinguished between pentacene-on-Ag interfaces, that form an ordered "thin film phase" structure with a hole injection barrier of 0.6 eV (circles in Fig. 3.5a), and the Ag-on-pentacene interface, in which the Ag is directly evaporated on pentacene, forming a nearly Ohmic Ag/Pentacene barrier (crosses in Fig. 3.5a). They also commented that their experimental data could not be explained with a field-dependent mobility model used for similar observations [126–130]. They suggested to incorporate the anisotropic band formation in the organic material into the hopping model.

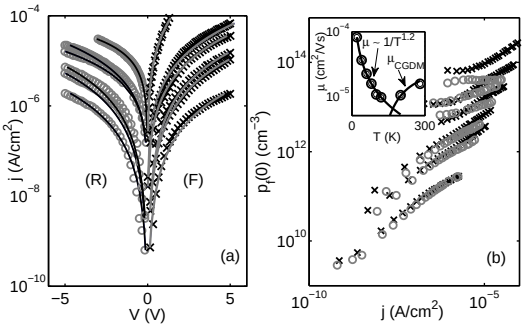

Figure 3.5: a) Comparison of current-voltages curves measured in a (Ag/Pentacene/Ag) diode at different temperatures (symbols) [125] with our numerical results using (3.10) and the parameters of Table 3.3 (solid lines). b) Free charge-carrier density to fit exactly the experimental data of Fig. 3.5a (T = 280, 120, 80, 60, 40 and 20 K from top to bottom; circles in forward bias and crosses in reverse bias). Inset: Values of the mobility used in the fitting.

Our model exactly matches the $j - V$ curves shown in Fig. 3.5a by using the values represented in Fig. 3.5b as a boundary condition for the free charge-carrier density at the interface, and the values of the mobility shown in the inset of this figure. The solid lines in the inset show the two different trends in the mobility model (3.11). The values of the parameters introduced in the mobility model (3.2) and (3.11) are $\mu_\infty = 3 \times 10^{-5}$ cm^2/Vs, $\sigma = 30$ meV, $a = 0$ nm and $\mu_0 T^{-n} = 3 \times 10^{-3} T^{-1.2}$ cm^2/Vs with T in K. The value of σ is small, but in agreement with a small activation energy and the low energetic disorder in pentacene, which is significantly lower than in other solution-processed organic devices [120]. The values of $p_f(0)$ in Fig. 3.5b can be reproduced with model (3.10) and the parameters of Table 3.3.

Table 3.3: Fitting parameters used in (3.10), (3.4) and (3.5) to reproduce the experimental data in Fig. 3.5a.

Temperature	K_1 (cm^{2m-3}/A^m)	m (-)	K_2 (cm^{-3})
20 K (F)	4.31×10^{14}	0.55	-
20 K (R)	4.31×10^{14}	0.55	-
40 K (F)	2.03×10^{15}	0.55	-
40 K (R)	1.47×10^{15}	0.55	-
60 K (F)	3.88×10^{15}	0.55	-
60 K (R)	2.80×10^{15}	0.55	-
80 K (F)	6.89×10^{15}	0.55	5.00×10^{12}
80 K (R)	3.45×10^{15}	0.55	5.00×10^{12}
120 K (F)	1.51×10^{16}	0.55	7.00×10^{12}
120 K (R)	8.62×10^{15}	0.55	7.00×10^{12}
280 K (F)	3.67×10^{16}	0.55	4.00×10^{13}
280 K (R)	-	0.55	4.00×10^{13}

Introducing the results of (3.10) in (3.4) and (3.5), the solid lines of Fig. 3.5 are obtained.

The authors in [125] observed experimentally the ILC-to-SCLC transition in Ag/pentacene/Ag diodes as a function of temperature. The crossover from an ILC to SCLC with decreasing temperature, irrespective of the injection barrier height, was theoretically predicted before [106]. This transition is confirmed with our unified treatment of both regimes and the analysis of Table 3.3 and Fig. 3.5. At high temperatures, the two regimes are clearly visible in the forward and reverse $j - V$ curves of Fig. 3.5a and in the $p_f(0) - j$ representation: more charges can be transported in the semiconductor than injected through a 0.6 eV barrier. As the temperature decreases, the free charge-carrier density decreases in both forward and reverse biasing. The parameter m in model (3.10) is again the same for all the curves, indicating that it depends only on the material. Parameter K_2 decreases when the temperature decreases, but it is the same for forward and reverse regimes. This parameter reflects the existence of thermal carriers, detected only at low voltages. Parameter K_1 decreases when the temperature decreases.

The parameters' values for forward and reverse biasing are different at high temperatures, but converge at low temperatures. This means that the parameter K_1 depends, on the one side on an effective barrier seen by the carriers at the metal-organic interface, which increases when the temperature decreases. On the other side, K_1 depends on effective barriers seen by the carriers in the hopping processes across the organic material, which also increase when the temperature decreases. The convergence of the values of K_1 for forward and reverse regimes at low temperature means that at low temperatures, the mechanism that imposes a limit to the current is the capability of the organic semiconductor to transport the injected charges, not the height of the barrier at the interface [106]. Actually, there is no barrier at the interface in the forward regime.

Throughout this chapter, we have analyzed experimental $j - V$ curves in metal-organic-metal struc-

tures with different interface energy barriers. We have studied the dependence with the temperature and the length of the organic material. We have also considered situations in which the carrier mobility follows different trends. All the current voltage curves have been interpreted by means of a common relation between the current density and the free carrier density at the metal-organic interface. This relation (3.10) includes three parameters. A constant value of the parameter m has been obtained for each of the cases studied throughout this chapter. The values of m in all the materials studied vary from 0.55 to 0.85. We have observed that this value is independent on the energy barrier at the interface, doping impurities or defects. Thus, parameter m must depend on the molecular organization of the organic material. We leave as an open question for future works to find a correlation between the internal parameters of the organic semiconductor and this parameter m. The effects of the interface energy barrier and the temperature reside in parameter K_1. K_1 controls the parallel displacement of the $p_f(0) - j$ relation and depends on the effective barrier seen by the carriers at the metal organic interface or effective barriers seen by the carriers in the hopping processes across the organic material. K_2 controls the flat region at low currents corresponding to the existing thermally generated carriers in the semiconductor, thus providing information about the doping atoms, traps or defects in the material. The usefulness of our model will be seen in the following chapter, in which metal-organic contacts subjected to controlled technological treatments or unintentional degradation processes are characterized. In these cases, we will show the importance of the evaluation of the free charge density in the organic semiconductor, in particular its value at the metal-organic interface.

4

Electrical characterization of controlled and unintentional modified metal–organic contacts

4.1. Introduction

Organic/Polymeric semiconductors are a group of materials characterized by their flexibility and low-cost manufacturing. They can be used in a wide range of niche applications such as smart windows, electronic paper, large-area displays or radio-frequency identification tags [131, 132]. These applications that require a combination of devices such as the organic light emitting diodes (OLEDs), organic thin film transistors (OTFTs) and organic solar cells (OSCs) constitute highly promising technologies. The fast advance towards functional devices is occurring despite some limitations. Among the main limitations that the research community face are the low carrier mobility, long-term stability [5], device integrity in ambient operating conditions [133] and the effect of the contacts acting as a limitation to the electrical performance of the devices.

Coping with these research challenges often means focusing on the effects of the contact region of the device [134, 135]. The addition of doping impurities to enhance the carrier mobility is accompanied by a modification of the electrical characteristics of the contacts [136]. The degradation of a device under exposure to ambient is often related to the contacts rather than the active layer of the device [137]. The technological treatment and control of the contacts and their interfaces is then necessary. Different options to improve the performance of the contacts are doping itself [136], and the use of self-assembled monolayers (SAMs) [135] or grafted dipolar molecules [104] at the interfaces. A scheme with different ways of modification of metal-semiconductor interfaces is depicted in Fig. 4.1.

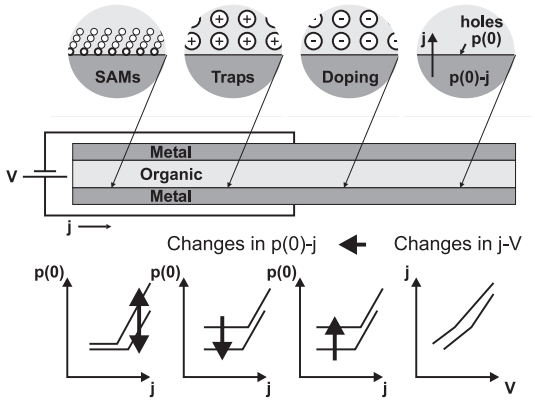

Figure 4.1: Scheme of different ways of modification of metal-semiconductor interfaces and their effects on current voltage curves and the value of the free charge carrier density at the interface.

The analysis of the improvement or degradation of the contacts requires a proper characterization tool that links a change in the electrical behavior of the structure with its physical and technological origins. However, it is difficult to separate the changes in the current density (Fig. 4.1) produced by changes in the free charge carrier concentration, in the mobility or in the injection barrier at the interface. The separation of this information from electrical characteristics of the contacts is a topic of continuous debate. In the literature, there are different characterization techniques or modeling procedures to evaluate and quantify the origin of such electrical changes. In some cases, the experimental

configurations can alter the device under test. The concentration of introduced molecules in a diode can be determined by Fourier transform infrared (FTIR) spectroscopy [104]. Capacitance measurements in metal-insulator semiconductor (MIS) structures are used to determine the free charge carrier density, and consequently the doping concentration [133, 138]. However, the use of a MIS structure to characterize a contact region can be questioned. The carrier mobility has been determined in the past with different techniques, such us the time-of-flight (TOF) method [139], the Charge Extraction by Linearly Increasing Voltage (CELIV) technique [140], the use of different organic diodes with different lengths ('electric potential mapping by thickness variation' POEM method) [141]. Once again, the use of extra structures is necessary to employ these techniques.

In order to avoid using additional structures, current-density vs. voltage $j-V$ curves and/or capacitance voltage ($C-V$) curves measured in the device-under-test should be studied. Even the analysis of these curves must be considered with caution. On the one side, the use of the classical Mott-Schottky method to determine doping densities from $C-V$ curves imposes a threshold for doping densities to be detected [142]. On the other side, the modeling of the curves in organic diodes requires some considerations, as different regimes can be found and modeled differently: ohmic [133], injection limited current (ILC) [8, 55, 110] and space charge limited current (SCLC), with distinction of low and high electric fields [112].

In the first part of this study [[143] , Sec. 3], we have described a compact model in which all these regimes are included and affect the value of the free charge-carrier density at the interface $p_f(0)$. The model relates the current density j with $p_f(0)$ as:

$$p_f(0) = K_1 j^m + K_2 \tag{4.1}$$

where the parameter K_1 depends on the barrier height at the interface, m depends on the organic material and K_2 controls a flat zone at low currents to include the dependence with thermal carriers and impurities. The purpose of this chapter is to provide a detailed electrical characterization of metal-organic contacts subjected to some kind of modification, so that the effects can be recognized and quantified from the current-density vs. voltage characteristics (Fig. 4.1). The study of the evolution of these parameters in metal-organic contacts provides a quick view of the physical origin of such modifications.

Our main goal is to determine this information in a low computational time. We do not propose to substitute any of the previous techniques, but to propose a fast and easy to use method by researchers. The objective is to detect modifications of the energy barrier at the interface or the presence of added impurities or traps in the organic material. Once these modifications are detected, a further quantification of these effects can be obtained with other techniques as needed.

In the following section, we summarize the procedure employed to characterize metal-organic contacts. In section 4.3, we analyze current voltage curves measured in contacts that underwent some kind of controlled technological treatment: the use SAMs or grafting with dipole molecules, doping, or even forced degradation. In section 4.4, a discussion on how to improve metal-organic contacts is made using the results of the previous sections. The main conclusions are provided in Chapter 9.

4.2. Characterization procedure

The details of the procedure employed to characterize metal-organic contacts can be seen in [[143] , Sec. 3]. Here, we provide the basic scheme of the method. The fundamental idea of our procedure is that any physical mechanism occurring close to the metal-organic interface (such as the injection through the energy barrier or the presence of impurities or traps) is reflected in the boundary value of the free charge density at the metal-organic interface $p_f(0)$ (Fig. 4.1). Thus, the main objective is to find and analyze the $p_f(0) - j$ relation extracted from experimental $j - V$ curves. The procedure consists of two main steps. First, the boundary value of the free charge density at the metal-organic interface pf(0) is extracted from $j - V$ curves measured in the organic diode. The relation $p_f(0) - j$ is obtained by an iterative method based on the combination of the transport equations:

$$j = q\mu[T, F(x)]p_f(x)F(x), \tag{4.2}$$

$$\frac{dF}{dx} = \frac{q}{\varepsilon_0\varepsilon_r}p(x), \tag{4.3}$$

$$V = \int_0^L F(x)dx, \tag{4.4}$$

where q is the absolute value of the electron charge, x is the distance from the injecting electrode, $F(x)$ is the electric field, ε_r and ε_0 are the relative permittivity and the permittivity of the free space, respectively, and $p(x)$ is the total charge density. The free charge density is a fraction θ of $p(x)$: $qp_f(x) = \theta qp(x)$. In these equations, we use the correlated Gaussian disordered model (CGDM) for the mobility [89]:

$$\begin{aligned} \mu_{CGDM}(T, F) &= \mu(T, 0)\exp(\gamma\sqrt{F}) \\ \mu(T, 0) &= \mu_\infty \exp\{-[3\sigma/(5k_BT)]^2\} \\ \gamma &= 0.78\{[\sigma/(k_BT)]^{3/2} - \Gamma\}[qa/\sigma]^{1/2} \end{aligned} \tag{4.5}$$

where a is the intersite spacing, k_B is the Boltzmann constant, T is the absolute temperature, σ is the width of the Gaussian density-of-states (GDOS) caused by the electrostatic coupling of a charged site to neighboring dipoles, and Γ is related to the positional disorder, usually $\Gamma \sim 2$.

Second, the $p_f(0) - j$ relation is modeled with (4.1) and the parameters K_1, K_2 and m are extracted from this model. The analysis of the variation of these parameters with the controlled treatment of the contacts will give clues about the physical origin of the changes produced in the structure.

4.3. Controlled and unintentional modification of the contacts

In this section, we analyze different cases that demonstrate the importance of determining the value of the free charge density in the organic semiconductor, and in particular its value at the interface.

This variable sheds light on different problems that affect the organic devices, such as the effect and treatment of the metal-organic contacts, the controlled or unintentional doping of the material or the instabilities.

4.3.1. Effects of self-assembled monolayers on the contact

There are different ways to diminish the detrimental effect of the contacts on the performance of an organic device [105, 144, 145]. One of them is by assembling monolayers at the metal-organic interface [135, 146, 147]. A self-assembled monolayer (SAM) consists of a well-organized single layer of molecules chemisorbed or grafted on a surface [148]. It has been demonstrated that charge injection in organic electronic devices can be controlled with the use of SAMs. SAMs allow for tuning the injection barriers for holes and electrons into the semiconductor through the formation of dipoles on the metal surface. The fabrication of self-assembled monolayers with modified doped molecules can further improve the properties of electronic devices [135]. Depending on the material used as monolayer, the Schottky energy barrier can decrease (or increase) and then the charge injection into the polymer can be improved (or degraded) [134, 149, 150]. SAMs are extensively used in many organic device such as OTFTs [147, 151], OLEDs [149, 150] or OSCs [152]. SAMs can be used to design single carrier devices with ohmic contacts by suppressing the contribution of electrons or holes to the current [149]. Monolayers are assembled to the most common electrodes such as ITO, Cu, Al, Au or Ag. In the cases of gold and silver, the metal work functions can vary over 1.4 and 1.7 eV, respectively, with the use of SAMs [134, 149]. Consequently, the hole current in a OLED can be tuned by more than six orders of magnitude.

The molecules used in SAM are mostly based on long alkyl chains that tend to self-arrange to form highly ordered single layers. One end of the chain is substituted with a group capable of inducing chemisorptions on the surface, while the other one can be used to control the properties of the modified surface [147]. A frequently investigated system of SAMs is formed by thiols on gold surfaces [134, 149, 153] and by the use of different aromatic and aliphatic compounds. [148, 154]. The advantages of thiols and aromatic compounds are their high selectivity of mainstay groups to suitable surfaces, which lead to a direct assembly on predefined metal electrodes without doping the bulk of the organic semiconductor. Alkane-thiols are large energy gap molecules that can block charge injection at the metal/polymer interface [134].

There are different reasons that explain the improvement of the injection with the use of SAMs. The change of the interface dipole between the electrode and the semiconductor [57, 155] can be accompanied with the alignment of the work function of the metal and the transport levels of the semiconductor. As the growth of a SAM layer is self-limited to a monolayer thickness, charge carrier tunneling between the metal and the semiconductor through the interfacial SAM layer is also feasible [156]. Furthermore, when the surface of a contact is modified with a self-assembled monolayer, the growth of organic semiconductor enhances the degree of organization for the entire deposition process, including the Al-Pentacene contacts [147, 152]. Unless this reorganization of the organic molecules is located in the close-vicinity of the SAM [150], the carrier mobility can even be improved. The combination of all these different reasons (interfacial, energetic and morphology) make the understanding of the SAM-modified electrodes in

organic devices more complex [157].

Now, we analyze $j - V$ curves measured in diodes treated with SAMs from two techniques. In the first one, the layer of molecules is formed by chemisorptions and in the second example by synthesis and grafting. We monitor the changes on the injection barrier and on the thermal generated free carriers produced by the layer of molecular dipoles. We distinguish each of these two effects by the inspection of the relation between the charge carrier density and the current density.

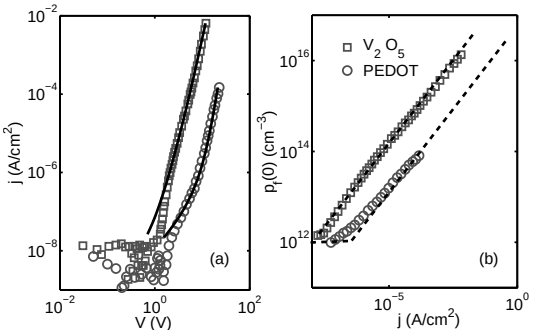

Figure 4.2: a) Comparison of experimental $j - V$ characteristics for ITO/V_2O_5/CBP(100 nm)/Hg (squares) and ITO/PEDOT/CBP(100 nm)/Hg diodes (circles) [146] with our calculations (solid lines) using the values of the free charge-carrier density at the interface shown in dashed lines in Fig. 4.2b and the CGDM mobility model. b) Charge-carrier density at the interface as a function of current density to fit exactly the experimental data of Fig. 4.2a (symbols). The dashed lines correspond to model (4.1).

In Fig. 4.2a, we compare experimental $j - V$ curves measured on ITO/4,4'-Bis(N-carbazolyl)-1,1'-bipheny (CBP) diodes treated with self-assembled monolayers [146] (symbols) with our procedure (solid lines). These authors used as monolayers a hole-injection layer of polyethylene dioxythiophene:polystyrene (PEDOT:PSS) (circles) and vanadium pentoxide (V_2O_5) (squares). They observed a clear increase of the current for the latter case. They proposed that the formation of an interface dipole and band bending results in a decrease in the effective barrier height of V_2O_5. This fact can be confirmed by the analysis of the evolution of the free charge-carrier density with the current density (Fig. 4.2b). The symbols in this figure are the values of the free charge-carrier density at the interface used in the transport equations (4.2)-(4.5) to reproduce, within 0.1 %, the experimental data of Fig. 4.2a. The values of the parameters of the CGDM model (5) are $\varepsilon_r = 3$, $\sigma = 60$ meV, $\theta = 0.14$, $\mu(T = 300$ K, 0)$= 5 \times 10^{-7}$ cm^2/Vs, and $a = 1$ nm. The dashed lines in Fig. 4.2b correspond to model (4.1), with $p_f(0) = 4.74 \times 10^{17} j^{0.7} + 8 \times 10^{11}$ cm^{-3} for the V_2O_5 layer and $p_f(0) = 4.30 \times 10^{16} j^{0.7} + 8 \times 10^{11}$ cm^{-3} for the PEDOT:PSS layer. Introducing this model in (4.2)-(4.4) with the mobility model parameters given above, the solid lines of Fig. 4.2a are obtained. (Note: The "noisy" data at low voltages are ignored). At high currents, the two curves in Fig. 4.2b are parallel. This displacement is controlled by the different value of K_1 in (4.1) and indicates different heights of the energy barrier for the two cases [[143] , Sec. 3]. The parameters m and K_2 are the same in both cases. Parameter m symbolizes the relationship with the organic layer and parameter K_2 with the thermally-generated carriers. Thus, no doping effects are observed. The change in the molecules used in the monolayer treatment only modifies the energy barrier at the interface, confirming the technological predictions. The effects produced by SAMs on

the electrical characteristics of the contacts depend on the organic material, electrode and fabrication technology [135, 148]. The following case is an example in which the treatment with molecular dipoles also affects the concentration of thermal generated carriers.

Another technique to modify the metal-organic contact is by the synthesis and subsequent grafting of dipolar molecules on the surface of the metal electrode. Sigaud et al. [104] used grafting of dipolar molecules with the purpose of increasing hole injection from the indium-tin oxide (ITO) electrode of ITO/poly-(9-vinylcarbazole) (PVK)/Al diodes. In order to relate the change of the energy barrier with the amount of grafted molecules at the metal-organic interface, they combined the study of j-V curves with other experimental techniques, such as the Fourier transform infrared (FTIR) spectroscopy [104]. We show here that the increase of the current density observed after grafting is not entirely due to a change in the energy barrier, but to a change in the thermal generated carriers. This information is obtained by the analysis of the free charge density at the interface that is extracted from the $j - V$ curves.

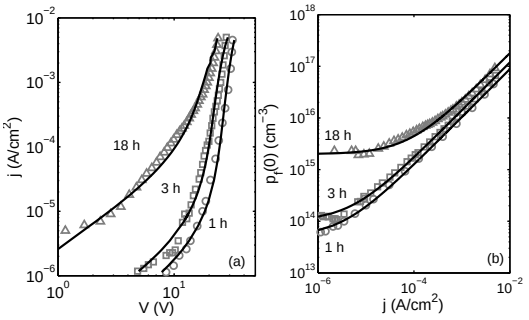

Figure 4.3: a) Comparison of experimental $j-V$ characteristics for ITO/PVK($L = 150$ nm)/Al diodes measured at different grafting times at room temperature (symbols) [104] with our model (solid lines). b) Free charge-carrier density at the metal-organic interface as a function of the current density, extracted with our numerical procedure to reproduce the experimental data in Fig. 4.3a within 0.1 % (symbols) and modeled with (4.1) (solid lines).

Fig. 4.3a shows the comparison of experimental current density versus voltage curves (symbols), of ITO/PVK/Al diodes measured at different grafting times (0 to 18 h) [104], with the results of our model. Our procedure extracts the values of the charge-carrier density at the interface (symbols in Fig. 4.3b) to fit the experimental data within 0.1 % with the transport equations (4.2)-(4.4), and the value of the parameters of the CGDM model (4.5): $\mu(T = 300$ K, 0)$= 2.3 \times 10^{-7}$ cm^2/Vs, $\varepsilon_r = 3$, $\sigma = 50$ meV, $\theta = 0.45$ and $a = 1$ nm. Subsequently, the extracted values of the free charge density at the interface are modeled with (4.1) (solid lines in Fig. 4.3b). The combination of (4.1) with (4.2)-(4.5) results in the solid lines of Fig. 4.3a. The parameter K_2 varies from 5.0×10^{13} cm^{-3}, 1.0×10^{14} cm^{-3} to 2.0×10^{15} cm^{-3} after 0, 3 and 18 hours of grafting time, respectively, in correlation with FTIR spectroscopy results that showed an increment of the surface concentration of grafted molecules with time: 1.5×10^{13} cm^{-2} and 5.7×10^{13} cm^{-2} after 3 and 18 hours of grafting time, respectively [104]. This corresponds to the increment of the charge-carrier density observed at low currents in Fig. 4.3b, confirming the existence of impurities that release free charges. The advantages of our method are not restricted to the low injection

regime. The high injection regime also provides information about the interfaces. The parameter m is 0.93 for the three curves, meaning that no structural change has been produced in the bulk of the organic material. The parameter K_1 slightly varies from 0.6×10^{19}, 0.9×10^{19} to 1.2×10^{19} cm^{2m-3}/A^m after 0, 3 and 18 hours of grafting time, respectively. We have observed that diodes with different barrier heights at the metal-organic interface produce parallel displacements of the $p_f(0) - j$ curves [[143] , Sec. 3]. In Fig. 4.3b, when the amount of injected charge is higher than the charge released from the impurities, the three curves tend to coincide. The values of the parameter K_1, related to the height of the energy barrier, are in the same order of magnitude. On the contrary, the values of parameter K_2, related to the thermal generated carriers, vary more than one order of magnitude. This result allows us to conclude that the height of the energy barrier at the interface in the samples of Fig. 4.3 is only slightly modified. Unlike the experiments of Fig. 4.2, these grafted molecules act mainly as dopant molecules.

4.3.2. Semiconductor doping

One common way to improve the performance of electronic devices is by doping the organic semiconductor. The addition of doping molecules is widely used to improve the efficiency of OLEDs [158] and OSCs [159]. These molecules donate free charge carriers to the host material and hence increase the conductivity of the organic semiconductors. Mobility changes have been detected when measuring the change in conductivity upon doping with inert salts, which produce anion–cation pairs without introducing extra mobile charges in the organic film [136]. They confirmed previous similar findings about the dependence of this doping dependent mobility [160–162]. Bulk-limited or contact-limited transports have been observed in devices with different doping levels, giving an indication of the effect of doping on the injection barrier [163]. Energy diagrams derived from ultraviolet and X-ray photo-emission spectroscopy (UPS and XPS) for undoped ZnPc on ITO and ZnPc doped with F4-TCNQ detect in both cases a rather large energy barrier for holes of about 1.2 eV. However, the electrical properties of such contacts distinguish between blocking and ohmic contacts, respectively [164]. They conclude that the basic mechanism of forming an Ohmic contact by thin tunnel barriers works as well as in inorganic semiconductors. Other authors have investigated the effect of redox inactive ionic species on the dielectric properties of conjugated polymers. They examined the corresponding impact that salt doping has on the optical and electrical properties of films of the conjugated polymers and their corresponding blends with electron accepting fullerene molecules [165]. Electrical characterization methods and time-resolved infrared (TRIR) spectroscopy [166] are combined to demonstrate that the charge carrier density and dielectric permittivity of the conjugated polymer can be significantly enhanced by the addition of Lithium Bis(Trifluoromethanesulfonyl)Imide (LITFSI) .

The doping treatment of an organic device has similar effects to those produced with SAMs: changes in the thermal generated carriers, mobility or interface injection barrier. As in the previous section, we again analyze current-voltage curves of organic diodes that have undergone any kind of doping change. In particular, we pay our attention to the transition from contact to bulk limited current in doped samples. Anjaneyulu et al. [167] studied the role of carrier density dependence in conduction mechanism, in particular in the transition from contact to bulk limited current. They stated that a single model

Table 4.1: Fitting parameters used in (4.1) in combination with (4.2)-(4.5) to reproduce the experimental data in Fig. 4.4a.

Diode	K_1 (cm^{2m-3}/A^m)	m (-)	K_2 (cm^{-3})
D1 (F)	8.0×10^{17}	0.85	7.0×10^{12}
D2 (F)	9.0×10^{17}	0.85	1.0×10^{12}
D3 (F)	1.1×10^{18}	0.85	3.0×10^{9}
D1 (R)	4.5×10^{17}	0.85	1.1×10^{13}
D2 (R)	4.5×10^{17}	0.85	1.0×10^{12}
D3 (R)	4.5×10^{17}	0.85	3.0×10^{9}

cannot explain the $j-V$ data for the entire range of applied voltages. In order to find such a dependence, they combined current-voltage, impedance and capacitance measurements of poly(3-methylthiophene) (P3MeT) devices in stainless steel (SS)/P3MeT/silver (Ag) sandwich geometry at various doping levels. Fig. 4.4a shows a comparison of their experimental measurements taken at room temperature (crosses for forward bias and other symbols for reverse bias) with our procedure (solid lines). Three diodes, with a decreasing doping level from D1 to D3, were analyzed. These devices have electrodes with asymmetric work functions, that is, SS ~ 4.9 eV, (P3MeT) HOMO $\sim 4.35 - 4.5$ eV, and Ag $\sim 4.2 - 4.6$ eV.

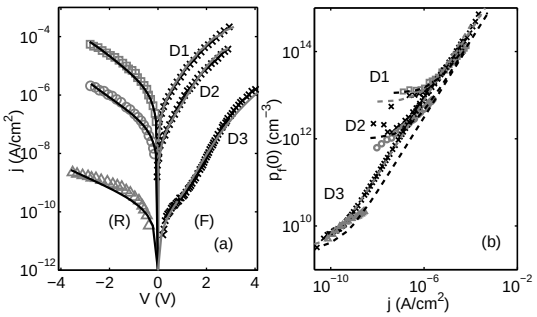

Figure 4.4: a) Comparison of current-voltage curves measured in doped P3MeT diodes (SS/P3MeT/Ag with Ag being positively biased) at room temperature (symbols) [167] with our numerical results (solid lines). b) Free charge-carrier density at the interface extracted with our procedure to reproduce the experimental $j-V$ curves of Fig. 4.4a within 0.1 % (symbols). The dashed lines follow the empirical model (4.1) with the parameters given in Table 4.1.

The boundary values of the free charge-carrier density at the interface used in the transport equations to reproduce within 0.1 % the whole set of experimental data in Fig. 4.4a are shown with their respective symbols in Fig. 4.4b. In the fitting, the following values of the CGDM model parameters are also used: $\theta = 0.6$, $\sigma = 40$ meV, $a = 3$ nm, $\varepsilon_r = 3$, and a doping dependent mobility $\mu_{D1}(300\text{ K}, 0) = 2.0 \times 10^{-4}$ cm^2/Vs, $\mu_{D2}(300\text{ K}, 0) = 1.1 \times 10^{-4}$ cm^2/Vs, $\mu_{D3}(300\text{ K}, 0) = 3.3 \times 10^{-5}$ cm^2/Vs. We confirm past results about the dependence of a doping dependent mobility [160–162]. The values of the mobility has been chosen in such a way that the distributions of $p_f(0)$ for D1, D2 and D3 overlap at high currents

in the forward regime. The diode curves in the forward regime are space-charge limited. Thus, there is no barrier at the Ag/P3MeT interface. If we considered the same value of mobility for each diode, the free carrier density would decrease with the amount of doping. It would mean that the energy barrier at the interface increases when the doping increases. This situation would be possible if the typical $j - V^2$ relation had not been observed in the forward regime for the three diodes. On the contrary, if we used an increasing value of the mobility when the doping decreases, the free carrier density would increase with the amount of doping in the high-current region. This would mean that the height of the energy barrier is reduced when the doping increases. This solution contradicts the fact that the diode curves in the forward regime are space-charge limited. We cannot reduce a barrier that does not exist. The free charge-carrier density at the interface is modeled with (4.1) and the parameters given in Table I (dashed lines in Fig. 4.4b). This model is introduced in (4.2)-(4.5) with the mobility model parameters given above, and finally, the solid lines of Fig. 4.4a are obtained, providing an excellent agreement with the experimental data.

The evolution of the free charge-carrier density with the current for the three diodes of Fig. 4.4b shows two different regions. At low positive or negative voltages (or low currents), $p_f(0)$ remains constant and independent on the injecting electrode. This flat region reflects a background of thermally generated charge carriers. The larger the doping, the greater is the value of this flat region. The second region is seen at high currents. In a logarithm scale, the $p_f(0) - j$ relation follows a straight line. The three forward curves (crosses) tend to coincide at high current corresponding to a SCLC regime for every measurement. The reverse regimes split from their respective forward regimes but run parallel. The separation between each two of the three pairs of curves is smaller as the doping increases (see also the values of K_1 in Table 4.1). This means that the doping not only affects the background of thermally generated carriers, but also affects the height of the energy barrier of the SS/P3MeT contact due to a realignment of quasi-Fermi level produced by a variable number of carriers at the interface. The constant value of the slope m for all the curves means that the doping variation does not affect any other morphological aspect of the organic semiconductor.

The strength and merits of our procedure can be checked by comparing our results with other experimental determinations. The values obtained for the free charge-carrier density in Fig. 4.4b are also in agreement with the values extracted from frequency-dependent capacitance measurements [167]. These authors obtained the following values for the free charge-carrier density at 4 V: 1.8×10^{15} and 6×10^{14} cm^{-3} for diodes D1 and D2, respectively and provided an approximated value 10^{11} cm^{-3} for diode D3. For these same diodes at the same voltages, we obtained free charge-carrier densities of 0.9×10^{15}, 3×10^{14} and 10^{12} cm^{-3}, respectively. The values obtained for diodes D1 and D2 agree quite well. The difference for diode D3 can be attributed to the small sensitivity of their capacitance measurements in the low-doped diode [142].

4.3.3. Instabilities

The importance of the study of the free charge density as a function of the current in the organic semiconductor is now checked for $j-V$ curves with hysteresis. In particular, we can determine the number

of traps filled during a hysteresis cycle caused by trapping and de-trapping in the semiconductor. Fig. 4.5a shows $j - V$ curves with hysteresis measured in the same three diodes studied in the previous section [167] (symbols). A larger hysteresis cycle is seen for the low-doped diodes D3. However, this does not mean that the doping effect is crucial to interpret these curves with hysteresis. These curves can be reproduced with our procedure (solid lines) by solving the transport equations with the values of the free charge-carrier density at the interface shown in Fig. 4.5b and the following assumptions for the evolution of the total charge in (4.3), $p(x) = p_f(x) + p_t(x)$, where p_t is the density of the filled traps.

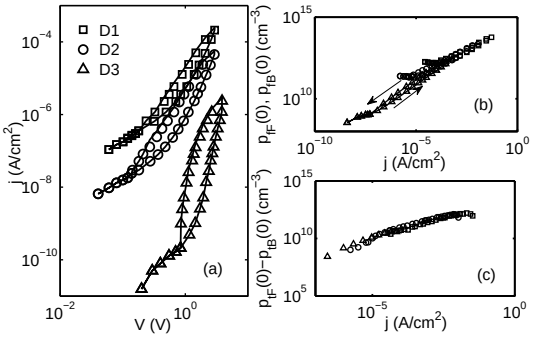

Figure 4.5: a) Comparison between $j - V$ curves with hysteresis for the diodes of Fig. 4.4a (symbols) [167] and our procedure (solid lines). b) Values of the free charge-carrier density at the metal-organic interface used in the transport equations to reproduce within the 0.1 % the experimental $j - V$ curves of Fig. 4.5a. c) Variation of the trapped charge during the hysteresis cycles of Fig. 4.5a.

In order to estimate the variation of traps filled during the hysteresis cycle, we consider the following assumptions and steps. We consider that at a constant voltage, the distribution of charge in the semiconductor is the same in the forward and backward scans $[p_f(x)+p_t(x)]_B = [p_f(x)+p_t(x)]_F$. Thus, any variation in the number of filled traps is compensated by a variation of the free charges, and then by a variation in the current density.

In a first step, we estimate the variation of the free charge during the hysteresis cycle, assuming that all the traps are filled during the forward scan (FS) and emptied during the backward scan (BS). In the FS, we consider the model proposed by Mark and Helfrich [102] for the maximum density of filled traps:

$$p_t(x) = N_{trap} \left(\frac{p_f(x)_F}{N_t} \right)^{1/l} \tag{4.6}$$

where N_{trap} is the total trap concentration, $l = T_c/T$, T_c is the characteristic temperature of the trap level distribution in the sample and N_t is the effective density of the trap states. In the BS, we consider $p_t(x) \ll p_f(x)$. The transport equations are solved in order to fit, within 0.1 %, the hysteresis data. The evolution of the free charge-carrier density at the interface is provided as solution, and thus its variation, $[p_{fB}(0) - p_{fF}(0)]$.

In a second iteration, we consider that all the traps are filled during the FS, following (4.6). In the BS, the traps are not considered empty but following the trend $p_{tB}(x) = p_{tF}(x) - [p_{fB}(0) - p_{fF}(0)]$, where $[p_{fB}(0) - p_{fF}(0)]$ is calculated in the first step, and $p_{tF}(0)$ in the FS of the second step. The

Table 4.2: Fitting parameters used in (4.1) in combination with (4.2)-(4.5) to reproduce the experimental data in Fig. 4.6.

Temperature	K_1 (cm^{2m-3}/A^m)	m (-)	K_2 (cm^{-3})
280 K	3.5×10^{17}	0.85	3.5×10^{12}
260 K	3×10^{17}	0.85	2×10^{12}
240 K	2.8×10^{17}	0.85	1.2×10^{9}
220 K	2.5×10^{17}	0.85	7.5×10^{11}
200 K	2.3×10^{17}	0.85	5×10^{11}
180 K	2.2×10^{17}	0.85	3.5×10^{11}

use of model (4.6) introduces additional fitting parameters. The most sensitive parameter is Ntrap. The convergence is achieved when the final variations of the free charge-carrier density and the trapped-carrier density tend to coincide, $[p_{fB}(0) - p_{fF}(0)] \approx [p_{tF}(0) - p_{tB}(0)]$. In the fitting of Fig. 4.5a, we have used $N_{trap} = 2 \times 10^{16}$ cm^{-3}, $N_t = 10^{19}$ cm^{-3} and $T_c = 400$ K. The values of the parameters of the mobility model (4.5) are the same as in the fitting of Fig. 4.4a.

The variation of the filled traps thus obtained during the hysteresis cycles is represented with symbols in Fig. 4.5c. The number of filled traps increases with the current density, following a trend that is independent of the doping. Actually, there are common current ranges in the three diodes where the number of filled traps is similar. This means that the effect of the doping on the hysteresis is only the modification of the free carriers in the organic semiconductor. However, a modification of the number of free carriers can also be achieved with the variation of the applied voltage to the structure.

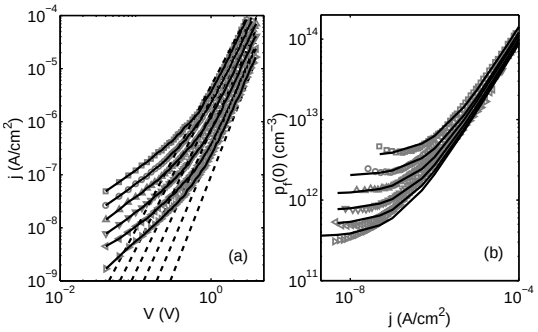

Figure 4.6: a) Comparison of current-voltage curves of the doped P3MeT D1 diode measured at different temperatures [167] (symbols) with our model (solid lines) and the trap-controlled SCLC model (4.7) (dashed lines). b) Values of the free charge-carrier density at the metal-organic interface used in the transport equations to reproduce the experimental $j - V$ curves of Fig. 4.6a (symbols). The solid lines represent the fitting with model (4.1) and K_1, K_2 and m given in the Table 4.2.

The values of these fitting parameters can be checked with an additional study at different temperatures in the same samples. Fig. 4.6a shows with symbols the evolution of $j - V$ curves with temperature measured by the same authors in diode D1 [167]. In solid lines, we represent the result of including our

model (4.1) in the transport equations. The values of the free charge-carrier density at the interface obtained from (4.1) are depicted with solid lines in Fig. 4.6b and compared with the symbols, which correspond to the values extracted by the fitting within 0.1 % of the experimental $j - V$ curves in Fig. 4.6a. The values of the parameters in the CGDM mobility model are the same as in the fitting of Fig. 4.4a. The free charge-carrier density can be reproduced with our model (4.1) and the values of the parameters shown in Table 4.2 (solid lines). The free charge-carrier density shows a uniform increment with the temperature. It is important to note that the slope of the $j - V$ curves increases when the temperature increases. However, the slope of the $\log[p_f(0)] - \log(j)$ representation [parameter m in (4.1)] does not depend on the temperature. Once more, this result confirms that m depends only on the organic material, making (4.1) more general.

As noted in [167], the thermally activated behavior of the $j - V$ curves is an indication of a trap-limited SCLC mechanism. This behavior was modeled in the past for an exponential distribution of traps in energy space [102]:

$$J = q^{1-l}\mu N_t \left(\frac{2l+1}{l+1}\right)^{l+1} \left(\frac{l}{l+1}\frac{\varepsilon_r\varepsilon_0}{N_{trap}}\right) \frac{V^{l+1}}{L^{2l+1}} \tag{4.7}$$

This model assumes a zero electric field at the interface (or an infinite free charge density at the same point). This means that it can reproduce only the high current regime, as can be seen in Fig. 4.6a with dashed lines. Unlike our model, the transition towards the Ohmic regime is not reproduced with (4.7). In any case, this model is still useful to estimate the trap concentration from the fitting at high voltages. The results of this fitting are $N_{trap} = 10^{16}$ cm^{-3}, $T_c = 480$ K, $\mu = 0.45 \times 10^{-6}$ cm^2/Vs, $N_v = 10^{19}$ cm^{-3}. The values of these parameters are similar to those obtained with our model applied to the hysteresis curves in Fig. 4.5a, thus validating our procedure. The only exception is the value of the mobility, which is lower. The reason is the assumption of an infinite charge density at the interface in model (4.7). The overestimation of the charge density is compensated with an underestimation of the mobility [133].

4.3.4. Unintentional doping degradation

Degradation is one of the main problems that affect the performance of organic devices. It limits their reliability and operating lifetime. Some of the causes of degradation are exposure of oxygen (O_2), water, other atmospheric contaminants or the diffusion of atoms of the metal into the organic material [168, 169]. Therefore, the characterization of these effects is important in order to find technological solutions that minimize the degradation, and thus achieve more efficient and stable materials. The degradation can be seen as an uncontrolled doping process with all its associated problems: the penetration of impurity traps in the semiconductor creating shallow/deep trapping levels [170] (which may produce a variation of the value of mobility as well as the free charge density) and the modification of the height of the energy barrier at the metal-organic interface [137]. Thus, investigation has been focused on transport mechanisms in organic semiconductor films and in the injection mechanisms in the metal-organic interfaces present in each organic device, with the metal-organic interface being one of the most sensitive regions of the devices [137, 171].

Table 4.3: Fitting parameters used in (4.1) in combination with (4.2)-(4.5) to reproduce the experimental data in Fig. 4.7

Ambient	K_1 (cm^{2m-3}/A^m)	m (-)	K_2 (cm^{-3})
Under HV	2.5×10^{17}	0.7	7.0×10^{14}
O_2-doped	2.5×10^{17}	0.7	1.2×10^{13}
Air-doped	0.9×10^{17}	0.7	2.0×10^{11}

Our characterization method is applied to ITO/ endcapped sexithiophene (EC6T) (200 nm)/Al diodes measured under high-vacuum (HV) (triangles in Fig. 4.7a), after O_2-doping (squares), and after doping with air (circles) at 300 K [133]. Fig. 4.7a shows the comparison of these experimental $j - V$ curves (symbols), with the results of our model (solid lines). The boundary values of the free charge-carrier density at the interface, used in the transport equations to reproduce within 0.1 %, the whole set of experimental data in Fig. 4.7a (symbols), are shown with their respective symbols in Fig. 4.7b. In the fitting, the CGDM model is approximated with a constant mobility $\mu = 5 \times 10^{-6}$ cm^2/Vs, as no high electric-field effects are detected. The value of theta is different for each diode: $\theta = 0.4$, 0.34 and 0.3, under HV, O_2 and ambient air, respectively. As expected, the number of traps is higher with ambient exposure. The free charge-carrier density at the interface is modeled with (4.1) and the parameters given in Table 4.3 (solid lines in Fig. 4.7b). This model is introduced in (4.2)-(4.5) with the value of the mobility shown above, and finally, the solid lines of Fig. 4.7a are obtained, providing an excellent agreement with the experimental data. There is only a small disagreement with the air-doped data at low current densities. In this case, the authors noted the existence of leakage currents affecting this region [133].

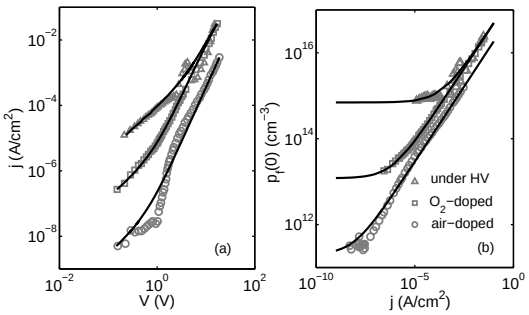

Figure 4.7: (a). Comparison of experimental $j - V$ characteristics for ITO/EC6T/Al diodes measured under air doped, oxygen doped and under high vacuum HV (symbols) [133] with our model (solid lines). (b) Charge density at the interface as a function of current density extracted from Fig. 4.7a (symbols). The solid lines represent the fitting with model (4.1) and K_1, K_2 and m given in the Table 4.3.

The exposure to air or O_2 produces a decrease of the charge density at low currents, confirming the existence of traps that capture the free charges. Based on our previous study [[143] , Sec. 3], diodes with different barrier heights at the interface produce a parallel displacement of the relation $p_f(0) - j$ at high

currents. In this regard, we can consider that the barrier height at the interface is not affected by the degradation processes of O_2. The only effect is the introduction of new traps, monitored with a change in the parameters K_2 and θ in our model (Table 4.3). The $p_f(0) - j$ curve for the air-doped sample is displaced and parallel to the others. In this case, a change of the energy barrier height is deduced from this displacement or from the change in the value of K_1. This effect is added to the introduction of traps that reduce the free carrier concentration.

4.4. Discussion. Improvement of the contacts

The improvement of the contacts is a topic that can be tackled in different ways depending on the kind of organic devices and their applications. In general, a proper contact requires good adhesion properties, it must present no barrier to the injection of charge carriers, and it must prevent the penetration of undesired impurities that give rise to trapping mechanisms and hysteresis. In particular cases, such as the organic solar cells, the optimization of their optical performance adds new requirements to the contacts. In this regard, researchers try to minimize the reflections of the light with several layers of different permittivity introduced above the metal contact. Simultaneously, they try to control the injection of charge in the metal-organic interface by tuning the height of the metal-organic energy barrier.

The electrical control of the interfaces is one of the most studied topics in order to improve the contact region. The fabrication of SAMs at the metal-organic interface, by chemisorptions or grafting, allows for controlling of the height of the energy barrier. However, in some situations, the introduced molecules act as dopant molecules, reducing their effects on the modification of the energy barrier. Theoretically, grafting and chemisorptions of SAMs change the energy barrier at the metal/organic interface by an amount proportional to the dipole moment μ' and the surface concentration of the molecules N attached to the metal electrode. According to Coulomb's law, the expected change in the barrier height induced by the layer of dipoles is: [144, 149, 172]

$$\Delta\phi = \frac{qN\mu'}{\varepsilon_r\varepsilon_0} \tag{4.8}$$

In some cases, the attachment of grafted or chemisorbed molecular dipoles at the surface of an ITO anode leads to an insignificant lowering of the injection barrier [149, 172]. The barrier is not as large as expected in (4.8). In this chapter, we have studied situations in which SAMs reduce the energy barrier, not affecting the thermal generated carriers (Fig. 4.2). In other cases, they affect mainly the number of thermal generated carriers (Fig. 4.3), confirming the results in [172]. The analysis of these two situations with model (4.1) shows that an increment in the thermal generated carriers enhances the current density only in the low current regime. They increase the range of voltage corresponding to the Ohmic region. However, the decrease of the energy barrier at the interface increases the current density in the entire $j - V$ curve. Evidently, this situation is preferable. In this last case, the attached molecules act as molecular dipoles. In the former case, only a fraction of N does contribute in (4.8), the rest act as dopant elements. Thus, the procedure to attach the molecules to the electrode must guarantee that most of them contribute to the dipole moment. Sigaud et al. [172] suggested to increase the density of packed dipoles as a way to increase N in (4.8).

The control and use of the dopant molecules in the metal-organic contact is also a necessity. We have studied cases in which the dopant molecules increase the free carrier concentration (Fig. 4) and others where they act as traps (Fig. 4.7), decreasing the free carrier concentration. These variations are detected mainly in the low current regime. In these same figures, we have detected how these molecules can increase, decrease or leave the interface energy barrier unaltered. The variation of the interface energy barrier affects the entire $j - V$ as it produces parallel displacements in the $p_f(0) - j$ relation. Nevertheless, in the situations studied in these figures, the effect of the doping on the barrier (injected carriers) is not as important as its effect on the thermal free carriers. In this regard, we would suggest the compensation of traps with doping molecules. It is expected that this effect would be noticeable only at low currents.

The effects of doping on hysteresis have been analyzed in Fig. 4.5. In this case, we have shown that additional doping does not modify the effects of hysteresis. The doping neither enhances nor reduces the hysteresis mechanism. At least, in these experiments, the effect of doping has served only to analyze different current ranges where the hysteresis is detected, being more noticeable at low current regimes. In this regard, the reduction of the hysteresis effect can come not by modifying the contact itself or compensating with doping molecules, but by avoiding different combinations of materials employed in the metal organic contact [173].

From an experimental point of view, the use of $j - V$ measurements to gain information about the contacts and the way to get a better design is still valid. The ability to determine charge carrier densities can aid in the interpretation of current-voltage curves. In some situations, neglecting the role of the charge carrier density can divert to over- or under- estimating the role of other variables such as the carrier mobility. We suggest the analysis the carrier density as a function of the current density as a powerful and rapid tool to analyze the effects of controlled or undesired treatments of contact interfaces. More precise and costly experimental techniques can use this information as the starting point.

5

Charge Density at the Contacts of Symmetric and Asymmetric Organic Diodes

5.1. Introduction

The metal-organic-metal (MOM) structure is an intrinsic part of organic devices such as organic solar cells (OSC), organic light emitting diodes (OLEDs) and organic thin film transistors (OTFTs). Both symmetric and asymmetric MOM structures are used, and the asymmetric one is the typical structure in OSCs and OLEDs. The extraction-injection of charge is one of the most important physical mechanisms that take places in organic devices [174]. At the same time, the metal-organic contact introduces detrimental effects on the performance of these devices. Therefore, to optimize the performance of these devices, a detailed physical description and the proper modeling and simulation of the metal-organic structure are necessary.

A key requirement in the simulation of the MOM structure, although frequently mishandled, is the selection of proper boundary conditions at the metal-organic interface. In this regard, a comprehensive understanding of the contacts is necessary [6, 73]. Recently, we focused on the contacts of organic thin film transistors [12, 13, 70, 71, 171]. In this chapter, we address the simulation and modeling of the organic diode or MOM structure, in particular, the effects of the contacts on the boundary conditions for simulation.

To develop the model, an important prerequisite is a proper understanding of the dark current of the MOM structure. The dark current in a diode provides insights into the injection mechanisms, charge transport, and trapping and recombination processes, which play important roles in the characteristics and parameters of organic devices [55, 175]. The electrical conduction in organic diodes is described by the drift-diffusion equations. The solutions of these equations depend on the boundary conditions (BCs) at the contacts. The charge transport equations in organic devices are similar to those used for inorganic semiconductor structures [176]. However, the boundary conditions for organic diodes are quite different [10, 177].

For simplicity, some authors use Boltzmann statistics to determine the value of free charge density at the interface [32, 43]. In this case, the charge density is constant, dependent only on the energy barrier height at the interfaces and independent of the current transferred through the contacts. However, there are multiple effects at the interfaces that can modify the value of the concentration of the electrons and holes [6]. Also, anomalous S-shaped current-voltage $J-V$ curves in organic solar cells under illumination are interpreted as due to the effect of the contacts [6]. The existence of doping introduced by oxygen and the presence of traps, impurities, and energy barriers for the extraction or injection of free charges can reduce the velocity at which the carriers are extracted or injected. In [6, 7], a recombination with constant velocity and low extraction/injection rates is used for numerical reproduction of such S-shapes. A constant interface recombination velocity results in a linear relation between the current density and the free charge density at the contact interface. In this regard, the charge density at the interface can be assumed as the result of the current flow from the metal to the semiconductor and vice-versa.

Other recombination models exist in organic diodes, such as the Langevin or direct recombination, Onsager-Braun model, Shockley-Read-Hall (SRH) and tail-state recombination [178–180]. Each mechanism is characterized by a particular recombination rate, $R(n, p)$, that actually provides a different relation with the electron or hole densities, n and p, respectively. A simple transformation of the conti-

nuity equation can provide an estimation of the relation of the current density J with the free charge density. Assuming steady state and no generation rate, the continuity equation of charge carriers can be transformed into

$$J_{n,p} = q \int R(n,p)dx \tag{5.1}$$

Therefore, different relations with the carrier density will appear, but the question, "what is this relation", remains. Different recombination models are used to analyze the injection of charge from electrodes into an organic material. The Langevin recombination model is combined with the thermionic emission model to provide a relation between the current density and the electric field at the interface [177]. For higher injection barriers, the Onsager-recombination is used to consider the escape probability from the organic material back to the electrode, in combination with other effects such as the reduction of the barrier height by the image charge effect [110]. The Langevin and Onsager models provide a relation of the current density with the electric field at the interface. In these models, the computational requirement is high and its validity is not extended to low barriers or Ohmic contacts [110].

In recent studies [10, 112, 143], we developed a relation between the current density J flowing through a metal-organic contact and the free charge density at the interface. We found that in symmetric diodes, controlled by the drift mechanism, the free charge density at the interface, $p(0)$, follows a power function of the current density: $p(0) = KJ^m$, where K and m are device related parameters. This relation is valid for different energy barrier heights at the contact. It is also valid for different regimes observed in the current-voltage curves of single-carrier metal-organic-metal structures, such as the Ohmic, the space-charge-limited or the injection-limited current regimes. The model was presented in [143]. There, the diffusion current was neglected as devices with very low built-in voltage V_{bi} were considered. The exclusion of the diffusion currents does not introduce considerable errors except when the device operates at low currents, as may be the case in photovoltaic devices [178]. The use of our model [143] in asymmetric structures, such as OSCs, is challenged by the presence of diffusion and also the presence of both electrons and holes in the current density. For these different situations, we explore the link between charge concentrations at contact interfaces and current in organic diodes.

This chapter is organized as follows. In Section 5.2, we present the drift-diffusion equations used for the simulation of organic diodes. In Section 5.3, we analyze symmetric MOM diodes with single-carrier conduction and propose analytical methods to extract the value of the charge density at the metal-organic interface from $J-V$ experimental data, confirming the power-law function of the charge-current relation proposed in [143, 181]. In Section 5.4, we validate our charge-current model also for asymmetric devices, in which charge diffusion takes place. For validation of the power law dependence with model parameters K and m, we compare diodes with symmetric and asymmetric contacts, different energy barriers at the contacts, and at different operating temperatures. We also study the physical significance of K and m. In Section 5.5, we finally extend our model to bipolar-conduction MOM structures.

5.2. Theory

The total current that flows in an organic semiconductor is determined by the electric field (drift) and the presence of carrier concentration gradients (diffusion). The following equations describe the drift-diffusion model of a diode:

$$J_p = qp\mu_p F - qD_p \frac{dp}{dx} \tag{5.2}$$

$$J_n = qn\mu_n F + qD_n \frac{dn}{dx} \tag{5.3}$$

$$\frac{dF}{dx} = \frac{q}{\varepsilon_r \varepsilon_0}(p - n) \tag{5.4}$$

$$\frac{dV}{dx} = -F \tag{5.5}$$

$$\frac{dp}{dt} = 0 = -\frac{1}{q}\frac{dJ_p}{dx} - R(x) + G(x) \tag{5.6}$$

$$\frac{dn}{dt} = 0 = \frac{1}{q}\frac{dJ_n}{dx} - R(x) + G(x) \tag{5.7}$$

$$R(x) = qnp(\mu_n + \mu_p)/(\varepsilon_r \varepsilon_0) \tag{5.8}$$

$$J_{AC} = J_p + J_n \tag{5.9}$$

where subscript p refers to holes and subscript n to electrons. In the above equations, q is the electron charge, D_p and D_n are the diffusion coefficients for holes and electrons, respectively, F is the electric field, V is the electrostatic potential, ε_r is the relative permittivity (dielectric constant) of the of the organic material and ε_0 is the vacuum permittivity. Equations (5.2) and (5.3) are the hole J_p and electron J_n current densities described by the drift-diffusion transport of charge. The electric field F is calculated according the Poisson's equation (5.4) and (5.5). Equations (5.6) and (5.7) are hole and electron continuity equations describing the generation and recombination of free charge carriers. The Langevin model is used in (5.8) for the recombination rate R of free electrons and holes in organic materials [182, 183]. The total current density from the anode to the cathode, J_{AC}, is given by (5.9).

The diffusion coefficient $D_{p,n}$ is assumed to follow the Einstein relation $D_{p,n}/\mu_{p,n} = V_T$, where $V_T \equiv k_B T/q$ is the thermal voltage, T is the absolute temperature, k_B is Boltzmann's constant and $\mu_{p,n}$ is the charge-carrier mobility. The mobility may depend on the temperature, electric field and charge concentration. A widely used model for the mobility that includes the effects of varying temperature and electric field is the correlated Gaussian disordered model (CGDM) [67, 85, 89] given by

$$\mu(T, F) = \mu(T, 0)\exp(\gamma\sqrt{F}) \tag{5.10}$$

where γ is a parameter that describes the enhancement of the mobility with electric field and $\mu(T,0)$ is the mobility at zero electric field.

Equations (5.2) to (5.9) describe bipolar conduction in organic diodes and are usually solved numerically by predetermined boundary conditions at the interfaces of the anode and cathode contacts. These equations can be simplified in some cases, such as for unipolar conduction and symmetric diodes. For example, the majority of organic semiconductors are with hole-only conduction [123]. Toward our objective of the bipolar conduction, we initially consider a hole-only MOM structure, in order to identify the factors that determine its behavior, and set up an analytical model. Then, we will show what adjustments in the model and extraction techniques are necessary for MOM structures with bipolar conduction.

5.3. MOM diodes with single-carrier conduction

In this section, we consider MOM structures with hole-only conduction in the organic semiconductor. Energy diagrams and $J-V$ curve of a MOM diode are shown in Figure 5.1a. The hole injecting contact is the anode at $x = 0$. The hole collecting contact is the cathode at $x = L$. The anode and cathode conductors have different work functions which creates a built-in voltage, $V_{bi} = (\Phi_A - \Phi_C)/q$. In the figure, Φ_1 and Φ_3 are the barriers observed by the holes and electrons from the anode towards the organic semiconductor, respectively. Φ_2 and Φ_4 are the barriers observed by the holes and electrons from the cathode towards the organic semiconductor, respectively. The barriers Φ_3 and Φ_4 are assumed large enough to prevent injecting electrons from contacts to the conduction band of the semiconductor. Also, the organic semiconductors are usually wide band-gap materials. Therefore, the thermal generation of carriers is negligible and so is not considered.

There are situations, especially at low electric fields, in which the mobility can be assumed constant. This is the case of the low voltage region in a current-density voltage curve ($J_{AC} - V_{AC}$). Here, V_{AC} is the applied voltage between anode and cathode and J_{AC} is the density of the current flowing from anode to cathode. A complete $J_{AC} - V_{AC}$ curve, shown schematically in Figure 5.1d, has two different regions. Each region is dominated by one transport mechanism. At low voltages, diffusion is dominant (Figure 5.1b), while at high voltages, drift prevails (Figure 5.1c). First, we consider the regions where one mechanism is dominant, and for which simplified methods and proposals can be found in the literature [143, 184]. Second, we treat the region around the built-in voltage where neither diffusion nor drift is negligible.

5.3.1. Symmetric organic diodes

A study of symmetric organic diodes was presented in [143]. For the sake of completeness, we include this study in this section, in which we add an analytical method to extract the value of the charge density at the metal-organic interface. This method complements the numerical method proposed in [143]. The procedure is validated with experimental data from publications of different groups.

In symmetric organic diodes, the built-in voltage V_{bi} is zero, and the charge transport of holes is

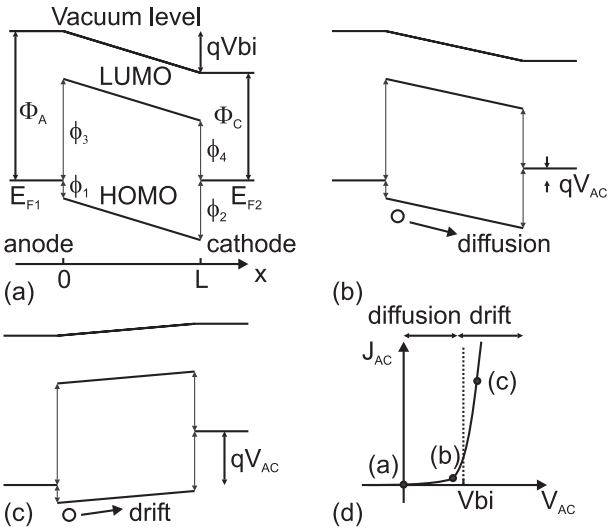

Figure 5.1: Energy band diagram of a hole-only MOM diode with asymmetric contacts that create a built-in potential, (a) at thermal equilibrium, (b) at an applied voltage smaller that the built-in voltage and (c) at an applied voltage larger that the built-in voltage. (d) Typical $J_{AC} - V_{AC}$ voltage characteristic with indication of the above regimes.

given by eq. (5.2) [112]. Also, Poisson's equation (5.4) uses only the hole concentration p. In darkness, the charge generation and recombination are ignored, which simplifies eq. (5.6). Thus, eqs. (5.3), (5.7) and (5.8) are irrelevant for hole-only MOM diodes, and are not considered in our numerical simulations. The total current density J_{AC} is given only by the hole current density (5.9), so $J_{AC} = J_p$. When a variable mobility is considered, then the mobility is given by eq. (5.10).

With the objective to relate interface charge density with current density, we use boundary conditions for potentials and experimental data for $J_{AC} - V_{AC}$, in order to obtain charge density profiles. The values for carrier mobility are adopted from the literature. Analytical models provide profiles for the product (charge density × mobility), and by dividing by the mobility, the charge profiles are determined. The charge profiles are immediately available from numerical simulation. From the charge profiles, we determine the charge density $p(0) = p_A$ at the anode interface ($x = 0$).

The experimental data for a symmetric MOM structure are for a glass /ITO /PEDOT:PSS /LEP /Pd organic diode at 295 K. The semiconducting layer is polyfluorene-based light-emitting polymer (LEP) of length $L = 122$ nm and relative permittivity $\varepsilon_r = 3.2$ [76]. We extract p_A by several methods. One method uses numerical simulation, considering drift-only charge transport. The second method uses numerical simulation, considering drift-diffusion charge transport. The third group of methods is based on an analytical model with constant or field-enhanced mobility, taking also the electric field with either an average value or with values at the anode interface, as explained later.

In the first method of numerical simulation with drift-only charge transport, we reduce the charge concentration in the equations. Taking $D_p = 0$, then $p = J_{AC}/q\mu F$ from eqs. (5.2) and (5.9) is

substituted in (5.4). Thus, the system of differential equations for drift-only transport becomes

$$\frac{dF}{dx} = \frac{J_{AC}}{\varepsilon_r \varepsilon_0 \mu F}, \ \frac{dV}{dx} = -F \tag{5.11}$$

where the current J_{AC} is the experimental current J_{exp}. Equation (5.11) is solved numerically with the boundary conditions for potentials $V(0) = 0$ and $V(L) = -V_{AC}$, because $V_{bi} = 0$ for a symmetric MOM. Since the charge concentration is reduced in the equations, then the interface charge density is determined from the current density and the electric field by

$$p_A = \frac{J_{AC}}{q\mu(T,0)F_0 \exp(\gamma\sqrt{F_0})} \tag{5.12}$$

where $F_o = F(0)$ is the electric field at the interface. Using $\gamma = 9.206 \times 10^{-5}$ $(\text{cm/V})^{1/2}$ and $\mu_o = 1.28 \times 10^{-6}$ cm^2/Vs in the numerical simulation [112], the result for the interface charge by drift-only charge transport is shown with squares in Figure 5.2a.

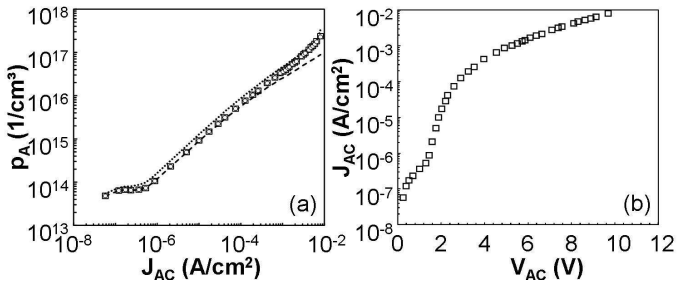

Figure 5.2: (a) Hole concentration at the anode as a function of current density J_{AC} in a symmetric organic diode with hole-only conduction, extracted from (b) the experimental current-voltage data [76]. In (a) symbols from numerical simulations with variable mobility, using drift-only charge transport (squares) and drift-diffusion transport (small circles), are practically superimposed. Lines are from the analytical model, considering constant mobility (dotted line) and enhanced mobility (dashed line).

In the second method of numerical simulation with drift-diffusion charge transport, we solve eqs. (5.2), and (5.4) to (5.6) with $n = 0$, a field-dependent mobility given in (5.10), with boundary conditions for the potentials $V(0) = 0$, $V(L) = -V_{AC}$, and equal charge densities at the cathode $p(L) = p_C$ and anode $p(0) = p_A = p_C$, since the MOM structure is symmetric. The current at the anode is set equal to the experimental current $J_{AC}(0) = J_{exp}$. The interface charge p_A is found from the numerical solver at $x = 0$, as before, and shown with small circles that match the squares in Figure 5.2a. Thus, the overlap between numerical simulations with drift-only and drift-diffusion transport indicates that the carrier diffusion has a marginal impact on the interface charges in symmetric devices.

The third group of simulation methods corresponds to an analytical model that considers drift-diffusion transport and given (although unknown in value) hole densities at the interfaces, p_A and p_C. The derivation of the analytical model also assumes a constant value for the mobility and a linear evolution of the potential along the organic material. The analytical model [42, 184, 185] and the procedure to extract the value of p_A from experimental data are detailed in Appendix I. For zero

Table 5.1: Parameters K_1, K_2 and m of the power-law model (5.14) extracted from the analysis of different organic diodes.

Ref.	anode	organic	cathode	qV_{bi} (eV)	barrier (eV)	K_1 ($\mathrm{cm}^{2m-3}\ \mathrm{A}^{-m}$)	K_2 (cm^{-3})	m	Fig.
[76]	ITO/ PEDOT:PSS	LEP (h)	Pd	0	0	6.7×10^{18}	10^{14}	0.76	5.2
[85]	ITO	CuPc (h)	Al	0.55	0.05	1.7×10^{18}	10^{14}	0.75	5.5
[85]	Al	CuPc (h)	ITO	0.55	0.6	3.9×10^{17}	10^{12}	0.74	5.5
[43]	MoO_3	PFO (h)	ZnO	1.8	1.8	1.2×10^{18}	10^{15}	0.50	5.5
[111]	ITO/ PEDOT:PSS	PCBM (e)	Au	0.4	3.0	$10^{0.009T+13.05}$	2.0×10^{10} (240 K) 7.5×10^{10} (290 K)	0.74	5.6
[186]	ITO	CuPc (h)	Cu	0.15	0.05	5.51×10^{17}	4.1×10^{14}	0.68	5.7
[186]	ITO	CuPc (h)	Al	0.55	0.05	1.3×10^{18}	1.7×10^{12}	0.74	5.7
[186]	Cu	CuPc (h)	ITO	0.15	0.2	2.5×10^{17}	2.1×10^{14}	0.65	5.7
[186]	Al	CuPc (h)	ITO	0.55	0.6	7.2×10^{16}	4.1×10^{10}	0.73	5.7
[187]	Nd	MEH-PPV (e)	Ca	0	0.2	1.3×10^{19}		0.81	5.8
[187]	ITO	MEH-PPV (h)	Au	0.5	0.2	9.8×10^{18}		0.81	5.8
[188]	Yb	PPV (h)	Ca	0.3	0.2	1.3×10^{18}		0.79	5.9
[188]	ITO/Ag	PPV (h)	Ag	0	0.3	4.1×10^{17}		0.77	5.9

built-in voltage in a symmetric MOM diode, the interface charge density is:

$$p_A = J_{AC}/(q\mu F_{AVG}), \text{ with } F_{AVG} = V_{AC}/L \tag{5.13}$$

The result for the interface charge considering constant mobility $\mu \approx \mu_o = 1.28 \times 10^{-6}$ cm^2/Vs is shown with dotted line in Figure 5.2a. The result for an enhanced mobility at the interface evaluated from (5.12) with $F_o \approx F_{AVG} = V_{AC}/L$ and $\mu(T, 0) = \mu_o = 1.28 \times 10^{-6}$ cm^2/Vs is shown with dashed line in Figure 5.2a. F_o is the electric field at the charge injecting interface, here at the anode contact, and F_o is approximately equal to the average electric field F_{AVG}, when space charge effects are negligible. The full relation between F_o and F_{AVG} is given in II.1.

Note in Figure 5.2a that the interface charge density p_A follows the recent model [143] of a power-law functional relation with the current density J_{AC}:

$$p_A = K_1 J_{AC}^m + K_2 \tag{5.14}$$

where the values of the parameters m, K_1 and K_2 are in Table 5.1. As detailed in [143, 181], the parameter K_1 depends on the barrier height at the interface and the temperature, m depends on the organic material, and K_2 describes the flat zone at low currents. K_2 depends on concentrations of thermally generated carriers and impurities. In the region of high currents in the $J_{AC} - V_{AC}$ curve, the parameter K_2 is not significant.

While the power-law behaviors of the different data series are similar in Figure 5.2a, there are also differences in the values of p_A when extracted by the different models and conditions. For example, relation (5.14) was developed for organic diodes considering drift-only charge transport, while diffusion, electric field and variable mobility may affect values of K_1, K_2 and m. The data in Figure 5.2a can be used to determine the impact of different factors under different transport conditions. Among the different factors that affect the values of p_A, the most important is the electric field at the interface. The next important is the mobility enhancement, which provides a better fit of $J_{AC} - V_{AC}$ and $p - J_{AC}$ curves simultaneously at higher currents. The least important factor is the carrier diffusion, because, as seen

in Figure 5.2a, the values of p_A are approximately the same for drift-only (squares) and drift-diffusion (small circles) numerical models.

The differences in Figure 5.2a, between the analytical model with constant mobility (dotted line) and the numerical result (symbols), are due to the fact that the constant mobility in the analytical simulation is lower than the enhanced variable mobility in the numerical simulations. In the first case, we use $\mu = \mu(0, T)$, and in the second $\mu = \mu(0, T) \times \exp(\gamma F^{1/2})$. From eq. (5.13), a higher concentration of charge is expected at lower mobility. This explains the almost parallel displacement.

The differences in Figure 5.2a between the analytical simulations with average electric field (dashed line, $F_o \approx F_{AVG} = V_{AC}/L$) and using the numerical value of the interface electric field (circles, $F_o = F(0)$ from the numerical simulation with the drift-diffusion model) are explained with Figure 5.3. Figure 5.3a compares the average electric field (dashed lines, $F_{AVG} = V_{AC}/L$) to the actual distribution of the electric field (solid lines) obtained from the numerical simulation with the drift-diffusion model. At low voltages, the electric field is almost constant and equal to the average electric field. Thus, the charge density for both methods is the same at low J_{AC} in Figure 5.2a. At higher bias voltages, the electric field at the interface is lower than the average electric field in Figure 5.3a, causing the extracted values for p_A from both methods to be different in Figure 5.2a, according to eqs. (5.12) and (5.13).

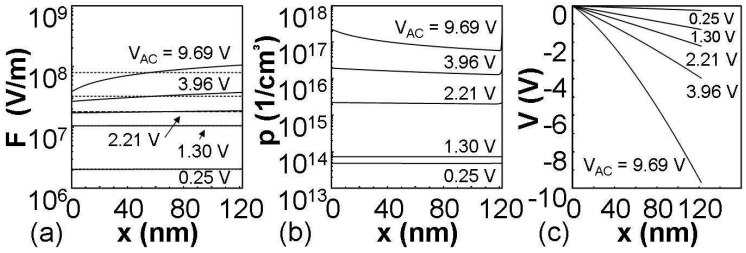

Figure 5.3: Evolution of the spatial distributions of the (a) electric field, (b) hole concentration and (c) potential in a MOM with the applied anode-cathode voltage V_{AC} = (0.25, 1.30, 2.21, 3.96, 9.69) V.

The reduction of the interface electric field (as compared to the average value) is due to the space charge shown in Figure 5.3b. Both the space charge and the interface charge increase at high currents. Space charge limited conduction (SCLC) [186] takes place at high currents, whereas the conduction is ohmic at low currents. It is seen in Figure 5.3c that the spatial distribution of potential evolves from linear at low biases to quadratic at higher biases. Since the interface electric field F_o is the most important factor for the accurate determination of the interface charge, but F_o is unavailable in the analytical model, then eq. (B.7) in II.1 provides for the relation between the interface field, F_o, the average electric field, $F_{AVG} = V_{AC}/L$, and the electric field from the space charge, F_{SCLC}.

5.4. Asymmetric organic diodes with single-carrier conduction

In this section, we validate of the power-law function (5.14) between charge and current for asymmetric MOM devices. In asymmetric organic diodes, the built-in voltage is different from zero, $V_{bi} > 0$. The charge transport of holes is given by the drift-diffusion transport by eq. (5.2). Since the MOM

structure is a hole-only device and smiliar to the previous case, we use only the hole concentration p and Poisson's equation (5.4). We again use both numerical and analytical methods to determine the free charge density at the injection interface $p(0)$ as a function of the current density.

In the numerical simulation with drift-diffusion charge transport, we solve eqs. (5.2), (5.4)-(5.6) with $n = 0$ and the field-dependent mobility eq. (5.10), with boundary conditions for the potential $V(0) = 0$, $V(L) = -V_{AC} + V_{bi} = -V_{exp} + V_{bi}$ with the experimental voltage V_{exp} and the current at the anode $J_A(0) = J_{AC} = J_{exp}$ is equal to the experimental current J_{exp}. The charge density at the cathode is taken to be zero, considering that the barrier for holes at the cathode is larger than the barrier at the anode. Under these boundary conditions, the solution of the above equations provides a value of $p(0)$ for the experimental point (J_{exp}, V_{exp}). In the simulation, the initial value of the built-in voltage is the difference of the work functions of the electrodes. Occasionally, the value for V_{bi} needed to be modified until physically meaningful solutions for $p(0)$ are obtained. In particular, if V_{bi} has an incorrect value, then an anomalous solution of abrupt increase of the value of $p(0)$ at very low current densities can be observed in numerical simulations. In general, V_{bi} often deviates from the guess made from the difference of the work functions of the contact materials [187].

In the analytical procedure, we employ a simplified extraction method for the charge density at the interface, using asymptotic expressions (A.10) and (A.12) in Appendix I when $V_{AC} > V_{bi}$ and $V_{AC} < 0$, respectively. These expressions follow from the analytical model (A.4) in Appendix I. Equations (A.10) and (A.12) provide relations between the charge density at the injecting interface (p_A for holes at anode or p_C for electrons at cathode) as a function of the derivative dJ/dV of the experimental current-voltage curve, assuming that the mobility is known. In that way, the hole charge concentrations are directly extracted without imposing the problem of an unknown value of the built-in voltage.

For an asymmetric MOM diode with moderate built-in voltage, we consider the experimental current-voltage curve from [85] for ITO/CuPc (copper phthalocyanine)/Al diode. The length of the CuPc layer is $L = 100$ nm. The squares in Figure 5.4 show the experimental $J - V$ curve measured at 320 K, both in forward and reverse bias. The ITO electrode provides an Ohmic contact to CuPc (barrier~ 0.05 eV). The difference between the aluminum work function and the LUMO of CuPc is approximately 0.6 eV. The values of the other parameters used in calculations and simulations are: relative permittivity $\varepsilon_r = 2.1$; constant mobility $\mu_p = 2 \times 10^{-6}$ cm^2/Vs [143]; and built-in voltage $V_{bi} = 0.55$ V.

For another asymmetric MOM diode with high built-in voltage, we analyze data from [43] for a MoO_3/PFO(poly(9,9-dioctylfluorene))/ZnO diode (triangles in Figure 5.4). The length of the PFO layer is $L = 180$ nm. The $J-V$ curve was measured at 295 K. The HOMO level of PFO is ~ 5.8 eV. The work function of the MoO_3 anode is ~ 5.8 eV and provides an Ohmic contact to PFO. The ZnO cathode is a hole-collecting contact with a lower work function of approximately 4 eV. The difference between the work functions of the electrodes is 1.8 V, but the built-in voltage of the MOM is $V_{bi} = 2$ V, as deduced from the analysis of p_A extracted from the experimental $J - V$ curves. The discrepancy of 0.2 V can be attributed to several factors, e.g., pinning Fermi level at interfaces, band bending at the injecting contacts due to accumulation of charge carriers [188], and energy shifts due to interface dipoles [57–62]. The other PFO parameters used in calculations and simulations are $\varepsilon_r = 3$, $\mu_p = 5.85 \times 10^{-6}$ cm^2/Vs, and $\gamma = 9.2 \times 10^{-5}$ (cm/V)$^{1/2}$.

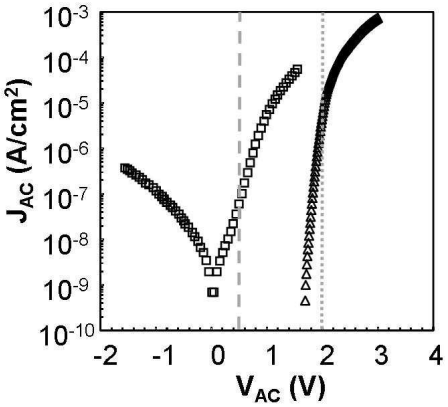

Figure 5.4: Experimental current-voltage curves for asymmetric diodes. The triangles are for a MoO_3/PFO/ZnO diode at 295 K [43]; the squares are for an ITO/CuPc/Al diode at 320 K [85]; and the dashed lines indicate the diodes' built-in voltages.

For the analyzed MOM diodes, the evolution of the hole concentration at the injecting interface (p_A at the anode or p_C at the cathode) are shown in Figure 5.5 as a function of J_{AC}. The open and filled squares are for the ITO/CuPc/Al diode, and the open and filled triangles are for the MoO_3/PFO/ZnO diode. The filled symbols refer to the analytical model (eqs. (A.10) and (A.12)). The open symbols are after numerical simulations of the drift-diffusion transport. The dot-dashed lines illustrate the power-law dependence between the charge density and the current density in eq. (5.14). The values of the parameters of this model that fit the forward and reverse curves of the ITO/CuPc/Al diode and the forward curve of the MoO_3/PFO/ZnO diode are in Table 5.1. The vertical dashed and dotted lines indicate the values of the built-in voltages of the ITO/CuPc/Al and MoO_3/PFO/ZnO diodes, respectively. In order to compare the results of these asymmetric diodes with symmetric MOM, we add the circles in Figure 5.5. The circles correspond to the data set in Figure 5.2a obtained from the numerical calculation of symmetric MOM diode. The first observation is that all the data in Figure 5.5 tend to follow a power law of $p \propto J_{AC}^m$, with $m \approx 0.75$, see again eq. (5.14).

An interesting observation in Figure 5.5 is that the $p - J$ dependences for different diodes virtually overlap at high forward biases, when $V_{AC} > V_{bi}$. In the case of the PFO diode, the filled triangles (analytical derivation) and the open triangles (numerical simulation) at higher currents follow almost the same power-law function. In the case of CuPc, the ratio between the full squares (analytical derivation, eqs. (A.10) and (A.12)) and the empty squares (numerical simulation) is almost two. This difference is attributed to the difference observed between the average of the electric field and the numerical electric field at the interface, as was discussed in the previous section.

In the transition region, $0 < V_{AC} < V_{bi}$, since $J \propto \exp(V)$, the analytical calculation with eqs. (A.10) and (A.12) is no longer valid, as seen from the results shown in Figure 5.5. Instead, the results from numerical simulation must be considered. At low currents, the charge concentrations deviate from the power-law trend, tending to a particular "constant" value, which corresponds to K_2 in eq. (5.14). The values of K_2 are different for different diodes and probably correspond to the charge emission through

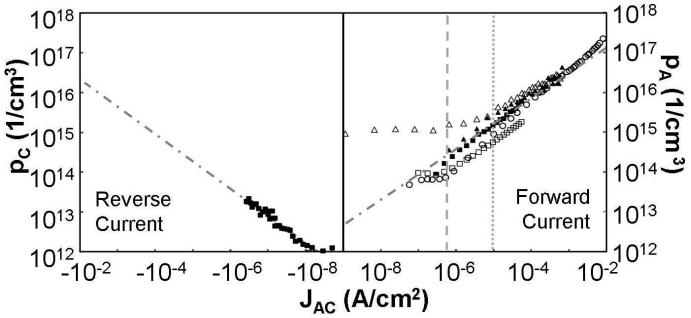

Figure 5.5: Hole concentrations at the anode p_A and the cathode p_C as function of current density J_{AC} in asymmetric organic diodes with hole-only conduction. Squares are for the ITO/CuPc/Al diode and the triangles are for MoO_3/PFO/ZnO diode. The open and filled symbols correspond to the numerical and the analytical simulations, respectively. The dot-dashed lines illustrate the power law dependence (5.14). The vertical lines indicate the value of V_{bi} as in Figure 5.4. The circles correspond to the numerical results of the symmetric MOM diode of Figure 5.2a.

the contact barriers.

Comparing the $J_{AC} - V_{AC}$ curves in Figure 5.2b and Figure 5.4, the current-voltage characteristics are very different for different organic diodes. The current density in the $J_{AC} - V_{AC}$ curves spans the range from a fraction of nA/cm^2 to tens of mA/cm^2, but the transitions from low to high currents are at apparently different ranges of bias voltages. In asymmetric diodes (Figure 5.4), the current rises around V_{bi}. Therefore, changing the materials for the anode and the cathode in MOM structures, one varies the differences between the work functions and V_{bi} changes. Consequently, the $J_{AC} - V_{AC}$ curves shift "horizontally" with V_{bi} along the voltage axis. The larger is the shift from zero, the larger is the difference (actually the ratio) between forward and reverse currents.

Another effect related to the built-in voltage is the slope of the transition region from low to high currents between $V_{AC} = 0$ and $V_{AC} = V_{bi}$. The transition is an exponential function of V_{AC}, with a steep slope of approximately $2.3k_BT/q$ V/dec in diodes with high V_{bi}, but the slope changes, and the $J_{AC} - V_{AC}$ curves become nearly linear when $V_{bi} = 0$. These variations in the $J_{AC} - V_{AC}$ curves as function of V_{bi} are present in the numerical simulations, as well as in the analytical model of eq. (A.4). The non-linear $J - V$ curves outside the transition region are due to the increment of the interface charge density, as explained above.

When V_{AC} is outside the transition region from 0 to V_{bi}, eqs. (A.9) and (A.11) predict a linear relation between V_{AC} and J_{AC} both for $V_{AC} > V_{bi}$ and $V_{AC} < 0$, if the charge concentrations and mobility are with constant values. However, as shown in Figure 5.2a and Figure 5.5, the charge concentrations vary as a power law function of the current.

The exponent m in the power law in eq. (5.14) can be seen as a parameter with information from the charge transport in the bulk of the organic material and from the recombination mechanism that is present at the metal-organic interface. In all cases shown in Figure 5.5, the exponent in the power law function is $m \sim 0.75$. This value of $m \sim 0.75$ is between the values corresponding to space-charge limited conduction (SCLC) and interface recombination with constant velocity, as described below.

Combining the typical $J_{AC} - V_{AC}$ relation for the SCLC,

$$J_{AC} = 9\varepsilon_r\varepsilon_0\mu V_{AC}^2/(8L^3) \tag{5.15}$$

with $J_{AC} = q\mu pF$ and considering the approximation of $F \approx V_{AC}/L$, then the applied anode-cathode voltage is $V_{AC} \approx J_{AC}L/(q\mu p)$. From these equations, the charge density at the interface is related to the current density through a power-law function with $m = 0.5$:

$$p_A \approx K_1 J_{AC}^m, \text{ with } K_1 = \sqrt{\frac{9\varepsilon_r\varepsilon_0}{8q^2\mu L}} \text{ and } m = 0.5 \tag{5.16}$$

At metal-organic contacts, an interface recombination process can be present [189]. The charges from the organic material move in the contact with a particular velocity, or opposite-polarity charges move in the semiconductor and "recombine" with the carriers in the semiconductor. The interface recombination process also provides a power law relation between the current density and the charge density, but the value of m might differ from 0.5. A generic recombination rate $R = c_1 \times (n, p)^{c_2}$, with c_1 and c_2 as constants [190], can be introduced in (5.1) resulting in

$$J_{n,p} = qc_1 \int_0^d (n, p)^{c_2} dx = qc_1 (n, p)^{c_2} d \tag{5.17}$$

where the integral is evaluated along a short distance d for the interface (usually a few nanometers) and the charge concentrations (n and p) are assumed constant in this short distance.

Interface recombination can be described by means of the recombination velocity at the contacts. For a constant value of the surface recombination velocity S, the charge density at the interface and the charge flow through the interface are related by a linear dependence [6, 174, 177]. For a constant value of S, the relation between the charge density and the current becomes a power-law function with $m = 1$, since

$$\begin{aligned} J_{AC} = qS(p_{A,C} - p_0) \text{ or } p_{A,C} = J_{AC}/(qS) + p_0 \\ \text{where } K_1 = 1/(qS),\ m = 1,\ K_2 = p_0 \end{aligned} \tag{5.18}$$

where p_0 is given by Boltzmann statistics at the contact.

For comparison, the ideal contact (a far from realistic situation in organic-metal interfaces) is following Boltzmann statistics, and the hole and electron densities at the metal-organic interface depend on the values of the corresponding energy barriers at the interface. (The barriers were illustrated in Figure 5.1a, being the differences between the HOMO and LUMO energy levels and the metal work functions). Thus, the charge density does not depend on the current and $m = 0$ in an ideal contact.

Returning to the cases analyzed in Figure 5.5, the exponent in the power law function, $m \sim 0.75$, indicates a combined contribution from space-charge limited conduction and recombination effects at the interfaces. The effect of other variables, such as the temperature or the energy barrier height at the interface, on the value of the parameters of our model (5.14) is studied in the following section.

5.4.1. Study of the relation $p_A - J_{AC}$ with Temperature

In this section, we study the dependence of the parameters of our model (5.14) with the temperature. Figure 5.6a shows a set of current density vs. voltage curves measured at different temperatures in an electron-only ITO/ PEDOT:PSS/ PCBM/ Au device with thickness $L = 170$ nm [111]. Figure 5.6b shows the free charge density concentration at the cathode interface as a function of the current density. The charge density is extracted from the experimental data with the numerical procedure detailed in Sec. 5.3.1. The estimated built-in voltage is $V_{bi} = 0.75$ V. The dielectric constant of PCBM is $\varepsilon_r = 3.9$, having electron mobility $\mu = 2 \times 10^{-3}$ cm^2/Vs at room temperature [111].

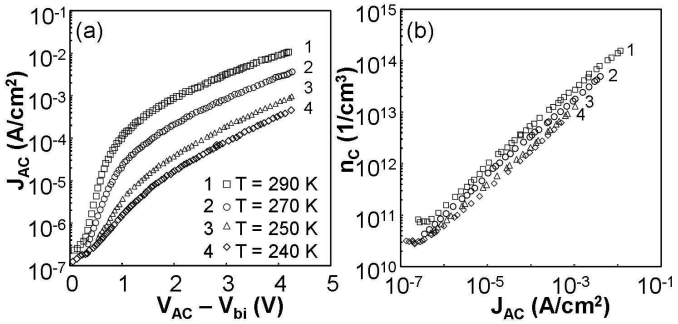

Figure 5.6: (a) Experimental current-density vs. voltage curves as a function of the temperature for an electron-only ITO/PEDOT:PSS/PCBM/Au device with thickness $L = 170$ nm taken from the reference [111]. The estimated built-in voltage is $V_{bi} = 0.75$ V. (b) Electron concentration at the cathode as a function of current density J_{AC} extracted from (a).

The dependence of the electron density on the current density at the cathode interface follows the model (5.14). The values of the parameters K_1, K_2 and m are in Table 5.1. The parameters K_1 and K_2 are temperature dependent with $K_1 = 10^{0.009T+13.048}$ cm^{2m-3}/A^m and K_2 varying from 2.0×10^{10} to 7.5×10^{10} cm^{-3} when T increases from 240 to 290 K.

The value of the parameter $m = 0.75$ is independent of the temperature, indicating that m depends only on the organic material. The parameter K_1, related to the energy barrier at the interface, shows the increase of the number of carriers injected through the barrier when elevating the temperature. The increase of K_2 with temperature indicates a larger number of thermally generated carriers at higher temperatures.

5.4.2. Study of the relation $p_A - J_{AC}$ with the Energy Barrier height at the injecting contact

In this section, we study the dependence of the parameters of our model (5.14) on the height of the energy barrier of the injecting interface. We consider the following asymmetric hole-only single-layer copper-phthalocyanine (Cu-Pc) based diodes: (1) ITO/CuPc/Al, (2) ITO/CuPc/Cu, (3) Cu/CuPc/ITO, and (4) Al/CuPc/ITO, where (4) is the reverse of (1) and (3) is the reverse of (2). For the sake of clarity, the first metal is always considered as the anode. Thus, there are three injecting interfaces (ITO/CuPc, Cu/CuPc and Al/CuPc) with different injection barriers ($\phi_1 = 0.05$, 0.2 and 0.6 eV respectively),

and three different collecting cathodes (CuPc/Al, CuPc/ITO and CuPc/Cu). The length of the organic material is $L = 200$ nm. Figure 5.7a shows the experimental $J_{AC} - V_{AC}$ characteristics of these structures measured at room temperature [191]. Figure 5.7b depicts the hole concentration at the anode and cathode as a function of current density J_{AC} extracted from the current voltage curves of Figure 5.7a, following the numerical method described in Sec. 5.3.1. The values of the parameters K_1, K_2 and m are in Table 5.1.

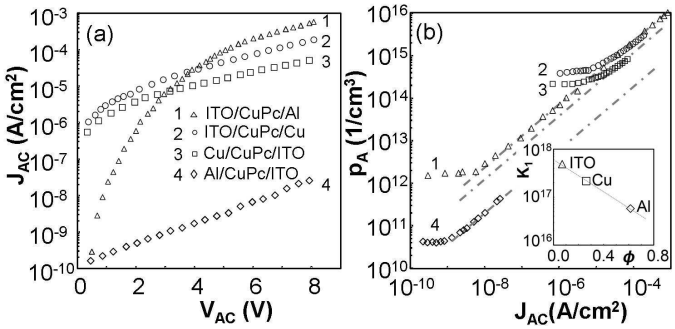

Figure 5.7: (a) Experimental current-voltage curves measured at room temperature for four hole-only diodes (ITO/CuPc/Al, ITO/CuPc/Cu, Cu/CuPc/ITO and Al/CuPc/ITO, where the first metal is always the anode) taken from [191]. (b) Hole concentration at the anode as a function of the current density J_{AC} extracted from (a). Inset: Parameter K_1 (in $\mathrm{cm}^{2m-3}\mathrm{A}^{-m}$) as a function of the energy barrier height ϕ (in eV) of the injection electrode.

In Figure 5.7a, we observe that when the energy barrier is increased, the current is reduced. The only anomaly is found in the curve 1 (ITO/CuPc/Al) diode at low currents because this diode is the one with the highest built-in voltage (0.6 V). The representation of the hole density at the anode in Figure 5.7b is useful to understand the exact relation between the current density and the energy barrier.

The first observation is that the slope of the four curves (parameter m) is approximately the same, confirming the strong relation of m with the organic semiconductor. The second observation is the inverse relation between the parameter K_1 and the energy barrier of the injecting electrode ϕ. K_1 decreases exponentially when ϕ increases (see inset of 5.7b). The current density of the diodes with the same anode interface (ITO/CuPc) but with different values of V_{bi} (curves 1 and 2 in Figure 5.7a), are clearly not the same. However, from curves 1 and 2 in Figure 5.7b, the relations $p_A - J_{AC}$ of both diodes converge within numerical or experimental errors, once the drift mechanism is dominant.

The flat region for the charge density at low current densities is observed in all the diodes. In symmetric diodes, this flat region is associated with an ohmic behavior in the $J_{AC} - V_{AC}$ curves. In asymmetric diodes, the flat region corresponds to the transition region $0 < V_{AC} < V_{bi}$, where the exponential dependence in the $J - V$ curves is controlled by the diffusion charge transport. The existence of this constant region with charge concentration K_2 can be related to thermally generated carriers, dopants or traps [181].

5.5. MOM diodes with bipolar-carrier conduction in darkness

In this section, we apply the previous procedures to bipolar diodes with the objective of checking whether the electron and hole densities can be considered as independent of each other, while functions of the interface values of the respective charge densities at injecting contacts. To do this, we analyze two sets of experimental curves. The first set of data was measured by Parker et. al in MEH-PPV (poly(2-methoxy, 5-(2'-ethyl-hexoxy)-1,4-phenylenevinylene)) based diodes (symbols in Figure 5.8a) [192]: a bipolar ITO/MEH-PPV/Ca diode (circles), an electron-only Nd/MEH-PPV/Ca diode (triangles) and a hole-only ITO/MEH-PPV/Au diode (squares).

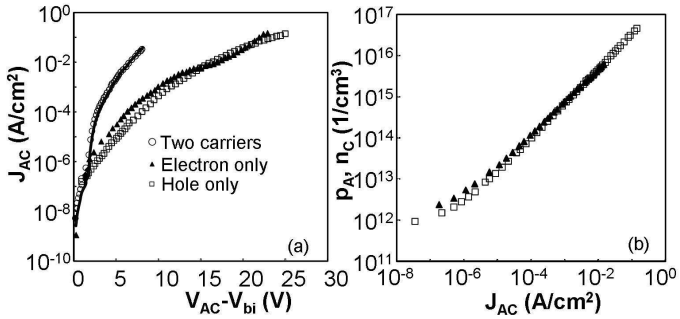

Figure 5.8: (a) Experimental current-density voltage curves of hole-only ITO/MEH-PPV/Au, electron-only Nd/MEH-PPV/Ca and bipolar ITO/MEH-PPV/Ca diodes, with a length of 120 nm, and measured at room temperature [192] (symbols). The grey solid line is the fitting of our model. (b) Extracted values from (a) of the hole and electron densities at the anode and cathode, respectively, as a function of current density J_{AC}. The mobility values used in the simulation are: $\mu_n = \mu_p = 10^{-7}$ cm^2/Vs.

In a first step, we apply the procedure described in the previous sections to determine the values of p_A as a function of the hole current density J_p in the hole-only diode (ITO anode in the ITO/MEH-PPV/Au diode); and the values of n_C as a function of the electron current density J_n in the electron-only diode (MEH-PPV/Ca cathode in the Nd/MEH-PPV/Ca diode). The values of the mobility used in the simulation are: $\mu_n = \mu_p = 10^{-7}$ cm^2/Vs [193, 194]. The values of p_A that make the transport equations matching the experimental data (squares in Figure 5.8a) are shown also with squares in Figure 5.8b. The squares in Figure 5.8b follow our power-law model $p_A = K_{1_p} J_p^{m_p}$ (J_p is the current density flowing through the hole-only diode) with m_p and K_{1_p} given in the Table 5.1. In the same way, the values of n_C extracted from the experimental data (triangles in Figure 5.8a) are shown also with triangles in Figure 5.8b, n_C follows our model $n_C = K_{1_n} J_n^{m_n}$ (J_n is the current density flowing through this electron-only diode) with m_n and K_{1_n} given in the Table 5.1. The identical values of $m_n = m_p = 0.81$ confirm our previous conclusion that m depends only on the organic material, and not on the contact metal. Similar values $K_{1_n} \approx K_{1_p}$ (see Table 5.1) are also found for the electron-only and hole-only diodes. This implies similar energy barrier heights at the injecting contacts in both single-carrier diodes. Moreover, both diodes are symmetric with $V_{bi} = 0$ V. Therefore, no value for K_2 is extracted, because no diffusion or ohmic region is found in the experimental $J - V$ curves at low voltages.

In a second step, the models for the electron and hole densities at the injection interfaces extracted

for single-carrier diodes are used. The expressions $n_C = K_{1_n} J_{exp}^{m_n}$ and $p_A = K_{1_p} J_{exp}^{m_p}$ are employed as boundary conditions in the numerical solution of the transport equations of the bipolar ITO/MEH-PPV/Ca diode. An essential note is that the total current J_{exp} that flows in the bipolar diode is used in the charge-current models of the injecting electrodes, ($n_C = K_{1_n} J_{exp}^{m_n}$ and $p_A = K_{1_p} J_{exp}^{m_p}$ for cathode and anode), instead of summing the current densities of electron-only and hole-only diodes, $J_{exp} = J_{n\&p} \neq J_{n-only} + J_{p-only}$. As observed by the authors who measured the data, the sum of the currents of the electron-only and hole-only devices is much lower than the current in the two-carrier device. The authors explained the increase of the current in two-carrier devices with the reduction of the net space charge in the organic semiconductor by the existence of polarons. The net charge of which is zero, since positive and negative charges are of the same amount in polarons. Consequently, and compared to unipolar diodes, the electric field due to space charge is reduced in the bipolar device, allowing for higher currents densities.

Thus, taking the total current J_{exp} of the bipolar diode in the power-law charge-current models from unipolar diodes, we use the models for the injecting electrodes as boundary conditions in the numerical simulation of the bipolar device, and obtained the $J-V$ curve shown with solid line in Figure 5.8a. All other parameters of the single carrier devices (e.g., mobility, permittivity, injection barriers, etc.) are kept unchanged by solving the transport equations of the bipolar device. Observe that the simulated $J-V$ curve (solid line) perfectly matches the experimental data (circles), confirming that the charge carrier densities at the injection interfaces follow the power-law dependence on the current density, and the dependence is on the total current through the device, but not on one or another component of the current. The values of electron and hole densities at the collecting interfaces (n_A and p_C, respectively) are small and not affecting our results. Therefore, they are taken independent of the current, considered to obey Boltzmann statistics and follow the relations $n_A = N_C \exp(-q\phi_3/k_BT)$ and $p_C = N_C \exp(-q\phi_2/k_BT)$, where the barriers ϕ_3 and ϕ_2 are defined in Figure 5.1, and N_C is the density of states in the organic material.

To ensure that our results are systematic, but not fortuitous, a second set of measurements on unipolar and bipolar diodes were taken from Woudenbergh et. al [195]. The experimental data are shown with symbols in Figure 5.9a and are for devices with 240 nm spin-coated layer of the polymer OC_1C_{10}-PPV sandwiched between three sets of electrodes. The ITO/PPV/Ca diode is a bipolar diode (circles), the Yb/PPV/Ca is an electron-only diode (triangles) and the ITO/Ag/PPV/Ag is a hole-only diode (squares). We apply the same procedure as in the previous set of data: we extract the values of the parameters of our model (5.14) for the electron and hole densities from the analysis of single-carrier diodes (triangles and squares in Figure 5.9b) and use the model for the injection electrodes to reproduce the $J_{AC}-V$ curve of the bipolar diode. The mobility used in the simulation is $\mu_n = \mu_p = 10^{-6}$ cm^2/Vs [111]. The values of the model parameters for the single carrier diodes are given in Table 5.1. The value of the parameter m for the electron ($m_n = 0.78$) and hole cases ($m_p = 0.76$) are again almost the same. The small difference can be attributed to numerical or experimental uncertainties. There is also a small difference in the values of the parameters K_1, which may be attributed to uncertainty for the effective value of the injection barriers. We have observed in the previous section that even a small variation in the energy barrier can noticeably change in K_1.

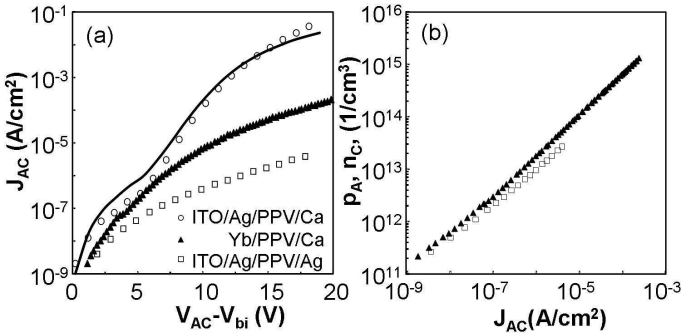

Figure 5.9: (a) Experimental current-density voltage curves at room temperature for electron-only Yb/PPV/Ca, hole-only ITO/Ag/PPV/Ag and bipolar ITO/Ag/PPV/Ca diodes with a length of 240 nm, measured at room temperature [195]. The solid line represents our numerical results for the bipolar diode. (b) Extracted values from (a) of the hole and electron densities at the anode and cathode, respectively, as a function of current density. The mobility values used in the simulation are: $\mu_n = \mu_p = 10^{-6}$ cm^2/Vs.

The carrier-density vs. current-density models extracted from the single-carrier diodes are introduced as boundary condition in the simulation of the two-carrier diode. The solid line in Figure 5.9a shows the simulated $J_{AC} - V$ characteristics, which is again in a good agreement with the experimental data (circles). This agreement confirms that the above conclusions are systematic, and not fortuitous. Thus, the charge-current models extracted from unipolar devices hold the information for the injection of charge also in bipolar devices. These models, when used as boundary conditions for the carrier density at injecting electrodes, are reliably predicting the $J_{AC} - V$ curves of bipolar-conduction diodes. Also, summation of currents of unipolar diodes grossly underestimates the current in bipolar devices. The relation between unipolar and bipolar devices is through the charge density at the charge injecting contacts, and the charge density at these interfaces are a power-law function of the total current through the device, as given in our model (5.14).

6

Boundary condition model for the simulation of organic solar cells

6.1. Introduction

Faced with the need of energy, solar light has been the most promised alternative source of energy for decades. Among the different methods to extract and convert the solar energy in electrical energy, the solar cells are in the spotlight of all researchers. However, the prices of electricity produced by photovoltaic devices are still uppermost compared to electricity produced by the conventional power industry [3]. Cheaper photovoltaic-electricity is possible by enhancing the power conversion efficiency (PCE) while keeping photovoltaic-material costs the same, or by reducing the costs with moderate efficiency photovoltaic materials. In this regard, organic-polymeric (hereafter, we use organic to mean both organic and polymeric) solar cells can play an important role in the future of photovoltaic-market as they can achieve higher power conversion efficiencies with low fabrication costs [3, 4]. Organic solar cells (OSCs) have the intrinsic advantages of the organic materials, such as the simplicity of the production processes, the low processing temperatures, printing over large and flexible substrates, low weight, and low environmental impact. Nevertheless, the current efficiency of OSC is still not economically attractive enough to use OSC in the energy industry. Thus, further research and development efforts are necessary to bring this technology up to the required level. Currently, the study and research on OSCs are focused not only in the enhancement of the efficiency but also in the need of stable and long-life devices [4, 5, 137].

This chapter is devoted to the modeling and simulation of organic solar cells. Device modeling allows for the reduction of technology development time and costs. The numerical simulations of OSCs consider the main physical-chemical mechanisms which govern OSC performance: light propagation in the materials, creation and dissociation of excitons into electrical charges, and drift-diffusion transport of the charge carriers. Several excellent works pay attention to the understanding of each mechanism and to the interactions between different mechanisms [22, 32, 43, 174, 189, 196–199]. In some cases, these studies are focused on finding analytical expressions that can be used in compact models [42, 45]. The analytical models provide a quick insight into the working performance of the solar cell and they are easy to implement in circuit simulators. The backbone of these models is the set of transport equations, which is constituted by the continuity, Poisson and drift-diffusion current equations. Drift-diffusion modeling of OSCs is a powerful tool used to describe the influence of every physical effect on the device performance and to determine the current-voltage characteristics of photovoltaic devices [6, 19]. The application of this set of differential equations (DE) to OSCs requires the use of proper values of physical parameters of the organic semiconductors. Moreover, the metal-organic (MO) interfaces in these models also require special attention. Actually, the aforementioned simulation studies differ mainly in the choice of the boundary conditions for the electron and hole concentrations at the material interfaces.

The charge carrier density at the MO interface can be controlled by several physical-chemical mechanisms (Fig. 6.1). These mechanisms can be classified in two groups: those that favor the injection of charge and those that favor the extraction[8, 63]. The main injection mechanisms are thermionic emission and tunneling. The dominance of any of them depends on the relation between the energy barrier seen from the metal Φ_B and the thermal voltage k_BT, where k_B is the Boltzmann constant and T is the temperature. Thermionic emission is dominant when $k_BT > \Phi_B$. In the opposite case, tunneling is dominant. Other mechanisms can also control the flux of charge carriers through the inter-

face, such as reduction-oxidation (redox) reactions, trap-assisted recombination, or band bending, which can be caused by effects such as Fermi-level pinning or dipoles at the interface. These different effects and mechanisms make the task of modeling the MO interfaces more complex. Different models for the extraction and injection of charge have been developed in order to find proper boundary conditions for the free charge density or the electric field at the MO interface [17, 109, 110, 200–202]. In practice, these models are not commonly used due to the numerical complexity, and approximations are preferred instead.

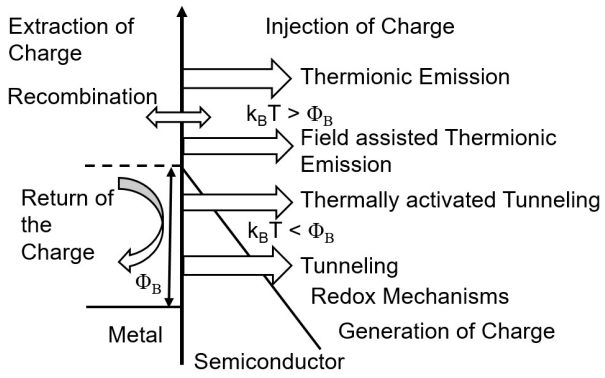

Figure 6.1: Charge extraction and injection mechanisms that take place at metal-organic interfaces.

In OSC modeling and simulation, typical boundary conditions at the material interfaces consider either constant charge density, determined by Boltzmann statistics in thermionic emission over energy barriers [54, 75], or constant surface recombination velocity, which establishes a linear relation between the variation of the interface charge density with the current density J [6, 174]: $n(,p) = -J/S + p_0(,n_0)$, where n, p are the electron and hole densities, n_0, p_0 are their respective values at equilibrium and S is the recombination velocity, commonly used to incorporate recombination losses at the interfaces. These simple approximations provide a first quick step in the modeling of OSCs. Although sometimes, they cannot provide precise information when OSCs operate far from ideal conditions.

Recently, we have proposed a more accurate and general relation between the free charge density at the MO interfaces and the current density flowing through them. This model was initially proposed in single-carrier and bipolar organic diodes in order to interpret their current-voltage characteristics (Chapter 5) [203]. We have observed that the free charge density at the injecting contact of a single-carrier diode ($n(0)$ or $p(0)$) is related to the current density following a power-law function,

$$n(0)[,p(0)] = K_1 J^m + K_2, \tag{6.1}$$

where m is a parameter that depends on the organic material, K_1 is a parameter related to the energy barrier at the injecting contact and K_2 is a parameter that models a flat region for the charge density at the interface at low values of the current density. In diffusion-dominated transport, at low bias close to the diode's built-in voltage, the charge density at the contact is almost constant with the current. The value of this charge is controlled with the parameter K_2. K_2 also provides information about the

existence of thermal carriers, the doping of the semiconductor or traps close to the interface (Chapter 5) [143, 181]. The power-law expression incorporates the above mentioned Boltzmann and linear $J - n(, p)$ approximations, with $m = 0$ and $m = 1$, respectively. It also takes into account intermediate situations that can describe a limited recombination velocity at the contacts or the contribution from space charge limited conduction (SCLC) in the organic semiconductor bulk. Experimental observations in OSCs [204, 205] also agree with our power law expression (6.1), initially proposed in organic diodes. In particular, a power-law relation between the charge stored in the active layer of an OSC with the current density in darkness, and with the current losses at open circuit ($J \propto n^{2.6}$) is found in these authors' work.

Our aforementioned analyses of experimental data established that the power-law model for the interface charge as a function of the current density is very consistent with experimental data for $J - V$ curves of organic diodes, including OSCs in dark. However, as we will see in this chapter, the extraction procedures developed in these analyses also indicated that direct use of power-law model is not accurate, when OSC is under illumination. In particular, it will be shown that K_2 is different and higher under illumination. In this chapter, we study the effect of the illumination on the power-law model (6.1) for the charge-current dependence at metal-organic interfaces od OSCs. We also assess the impact of this interface effects on the $J - V$ curves of the OSCs. The objective is to find a proper model for the values of the free charge carrier densities at the anode and cathode of OSCs that can be used in simulators of these devices. Bearing this in mind, Section 6.2 describes the optical and electrical models used for the simulation of OSCs [23, 43]. In Section 6.3, we adapt the boundary conditions at the metal-organic interfaces, initially proposed for organic diodes, to OSCs. In Section 6.4, numerical $J - V$ curves are simulated and comparisons with experimental data are developed. A procedure to extract the values of our model parameters from these comparisons is also proposed. In darkness, $J - V$ curves are analyzed both in forward and reverse regimes, corresponding to the injection from both contacts. In these situations, our previously developed model for single carrier diodes is completely valid. Under illumination, the power-law function used in darkness is modified considering previous experimental observations [204, 205] and suggestions for boundary conditions in simulation [206]. A definite proposal is given, in which the charge density at the interface increases when the intensity of the incident light increases, following again the power-law function. The main conclusions are provided in Chapter 9.

6.2. Theory

A typical organic solar cell is a multilayer structure with a metallic cathode with a low work function, an anode with a high work function, an organic active layer where the light is absorbed, and a substrate that supports the entire structure. The active layer is composed of an acceptor layer, usually a fullerene that transports photo-generated electrons, and of a donor layer, usually a polymer that transports photo-generated holes. These two layers can be separated by a well-defined interface, giving rise to the so called bilayer OSC, or can be blended together in the case of the bulk-heterojunction (BHJ) solar cell. The later case achieves greater efficiencies than the former one. For this reason, this structure is analyzed in this chapter.

For simulation purposes, the active layer is considered as a uniform material, which can be modeled with an effective band gap E_G defined as the energy difference between the lowest unoccupied molecular orbital (LUMO) of the acceptor material and the highest occupied molecular orbital (HOMO) of the donor layer. This assumption is commonly denoted as effective medium approach (EMA). A schematic energy-level diagram of a BHJ solar cell is shown in Fig. 6.2(a). The different value of the work functions of the contacts creates an internal built-in voltage V_{bi} which facilitates the transport of the photogenerated charge carriers. The asymmetry of the structure creates an asymmetry in the current-voltage curves in forward and backward operation under dark condition. The energy injector barriers that electrons and holes see from the contacts towards the organic semiconductor are higher in backward operation than in forward operation.

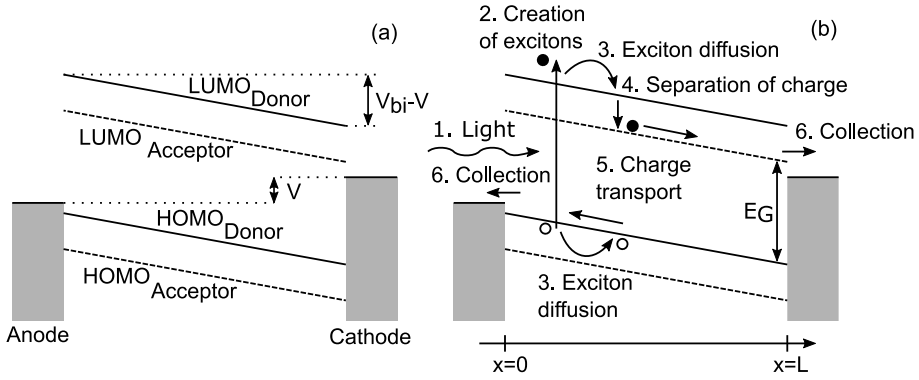

Figure 6.2: (a) Schematic energy diagram of a BHJ solar cell. (b) Mechanisms that take place in an organic BHJ for the transformation of the sunlight.

Under illumination, the current-voltage characteristic of an OSC is the result of different optical and electrical mechanisms (a scheme is seen in Fig. 6.2(b). These mechanisms can be grouped in:

i) *Optical Mechanisms*, which include (1a) optical propagation, described with the electric field component of the electromagnetic wave of the light [22]; and (1b) photon absorption. In order to estimate the photocurrent in an OSC, the absorbed light power density must be determined in the first place.

ii) *Opto-Electrical conversion*, which creates free electron-hole pairs from the photons absorbed in the semiconductor. This requires several steps: (2) exciton (or bound electron-hole pair) formation, (3) exciton migration and (4) exciton dissociation. The excitons are dissociated at the acceptor-donor interfaces, impurities, defects or under the presence of high electric fields create free electron-hole pairs. Thus, the free electron-hole pair generation rate is a function of the exciton generation rate.

iii) *Electrical transport*, which finally produces the current in the OSC. This electrical current is controlled by drift-diffusion mechanisms (5) and recombination processes in the semiconductor and by the features of the metal-organic extracting contacts (6).

In the literature, we can find different simulation models that describe the previous mechanisms. In

the following sections, a more detailed description of these mechanisms with state-of-the-art optical and electrical models are found. The sections are ordered following the above classification and the scheme of Fig. 6.2(b).

6.2.1. Optical models

The photocurrent density in an OSC is controlled by the charge carriers generated in the active layer of the device. Concurrently, the generated electron-hole pairs depend on the number of generated excitons, which varies with the value of the optical electric field energy. When the thickness of the OSC layers is below a critical value, optical interference can appear in the system. Under these conditions, the distribution of the optical electric field energy, and the distribution of excitons along this stratified system can be determined with the well-known Transfer Matrix Method (TMM) [22, 197, 207, 208].

Since the electric and the magnetic fields are connected by the Maxwell equations, it is sufficient to determine only the electric field component $F(x)$. It is decomposed into two electromagnetic waves, one propagating in the positive direction (incident) $F^+(x)$ and another one in the opposite direction (reflected) $F^-(x)$ (with $F(x) = F^+(x) + F^-(x)$). The positive direction of the x axis is taken from the illuminated surface towards the bulk of the OSC.

In this method, structures with isotropic and homogeneous media and parallel-plane interfaces can be described by 2×2 matrices. They describe how the vector $(F^+(x), F^-(x))$ is transformed due to Fresnel reflections and transmissions at the interfaces, and phase changes and magnitude decays during the propagation within the different layers. This formalism is justified due to the fact that the equations governing the propagation of the electric field are linear and that the tangential component of the electric field is continuous [209],[210].

The physical transformations that undergoes the electric field are described in the method with two types of transfer matrices: the interface matrices I and the layer matrices L. The former ones describe each interface in the structure and contain information of the Fresnel complex reflection and transmission coefficients at each interface. The latter ones describe the phase changes the wave experiences as it traverses each layer.

Each layer j has a thickness d_j and its optical properties are described by its wavelength-dependent refractive index $n_j = \eta_j + i\kappa_j$; where the real part of the refractive index, η, describes the phase velocity of light within the medium and κ is the extinction coefficient accounting for the attenuation of the optical electric field due to photoexcitation.

An incident optical electric field from the air $F_0^+(\lambda)$ is thus transformed by a sequence of reflections and transmissions at the interfaces and propagation in the different layers. After all these transformations, the electric field at any point of the structure can be expressed as $F(x, \lambda) = F_0^+(\lambda) f(x, \lambda)$ where $f(x, \lambda)$ is the transfer function, which contains information of the coefficients of the different interface and layer matrices of the structure, and λ is the wavelength of the incident light.

The value of $F_0^+(\lambda)$ depends on the light source. For solar energy applications, solar cells are tested and compared following the standard AM 1.5G spectrum of the sun light. Its irradiance $B(\lambda)$ is represented in Fig. 6.3. For numerical purposes, this spectrum can be treated as a set of tabulated values or

approximated by the terrestrial black-body radiation spectrum with irradiance

$$B_{BB} = \frac{2\pi hc^2}{\lambda^5} \frac{1}{\exp[hc/(\lambda k_B T)] - 1}, \tag{6.2}$$

evaluated at a temperature of $T = 5630K$, and normalized to provide a maximum power density $B_{max} = 1.5$ W/m^2/nm at $\lambda = 515$ nm (Fig. 6.3):

$$B(\lambda) \approx \frac{B_{BB}(\lambda)}{B_{BB}(\lambda = 515nm)} \times 1.5 \text{ W/m}^2\text{/nm} \tag{6.3}$$

where h is the Plank constant, k_B is Boltzmann constant, c is constant light speed in free space and T is the temperature.

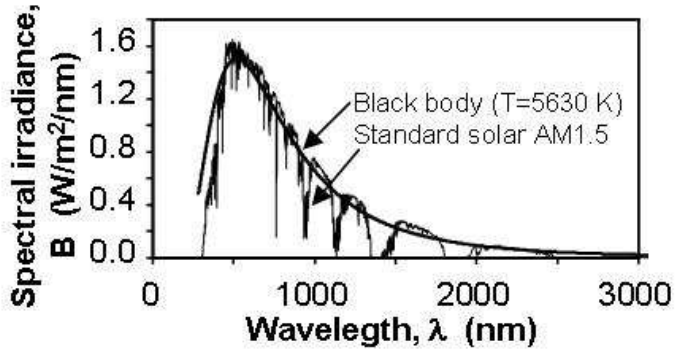

Figure 6.3: Standard Solar Spectra AM1.5 and the normalized terrestrial black-body radiation spectrum at $T = 5630K$

Using the Poynting vector formulation, the squared magnitude of the optical electric field in the air is related to the irradiance as:

$$|F_0^+(\lambda)|^2 = \frac{2B(\lambda)}{c\varepsilon_0} \tag{6.4}$$

Once the value of the electric field $F(x, \lambda)$ at normal incidence is known, the time average of the energy dissipated per second at the same point can be determined. We have to bear in mind that the number of excited states (excitons) at a given position in a structure is directly dependent on the energy absorbed by the material. Based on the concept of the Poynting vector, the time-averaged energy-flow dissipation per time unit at the same point is

$$Q(x, \lambda) = 2\pi \frac{c\varepsilon_0}{\lambda} \eta_j k_j |F(x, \lambda)|^2 \tag{6.5}$$

This means that the energy absorbed at position x in the layered structure is proportional to the product of the modulus squared of the electric field, the refractive index η_j, and the absorption coefficient $\alpha_j \equiv 4\pi\kappa_j/\lambda$.

Assuming that one photon produces one exciton, the integration of the absorbed optical power

density Q over the photon energies produces an exciton density, or exciton generation rate:

$$G_{exciton} = \int_0^{\lambda_{max}} \frac{Q(x,\lambda)}{hc/\lambda} d\lambda \tag{6.6}$$

The exciton energy must be large enough to bring a localized electron from the HOMO to the LUMO of the organic material. Note that the energy of the exciton is equal to the energy of the absorbed photon hc/λ. Then, the photon energy $h\nu > h\nu_{min} \approx |LUMO - HOMO|$, (reciprocally $\lambda < \lambda_{max} \approx hc/|LUMO - HOMO|$) is larger than the energy difference between LUMO and HOMO at the dissociation place. Thus, the exciton can be seen as a non-electromagnetic carrier with energy hc/λ in the organic material. The transfer of the electromagnetic photon energy into the non-electromagnetic exciton energy comprises the first step of the photo-electrical conversion.

6.2.2. Opto-Electrical Models

The exciton is considered a quasiparticle that is generated when an electron of the HOMO level catches the energy from a photon. An exciton can also be seen as an electron with an increment of its kinetic and potential energies. Figure 6.4 shows a scheme and a graphical representation of the mechanisms and the principles on which the excitons are built up and dissociated in the blend of a BHJ solar cell. In a donor-acceptor blend, the photon is absorbed mainly in the donor semiconductor (polymer). Once photons are absorbed in the donor layer, excitons are created with a rate $G_{exciton}$. Excitons diffuse through the donor material until they reach a donor-acceptor interface. Along the diffusion path, excitons can decay to the ground state with a decay rate k_f, and their energy can be released as photons or phonons. At the donor-acceptor interface, the electron can be transferred to the acceptor, thus forming a bound electron-hole pair or a polaron. This pair can either dissociate into free carriers with a rate k_{diss} or decay again to the ground state with a recombination rate k_f. At the interface, the free carriers can recombine back into polarons with recombination rate R'. Thus, the final separation into free carriers is a competition between dissociation (rate constant k_{diss}) and recombination rate R'. The recombination rate R' is assumed to be the bimolecular recombination rate [182, 211, 212]:

$$R' = k(np - n_i^2) \tag{6.7}$$

where n and p are the electron and hole densities, respectively, and k is the bulk rate constant. Langevin calculated the bulk rate constant by assuming that recombination between an electron and a hole occurs when their separation is zero: $k = \frac{q}{\varepsilon_0 \varepsilon_r}(\mu_n + \mu_p)$, where μ_n and μ_p are the electron and hole mobilities, respectively, and ε_0 and ε_r are the vacuum and relative permittivity of the material, respectively [182]. In an effort to reproduce experimental recombination rate constants in OSCs, not predicted by Langevin theory, Hilczer and Tachiya proposed an extension of Langevin theory [211]. They considered the case in which an electron and a hole recombine at a nonzero separation with a finite intrinsic recombination rate and in the presence of an external electric field (see Eqs. (14)-(16) in [211]). In the Onsager-Braun theory [30, 31], the probability of electron-hole pair dissociation P is given

by

$$P = \frac{k_{diss}}{k_{diss} + k_f} \tag{6.8}$$

where k_{diss} is the polaron pair dissociation rate. The aforementioned forward and backward transformations into bound electron-hole pairs can be grouped in a continuity equation. This equation describes the evolution of the exciton density n_{exc} with time:

$$\frac{dn_{exc}}{dt} = G_{exciton} - k_f n_{exc} - k_{diss} n_{exc} + R' \tag{6.9}$$

The existence of the exciton as an intermediate state between the free charges and the ground state means that after bimolecular recombination, the carriers are not necessarily lost. This intermediate bound electron-hole pair can either dissociate again into free carriers or decay to the ground state, in which case the carriers are finally lost. In steady state, (6.9) is written as [43]

$$G_{exciton} - k_f n_{exc} = k_{diss} n_{exc} - R' \tag{6.10}$$

The second term of (6.10) is the net number of generated free carriers $U = G - R$, where G and R are the respective generation and recombination rates of free carriers. Combining (6.8) and (6.10) results in $k_{diss} n_{exc} = P G_{exciton} + P R'$. Thus, the net number of generated free carriers can be written as

$$U = G - R = P G_{exciton} - R'(1 - P) \tag{6.11}$$

This theory identifies the generation term as $G = P G_{exciton}$ and the recombination term as $R = R'(1 - P)$, where P describes the probability of the dissociation of a charge transfer (CT) state. Hilczer and Tachiya extended Onsager model of geminate recombination and calculated the dissociation probability $P = 1 - \kappa$ [211], where κ is the recombination probability, which is given by Eqs. (5)-(7) in [211]. In this calculation, they again considered that an electron and a hole can approach each other by Brownian motion only up to a distance d which is not zero, and recombination occurs there by back electron transfer with a finite rate constant.

A further study on the theory of charge pair generation can be seen in a recent review developed by Few et al. [213]. They focus on electronic structure calculations, electrostatic models and approaches to excited state dynamics. From studies on electrostatics, they point out how changes in the dielectric constant, the static internal electric fields, and the structural disorder, all can influence the energetic landscape close to the heterojunction, which in the end affects the dissociation efficiency. The detailed information on the structure and the dynamic, the timescales of the main processes, are also relevant for the charge transfer processes.

6.2.3. Electrical models

Once the free electrons and holes are created in the active layer of the OSC they must be transported towards their respective extracting contacts. The electrical behavior of OSCs is governed by the drift-

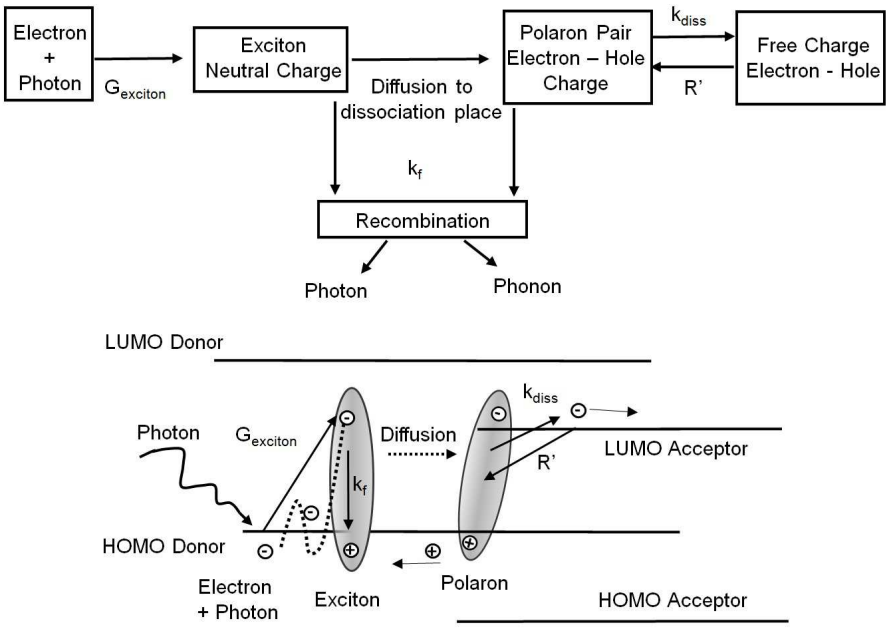

Figure 6.4: (a) Scheme and (b) graphical representation of the mechanisms and the principles that follow the absorption of photons in the blend of the BHJ solar cell.

diffusion model, Poisson equation and the continuity equations for electrons and holes. The Poisson equation is:

$$\frac{\partial F}{\partial x} = \frac{q}{\varepsilon_0 \varepsilon_r} (p - n + N_D - N_A) \tag{6.12}$$

where q is the electron charge, F is the electric field, ε_0 and ε_r are the vacuum and relative permittivity of the material, respectively, N_D and N_A are the concentrations of ionized donor and acceptor impurities, respectively, and n and p are the free charge densities of electrons and holes, respectively.

The continuity equations for electrons and holes are:

$$\frac{\partial n}{\partial t} = +\frac{dJ_n}{qdx} + G - R \tag{6.13}$$

$$\frac{\partial p}{\partial t} = -\frac{dJ_p}{qdx} + G - R \tag{6.14}$$

In this chapter, the organic solar cell is analyzed in the quasi-static limit, neglecting transient behaviors. In this case, the derivative of the hole and electron concentrations are zero ($\partial n/\partial t = 0$, $\partial p/\partial t = 0$) in (6.13)-(6.14).

The electron and hole current densities, J_n and J_p, respectively, are controlled by drift and diffusion:

$$J_n = qn\mu_n F + qD_n \frac{\partial n}{\partial x} \tag{6.15}$$

$$J_p = qp\mu_p F - qD_p \frac{\partial p}{\partial x} \tag{6.16}$$

where D_n and D_p are the diffusion coefficients for electrons and holes. The diffusion coefficients are assumed to follow the Einstein relation $D_{n,p}/\mu_{n,p} = V_T$ where μ_n and μ_p are the electron and hole mobilities, respectively. In highly disordered systems or semiconductors with large values of the charge carrier density and traps, this relation can be altered [214][215]. Several authors propose this relation to be $D_{n,p}/\mu_{n,p} = nV_T$, where n is an ideality factor which is induced from trap assisted recombination processes [174, 214]. Other authors use a carrier-density dependent diffusion-coefficient in the Einstein relation for the transport in Gaussian or Exponential Density of State (DOS) systems [76][216].

The set of transport equations is completed with the relation between the electrostatic potential V and the electric field:

$$\frac{\partial V}{\partial x} = -F \tag{6.17}$$

From (6.17), the difference of the electrostatic potential between anode and cathode is

$$V(0) - V(L) = \int_0^L F dx = V - V_{bi} \tag{6.18}$$

where $V = V_{anode} - V_{cathode}$ is the external applied voltage between anode and cathode, L is the device length, $V_{bi} = (\phi_A - \phi_C)/q$ is the built-in voltage and ϕ_A and ϕ_C are the work-functions of the metallic contacts of the anode and cathode, respectively.

The total current density in OSCs is given by:

$$J = J_n + J_p + J_d = J_n(x,t) + J_p(x,t) + \varepsilon_0\varepsilon_r \frac{\partial E(x,t)}{\partial t} \tag{6.19}$$

where the displacement current density $J_d = \varepsilon_0\varepsilon_r \partial E(x,t)/\partial t$ is equal to zero under the quasi-static assumption. Furthermore, since the total current density is uniform in the device, then (for the same quasi-static case)

$$\frac{\partial J}{\partial x} = \frac{\partial J_n}{\partial x} + \frac{\partial J_p}{\partial x} = 0 \tag{6.20}$$

The system of equations (6.12)-(6.17) has been used extensively in the literature to model the transport in OSCs. However, there are particular aspects that differ among different researchers, such as the models used for the charge-carrier generation and recombination, the mobility or the boundary values for the charge carrier concentration, the last one being the objective of this chapter.

Regarding the generation rate G, which accounts for the optical illumination, this rate is ussualy assumed constant for simplicity [217, 218]. In our case, the generation and the recombination rates of free charge pairs follow Onsager-Braun theory: $G = PG_{exciton}$ and $R = (1-P)R'$, respectively, where $G_{exciton}$ is the generation rate of bound electron-hole pairs defined in (6.6) in agreement with the TMM and R' is the bimolecular recombination rate (6.7). In darkness, excitons do not intervene in the generation-recombination processes in the semiconductor, only non-geminate recombination appears in the semiconductor. In this case, $G = 0$ and $R = R'$.

The mobility can depend on variables such as the temperature, the electric field, the charge-carrier

concentrations, or the density of states of the organic materials [95, 219, 220]. Nevertheless, there exist large ranges of these variables in which the mobility can be assumed constant [7, 221, 222]. This assumption simplifies complex numerical treatments as the ones found in OPV systems. In fact, the mobility in OPV devices does not seem to vary much with bias, at low electric fields and low injection of charge [223]. For these reasons, the mobility is assumed constant in this chapter. The third aspect that also affects the solution of the transport equations (6.12)-(6.17) is the election of proper boundary conditions, which is treated in the next section.

6.3. Boundary-condition model. Adaptation from organic diodes.

The boundary conditions at the OSC contacts represent known values for some physical quantities at the edge of a spatial mesh, in which the integration of the differential equations is performed. At the contacts, the boundary conditions reflect the physics of charge injection and extraction and must match the biasing voltages. The boundary conditions must be chosen to guarantee a self-consistent solution of the numerical model. The basic one-dimension (1-D) semiconductor equations are solved considering the origin $x = 0$ at the anode-semiconductor interface and the end of the device $x = L$ at the cathode-semiconductor interface. We need as many boundary conditions as the number of differential equations and physical variables. There are six differential equations (6.12)-(6.17) and the same number of physical unknown parameters (V, F, n, p, J_n and J_p). Two of the boundary values correspond to the potential at the contacts (anode- and cathode-organic interfaces). The origin of the potential is set at the anode, and its value at the cathode comes from (6.18):

$$V(x = 0) = 0 \text{ V}, V(x = L) = -V + V_{bi} \tag{6.21}$$

The other four boundary conditions are related to the values of the free charge carrier densities at the anode and cathode of the OSC. As mentioned in the introduction, simple approximations are commonly used in the literature: constant values of the free carrier density, based on the Boltzmann approximation; or constant values of the surface recombination velocity, which account for recombination mechanisms at the interfaces, and determine the interface charge density as a linear function of the current density J [6, 174]. More accurate models that relate the electric field at the metal-organic interface with the current density can also be found, although their major inconvenience is the computational requirement [200, 224].

A compromise between simplicity and accuracy can be found in previous studies we made in darkness for the conduction in single-carrier and bipolar organic diodes [203]. We observed that the free charge density at the injecting contact of single-carrier and bipolar diodes is related to the current density following the power-law function (6.1). Fig. 6.5(a) captures the main conclusions of our previous studies on bipolar organic diodes and its application to OSCs in darkness [203]. It shows the evolution of the free charge density (electrons and holes) at the anode and cathode of an OSC as a function of the current density. This scheme points out the following features:

- At forward bias, or positive current densities ($J \equiv J_f$), the anode injects holes and the cathode injects electrons, the values of the hole density $p_A = p(0)$ at the anode and electron desity $n_C = n(L)$ at the cathode follow (6.1). The subscripts n, p, A, C indicate that the parameter belong to electron, hole, anode and cathode, respectively. We consider that p_A and n_C are the same for two reasons, both following $p_A = n_C = K_{2pA} + K_{1pA}J^m$. The first one comes from experimental observations, in which the extracted electron and holes densities at the injecting electrodes of bipolar organic diodes were very similar [203]. The second reason comes from the meaning of the parameters in (6.1) [143, 181], m depends on the organic material, being the same for the OSC; K_1 is related to the energy barrier the charge carriers see when injected towards the organic material. For a proper performance of an OSC, ohmic and similar energy barriers for electrons and holes are expected at the cathode and anode, respectively. Thus, K_1 is also expected to be the same for both, $K_1 = K_{1pA} = K_{1nC}$. The evolution of $p_A = n_C$ is thus the following. At low current densities, the carrier densities at the injecting contacts are constant ($p_A = n_C = K_{2pA}$). Once a threshold value of the current density J_{Kf} is surpassed, the charge density evolves with the current density as $K_{1pA}J^m$.

- At forward bias, the values of the charge densities at the extracting contacts ($p_C = p(L)$ and $n_A = n(0)$) are very small with no effect on the simulation results ($p_C = n_A = K_{2pC}$). However, a relation between p_C and p_A can be established at low current densities by imposing the condition $J = 0$ at zero applied voltage $V = 0$ V. In analytical $J - V$ relations for organic diodes (see (A.4) in [203]): $p_C \approx p_A \times exp(-V_{bi}/V_T)$, which at low current densities means $K_{2pC} \approx K_{2pA} \times exp(-V_{bi}/V_T)$, where K_{2pA} and K_{2pC} are the flat values of p_A and p_C, (see (6.1) and Fig. 6.5(a)).

- At reverse bias, or negative current densities ($J \equiv -J_r$), the roles of the anode and cathode are changed, the anode injects electrons and the cathode injects holes, the values of the hole density $p_C = p(L)$ at the cathode and the electron desity $n_A = n(0)$ at the anode follow (6.1). For the same reasons as in forward bias, n_A and p_C are considered the same ($p_C = n_A = K_{2pC} + K_{1pC}J_r^m$). The only difference is that holes and electrons see a higher energy barrier at their injecting contacts. The effect of these different energy barriers in forward or in backward is reflected in different values of the parameter K_1, being greater for forward bias ($K_{1pA} > K_{1pC}$). The value of m in (6.1) is the same for positive and negative current densities as it only depends on the properties of the organic material [143, 181, 203].

- At reverse bias, the values of the carrier densities at the extracting contacts, $p_A = p(0)$ and $n_C = n(L)$, are constant values and, for consistency, equal to their value in the flat region of these same variables at $J = 0$.

- The evolution of the charge densities in Fig. 6.5(a) shows sharp transitions at the threshold values J_{Kf} and J_{Kr}. However, if we represent (6.1) a smoother transition is obtained. In order to control this transition, which can affect the determination of current-voltage characteristics of OSC, the

paramenter *sharp* is introduced in the power law model (6.1):

$$p_A = n_C = K_{2pA}\left\{1 + \left[max\left(0, \frac{J}{J_{Kf}}\right)^m\right]^{sharp}\right\}^{\frac{1}{sharp}} \tag{6.22}$$

where $sharp = 1$ for a smooth transition ((6.22) coincides with (6.1)) and $sharp \approx 10$ for sharper transitions. In any case, the power-law function is obtained at current densities larger than the threshold current density J_{Kf}:

$$J \gg J_{Kf},\ p_A = n_C \simeq K_{2pA}\left(\frac{J}{J_{Kf}}\right)^m \tag{6.23}$$

with $J_{Kf} = (K_{2pA}/K_{1pA})^{(1/m)}$. The flat region is also reproduced with (6.22) at current densities lower than the threshold voltage J_{Kf}:

$$J \ll J_{Kf},\ p_A = n_C \simeq K_{2pA} \tag{6.24}$$

An identical relation to (6.22) can be written for the evolution of $p_C = n_A$ with J, using subscripts pC instead of pA, J_{Kr} instead of J_{Kf} and $J_r = -J$:

$$p_C = n_A = K_{2pC}\left\{1 + \left[max\left(0, \frac{J_r}{J_{Kr}}\right)^m\right]^{sharp}\right\}^{\frac{1}{sharp}} \tag{6.25}$$

The model for the boundary values of the free charge density at the anode and cathode of OSCs ((6.22) and (6.25) or Fig. 6.5(a)) reflects the main conclusions extracted from our previous works in darkness [143, 181, 203]. In order to complete or adapt this model for illumination, ideas from other researchers are incorporated. In studies of the compensation voltage in light emitting diodes and photovoltaic cells, Malliaras et al. proposed that the free charge densities at the anode and cathode interfaces increase with the illumination [206]. The compensation voltage is the voltage at which the net photocurrent (the photocurrent minus the dark current) is zero. Other authors determined experimentally in different solar cells a relation between the charge carrier density and the open-circuit voltage V_{oc} [204, 205, 225, 226]. Shuttle et al. measured the stored charge in the active layer in darkness and at open circuit voltage for different illumination intensities [204]. They showed that the charge density increases with V_{oc}, and consequently with the illumination intensity. They evaluated the current density in darkness and the current losses at V_{oc} as a function of the charge density obtaining the same evolution in both cases: $J \propto n^{2.6}$. This points out that the physical process governing both processes in dark and illumination may be the same. Also, this relation is very similar to our power-law function between the current density and the charge density at the interfaces.

These authors' conclusions under illumination are related to the open circuit voltage region, or current density close to zero. In this regard, we propose to increase the value of the charge density at the contacts just in the low current region (close but below the open-circuit voltage). For applied

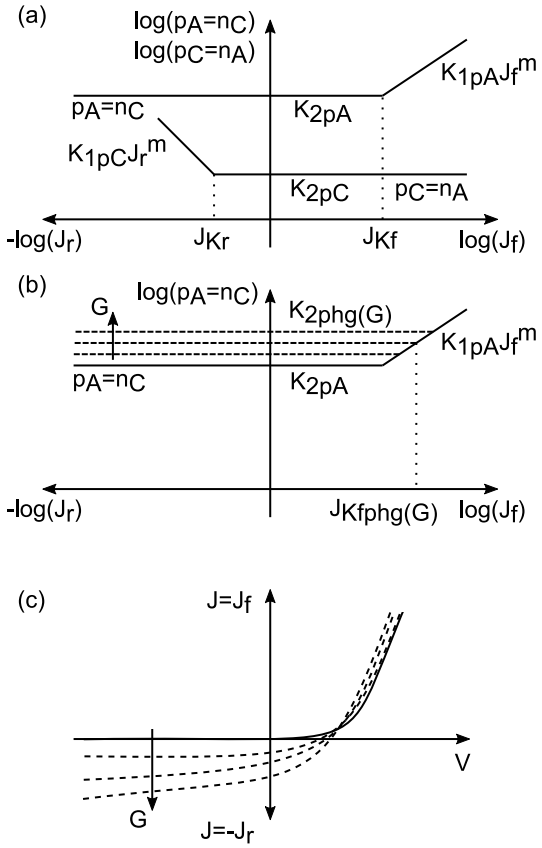

Figure 6.5: (a) Model for the boundary values of the free charge densities at anode and cathode in an OSC in darkness following the power-law function (6.22) and (6.25). (b) Adaptation of the model for the device working under illumination. (c) Typical $J-V$ curves in dark (solid line) and illumination (dashed lines).

voltages greater than V_{oc} the current density is controlled by drift mechanisms. In this region, diffusion and illumination play a minor role. Thus, the relation $p_A - J$ is expected to follow our power law function found at high current densities (6.23). With these ideas, the values of the charge density at the contacts under illumination can be redefined as:

$$p_A = n_C = K_{2phg}(G)\left\{1 + \left[max\left(0, \frac{J}{J_{Kphg}}\right)^m\right]^{sharp}\right\}^{\frac{1}{sharp}} \tag{6.26}$$

where $K_{2phg}(G) = K_{2pA} + \Delta K_{2phg}$, ΔK_{2phg} is the density of photogenerated electrons and holes, with quite similar values, and $J_{Kphg}(G) = (K_{2phg}(G)/K_{1pA})^{(1/m)}$. The modification of our model under illumination is depicted in the scheme of Fig. 6.5(b). In this figure, only the evolution of $p_A = n_C$ with the intensity of light is shown.

The representation of $p_C = n_A$ is not depicted in Fig. 6.5(b) for the sake of clarity. The values of the photogenerated carriers inside the active layer are distributed along the active layer according to the TMM results. The values of the charge density at the extracting electrodes may be a little greater

than their values at the opposite electrodes ($p_C \preceq p_A$ and $n_A \preceq n_C$). In this regard, we can assume $p_C = n_A = K'_{2phg}(G) \leq K_{2phg}(G)$, where $K'_{2phg}(G)$ is constant for each value of G.

The only question is how the photogenerated charge at the contact increases with the intensity illumination, and how the values of $K_{2phg}(G)$, $J_{Kphg}(G)$ and $K'_{2phg}(G)$ evolve accordingly. For the sake of a better comprehension of our work, we prefer to leave these as open questions till the validity of our model in darkness is checked. All this is done in the next section. In the first place, $J-V$ curves in darkness are calculated and compared with experimental data. In the second place, a procedure to extract the parameters that define our model in dark is also proposed. Then, the model under illumination is completed in order to find the evolution of $K_{2phg}(G)$, $J_{Kphg}(G)$ and $K'_{2phg}(G)$ with the light intensity. Finally, the complete model is validated under illumination conditions.

6.4. Boundary condition model. Final proposal and verification.

6.4.1. Darkness

In order to validate the model in darkness [(6.22), (6.25) and Fig. 6.5(a)] for the boundary values of the charge density at the MO interfaces of OSCs, current-voltage curves are calculated with the set of differential equations (6.12)-(6.17). In order to reproduce an experimental current-voltage curve in dark, the values of the parameters μ_n, μ_p, V_{bi}, n, K_{1p_A}, K_{1p_C}, m, and K_{2pA}, must be introduced in these equations. Most of them are extracted from the experimental $J-V$ curves to be compared with.

In our calculation, we assume that the carrier mobility in the organic materials is well described by constant values provided in the literature. The nominal value of the built-in potential V_{bi} is given by the difference of the work functions of the electrodes. However, this value can be modified by different mechanisms such as Fermi-level pinning, spontaneous orientation polarization or band-bending phenomena. There are light-irradiation techniques to estimate this value [187, 227, 228]. At a starting point, we follow the method given by Mantri et al. [187], in which the value of V_{bi} is extracted from the transition voltage at which the slope of the $J-V$ curve changes (point K in Fig. 6.6). The ideality factor of the Einstein relation n is considered initially as $n = 1$. The values of V_{bi} and n can be modified slightly during the extraction of the rest of the parameters.

The extraction procedure depends on the existence or not of parasitic losses in the OSC, the second case being the most frequent. A typical $J-V$ curve of an OSC without parasitic losses in dark is shown in dashed line in Fig. 6.6(a). The curve can be divided in three regions (I)-(III) in which the above parameters can be extracted with the following steps. In each step, one parameter is varied until a good agreement is obtained between our calculations and the experimental data.

Step i Regions I and II in the forward bias show different slopes and are separated at the point K (V_{bi}, J_{Kf}). This corner region provides a first estimation of the values of V_{bi} and J_{Kf}. The parameter K_{2pA} can be extracted by iteration comparing the experimental data in region I with our numerical results imposing $p_A = n_C = K_{2pA}$ and $p_C = n_A = K_{2pC}$, where $K_{2pC} \approx K_{2pA} \times exp(-V_{bi}/V_T)$ as

mentioned in Sec. 6.2.3.

Step ii In this step, the parameters V_{bi} and n (initially $n = 1$) can be modified slightly to improve the fitting. After that, the experimental and calculated curves should agree in region I. In region II, the calculated curve differs from the experimental one. This difference is greater for larger values of J. A more precise value for J_{Kf} can be defined at the point in which the experimental and calculated curves differ 5 % in value.

Step iii The parameters K_{1pA} and m can be extracted from region II, as they control the high current regime in forward bias. In this region, we use as boundary values $p_A = n_C = K_{2pA} + K_{1pA}J^m$ with $K_{1pA} = K_{2pA}/J_{Kf}^m$ and $p_C = n_A = K_{2pC}$. After this step, the calculated curve should agree with the experimental one in regions I and II.

Step iv The analysis of region III provides the value of the last parameter to be extracted: K_{1pC}. The rest of the parameters were extracted in the previous steps. Note that parameter m depends only on the organic material and thus, the value extracted from the forward bias is employed. In the comparison between the experimental and calculated curves in region III, $p_A = n_C = K_{2pA}$ and $p_C = n_A = K_{2pC} + K_{1pC}J^m$ are used.

The existence of a parasitic current such as the one depicted with dotted line in Fig. 6.6(a) (characterized with a typical shunt resistance and symmetric $J-V$ behavior) can mask the low-current regime of the intrinsic diode. This fact adds a new parameter to take into account in the extraction procedure, the shunt resistance R_s. However, a new region also appears in the characteristic $J-V$ curve, as shown in Fig. 6.6(b) (region IV). This figure corresponds to a typical $J-V$ curve of an OSC in dark with parasitic losses.

The sequence of steps needed to extract the set of parameters of our boundary-value model for an OSC in dark with parasitic losses is detailed next. The former case without losses is not frequent as losses are difficult to avoid. However, it is useful to better understand the following extraction procedure.

Steps i'-iii' These steps coincide with the respective *steps i-iii* above. The only difference is that the region I is smaller, due to the parasitic losses. Regions I and IV are separated by the inflection point L in Fig. 6.6(b).

Step iv' In this step, region IV is analyzed. The loss current component is calculated and compared to the experimental curve in the region IV, providing an initial value for R_s. Then, the loss current is added to the current of the intrinsic OSC and compared to the complete $J-V$ curve in forward bias (regions I, II and IV). Some iterations may be needed to redefine the initial value of R_s and obtain a good fitting.

Step v' In this step, the reverse bias region (region III) is analyzed, similarly to *Step iv*. In the comparison between the experimental and calculated curves, we use $p_A = n_C = K_{2pA}$ and $p_C = n_A = K_{2pC} + K_{1pC}J^m$, where the only unknown parameter to be modified in the fitting process is K_{1pC}. The rest of the parameters were extracted in the previous steps, including R_s. The total current

density in reverse bias (intrinsic plus loss current) is compared to the experimental curve in this region III. The effect of the intrinsic current density must be observed at high currents.

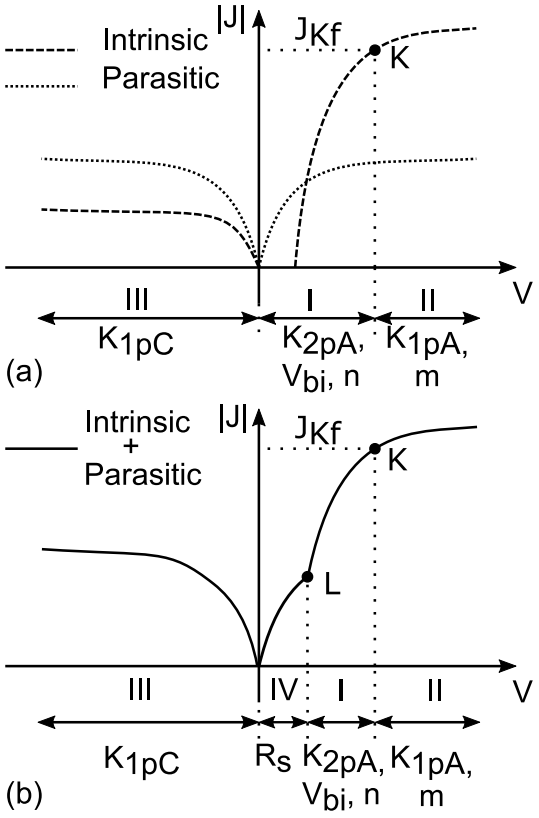

Figure 6.6: (a) Typical current-voltage curve for a OCS in dark (dashed line) with regions I-III in which the parameters of our boundary model (Fig. 6.5(a)) can be extracted in sequence; and typical parasitic current modeled with a shunt resistance (dotted line). (b) Typical current-voltage curve for a OCS in dark including the parasitic current. In this case, four regions are distinguished, indicating the parameters of the model to be determined in each one.

As a way of validation of our procedure, we analyze experimental $J-V$ curves of a bulk heterojunction (BHJ) solar cell based on the blend of poly(3-hexylethiophene) (P3HT) and phenyl [6,6] C_{61} butyric acid methyl ester (PCBM) [42] and depicted with circles in Fig. 6.7. The blend is sandwiched between two ohmic contacts, indium tin oxide ITO for holes, and aluminium, Al, for electrons. The complete configuration is ITO/poly(ethylene dioxythiophene):poly styrene sulphonate (PEDOT:PSS)/P3HT:PCBM/Al. Figure 6.7 shows the comparison of these experimental data with our numerical results (solid line). The $J-V$ characteristic shows clearly the four regions depicted in Fig. 6.6(b), including the loss-current region IV. The values of the free charge-carrier density at the metal-organic interface used in the numerical calculation are represented in Fig. 6.8. The exponent of the power-law lines in this logarithmic representation is $m = 0.35$. The rest of the parameters used in the calculation are: $R_s = 1.5$ KΩ, T=295 K, V_{bi} =0.55 V, $\mu_n = \mu_p$ =10^{-4} cm^2/Vs, $n = 1.85$, $\varepsilon_r = 3$ and $L = 150$ nm. A very good agreement is

achieved between the experimental and the calculated curves in dark using our model detailed in Fig. 6.5(a).

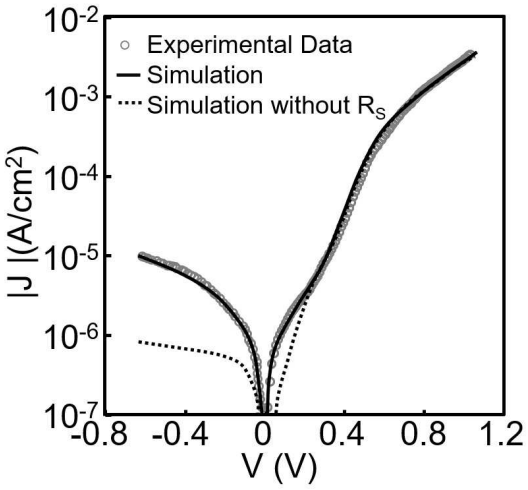

Figure 6.7: Comparison of an experimental current-voltage curve measured at room temperature for an ITO/PEDOT:PSS/P3HT:PCBM/Al solar cell in dark (symbols)[42] with our numerical results, including the effects of a shunt resistance (solid line) and without these effects (dashed line). The values of the free charge-carrier density at the metal-organic interface used in the numerical calculation are represented in Fig. 6.8.

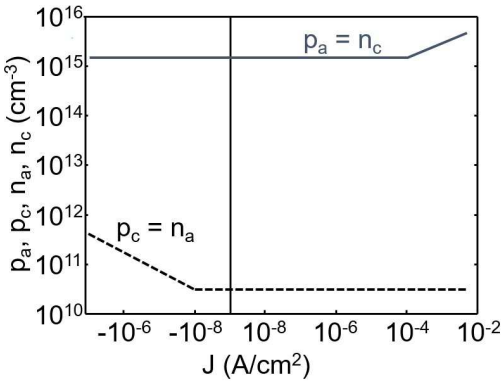

Figure 6.8: Hole and electron densities at the anode and cathode as a function of the current density, used in the numerical calculation to reproduce the experimental data in Fig. 6.7. The evolution of $p_A = n_C$ is described with: $m = 0.35$, $J_{Kf} = 10^{-4}$ A/cm^2 and $K_{2pA} = 1.4 \times 10^{15}$ cm^{-3}. The evolution of $p_C = n_A$ is described with: $m = 0.35$, $J_{Kr} = 10^{-8}$ A/cm^2 and $K_{2pC} = 3 \times 10^{10}$ cm^{-3}.

In order to show the effect of the leakage current, a curve without the effect of the shunt resistance was calculated (dotted line in Fig. 6.7). The fitting is accurate in regions I and II, but not at low voltages (regions III and IV). It is important to note that the high current range of region III cannot be reproduced with the leakage current alone (dashed line in Fig. 6.7). *Step v'* was necessary in order to find proper values for K_{1pC}.

6.4.2. Illumination

In this second part, we apply our model to experimental $J-V$ curves measured in an OSC under different intensities of illumination. The generation of electron-hole pairs takes place in the entire active layer. In BHJ solar cells, this includes the region close to the contacts, as the active layer coincides with the whole bulk. Again, the solution of the set of differential equations (6.12)-(6.17) for the generated charge is influenced by the charge at the edges. The question that was kept unanswered in the previous section was how the photogenerated charge at the contact increases with the illumination intensity. We also bear in mind two important proposals made by Shuttle and collaborators after experimental observations on OSCs [204]. The first proposal is the existence of similar relations between the stored charge density in the active layer of the solar cell with the current density in darkness and between the stored charge density with the current losses at V_{oc} [204]. That means that the physical process governing both processes is the same. In both cases, holes flow across the anode, although in opposite directions. The same occurs with the electrons through the cathode.

In an OSC, the holes cross the anode (and electrons the cathode) under three different situations. (1) When the current density is positive, both in darkness and illumination, holes are injected from the anode (and electrons from the cathode). In a typical OSC, these carriers see small barriers that impose no limitation to the current. (2) In darkness, the negative or reverse current density is controlled by the electron-injection barrier at the anode and the hole-injection barrier at the cathode. The asymmetry of the OSC contacts means that these barriers are high, impose a constriction to the current, and thus the resulting reverse current is lower than the forward current. The injected carriers travel trough the active material and are extracted at the opposite contacts: holes are extracted at the anode and electrons at the cathode. (3) Under illumination, the origin of the negative current density is different. The current is composed of photogenerated carriers inside the bulk. These carriers are no longer constricted by these high energy barriers the dark injected carriers see: the electron-injection barrier at the anode and the hole-injection barrier at the cathode. The only limitation is the extracting barriers the electrons see at the cathode and holes at the anode. For ideal OSCs, (i.e. ohmic contacts for injected electrons and holes at cathode and anode, respectively, and no recombination effects during the extraction of these carriers in the same electrodes), a symmetric behavior at the contact is expected: the injection should be similar to the extraction. This would also agree with Shuttle's second observation in which the relation between the stored charge density with the current losses at V_{oc} follows a the power-law function [204]. In this regard, the value of $p_A = n_C$ under illumination and at $J < 0$ should evolve the same as at $J > 0$. We propose to model this symmetric behavior with the scheme of Fig. 6.9(b) and the following expression:

$$p_A = n_C = K_{2phg}\left\{1 + \left[max\left(\frac{J}{J_{Kfphg}}, \frac{J}{J_{Kephg}}\right)^{m}\right]^{sharp}\right\}^{\frac{1}{sharp}} \tag{6.27}$$

where $J_{Kfphg} = (K_{2phg}/K_{1pA})^{(1/m)}$ and $J_{Kephg} = -(K_{2phg}/K_{1pAe})^{(1/m)}$ are the threshold values of the current density at which the charge densities start to increase over the flat value K_{2phg}, at injection regime (positive current) and extraction regime (negative current), respectively. They define the limits

of the flat region, in which the value of the charge density at the interfaces depends on the illumination:

$$J_{Kephg} \leq J \leq J_{Kfphg},\ p_A = n_C \simeq K_{2phg}(G) \tag{6.28}$$

K_{1pA}, K_{1pAe} and m are independent of the illumination as they describe the power law trend at injection and extraction, respectively (see the right and left high current regions in Fig. 6.9(b)):

$$J \gg J_{Kfphg},\ p_A = n_C \simeq K_{2phg} \left(\frac{J}{J_{Kfphg}} \right)^m = K_{1pA} J^m \tag{6.29}$$

$$J \ll J_{Kephg},\ p_A = n_C \simeq K_{2phg} \left(\frac{J}{J_{Kephg}} \right)^m = K_{1pAe} |J|^m \tag{6.30}$$

Under illumination, with the assumption of symmetric behavior for the injection and extraction mechanisms (ideal contacts), then $J_{Kephg} = -J_{Kfphg}$ and $K_{1pA} = K_{1pAe}$. We prefer to use different notations for J_{Kfphg} and J_{Kephg} and K_{1pA} and K_{1pAe} in order to extend the model to other cases in which the injection and extraction of charge are not necessarily symmetric. These cases will be treated in the next section.

In order to determine the dependence of the flat region with the illumination intensity $K_{2phg}(G)$, we analyze typical $J-V$ curves under illumination, as depicted in Fig. 6.9(a). In OSCs, the negative current density is limited by the maximum photogenerated current $J_{sat,i} = -J_{sat}(G)$, where i is an index the $J-V$ curves under illumination are referred with. This maximum value $J_{sat,i}$ is close to current density at V_{oc}, as the slope of the $J-V$ curve in the third quadrant is low. In an ideal case, the slope is zero and $J_{sat} = J_{sc}$. In this regard, we propose to relate the free charge density at the interfaces under illumination with the maximum photogenerated current as:

$$K_{2phg}(G) = K_{2pA} + \Delta K_{2phg}(G) = K_{2pA} + K_{1pA} \left(|J_{sat}(G)| \right)^m \tag{6.31}$$

At high illumination intensities, the total charge density can be approximated by the net photogenerated charge density:

$$K_{2phg}(G) \simeq \Delta K_{2phg}(G) = K_{1pA} \left(|J_{sat}(G)| \right)^m . \tag{6.32}$$

In a similar way, a study of the evolution of the flat value of the free charge density with temperature would lead to extend (6.31) to a similar relation: $K_{2pA}(T) = K_{2pA}(T_{low}) + K_{1pA}(J_{sat}(T))^m$, where T is the temperature and T_{low} is a reference value at low temperatures. The idea that lies beneath our proposals is that the charge density at a contact interface is the one which supports a fixed current through it, no matter the direction and no matter what is the origin. In other words, the absolute value of the current density fixes the value of the charge density at the interface, and vice versa.

The relations (6.31) and (6.32) are represented with dotted line in Fig. 6.9(c). This scheme defines the procedure to extract the values of the charge density at the extracting electrodes ($p_A = n_C$) from experimental $J-V$ curves under illumination. Basically, they are controlled by the parameter K_{2phg}, as the parameters m, K_{1pA} and K_{2pA} are extracted previously from the curve in darkness. For the curve i, the value of K_{2phg} is calculated by introducing in (6.31) the saturation current density $J_{sat,i}$. For

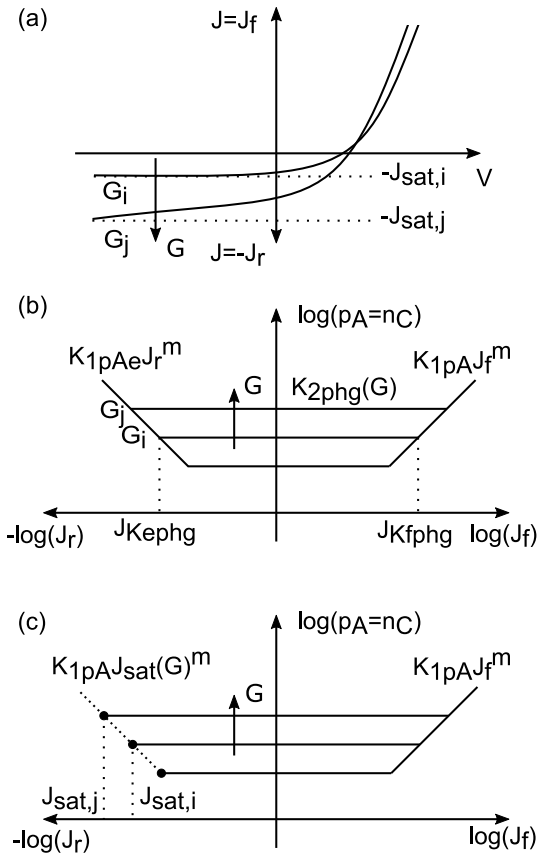

Figure 6.9: (a) Typical current-voltage curves of an OSC under illumination. (b) Graphical representation of (6.27) for the boundary values of the free charge density at the interfaces of an OSC under illumination. The injected (right) and extracted (left) charge density follow a power-law function. The scheme shows a general case in which injection and extraction of charge are not necessarily symmetric. (c) Particular symmetrical case of (b) applied to typical OSCs under illumination.

the same curve i, the parameter K'_{2phg}, which defines the value of the charge density at the opposite electrodes ($p_C = n_A$), will be initially considered as $K'_{2phg} = K_{2phg}$. Although, this value will be reduced in order to obtain a better fitting between the experimental data and our calculations, as was justified in the previous section.

An example of validation of the model under illumination (6.27) and (6.31) for the boundary values of the free charge density in OSCs is seen in Fig. 6.10. In this figure, we compare our numerical results with experimental data measured in the same OSC analyzed in dark (Fig. 6.7) [42]. A perfect agreement is achieved by introducing the boundary values for the electron and hole densities shown in Fig. 6.11 in the set of transport equations (6.12)-(6.17). The parameter K_{2phg}, which controls the value of the charge density at the extracting electrodes under illumination, follows the power-law relation (6.31) with exponent $m = 0.35$, like in darkness (see Fig. 6.10(a)). The values of the parameter K'_{2phg}, which controls the value of the charge density at the opposite electrodes under illumination, are lower than the values of K_{2phg}. We have found the relation $K'_{2phg} \simeq K_{2phg} - 2.4 \times 10^{15}$ cm^{-3}, meaning that there is a

correlation between the boundary values of the charge density under illumination in the two contacts. At high illumination intensities, these parameters tend to the same value (see Fig. 6.10(b)). The rest of the parameters coincide with the ones used in darkness.

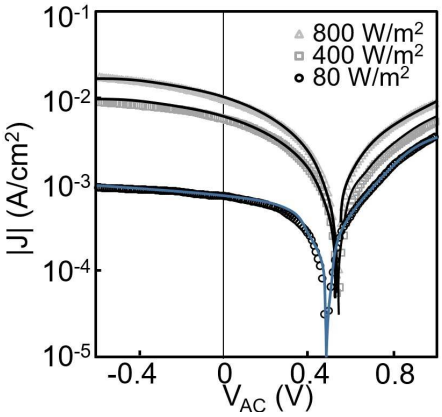

Figure 6.10: Comparison of experimental current-voltage curves measured at room temperature for an ITO/PEDOT:PSS/P3HT:PCBM/Al solar cell under different radiation intensity (symbols)[42] with our numerical results (solid lines). The values of the free charge-carrier density at the metal-organic interface used in the numerical calculation are represented in Fig. 6.11.

In order to show that the comparison between the experimental data in Figs. 6.7 and 6.10 is not fortuitous, we compare the value of the exponent of the power law extracted from this analysis ($m = 0.35$) with the value proposed in Schuttle's work [204]. They analyzed a similar structure to the one studied in this work. They determined a relation between the stored photogenerated charge density in the bulk and the current density of $n \propto J^{0.38}$ (or $J \propto n^{2.6}$). Our power-law model relates the current density with the values of the free charge density at the interfaces. The similarity between these relations (current density vs. charge density in the bulk or at the interfaces) highlight the importance of the use of proper boundary conditions in simulation. The boundary values provide a clear picture of what is happening in the active region of the solar cell.

6.4.3. Non-ideal blocking contacts

The existence of unintentional doping introduced by oxygen, the presence of traps and impurities or the poor quality of interfacial layers can create energy barriers for the extraction of free charges and then, they can reduce the velocity at which the carriers are extracted in an illuminated OSC [6, 7]. In these cases, an accumulation of charge at the extracting electrode takes place. This accumulation of charge reduces the value of the photocurrent in the fourth quadrant, and gives rise to anomalous S-shape $J-V$ curves. These anomalous shapes have been interpreted in the past with low values of the surface recombination velocity S in the boundary relation $J = -S(p_A - p_0)$ [6, 7], where p_A is the hole density at the anode and p_0 its value at equilibrium (a similar relation can be written for the extraction of electrons at the cathode).

Our boundary-condition model as defined in (6.27) can also reproduce these anomalous S-shapes.

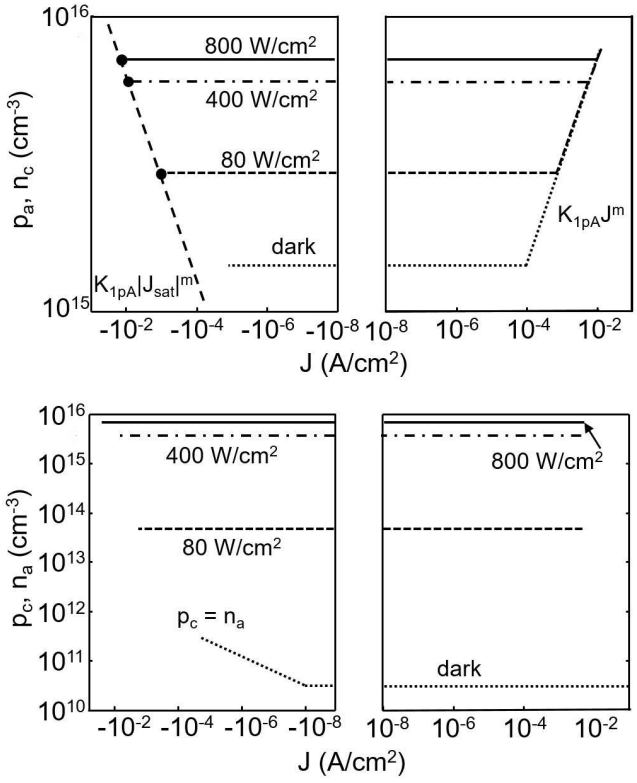

Figure 6.11: Hole and electron densities at the anode and cathode as a function of the current density. They are used in our numerical procedure to reproduce the experimental data in Fig. 6.10. (a) The evolution of $p_A = n_C$ is described with: $m = 0.35$, $K_{1pA} = K_{1pAe} = 3.5 \times 10^{16}$ cm^{2m-3}A^{-m}, $J_{Kf} = 10^{-4}$ A/cm^2, $K_{2pA} = 1.4 \times 10^{15}$ cm^{-3}, $K_{2phg}(80, 400, 800$ W/cm$^2) = 2.9, 5.9, 7.2 \times 10^{15}$ cm^{-3}. (b) The evolution of $p_C = n_A$ is described with: $m = 0.35$, $K_{1pC} = 1.9 \times 10^{13}$ cm^{2m-3}A^{-m}, $J_{Kr} = 10^{-8}$ A/cm^2, $K_{2pC} = 3 \times 10^{10}$ cm^{-3}, $K'_{2phg}(80, 400, 800$ W/cm$^2) = 6 \times 10^{13}$, 3.5×10^{15}, $5.7 \times 10^{15} cm^{-3}$

The accumulation of charge at the extracting electrodes is taken into account with a loss of symmetry between injection and extraction. This asymmetric behavior is controlled in our model (6.27) with the parameters J_{Kephg} and K_{1pAe}, which must fulfill the condition $J_{Kephg} \neq -J_{Kfphg}$ and $K_{1pA} \neq K_{1pAe}$. The reduction of $|J_{Kephg}|$ or the increase of K_{1pAe} make the value of the extracted charge density at the interfaces $p_A = n_C$ to increase.

Figure 6.12 shows a study of the effect of the boundary values for the free charge density at the interfaces $p_A = n_C$ and $p_C = n_A$ (Fig. 6.12(b)) on the $J - V$ curves of OSCs under illumination (Fig. 6.12(a)). Four cases are considered: (i) constant values for $p_A = n_C$, typical of ideal ohmic contacts using Boltzmann conditions ($J_{Kfphg} \to \infty$, $J_{Kephg} \to \infty$); (ii) an OSC with non-blocking extracting contacts and symmetric behavior for the injection and extraction mechanisms ($J_{Kephg} = -J_{Kfphg}$ and $K_{1pA} = K_{1pAe}$); (iii) an OSC with blocking extracting contacts and asymmetric behavior for the injection and extraction mechanisms ($-J_{Kephg} < J_{Kfphg}$ and $K_{1pA} > K_{1pAe}$); and (iv) an OSC with much greater blocking extracting contacts ($-J_{Kephg} \ll J_{Kfphg}$ and $K_{1pA} \gg K_{1pAe}$). The value of $p_C = n_A$ is

considered constant and uniform for the four cases, fulfilling the condition $p_C = n_A = K'_{2phg} < K_{2phg}$, where K'_{2phg} and K_{2phg} are the values of the flat region of $p_C = n_A$ and $p_A = n_C$, respectively. This condition is consistent with our observations of the previous section, although the value of K'_{2phg} does not alter the conclusions of this study.

In the first quadrant ($V > V_{OC}$), the current density is controlled by the injection of holes and electrons from the anode and cathode, respectively. Their densities at these interfaces are depicted on the right hand side of Fig. 6.12(b). Case (i) is the only that differs from the rest (ii)-(iv). Case (i) corresponds to constant $p_A = n_C$ while cases (ii)-(iv) follow the power law at high J. Although these differences seem to be small, the differences in the $J - V$ curve are large (Fig. 6.12(a)). This result confirms the importance of our power-law model in order to interpret the injection region of the current voltage characteristics of OSCs ($V \geq V_{OC}$). Actually, the value of V_{OC} can also be modified as seen in Fig. 6.12(a).

The fourth quadrant of the $J-V$ curve (Fig. 6.12(a)) is controlled by the extraction of photogenerated carriers. Cases (i) and (ii) produce the same typical response of an OSC, similar to that studied in Fig. 6.10. Cases (iii) and (iv) show anomalous S-shape responses, more pronounced in (iv). The difference is explained by the different value of $p_A = n_C$ at $J < 0$ which is controlled by the parameter J_{Kephg} (Fig. 6.12(b)). Case (i) imposes no limitation at all for the extracted charge with $J_{Kephg} \to \infty$; case (ii) does not impose any limitation either, it corresponds to contacts that show a symmetric increment of the injected and extracted charge at high values of $|J|$ ($-J_{Kephg} = J_{Kfphg} = 1$ mA/cm^2), the value of $|J_{Kephg}|$ is in the limit to impose constrictions to the extracted charge; and cases (iii) with $J_{Kephg} = -10^{-5}$ mA/cm^2 and (iv) with $J_{Kephg} = -10^{-7}$ mA/cm^2 consider the accumulation of charge carriers at very low values of the photocurrent density. After this theoretical study, we conclude that the S-shape can be explained by means of the accumulation of photogenerated charges at the extracting interfaces (Fig. 6.12) and not by imposing limits to the injecting interfaces.

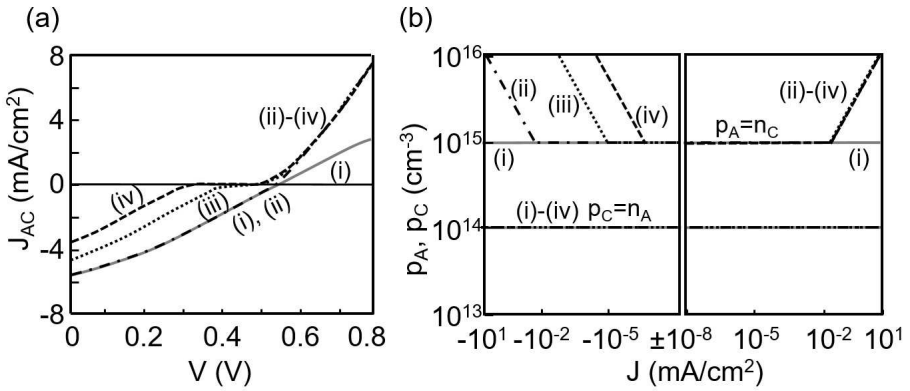

Figure 6.12: (a) Current-voltage curves of an OSC under illumination generated with four different boundaries values for the free charge density $p_A = n_C$ and $p_C = n_A$ (named (i)-(iv) in (b)). (b) (i) Ideal extracting contact using Boltzmann conditions ($J_{Kfphg} \to \infty$, $J_{Kephg} \to -\infty$); (ii) contacts with symmetric increment of the injected and extracted charge at high values of $|J|$ ($|J_{Kephg}| = J_{Kfphg}$); (iii)-(iv) contacts imposing limits to the extracted charge. The common parameters used in the simulations are: T=295 K, V_{bi} =0.55 V, $\mu_n = \mu_p$ =10^{-4} cm^2/Vs, $\varepsilon_r = 3$, $L = 150$ nm and $sharp = 10$. The specific parameters are: (1) $m = 0$, $K_{2phg} = 10^{15}$ cm^{-3}, $K'_{2phg} = 10^{14}$ cm^{-3}; (2) $m = 0.7$, $K_{2phg} = 10^{15}$ cm^{-3}, $-J_{Kephg} = J_{Kfphg} = 1$ mA/cm^2 and $K'_{2phg} = 10^{14}$ cm^{-3}; (3) $m = 0.7$, $K_{2phg} = 10^{15}$ cm^{-3}, $J_{Kephg} = -10^{-5}$ mA/cm^2, $J_{Kfphg} = 1$ mA/cm^2 and $K'_{2phg} = 10^{14}$ cm^{-3}; (4) $m = 0.7$, $K_{2phg} = 10^{15}$ cm^{-3}, $J_{Kephg} = -10^{-7}$ mA/cm^2, $J_{Kfphg} = 1$ mA/cm^2 and $K'_{2phg} = 10^{14}$ cm^{-3}.

7

Compact Modelling and Contact Effects in Thin Film Transistors

7.1. Introduction

Emerging technologies, based on organic or polymeric materials [55]-[229], two-dimensional materials such as graphene [230], semiconducting dichalcogenides, MoS_2 or WSe_2 [231], or nanowire (NW) devices [232], are promising solutions in the fields of nanoelectronics, sensing and photonics. Apart from having common applications, these materials share an additional common feature: the connection to the outer world via metal contacts.

In order to treat this common contact problem, we focus on one of these emerging technologies and one of its outstanding devices, the organic or polymeric (hereafter, the term organic is used for both) thin film transistor (OTFT). These transistors are especially important as drive elements in niche applications such as the displays of mobile devices and televisions using the Active-Matrix Organic Light-Emitting Diode (AMOLED) technology. Sensors, smart labels, solar cells or smart clothing are other emerging and innovative applications where these transistors work as the main or control element. These transistors, and other organic devices, have received considerable attention because of the attractive properties of the materials they use. One key advantage of the organic materials is that they can be solution processed [233]. The combination of soluble deposition techniques such as drop casting, spin coating, layer-by-layer, or roll-to-roll on flexible sheets with low-cost patterning equipment, such as ink-jet printers [234], reduces both capital and manufacturing costs compared with conventional crystalline electronics [51].

Contact effects in OTFTs are affected by the materials used for substrates, electrodes or semiconducting films; the vertical and horizontal layout differences; the different processing steps such as vacuum processing, spin coating, printing or stamping; the functionalization of interfaces; and the self assembling of organic materials. Though important in all devices, the contact effects are even stronger at the nanoscale [235]. To understand the effects of the contacts in OTFTs, the physical or geometrical origins of these effects are treated jointly in nano-scale and organic-thin-film structures.

The prediction and optimization of the performance of integrated circuits is necessary. For practical applications, compact models for electronic devices play an important role. Compact models must include the effects of beneficial and detrimental mechanisms that affect the device performance. In this chapter, we focus on the incorporation of the contact effects in compact models of OTFTs.

The chapter begins with the analysis of the properties of the contacts from a general point of view, treating common effects at nano and large scale (Sec. 7.2). In Sec. 7.3, we analyse the advantages and disadvantages of previously developed models that describe the current-voltage curves of OTFTs with contact effects. In Sec. 7.4, we propose a compact model for the contact region of OTFTs that unifies different trends found in the literature. This model is introduced in Sec. 7.5 in a previously developed generic model for OTFTs. In the following sections, the resulting model is applied to describe recent experimental data in OTFTs with contact effects.

7.2. Properties of metal contacts

Although the basic ideas of the metal-semiconductor contacts are reasonably well understood [216], [236], there are many side effects that impact their electrical behaviour (Fig. 7.1). Here, we analyse the

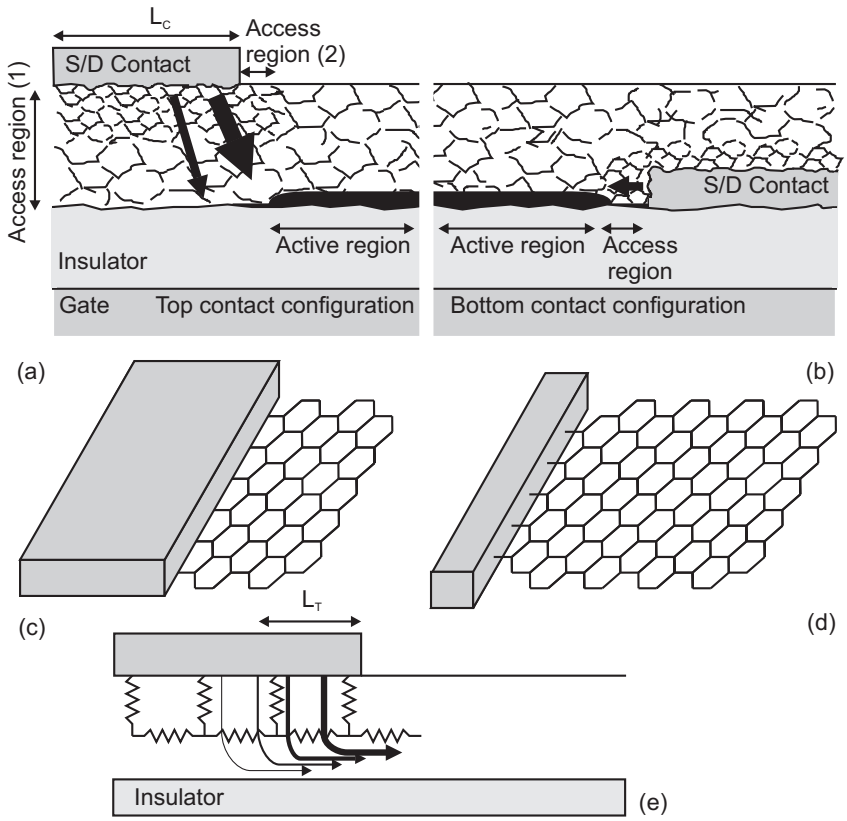

Figure 7.1: Bottom-gate (a) staggered and (b) coplanar configurations showing side effects that determine the electrical behaviour of a metal-semiconductor structure. (c) Side contact. (d) End or edge contact. (e) Current crowding modelled with a transmission line model.

role of metal contacts in general terms, distinguishing between physical and geometrical effects.

Metal and semiconductor work functions

According to the earliest and simplest models of the metal-semiconductor junction [237], [238], the difference between the metal and semiconductor work functions determines the ohmic or rectifying behaviour of the contact. As an example, in graphene, Pd and Ni have been shown to provide a relatively low contact resistance. A higher contact resistance has been observed with Ti, Cr, and Al contacts [239]-[240].

The doping level in the semiconductor, even in bulk metal-semiconductor junctions, determines the position of the Fermi level in relation to the band edges, and thus the semiconductor work-function. Graphene displays an even stronger effect known as metal doping. Since monolayer graphene is gapless, re-alignment of the Fermi level due to the metal work function and the accompanying charge transfer can produce p-type or n-type behavior. In fact, a very small amount of electron transfer shifts the Fermi level significantly in graphene [241]. Thus, contacts in graphene can be chosen as n-type or p-type by selecting a metal with the suitable work function. When the graphene layer is deposited on a bottom

gate, separated from it by a thin insulator layer, and then covered by a top contact, the bottom gate bias has also been found to contribute to the metal-graphene contact resistance by changing the charge density in the graphene layer [239], [242].

Quality of the contact and the near-interfacial region

The position of the Fermi level is also affected by the bond structure of the contact region, with possible bond polarization [243] and/or a high interface state density in the semiconductor gap [244], [245]. A charge neutrality level is defined at the position of the Fermi level at the interface for which the net charge in the interface states is zero. The Fermi level is said to be pinned [246], [247]. It cannot shift very much from this position without a huge charge transfer. Thus, the resulting barrier height may be significantly different from that predicted by using the work functions of the separate materials. There are approaches to de-pin the Fermi-level and tune the metal-organic contact behaviour such as the introduction of ultrathin interfacial insulators (Si_3N_4) [248]; the treatment of the contacts with a self-assembled monolayer (SAM) [249]; the introduction of a thin polyelectrolyte layer between the electrodes and the semiconductor [250]; or using a solid electrolyte directly as dielectric layer [251]. These observed reductions in the contact resistance can be explained either by a decrease of the barrier energy or by changes in the surface morphology [249].

Examples of this last effect can also be seen in different materials as graphene, MoS_2 or nanowires. Graphene can be subjected to strong modifications originated by charge inhomogeneities induced by the metal [252], [253]. Questions have arisen as to whether the original work function of the graphene is preserved after the contact [240]. Density functional theory calculations have shown that the energetic separation between the Fermi level and the Dirac point in the contacts is a sensitive function of the metal-graphene distance [241]. In [252], it was found that the metal-graphene coupling strength is moderate, resulting in a modification of the graphene density of states (DOS) underneath the contacts small enough so that Fermi level pinning does not occur due to a lack of screening of the gate field. Furthermore, although capacitance-voltage measurements have shown that the original work function of graphene is not preserved, but it is pinned to the work function of the metal when the coupling is strong, the measurement of the quantum capacitance of graphene in the strong accumulation mode seems to prove that the characteristic properties of the graphene density of states are maintained [240].

A further difference in behavior of graphene contacts has been proposed to distinguish between side-bonded (Fig. 7.1(c)) and end- or edge-bonded (Fig. 7.1(d)) contacts [254]. While end contacts form strong covalent bonds to the dangling bonds at the edges, top and bottom contacts form weaker van der Waals bonds. In both cases, results show that Fermi-level pinning has a small influence in the barrier height, in contrast with what happens in bulk metal-semiconductor junctions.

In the case of contacts to layered MoS_2, the widely used Au contact has been proposed to form a tunnel barrier and be the cause of the low values of the measured mobility [231], while metals with a low work function would efficiently inject electrons into the conduction band and would solve this problem. MoS_2 transistors with Sc [255] and Ti ohmic contacts [256] have been demonstrated, but the quality of the contacts should be improved in order to achieve the expected advantages of these materials.

While metal-induced gap states often determine the barrier height in bulk contacts, they can have a weaker impact in nanowires. The electrostatics at reduced dimensions prevents the Fermi-level from being pinned since a strong band bending cannot be established due to the small size of these nanostructures. The region of a nanowire under the metal has also been shown to change its electrical properties after the application of a thermal treatment [232], [257].

In the case of OTFTs, the quality of the contacts also depends on the relative position of the source/drain (S/D) contacts, dielectric and organic films. Bottom-gate OTFTs can be found in two typical structures: top-contact (TC) or staggered configuration (Fig. 7.1(a)) and bottom-contact (BC) or coplanar configuration (Fig. 7.1(b)). The BC configuration is known to give inferior performance to the TC configuration for a range of deposition conditions and material thickness [258]. This can be attributed to the different arrangement of molecules in the organic material in relation to the proximity with other materials [258], [259].

Geometry of the contact

The size and geometry of the electrodes are other factors that affect the performance of the transistors [260]. The description of the current flow through the contact region often requires a two-dimensional analysis, in particular for the TC staggered configuration [261], since the electrodes, dielectric and semiconductor channel are not adjacent to each other (Fig. 7.1(e)). A widely used model to deal with these aspects is the transmission-line (or transfer length) model (TLM) [262]. According to this model, instead of the physical length L, a contact transfer length, L_T, can be defined as the effective length over which injection occurs from the contact edge. In contacts to bulk and thin-film materials, $L_T = \sqrt{\rho_c/R_s}$, where, ρ_c is the contact resistivity and R_s is the sheet resistance under the contact. The transfer length determines the contact resistance through the relation $R_c = \sqrt{\rho_c R_s}\tanh^{-1}(L/L_T)/w$ [262], [263], where w is the width of the contact.

The conventional expression of the TLM model has been applied to graphene [264]. To compute the transfer length in this system, a phenomenological expression for the sheet resistance of graphene under the contact [265] has to be used. This sheet resistance underneath the metal contact depends on the mobility which in turn is strongly dependent on the deposition processes [235]. Experimental values of the contact transfer length in graphene show a dependence with the type of electrode [262]. The dependence on the material can be explained by the strength of the coupling between the metal and the semiconductor, since stronger coupling produces higher electron scattering and thus smaller L_T values. The TLM has also been applied to nanowires [266]. However, corrections are introduced due to the small dimensions of these structures: the contact length in many nanowire devices is typically comparable to the NW length; and the depth of the depleted or accumulated semiconducting region in metal-NW interfaces is typically comparable to the NW radii [267].

Transition region

The region within the semiconductor in which the effects of the contact are still strong is called the transition or access region (Figs. 7.1(a)-(b)). The band bending due to the contact can be extended

on a length scale of tens of nanometers to micrometers. This region, called depletion layer in bulk junctions, develops beneath the contact, but it can spread out laterally towards the channel in thin films and nanostructures. If the thickness of the depletion layer, W, is greater than the film thickness or the radii of the nanostructure, then W becomes size dependent and increases strongly at low doping concentrations. A long-distance band bending has been observed in nanowires [268] and graphene [269]. A correct determination of W is important since its value strongly influences the charge-injection in the contact [270]. As in bulk contacts, a heavy doping can be used in end-bonded nanowires to reduce W, thus allowing electrons to tunnel though the barrier. Nevertheless, this method cannot be used in the case of side contacts since, for this to be useful, W has to be smaller than the section diameter and a high doping level should be required when the nanowire diameter is reduced [270].

The change in the work function of graphene under metal also leads to band bending from the contact edge towards the channel [269], [271]. In the application of the TLM model to graphene, the contact resistance has been separated into two components: the actual contact resistance at the metal-graphene contact, R_{CI}, and the additional resistance due to the metal-contact doping, R_{CD} [264]. This component, R_{CD}, arises in the transition region along which the Fermi level varies from the value pinned by the metal due to metal doping to the value in the channel region. Thus, it depends on the type of metal and differs significantly for each metal. The very small DOS around the Fermi level for graphene increases the screening length. The resulting long charge transfer region is a unique characteristic of the metal/graphene contact [235] and was reported to be $\simeq 0.5$ μm [271].

In the transition region of the contacts of OTFTs another mechanism takes place. The charges that are created near the surface of the electrode move through the organic material due to the electric field and the charge transport is space-charge limited. In the following sections, we discuss contact effects in TFTs.

7.3. Contact effects in OTFTs

7.3.1. Models of contact effects

The objective, when modelling the contacts of OTFTs, is the reproduction of the current-voltage curves in the contact ($I_D - V_C$), where V_C is the voltage drop in the contact region, and their dependences on bias voltages, temperature and material parameters [272], [273]. The incorporation of physical models of the contacts, [216], [18], into the classical transistor models is not a trivial task because the contact effects interfere with other dependences in OTFTs [55]. In the literature, there are different electrical models that incorporate the voltage drop at the contacts (Fig. 7.2(a)). There are also associated methods to extract this voltage drop from the output characteristics of a transistor [274], [275]-[10].

The low conductivity region close to the contact is usually modelled with a parasitic resistance R_C (Fig. 7.2(b)). Experimental investigations show that the magnitude of R_C is dependent on the gate bias, temperature and ambient gas environment [274], [260], [276], [277].

Non-linear behaviour, also observed in the literature, are treated with a drain-voltage dependent resistance [278], [279]. The slope of the $I_D - V_C$ curve increases with V_D, thus decreasing the contact

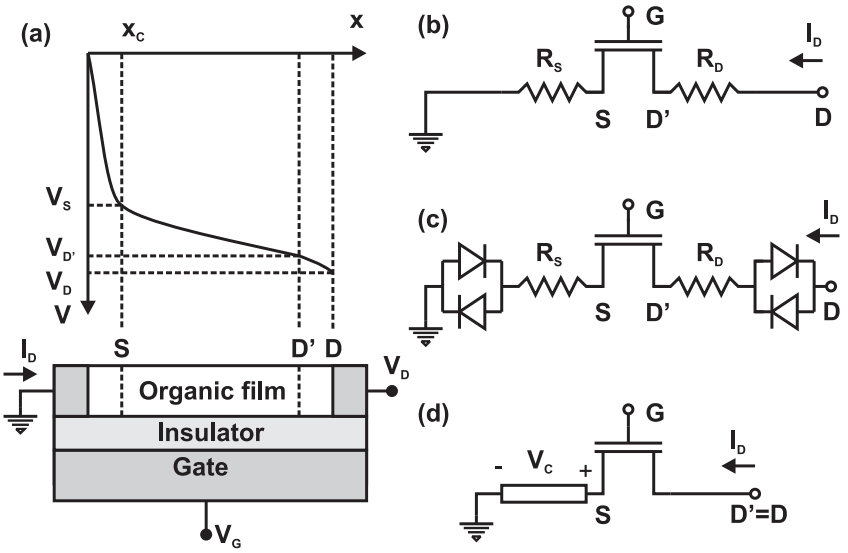

Figure 7.2: a) Separation of the channel of an OTFT in the active channel and the contact regions. Equivalent circuits of an $OTFT$ including: b) linear source and drain contact resistances; c) a non-linear model for the source and drain contact regions [275]; and d) our unified $I_D - V_C$ model for the source contact assuming negligible the voltage drop at the drain contact [272].

resistance, being negligible in the saturation region [280]. This may be one reason for some authors to extract the field-effect mobility from the saturation region using the ideal MOS model [278], [281], [282]. However, this way to model non-linear behaviour can lead to confusion as noted in [283], where a diode was added in series with the contact resistance to model the non-linear response. A study of the error made in the extracted values of the threshold voltage and mobility when considering the ideal MOS model in saturation is given in Sec. 7.6-A and Fig. 7.3. Better approaches that considers highly non-linear drain and source contact series resistances and a gate-voltage dependant mobility, $(\mu \propto (V_G - V_T)^\gamma, \gamma > 0)$, can be found in the literature [275], [283]-[71]. This mobility dependence is extracted from theories such as the charge drift in the presence of tail-distributed traps ($TDTs$) [284] or variable range hopping (VRH) [285], [286]. In order to simulate non-linear $I_D - V_D$ output characteristics for organic bottom contact $TFTs$, an equivalent bottom contact TFT circuit that consists of the TFT with linear source and drain access resistances R_D and R_S, respectively, and a pair of anti-parallel leaky Schottky diodes connected to each access resistor in series, see Fig. 7.2(c), was proposed [275]. Two diodes in parallel are needed to obtain symmetric current-voltage characteristics. The diode non-ideality factor, η, which is responsible for the steepness of the current-voltage characteristic, and the access resistances are the fitting parameters [275].

Recently, Schottky barriers at both drain and source contacts and electric field dependent mobilities have been incorporated in two-dimensional numerical simulations to provide a vision on how the current spreads over the contact electrode [287], [288]. Although this model reproduces experimental data, the authors noted the sub-optimal values of some of the model parameters, such as the barrier height [288] or the diode non-ideality factor, η [275]. Our interpretation is that simple electrical models valid for

crystalline structures are substituting the two main physical theories that describe the metal-organic structure, injection and space-charge limited theories, thus providing suboptimal values for the model parameters.

7.3.2. What is missing?

Linear or non linear contact behaviours are observed experimentally at low drain voltages in the output characteristics of the transistor. Different physical mechanisms have been proposed to explain such behaviour [8], [9]. However, many of the models used to interpret the effect of the contacts on these I-V curves are reduced to finding a value for the contact resistance.

A suitable OTFT model should incorporate both linear and non-linear behaviours for the contact I-V curves, with a method that unifies in some of its parameters the injection and transport mechanisms present in the metal-organic contacts and that considers the dependence of the I-V curves with the gate voltage and the temperature. In the following sections, we present such a model.

Also needed is a method that can be used to extract, from the $I-V$ experimental data of a single transistor, [289] the parameters of the transistor, including those associated with the contact region. Many methods to extract the parasitic resistance are based on a set of transistors with different lengths, or on more complex techniques such as the four-probe method or the sophisticated electrical scanning probe microscopy techniques [290]-[291]. In this chapter, we combine the proposal of a compact model for OTFTs including contact effects with a method to extract I-V curves at the contact from output characteristics measured in a single transistor.

7.4. Compact model for the contact region of OTFTs

Different physical ways to inject charge from the metal contact (ohmic contacts, Schottky barriers, tunnel injection) give way to linear or non-linear contact behaviour. Our method unifies all these physical mechanisms and behaviours by considering them as part of the boundary value for the charge density at the metal-organic interface, $qp(0)$. Its value must contain information about the physical, morphological and/or geometrical features of the contact region. Some of the charges get trapped, with no contribution to the current. The rest, the free charge density $q\theta p(0)$, where θ is the ratio of free to total charge density, drifts through localized sites in the transition region of the contact, as mentioned at the end of Sec. 7.2. Independent of the value of $p(0)$, or how this charge has appeared at the metal organic interface, a relation between the current density j and the applied voltage V_C can be found by solving the transport equations in the semiconductor [10], [8]:

$$\begin{aligned} V_C &= (2/3)\left[2j/(\varepsilon\mu\theta)\right]^{1/2}\left[(x_C+x_p)^{3/2}-(x_p)^{3/2}\right] \\ x_p &\equiv j\varepsilon\theta/\left\{2\mu\left[\theta qp(0)\right]^2\right\} \end{aligned} \tag{7.1}$$

where $j = I_D/S$, S is the cross section of the channel where current I_D flows, x_p is a characteristic length defined as the point from the contact interface towards the organic film, at which the charge density $qp(x_p)$ decays to $qp(0)/\sqrt{2}$, ϵ is the organic dielectric constant and x_C is the length of the contact region in the organic material, which may include the transition layer defined in Section II. Equation (7.1) was demonstrated to have two asymptotic trends: a linear or Ohmic behaviour if the characteristic length x_p is a few times larger than the contact length x_C,

$$I_D \approx S\theta qp(0)\mu V_C/x_C \equiv V_C/R_C \tag{7.2}$$

and a quadratic behaviour (Mott-Gurney law) if the characteristic length x_p is much smaller than the contact length x_C [10], [12],

$$I_D \approx \frac{9}{8}\varepsilon\mu\theta S V_C^2/x_c^3 \equiv M V_C^2 \tag{7.3}$$

The two asymptotic situations defined in (7.2) and (7.3) also define limit distributions of the free charge density in the contact, $qp_{contact}$. In the case of linear characteristics, $qp_{contact}$ is constant and its value can be represented by the value this variable takes at $x = 0$, $qp_{contact} = \theta qp(0)$, which is the value that appears in (7.2). The effective area of the contact where the current flows can be expressed as $S = w \times t_C$, where t_C is an effective thickness, and w is the contact width. Considering the free-charge surface density $\sigma_{contact} = \theta qp(0)t_C$, the following relation is obtained from (7.2):

$$\sigma_{contact} = x_C/(w\mu R_C) \tag{7.4}$$

In the case of quadratic behaviour, the distribution of the free charge density, not uniform along the contact region [18], is given by:

$$qp_{contact}(x) = \left[(j\varepsilon\theta)/(2\mu x)\right]^{1/2} \tag{7.5}$$

If the parameter M is known (in Sec. 7.6 a parameter extraction method is proposed), $p_{contact}$ can be evaluated as a function of arbitrary values of the contact voltage V_{SC} and the position x_0 close to the contact. This provides physical information about the extracted parameter M. In order not to work with the unknown effective thickness t_C, the free charge surface density is evaluated instead, $\sigma_{contact} = qp_{contact}(x_0) \times t_C$. Thus, combining (7.3), (7.5) and $j = M \times V_{SC}^2/S$, the following relation results:

$$\sigma_{contact}(x_0) = (2MV_{SC})/(3\mu)\left[(x_C^3)/(x_0 w^2)\right]^{(1/2)} \tag{7.6}$$

The inverse of the contact resistance R_C in (7.4), and the parameter M in (7.6) are proportional to the free-charge surface-density $\sigma_{contact}$. Thus, whatever trend $\sigma_{contact}$ has with the gate voltage, the parameters $1/R_C$ and M will have the same trend, except for a multiplying factor.

7.5. Incorporation in an OTFT model.

The model for the contact region presented above is useful when integrated in a compact model for OTFTs. For this reason, we consider a generic analytical model for the current-voltage characteristics

of $OTFTs$ [70], [71]. In that work, the authors related the drain current I_D and the voltages at the borders of the intrinsic transistor, V_G, V_D and V_S (Fig. 7.2(c)):

$$\begin{aligned} \frac{I_D}{k_o} &= \frac{[(V_G - V_T - V_S)^{\gamma+2} - (V_G - V_T - V_D)^{\gamma+2}]}{\gamma + 2} \\ k_o &= \mu_o C_i w/L \end{aligned} \tag{7.7}$$

where $C_i = \varepsilon_i/t_i$ is the gate insulator capacitance per unit area, ε_i is the insulator dielectric constant, t_i is the insulator thickness, V_T is the threshold voltage, w is the transistor width and L the channel length. The result is equivalent to the well-known and widely used generic FET model with a constant mobility. This model is derived considering that the voltage drop at the drain contact is small in comparison to the voltage drop at the source contact [272] (Fig. 7.2(a)). Thus, the contact voltage is reduced to the voltage drop between the external source terminal and the internal source ($V_S \equiv V_C$) (Fig. 7.2(d)). It also considers that the mobility μ is written according to the aforementioned common theoretical result [284], [285], [67],

$$\mu = \mu_o (V_G - V_T - V_x)^{\gamma},\ \gamma = 2T_o/T - 2 \tag{7.8}$$

where V_x is the potential in the semiconducting film of the TFT, γ is the mobility enhancement factor, T_o is the specific equivalent temperature that represents the steepness of the DOS exponential tail and μ_o is the mobility-related parameter with dimensions $\mathrm{cm}^2/(\mathrm{V}^{1+\gamma}\mathrm{s})$. In order to provide a single value for the voltage dependent mobility, the mobility is evaluated at $V_{GT} = V_G - V_T = 1$ V [70], thus $\mu(V_{GT} = 1\mathrm{V})$=$\mu_o$ in $\mathrm{cm}^2/(\mathrm{Vs})$.

This model (7.7) is complemented with a model for the current-voltage curves in the contacts, as defined in (7.2) or (7.3). A new parameter, R_C (or M), not present in (7.7), is added to the set of parameters of the model. The parameters R_C and M are expected to depend on the gate voltage, as many experiments have shown the dependence of the $I - V$ curve at the contacts with the gate voltage [274], [276], [292].

To describe this dependence, we analyse the two regions of different conductivity distinguished along the channel of the organic transistor [229], [272], [293]: the low conductivity region close to the contact defined by the free-charge surface-density $\sigma_{contact}$ and the high conductivity region in the intrinsic channel defined by its counterpart free-charge surface-density, usually expressed as [294]:

$$\sigma_{channel} = C_i (V_G - V_T) \tag{7.9}$$

The free charge density in the contact region can be considered a fraction of the last one: $\sigma_{contact} = \sigma_{channel}/K$. Although K is an undetermined constant, there is no physical reason to believe that the mobile charges in these two adjacent regions start appearing at very different gate voltages, or follow very different trends, unless local non-uniformities were present just at the contact region. Therefore, $\sigma_{contact}$ can be assumed proportional to $(V_G - V_T)$. Introducing this dependence and the gate voltage

dependence of the mobility (7.8) in (7.4) and (7.6), we can write, respectively:

$$\begin{aligned} 1/R_C &= [(wC_i\mu_o)/(Kx_C)](V_G - V_T)^{(1+\gamma)} \\ M &= \frac{3C_i\mu_o}{2KV_{SC}}\left[\frac{x_0 w^2}{x_C^3}\right]^{1/2}(V_G - V_T)^{(1+\gamma)} \end{aligned} \tag{7.10}$$

or by defining the parameters α_1 and α_2:

$$\begin{aligned} 1/R_C &= \alpha_1(V_G - V_T)^{(1+\gamma)} \\ M &= \alpha_2(V_G - V_T)^{(1+\gamma)} \end{aligned} \tag{7.11}$$

Thus, we can express (7.2) and (7.3) in a more compact way:

$$V_C = \alpha_m^{-1} I_D^{1/m}(V_G - V_T)^{-(1+\gamma)/m},\ 1 \leq m \leq 2 \tag{7.12}$$

Although the range $1 \leq m \leq 2$ includes all the cases covered by (7.1), the practical cases can be restricted to the limit cases $m = 1$ and $m = 2$. The election of $m = 1$ or $m = 2$ is decided by a simple linear regression study of the $I_D - V_D$ curves at low values of V_D.

The combination of (7.7) and (7.12) defines a compact relation between the drain current and the external terminal voltages. This model has parameters that can be characterized relatively easily, or even guessed, preventing unnecessary phenomenological fitting parameters or even the use of transistors with different channel lengths. Our model is complemented with an extraction procedure of its parameters V_T, μ_o, γ and α_m (or the equivalent $M(V_{GS})$ or $R_C(V_{GS})$ from the current-voltage curves of an OTFT. It follows the main ideas of the procedure proposed in [70], [71]. However, some modifications are made in order to eliminate errors in the determination of the model parameters when large contact voltages are present and to extend its application to output characteristics measured in single-length transistors. As different models or different sets of values of our model can reproduce the experimental data, tests are also provided in order to validate the physical meaning of the extracted values for the parameters.

7.6. Parameter extraction method

The objective of the extraction method is to determine the values of the parameters μ_o, γ, V_T and α_m that define the compact model for the OTFT (7.7) including the contact effects (7.12). The independent determination of M (or R_C) for each V_{GS} is preferred to the determination of the compact parameter α_m. It is slower but more general, since it can be applied to situations where instabilities or trapping effects appear in the transistor [295]. In these cases, the evolution of $\sigma_{channel}$ with V_G (7.9) can separate from a straight line due to slight modifications in the threshold voltage.

We propose a five step procedure with several tests to check the physical meaning of the results. In a previous work [12], we proposed a method to extract the parameters of this model from experimental $(I_D - V_D)$ curves including the voltage drop at the contact. It was applied and tested successfully in an hypothetical p-type OTFT with known parameters [15]. It was adapted later to $I_D - V_D$ curves

with hysteresis [296]. In this chapter, we compile all the previous ideas to make the method completely general and applicable to OTFTs.

7.6.1. Importance of a compact model with contact effects

Prior to the presentation of our characterization procedure, we highlight the importance of using a proper compact model for OTFTs with contact effects in the determination of essential device parameters such as the mobility μ and the threshold voltage V_T. It is deduced from many of the references cited in this chapter that the apparent mobility extracted from current-voltage curves with contact effects is different from the real one. However, in many publications, the classical MOS model is still used to characterize the mobility. In saturation, the effects of the contacts are lower than in the linear region of operation. However, the saturation region is not free from errors. In the following, we determine such errors. To do this, we create a set of output characteristics for a hypothetical transistor for which we know all its parameters: $k = \mu_o C_i w/L$, γ, V_T and M (or R_C). We build the output characteristics of this transistor by combining an intrinsic transistor modelled with the ideal MOS model plus a contact region at the source (Fig. 7.2(d)). The classical MOS model can be easily deduced from (7.7) by assuming $V_S = 0$ V and $\gamma = 0$. The contact region is modelled by (7.2) or (7.3).

Once the output characteristics are created, the ideal MOS equations are used to extract the parameters of such a hypothetical transistor. Figure 7.3 represents the errors in this determination in the saturation region. The test is done for different values of k, M and R_C (M and R_C are assumed independent of the gate voltage; a dependence with the gate voltage would increase the error). Figure 7.3 defines the ranges of these parameters where the relative error is not negligible and the classical MOS model is inaccurate. This figure is also useful since we can establish a relation between the values of M and R_C that produce the same effects.

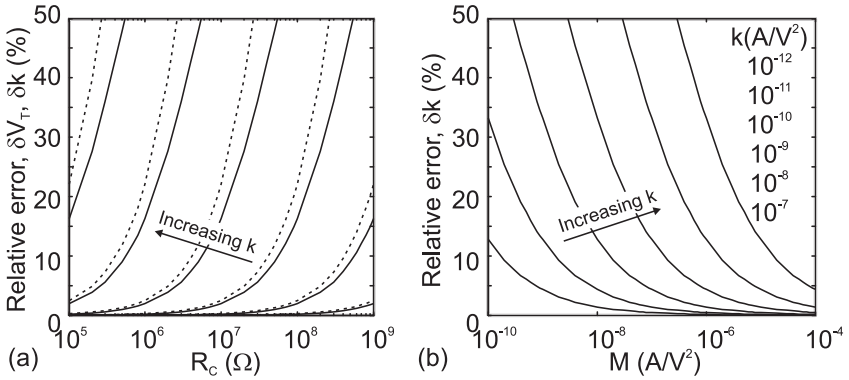

Figure 7.3: Relative error in the determination with the ideal MOS model of the transconductance FET parameter, δk (solid lines) and the threshold voltage δV_T (dashed lines) in an OTFT with contact effects. The error is evaluated as a function of the contact related parameters M and R_C for different values of the transistor transconductance parameter k.

7.6.2. Our extraction method

The five steps of our extraction procedure are (Fig. 7.4) now presented:

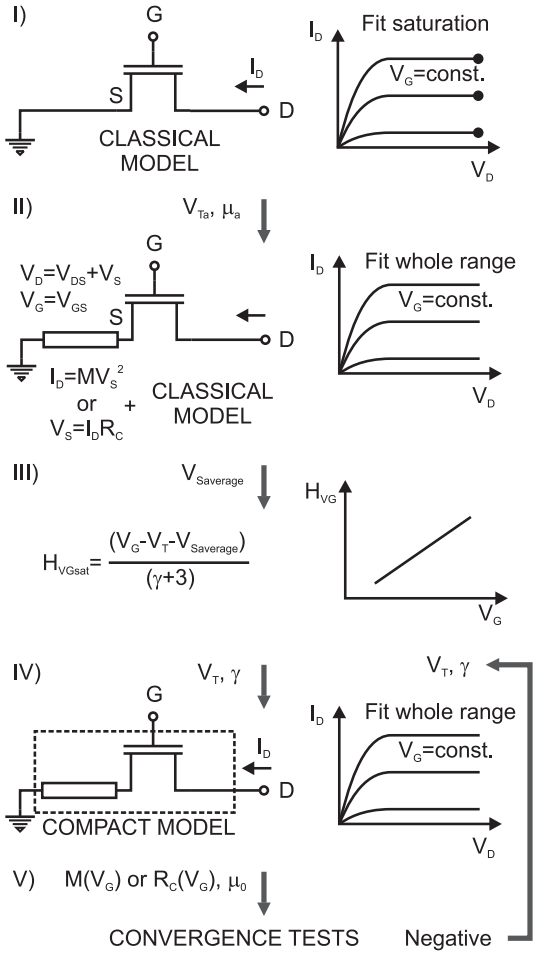

Figure 7.4: Steps of the parameter extraction method indicating the models used (left) to analyse the experimental data (right).

I) Initial estimation of μ and V_T. The experimental data in the saturation region are fitted with the classical MOS model ((7.7) with $\gamma = 0$ and $V_S = 0$) to determine apparent values for the threshold voltage and the mobility.

II) Initial estimation of M (or R_C). The contact model is added to the drain voltage by combining $V_D = V_{DS} + V_S$ and (7.3) (or (7.2)) and assuming $V_G = V_{GS}$ (Fig. 7.4(II)). The resulting equations are used to fit the whole experimental $I_D(V_D, V_G)$ curves to extract values of $M(V_G)$ (or $R_C(V_G)$). Then, an averaged value for the contact voltage in saturation, $V_{C_{average}}$, can be obtained.

III) Extraction of V_T and γ with the H_{VG} function [70], [297] applied to the experimental data in

saturation. The H_{VG} function is defined as

$$H_{VG}(V_G) = \frac{\int_{<V_T}^{V_G} I_D dV_G}{I_D(V_G)}. \quad (7.13)$$

The H_{VG} function can be derived from the TFT generic model (7.7) in the linear and saturation modes. In the saturation mode ($V_D > (V_G - V_T)$), H_{VG} is linear with V_G [70]:

$$H_{VG}(V_G) = \frac{(V_G - V_T - V_S)}{(\gamma + 3)} \quad (7.14)$$

The values of γ and the threshold voltage V_T can be extracted easily from the slope of $H_{VG}(V_G)$ and intercept with the V_G axis, by assuming $V_S = V_{C_{average}}$ in (7.14).

IV) Extraction of μ_o and M or R_C (or α_m). Assuming the previous values of V_T and γ as correct, the parameters μ_o and M are iteratively modified until a good fitting is obtained between the theoretical model (7.7) and (7.3) (or (7.2)) and the experimental data. As initial guessed values for the parameters μ_o and M, the ones obtained in steps (I) and (II), respectively, can be used. Since the experimental data are reproduced with a model that depends on several parameters different solutions may be expected. Thus, some tests must be done to validate the solution.

V) Tests of the solution. A) The values of the parameters (μ_o, γ and V_T) and the experimental data are introduced in the compact model (7.7). The $I_D - V_C$ curves at the contact are extracted, and must be consistent with the trends expected by (7.3) (or (7.2)). In case of a negative test, new values of γ and V_T must be proposed in part (IV). B) Parameters M (or $1/R_C$) are represented as a function of V_G. These parameters include information about the free charge density at the contact region. Assuming that the free charge density in the channel and contact appears at the same voltage, the evolution of M (or $1/R_C$ with V_G) must intercept the V_G-axis at the value obtained for V_T. In case of a negative test, a new value of V_T must be proposed in part (IV).

7.7. Results and discussions

To check the validity and applicability of our compact model with contact effects, (7.7) and (7.12), and the extraction method, we analysed published $I_D - V_D$ experimental curves from pentacene-based OTFTs at different conditions. We analysed the effects of temperature, contact length, material length, barrier height at the interface, TC and BC configurations, and linear or non-linear behaviour. We also show a situation in which the parameters R_C or $1/M$ do not follow the trend with V_G indicated in (7.11). This can be typical of OTFTs with trapping effects.

7.7.1. Effects of the size of the structure

Fig. 7.5(a) shows a comparison of experimental data (symbols) with the results of our model (solid lines). They correspond to inverted-staggered OTFTs with thermally evaporated pentacene and Au

Table 7.1: Fitting parameters used with different models to reproduce the data of Fig. 7.5

Model	Ideal	H_{VG} ($V_S = 0$)	H_{VG}	Compact
V_T (V)	-10.31	-0.79	-3.14	-3.14
γ	0	0.49	0.49	0.52
μ_o $(cm^2/V^{1+\gamma}s)$	0.65	-	-	0.09

S/D contacts [298], two different channel lengths (L = 100 and 150 μm) and different thickness of the pentacene semiconductor or contact lengths (x_C = 50, 100 and 150 nm). The whole set of curves is reproduced with our model with the same set of parameters: $V_T = -3.14$ V, $\gamma = 0.59$, $\mu_o = 0.09$ cm^2/V$^{1+\gamma}$s, and $\alpha_2 = 3.9 \times 10^{-8} \times (50\text{ nm}/x_C)$ A/V$^{3+\gamma}$. A convergence test is made to validate these parameters (Fig. 7.5(b)). Combining in (7.7) the above values of μ_o, γ and V_T with the experimental values (I_D, V_D) corresponding to x_C = 50 nm of Fig. 7.5(a), then the current-voltage curves at the contact can be obtained (symbols in Fig. 7.5(b)). In the same figure, the curves $I_D - V_C$ calculated from (7.3) and (7.11) with $\alpha_2 = 3.9 \times 10^{-8}$ A/V$^{3+\gamma}$are shown in solid lines. The matching of the symbols and solid lines indicates that the solution is physically acceptable. Table 7.1 shows the values of the parameters of the model extracted during the different steps of the fitting procedure. The value of the threshold voltage is modified in the different steps. This value depends on the model employed and whether contact effects are included or not. Actually, the value extracted from the H_{VG} is valid only when the averaged contact voltage ($V_S = V_{C_{average}}$) is considered in (7.14). The value of the mobility is also altered during the fitting procedure, from a constant value with the ideal MOS model to a gate-voltage dependent relation modelled by μ_o and γ. In the table, the value of the mobility obtained with the ideal MOS model is greater than the one obtained for μ_o with the compact model. The value of μ_o must be understood as the value of the mobility at V_{GT} = 1 V. The value at V_{GT} = 40 V is μ =0.61 cm^2/Vs. For these samples, the value obtained with the compact model represents an averaged value, since the averaged contact voltage is not too large $V_{C_{average}} \approx -2.4$ V.

The value of μ_o is in agreement with the value reported in [298] for the mobility in the conducting channel, in the range of 0.3-0.5 cm^2/Vs. In [298], the path that the current follows from the top contact down to the conducting channel is modelled with a factor about 3 lower mobility, attributed to an anisotropic mobility. The anisotropic conduction in the contact region and in the intrinsic channel is also compatible with our model. Assuming the same value for the mobility in the contact region and in the conducting channel and introducing the value extracted for α_2 and the geometrical parameters of the OTFTs [298] in (7.3) and (7.11), the free to total charge ratio θ is found to be greater than one. Thus, a lower value of the mobility is necessary to obtain values of θ with a physical meaning. A value around 10^{-4} cm^2/Vs, as provided in [298], results in values of θ in the range $[0.001, 0.0071]$ for gate voltages in the range $[-20, -60]$ V.

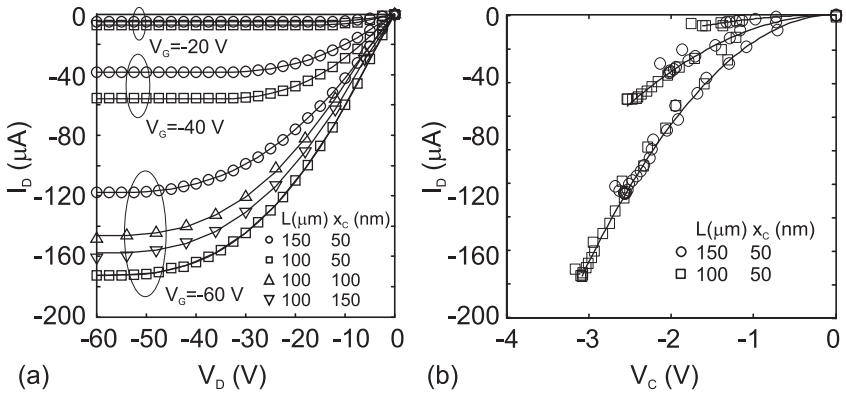

Figure 7.5: a) Comparison of output characteristics measured in pentacene-based OTFTs with Au S/D contacts (symbols) [298] and our numerical results (solid lines). Transistors with different channel length L and organic thickness x_C are studied. b) $I_D - V_C$ curves extracted by inserting in (7.7) the experimental data of Fig. (a) and the fitting values $V_T = -3.14$ V, $\gamma = 0.59$ and $\mu_o = 0.09$ cm^2/V$^{1+\gamma}$s (symbols); and by using (7.3) and (7.11) with $\alpha_2 = 3.9 \times 10^{-8}$ A/V$^{3+\gamma}$ (solid lines).

7.7.2. Transistors with instabilities

Figs. 7.6(a) and (b) show, with symbols, the output characteristics with hysteresis measured in a top gate staggered pentacene OFET with Au S/D electrodes [299]. The gate dielectric is Poly(vinyl alcohol) (PVA), known to produce hysteresis in OTFTs. The dielectric thickness is $t_i = 1\mu$m, the channel length L=100 μm, the transistor width $w = 1$ mm and the organic-film thickness $t_o = 100$ nm. These current-voltage curves in the forward scan (FS) and the backward scan (BS) are compared with the compact model (7.7) in combination with the linear model (7.2). Our numerical results are shown in solid lines in Fig. 7.6(a) and (b). The parameters obtained from the fitting procedure are: $\mu_o = 0.0041$ cm^2/(V$^{1+\gamma}$s), $k_0 = 1.4 \times 10^{-10}$ A/V$^{2+\gamma}$, $\gamma = 0.05$, $V_{T_{FS}} = 5.18$ V and $V_{T_{BS}} = 3.55$ V. The values of $1/R_C$ in (7.2) are represented as a function of V_G for the FS and BS in Fig. 7.6(c). Since the charge density in the contact is proportional to $1/R_C$, this figure shows how the threshold voltages of the charge density in the contact (7.4) coincide with the values of $V_{T_{FS}}$ and $V_{T_{BS}}$ found in the fitting procedure. Thus, the values of the fitting parameters are coherent among themselves and the solution can be considered physically acceptable.

At higher voltages, the evolution of the charge density at the contact deviates from the linear trend. The free charge density usually follows a linear trend with the gate voltage (7.9). However, in situations where instabilities or trapping effects appear in the transistor, the threshold voltage can vary and $\sigma_{channel}$ can deviate from this trend. In cases of slight modifications of the threshold voltage, our model is still valid [296]. Instead of combining (7.7) and (7.12), (7.7) must be combined with (7.2) or (7.3). In these cases, the independent determination of M or R_C for each V_{GS} is preferred to the determination of the compact parameter α_m. We have reported how information of the trapping processes during hysteresis can be extracted with the analysis of the contact region of the transistor [296].

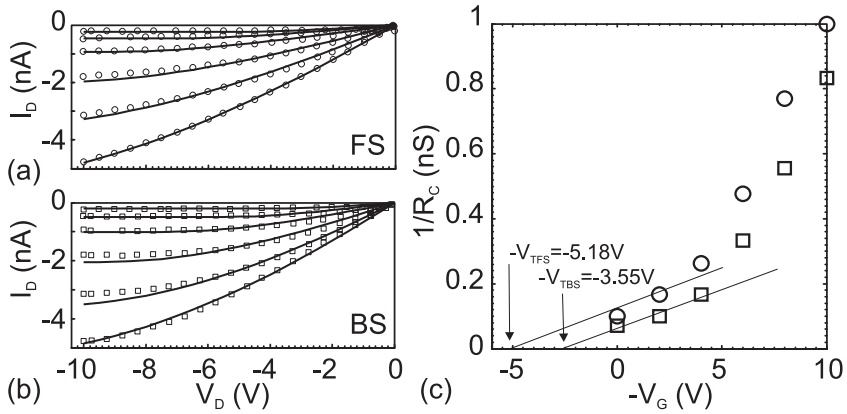

Figure 7.6: (a), (b) Comparison of experimental output characteristics of a top gate staggered PVA / pentacene / Au $OFET$ [299], with our compact model (solid lines). $V_G = 0$ to -10 V from top to bottom with a -2 V step (FS, circles; and BS, squares). (c) Extracted values of $1/R_C$ in the FS (circles) and BS (squares). The extrapolation of the data at low gate voltages intercept with the V_G-axis at points close to $V_{T_{FS}} = 5.18$ V and $V_{T_{BS}} = 3.55$ V.

7.7.3. Effects of the temperature

In Fig. 7.7, we analysed experimental data measured at different temperatures on bottom gate evaporated-pentacene based OFETs with top Au S/D contacts, $L = 100$ μm and $w = 700$ μm [281]. The thickness of the SiO_2 is 270 nm and the pentacene thickness, which is the same as contact length x_C, is 70 nm. The experimental curves have been reproduced with our model with the parameters shown in Table 7.2. On the one side, the variation of the threshold voltage with temperature can be considered large. This variation can be attributed to propagation of errors in the determination of the contact voltage. In any case, the result improves the much greater variation obtained in [281]. Studies focusing on OTFTs without contact effects obtain an even lower variation of the threshold voltage [300]. On the other side, the parameter γ follows the trend with the temperature given in (7.8) with $T_o = 373.8$ K, and μ_o also follows the trend with temperature proposed in expression (15) in [285] with $\sigma_0 = 10^8$ S/cm and $\alpha^{-1} = 0.31$ Å, thus validating our results.

The average contact voltage is estimated from these parameters, resulting in $V_{C_{average}}$ =-1.8, -0.4, -0.1 V at 300, 325 and 350 K, respectively. The contact effects decrease when the temperature increases. Another way to analyse the effects of the contacts with the temperature is by evaluating the surface free-charge density at the contact region. Assuming $V_{SC} = -1$ V in (7.6), the surface concentration of free charges at the contact can be compared with the surface concentration of free charges along the channel. Fig. 7.7(d) shows this comparison evaluated at $V_G = -20$ V. At 350 K the effect of the contact region is almost negligible since the free charge density is almost uniform along the whole structure. However, at 300 K, the free charge density in the contact region is almost four orders of magnitude lower than in the channel.

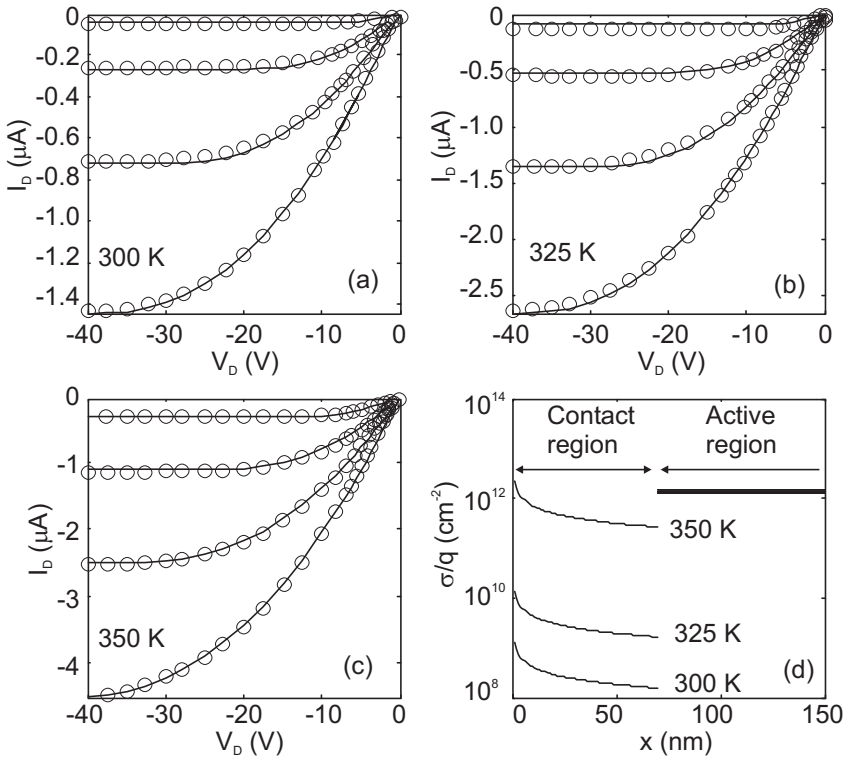

Figure 7.7: (a)-(c) Comparison of experimental output characteristics taken at different temperatures of a bottom gate pentacene based *OFET* with Au top contacts [281] (symbols), with our compact model (solid lines). V_G = -10, -20, -30, -40 V from top to bottom. d) Surface concentration of free charges along the channel of the OTFT at different temperatures for $V_G = -20$ V.

Table 7.2: Fitting Parameters used to reproduced the experimental data of Fig. 7.7.

T (K)	V_T (V)	γ	k_0 (A/V$^{2+\gamma}$)	μ_o (cm^2/V$^{1+\gamma}$s)	α_2 (A/V$^{3+\gamma}$)
300	0.3	0.49	3.4×10^{-10}	0.005	2.4×10^{-9}
325	0.44	0.3	1.3×10^{-9}	0.015	10^{-7}
350	2	0.14	3.4×10^{-9}	0.042	5.0×10^{-6}

7.7.4. Effects of the energy barrier

In Fig. 7.8, we analysed the experimental data measured in a BC pentacene TFT with Au-Pd contacts [274]. The dimensions of the transistor are $L = 10$ μm, w=220 μm, and the gate dielectric is SiO_2 with 290 nm thickness. Fig. 7.8(a) corresponds to the configuration Au-source/Pd-drain, and Fig. 7.8(b), to the configuration Pd-source/Au-drain. The solid lines in both figures show the results of our model using the parameters: $V_T = 16$ V, $\gamma = 0.18$ and $\mu_o = 0.47$ cm^2/V$^{1+\gamma}$s, ($k_o = 5.02 \times 10^{-8}$ A/V$^{2+\gamma}$). The effect of changing the electrode only affects the value of the parameter α_2: $\alpha_2(\text{Au}) = 2.61 \times 10^{-9} A/V^{3+\gamma}$ and $\alpha_2(Pd) = \alpha_2(\text{Au})/5.19 = 5.04 \times 10^{-10} A/V^{3+\gamma}$. However, the use of the classical MOS model to

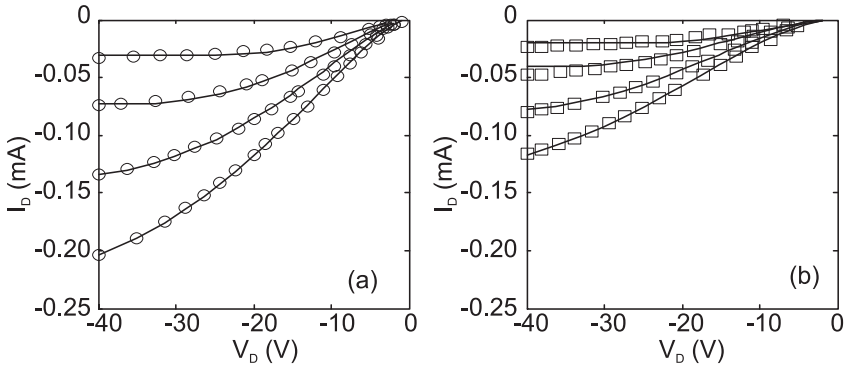

Figure 7.8: Comparison of experimental output characteristics measured in a BC pentacene based $OFET$ with Au-Pd contacts [274] (symbols), with our compact model (solid lines). V_G = -10, -20, -30, -40 V from top to bottom. (a) Au source/Pd drain. (b) Pd source/Au drain.

characterize the transistor in Fig. 7.8 gives different values for the mobility and the threshold voltage: $\mu =$ 0.63 and 0.42 cm^2/Vs and $V_T = 15$ and 14 V for Figs. 7.8(a) and (b), respectively [274]. The importance of using a proper compact model that includes the contact effects of OTFTs is again demonstrated. On average the voltage drop at the contacts is $V_{Caverage} = -9.64$ V.

7.8. Ideas for future work

One of the strengths of our model is the capability to separate the charge density at the contact region from the charge density in the channel. We have seen that changes in the temperature lead to small changes in the free charge density in the channel but large changes in the contact region (Fig. 7.7(d)). Some of the niche applications where OTFTs play an important role are as sensors [301], [302] or photodetectors [56], for example. Monitoring the free charge density in the contact region under the presence of different atmospheres or irradiation might help to explain the sensing characteristics of these devices. In this regard, our model is a potential tool for this task.

In fact, these suggestions agree with recent studies of chemical sensors [302] and phototransistors. [56]. The generation of charges by different physical or chemical mechanisms and the trap charging in the contact regions decrease the contact resistance. The chemical or irradiation effects on the TFT parameters such as the off-current, threshold voltage, bulk mobility, and field-effect mobility can be investigated using our model. A link between the contact resistance and the threshold voltage would open the possibility of designing the source and drain contacts using different metals or incorporating self-assembled monolayers to optimize R_C and maximize the sensing effect in organic TFTs.

Another strength of our model is its applicability to OTFTs that differ in structure and morphology. The parameter α_m added to the generic drift MOS model is enough to quantify the effects of the contacts. One step forward in the improvement of OTFTs would be to find the relation between this parameter and structural variations in the active organic material, such as grain boundaries, interface states or defects. This would help to achieve good reproducibility in the fabrication of OTFTs. We have

seen in this chapter an example of what is found in the state-of-the-art OTFTs: a great variability in the characteristics of similar OTFTs. Until the technology achieves good reproducibility in the fabrication of OTFTs, simple and tunable compact models such as the one presented in this chapter must run in parallel with high accuracy measurements [290], [303].

8

Ferroelectric mechanisms in solar cells

8.1. Introduction

Ferroelectricity is an appealing property for PV applications as it allows the control of the internal electric fields and injection barriers, which lie at the heart of the PV mechanism. When ferroelectric materials are sandwiched between electrodes and illuminated, they can exhibit a variety of rich phenomena including the generation of photo-excited charge carriers. The ferroelectric layer provides a polarization-induced internal electric field, which can help in separating the photo-excited carriers, generating effective built-in fields at the ferroelectric/electrode interface due to Schottky barriers that can deplete the ferroelectric layers, etc. In addition, the ferroelectric materials give rise to unique PV behavior based on atomistic asymmetry of current generation, the bulk PV effect.

The ferroelectric oxides are an intriguing class of photovoltaic materials, known to produce a very high photovoltage, up to orders of magnitude larger than the bandgap, but rather a small photocurrent. Thus, power conversion efficiencies have been orders of magnitude smaller than for classical photovoltaic devices for many decades. However, in recent years there has been a significant enhancement in efficiencies (Fig. 1 in [304]). The most significant advance has been obtained with Bi_2FeCrO_6 (BFCO), which is a multiferroic material yielding a power-conversion-efficiency (PCE) from 3.3 % in single layers to 8.1 % in a multi-absorber system based on BFCO, obtained by stacking three layers with different bandgaps [305].

Building on this success, lower cost materials and device fabrication approaches for high efficiency ferroelectric PV should be developed for practical and reliable applications. Attaining this objective requires an in depth understanding of the operation mechanism of the ferroelectric PV effect in such materials, which in turn will require close collaboration between experiment and theory. A variety of interesting phenomena arise from the photoinduced effects in ferroelectrics, for example, the deformation induced by irradiation of light, which can be explained as the combination of photovoltaic and piezoelectric effects. The better understanding of these mechanisms should be in the focus of the community in order to enhance the performance of ferroelectric solar cells. Nowadays, there is still an intense debate regarding the mechanism which underpins the photovoltaic effect observed in ferroelectric materials and how to improve the power conversion efficiency.

Ferroelectricity is characterized by permanent electric dipoles in the material that remain in the absence of an applied electric field. In contrast to ordinary dipolar polarization, the material is always in a polarized state in which a *remnant polarization* P_r exists even if the applied electric field F is removed. Furthermore, the polarization direction can be reoriented (switched) by an applied field larger than a certain value, which is denoted *coercive field*, F_c. From a theoretical point of view, the ferroelectric polarization affects the transport behavior in semiconductors by means of changes in the band bending and electrical field effects [306–308]. It has been observed in experimental and numerical works [309–311] that polarization-modulated Schottky-like barriers at metal/ferroelectric interfaces produce a switchable rectifying behavior in a ferroelectric thin film. Thus, controlling the polarization with an external field allows electrical tuning of charge transport and hence achieving unidirectional electric conduction.

The electrical current and voltage generated in ferroelectric solar cells has in fact two origins[312]. The first one is the conventional photovoltaic effect (sometimes called barrier photovoltaic effect), as in

classical non-ferroelectric solar cells. It is due to an asymmetry in the real space, but it may be influenced by polarization charges. The second effect is the bulk photovoltaic effect which arises from asymmetries in k-space. In this chapter, we will focus our study on the first origin, the electrical current influenced by the polarization charges. For the sake of clarity, we provide in Section 8.2, a study of the photovoltaic mechanisms in classical solar cells, based on the mechanisms of charge separation and charge collection, which can be obtained with normal non ferroelectric semiconductors. Then, in Section 8.3, we discuss the actual phenomenology of ferroelectric solar cells, including the typical response of the solar cell, as well as the best results obtained so far in terms of performance. Finally, in Section 8.4, we develop a systematic evaluation of the different photovoltaic mechanisms that are influenced by ferroelectric polarization, and we discuss systematic simulations based on numerical modeling to illustrate the effects of these mechanisms.

8.2. Photovoltaic mechanisms in conventional solar cells

A number of general photovoltaic operation principles and general properties of solar cells [313–315] are summarized here for later comparison with the ferroelectric photovoltaic devices (see [304] for a detailed description).

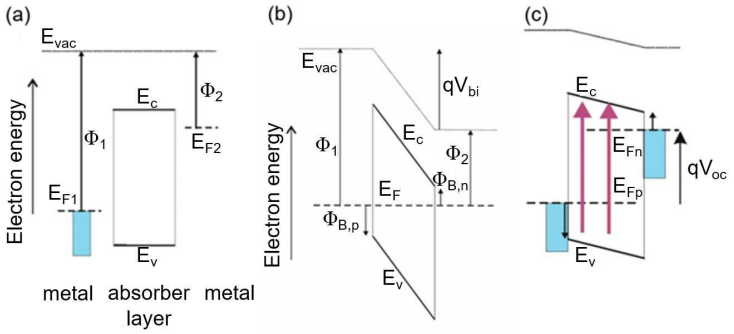

Figure 8.1: Energy diagram for a metal/semiconductor/metal MSM structure. (a) Separate materials, a semiconductor with conduction band edge minimum E_c and valence band maximum E_v, and two contacts with work function Φ_1 and Φ_2. (b) Energy diagram for a MSM after contact of electrode materials, showing the built-in voltage given by the difference in work functions between both metals. (c) Photovoltage under illumination. The Fermi levels are flat, and for each carrier the diffusion current equilibrates the drift current.

The photovoltaic model can be explained with the metal-semiconductor-metal structure of Fig. 8.1a. By simplicity, the semiconductor bands are tilted as in an insulator. In Fig. 8.1a, we represent a light absorbing semiconductor with valence and conduction band edges, E_v and E_c, respectively, that define the semiconductor bandgap $E_g = E_c - E_v$. To produce electricity, the optically active semiconductor layer needs to have suitable contacts. An asymmetry needs to be built in the device that will turn the process of generation of electrons and holes into a photovoltage and photocurrent. This asymmetry is realized by using contacts of different work functions. To simplify the present matter, we show in Fig. 8.1a a simple planar geometry, in which the semiconductor and the metals with work function Φ_1 and Φ_2 are not yet in contact. In Fig. 8.1b, equilibration leads to a common Fermi level E_F. The energy

barrier for electron injection is defined as the difference between the energy level in the semiconductor and the metal, namely $\Phi_{B,n} = E_c - E_{F2}$, and the barrier for hole injection is $\Phi_{B,p} = E_v - E_{F1}$. In the model of Fig. 8.1a, the initial injection barriers of 8.1b are considered fixed, so that no surface dipole is available for the Fermi levels to align. Therefore, the built-in voltage is distributed along the whole absorbing layer, and is given by the difference of work functions:

$$V_{bi} = \frac{\Phi_1 - \Phi_2}{q} \tag{8.1}$$

in terms of positive elementary charge q.

The electric field is related to the electrostatic potential distribution along a device $\Phi(x)$ as

$$\frac{dV}{dx} = -F \tag{8.2}$$

The voltage V, externally applied to the device, creates a separation of the Fermi levels of the contacting materials [316]. If d is the thickness of the semiconductor and if the cathode is at $x = 0$ and the anode at $x = d$, we have

$$qV = E_{Fn}(0) - E_{Fp}(d). \tag{8.3}$$

In the case of MIM, the drift field has the value:

$$F = \frac{V_{bi} - V}{d}. \tag{8.4}$$

Eqs. 8.2 and 8.4 indicate that an applied voltage also corresponds to the variation of VL across the full device thickness. Under illumination, the drift field will be reduced as the Fermi levels of electrons and holes are separated further away from their equilibrium position.

The displacement vector is a fundamental quantity for the description of the semiconductor electrostatics. Such vector contains contributions from the electric field and the polarization vector P. The dielectric displacement vector is given by:

$$D = \varepsilon_0 F + P \tag{8.5}$$

where ε_0 is the vacuum permittivity. The dielectric displacement is related to the free space charge density as

$$dD/dx = \rho_f. \tag{8.6}$$

Combining (8.5) and (8.6) results in

$$\frac{dD}{dx} = \varepsilon_0 \frac{dF}{dx} + \frac{dP}{dx} \tag{8.7}$$

$$\frac{dF}{dx} = \frac{1}{\varepsilon_0}\frac{dD}{dx} - \frac{1}{\varepsilon_0}\frac{dP}{dx} = \frac{1}{\varepsilon_0}(\rho_f + \rho_{pol}) = \frac{\rho_f}{\varepsilon_0} \tag{8.8}$$

where the polarization charge density is

$$\rho_{pol} = -\frac{dP}{dx} \tag{8.9}$$

and $\rho_T = \rho_f + \rho_{pol}$. For the particular case of a semiconductor with space charges, then Eq. (8.8) would read

$$\frac{dF}{dx} = \frac{\rho_T}{\varepsilon_0} = \frac{\rho_f + \rho_{pol}}{\varepsilon_0} = \frac{q}{\varepsilon_0}(p - n - N_A^- + N_D^+ + \rho_{pol}) \tag{8.10}$$

where the space-charge density, $(p - n - N_A^- + N_D^+)$, includes the free electron, n , and hole p densities, the fixed ionized donor density N_D^+ and the acceptor density N_A^-. The total charge density across the semiconductor, ρ_T, also includes the ρ_{pol}. For the general treatment of linear non-ferroelectric dielectrics and ferroelectric materials, the relative dielectric permittivity is defined as

$$\varepsilon_r \equiv \frac{1}{\varepsilon_0}\frac{dD}{dF}. \tag{8.11}$$

Combining Eq. (8.11) ($dD/dx = \varepsilon_0 \varepsilon_r dF/dx$), with Eqs. (8.7) and (8.9), the polarization charge density is related to the free space-charge density as

$$\rho_{pol} = -\frac{dP}{dx} = -\left(\frac{dD}{dx} - \varepsilon_0 \frac{dF}{dx}\right) = -(\varepsilon_r - 1)(\rho_{pol} - \rho_f) = -\frac{\varepsilon_r - 1}{\varepsilon_r}\rho_f. \tag{8.12}$$

From Eq. (8.12), Eq. (8.6) can be written as:

$$\frac{dF}{dx} = \frac{\rho_f}{\varepsilon_0 \varepsilon_r(P, F)} \tag{8.13}$$

where the relative permittivity ε_r is given by the slope of the polarization curve in the linear regime, beyond the coercive field (Eqs. (8.5) and (8.11)), as:

$$\varepsilon_r(P, F) = 1 + \frac{1}{\varepsilon_0}\frac{dP}{dF}. \tag{8.14}$$

In a linear non ferroelectric dielectric, the dielectric polarization is proportional to the electric field F and ε_r is a constant, which can be defined as the effective relative permittivity in absence of spontaneous polarization. Thus,

$$P(F) = \varepsilon_0(\varepsilon_r - 1)F \tag{8.15}$$

and

$$D = \varepsilon_0 \varepsilon_r F. \tag{8.16}$$

In a ferroelectric material, P is not linear with F, exhibiting a hysteresis cycle (Fig. 1 in ref. [317]). For these materials, the relative permittivity follows the general expression (8.14). Depending on the models used for the $P - F$ relation, different effects can be described for a ferroelectric sandwiched between two metal contacts, which will be discussed in detail in subsequent sections. In some cases, the $P - F$ hysteresis cycle is modeled by the switching between two constant values for the polarization when the coercive fields are surpassed. This means that the polarization is spatially independent along the ferroelectric polarization direction with a discontinuity at the contacts. This situation creates polarization-induced surface charges of opposite sign at the contact with the electrodes. Other models

consider that the polarization is electric-field dependent, as shown in Fig. 1 in ref. [317], even at values different from the coercive fields. In this case, the polarization is spatially dependent giving rise to the surface polarization charges plus a non-negligible distribution of polarization charges within the ferroelectric bulk. In addition to the previous electrostatic features, the model of a solar cell requires the knowledge of the charge carrier transport, through the current densities of electrons and holes $J_{n,p}$, which include the drift and diffusion components:

$$J_n = qn\mu_n F + qD_n \frac{dn}{dx} \tag{8.17}$$

$$J_p = qp\mu_p F - qD_p \frac{dp}{dx}. \tag{8.18}$$

Here μ_n and μ_p are the charge carrier mobilities and D_n and D_p are the diffusion coefficients, for electrons and holes, respectively. The diffusion coefficients and the mobilities are connected via the Einstein relation $D_n/\mu_n = D_p/\mu_p = k_B T/q$, where k_B is the Boltzmann constant and T is the absolute temperature. Electron and hole conductivities are defined as $\sigma_n = qn\mu_n$, $\sigma_p = qp\mu_p$. In general the total current density of each type of carrier is directly related to the gradient of their Fermi level as follows

$$J_n = \frac{\sigma_n}{q} \nabla E_{Fn} \tag{8.19}$$

$$J_p = \frac{\sigma_p}{q} \nabla E_{Fp}. \tag{8.20}$$

The total current is:

$$J = J_n + J_p. \tag{8.21}$$

Finally, the continuity equations relate the electron and hole current densities to the charge carrier generation and recombination rates, $G(x)$ and $R(x)$, respectively:

$$\frac{J_n}{dx} = -q[G(x) - R(x)] \tag{8.22}$$

$$\frac{J_p}{dx} = q[G(x) - R(x)]. \tag{8.23}$$

Different expressions for the boundary conditions related to selective contacts are described below:

$$J_p(d) = qS_p\,(p - p(d))\ \ with\ p(d) = N_v exp(-q\varphi_1/kT) \tag{8.24}$$

$$J_n(0) = qS_n\,(n - n(0))\ \ with\ n(0) = N_c exp(-E_G + q\varphi_2/kT) \tag{8.25}$$

$$J_p(0) = -qS_p\,(p - p(0))\ \ with\ p(0) = N_v exp(-q\varphi_2/kT) \tag{8.26}$$

$$J_n(d) = -qS_n\,(n - n(d))\ \ with\ n(d) = N_c exp(-E_G + q\varphi_1/kT) \tag{8.27}$$

where the N_c and N_v are the density of sites for the conduction and valence bands, respectively. The

Table 8.1: Fitting parameters used in the simulations for the metal-ferroelectric-metal.

ε_0 (F/cm)	8.854×10^{-14}	N_D (cm^{-3})	0
$\varepsilon_{\text{ínf}}$	10	N_A (cm^{-3})	10^{18}
$\mu_{p,n}$ (cm^2/Vs)	10	N_c, N_v (cm^{-3})	10^{19}
d (nm)	200	B (cm^3/s)	10^{-6}
Φ_1 (eV)	0.06	E_G (eV)	2
ϕ_2 (eV)	1.4	kT/q (V)	0.026
E_{c0} (eV)	2	E_{v0} (eV)	0
Ψ_0 $(cm^{-4}s^{-1})$	10^{17}	F_c (kV/cm)	100
P_r $(\mu C/cm)$	5	α (cm^{-1})	10^5

remaining two boundary values are related to the local potential $\phi(x)$, represented in Fig. 8.2, and are defined as: $\phi(0) = \Phi_0/q$ and $\phi(d) = V_{bi} - V + \Phi_0/q$. The values of the parameters used in this work for the structure of Fig. 8.2 are shown in Table 8.1.

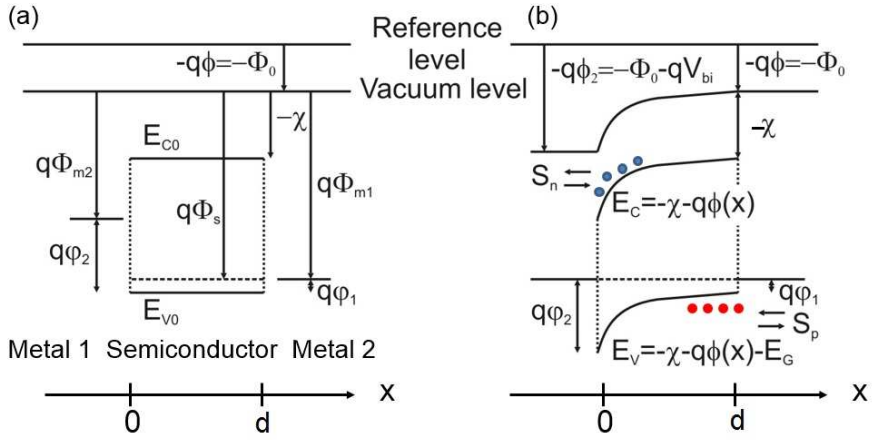

Figure 8.2: Electron energy diagrams of (a) the separate materials of a metal–semiconductor–metal structure and (b) the complete structure in equilibrium with the parameters used in the model for numerical simulation. Metal 1 is the cathode and metal 2 the anode. For the kinetic of the contacts, S_n and S_p are the interface recombination velocities for electrons and holes, respectively.

The main figure of merit of a solar cell for the purpose of solar energy conversion is the current density-voltage ($J-V$) characteristic. From the $J-V$ curve, one can extract an important parameter, the solar to electric power conversion efficiency (PCE, also denoted η) which is the ratio between the maximum generated electrical power and the incident power (P_{in}). The maximum power point (mp) is usually written in term of the open-circuit voltage ($V_{oc} = V(J = 0)$), the short-circuit current density

($J_{sc} = J(V = 0)$), and the fill factor (FF):

$$\eta = \frac{J_{sc} V_{oc} FF}{P_{in}} \tag{8.28}$$

where, FF is related to the voltage and current density of maximum power generation as:

$$FF = \frac{J_{mp} V_{mp}}{J_{sc} V_{oc}}. \tag{8.29}$$

The standard reference for illumination is AM1.5G that simulates solar spectral irradiation with an integrated power of 1000 W m^{-2} = 100 mW cm^{-2} (one sun intensity). Due to the very low efficiency of ferroelectric solar cells, normally the detailed spectral characteristics of incident light are not reported and simply it is labeled as monochromatic, white light or UV light.

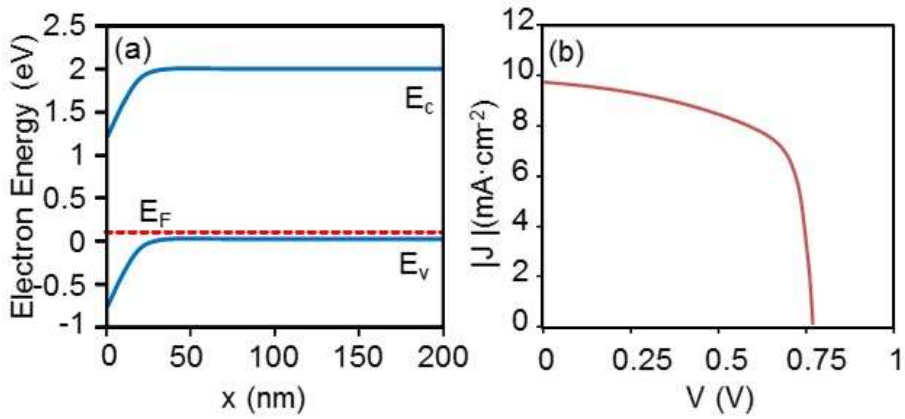

Figure 8.3: (a) Band diagram for a Schottky barrier solar cell in the dark. (b) Corresponding current density-voltage characteristic. The parameters used in the numerical simulation are reported in the Table 8.1.

An important PV model is based on the Schottky barrier formed at the contact. In Fig. 8.3, a p-type semiconductor is shown with an ohmic contact for the majority carriers, at $x = d$, and a rectifying contact for the minority carriers at $x = 0$. The built-in potential of the Schottky barrier in equilibrium is given by the difference in work function between the metal contact, Φ_1, and the one of the semiconductor, $\Phi_{sc} = \Phi_2$, where Φ_2 is the work function of the metal at $x = d$:

$$V_{bi} = \frac{\Phi_1 - \Phi_{sc}}{q} \tag{8.30}$$

It is important to remark that Eq. 8.30 assumes vacuum level alignment after the formation of the interface, that is, all the difference of work functions is established in the semiconductor space charge layer.

Concerning the operation of the Schottky barrier solar cell shown in Fig. 8.3, a simple model approach assumes fast charge separation in the space charge layer (SCL) [318], while in the neutral layer, collection

is determined by the diffusion length as in Gärtner's model [319]. At the rectifying junction, illumination induces a separation of the minority carrier Fermi level from its equilibrium position, which gives rise to the photovoltage. It should be remarked that Schottky barrier solar cells usually exhibit a low fill factor, see Fig. 8.3 b, due to the fact that the increase of forward voltage reduces the extent of space charge layer, increasing recombination exponentially while the photo-generated current drops.

8.3. Phenomenology of ferroelectric solar cells

In this section, we present a general overview of typical PV behavior observed in solar cells made with a ferroelectric semiconductor as the central absorbing material. We describe the actual phenomenology and results that have been generally obtained so far, while specific physical mechanisms and characteristics will be reviewed in the next section.

Figure 8.4 shows typical $J-V$ curves of metal-ferroelectric-metal structure after poling in opposite directions. In general, we define up, upward or positive poling when the remnant polarization points to the top electrode and down, downward or negative poling when the remnant polarization points to the bottom electrode (see Fig. 8.5, and 8.6). The behavior observed in Fig. 8.4a, consisting of a linear $J-V$ plot, is rather characteristic in many ferroelectric materials such as BFO and $BaTiO_3$ [317, 320]. First of all, we remark the total inversion of the $J-V$ curve by poling. This effect indicates that the operation of these cells is very different from the picture established in the classical solar cell, in which each contact has a fixed extraction property for either electrons or holes. Although the contacts in ref. [317] are asymmetric (Pt and Ag), the charge extraction properties of the contacts of these devices are not permanent but can be modified by the applied polarization, as shown in Fig. 8.4a providing a nearly symmetric photovoltages. This is usually explained in terms of a model in which the contact Schottky barriers are modified by poling, as shown in Fig. 8.5 and 8.6, and discussed in section 8.4.2.

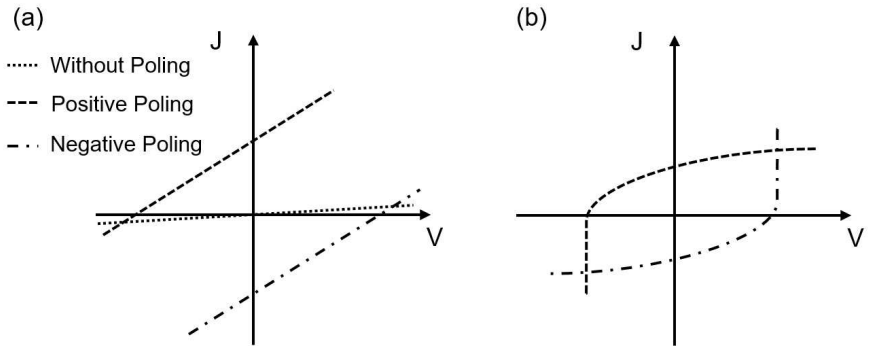

Figure 8.4: Typical $J-V$ characteristics of metal-ferroelectric-metal structure working under illumination conditions: (a)ohmic characteristic and (b) rectifying behaviour as in the cases of refs. [317] and [321], respectively.

This linear characteristic have been observed in many ferroelectric solar cell material, which is in contrast to the exponential diode characteristic that is typical of high performance solar cells. However, in recent years materials demonstrating rectifying behavior have been reported, as shown in the

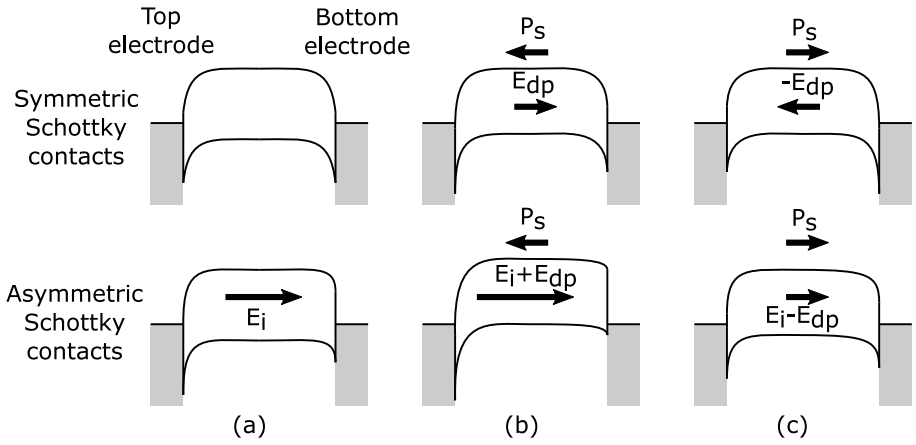

Figure 8.5: (a) Model of Schottky barriers modified by (b) positive or up and (c) negative or down ferroelectric polarization.

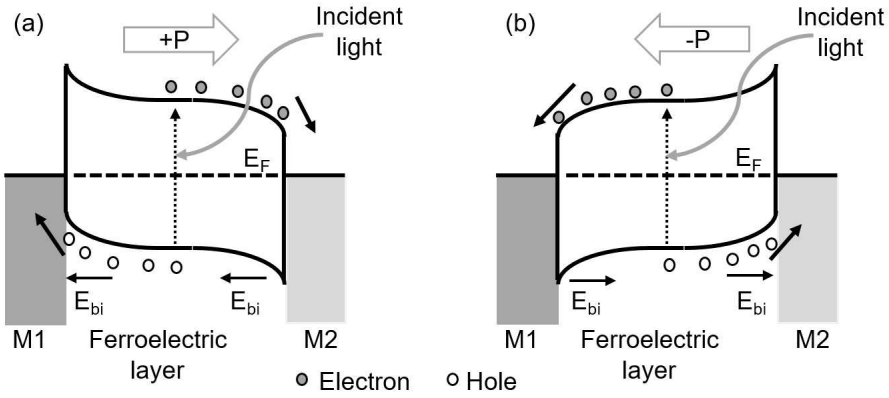

Figure 8.6: Schematic description of the photovoltaic effect in a metal-ferroelectric-metal structure for (a) the upward and (b) downward polarization states. The slope of the band edges at the interfaces can generate a built-in field (E_{bi}). M1 and M2 are the bottom and top metal electrode, respectively.

$J-V$ curves in [321] (schematically in Fig. 8.4b). In addition, the diode characteristic is completely switchable by the applied electric field [322]. Yang et al. [323] showed that the $J-V$ characteristic of $La_{2/3}Sr_{1/3}MnO_3$/BFO/ITO at one sun illumination could be switched by polarization. In the upward direction, the curve is rectifying and the photocurrent is proportional to light intensity, while in the downward state the curve is linear. The photocurrent is always opposite to the polarization direction. These results are explained by a modification of Schottky barriers induced by polarization.

8.4. Ferroelectric mechanisms in solar cell devices

The photovoltaic performance of different materials and their combinations is controlled by a wide variety of properties that must work in a beneficial way. Polarity and ferroelectricity affect fundamental aspects of the operation mechanism, as we have highlighted in the previous section. They modify the

overall energy diagram by affecting the band bending and the surface barriers.

Fig. 8.1 shows the energy diagram of an insulator capacitor with asymmetric contacts, which is also a primitive model of a solar cell. At equilibrium, surface charges are present which are related to the bound polarization charges at the metal-ferroelectric contact as $\sigma_{pol} = P$. Such density of charges can be determined by Eq. (8.7). This charge is partially compensated by free charges accumulated at each contact with surface density $\pm\sigma_{f,eq}$, as depicted in Figure 8.7.

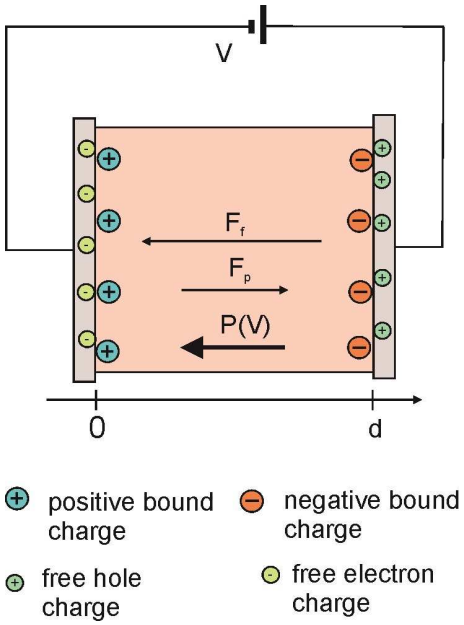

Figure 8.7: Polarization of a dielectric or ferroelectric, indicating the polarization vector P, the electric field due to the bound charge F_p, and the electric field due to the free charge F_f.

In a solar cell device with selective contacts, we define as positive or forward bias a negative voltage applied to the electron extraction contact (right contact in Fig. 8.1b), or a positive voltage applied to the hole extraction contact (left contact in Fig. 8.1b). If electrodes are symmetric, the positive voltage needs to be defined with respect to some geometry consideration, such as top or bottom electrode, as mentioned earlier. The effect of the positive voltage is shown at the right of Fig. 8.1c: it tends to flatten the conduction band, which counteracts the effect of V_{bi}.

8.4.1. Change of injection barriers and depolarization field

The specific mechanism of charge compensation at the external contacts has rather significant consequences for the distribution of electrical field and heights of the injection barriers in a ferroelectric solar cell. For this reason, we consider this point in some detail. When a ferroelectric material has been poled by an applied electric field, the spontaneous polarization, P, needs to be considered in the charge balance, as shown in Fig. 8.7. This polarization is assumed to be independent of the changes of voltage as long as the coercive field is not exceeded. Under a larger voltage, the polarization direction can be

reversed. The positive poling is achieved by applying a reverse bias voltage in excess of the coercive voltage, while negative poling requires a forward voltage. In ferroelectric materials, the asymmetry of the polarization curve is also due to the imprint, that is a preference for one polarized state in the material [324].

For simplicity, we consider a Metal-Ferroelectric-Metal (MFM) junction with symmetric metal contacts having the same work function, see Fig. 8.8. As the central layer is polarized, the vacuum level (VL) is tilted even when the materials are separated, as shown in Fig. 8.8(a). Obviously, if the system reaches equilibrium with flat Fermi level, the VL will be flattened and no electrical field exists within the device. This is because the free charges coming to the electrodes exactly cancel the polarization field F_p. However, one should take into account an important remark in [325]. The polarization bound charge is not located in the metal contact but a distance δ away from it, which may be of atomic dimension. This is due to the fact that ferroelectricity is suppressed gradually and not abruptly at the interface [326]. Therefore, surface dipole layers are formed, as indicated in Fig. 8.8(b) that modify the effective surface injection barriers Φ_B. If originally there is a built-in voltage due to different metal work functions, V_{bi}, it is modified by polarization at each boundary. The modified built-in potential, V'_{bi}, reads:

$$V'_{bi} = V_{bi} \mp \frac{P_s \delta}{\varepsilon_0 \varepsilon_r} \tag{8.31}$$

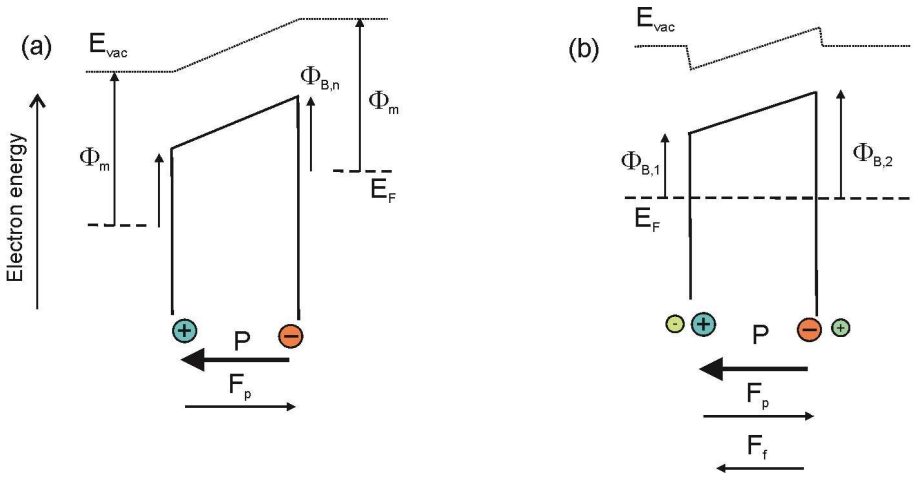

Figure 8.8: (a) Energy diagram of a MFM structure with ferroelectric polarization in the central layer, indicating bound polarization charges at the edges of the layer. Two metals of same work function Φ_m are shown, and also the preliminary height of the electron injection barrier $\Phi_{B,n}$ is represented. (b) In equilibrium, free charges appear in the metals achieving the alignment of the Fermi levels. Dipole layers at the contacts, created by the spatial separation between the bound and the electrode charges, produce modifications of the initial injection barriers. Note that $V_{bi} = 0$ is conserved along the VL.

The modification of the conduction band at a $BiFeO_3$/metal interface can be estimated as $P_s\delta/\varepsilon_0\varepsilon_r 0 = \pm 0.6$ V for $P_s = \pm 65$ μC cm^{-2}, $\delta = 1$ nm, and $\varepsilon_r = 100$ [321]. Fig. 2 in ref. [327] shows how the change of injection barriers due to the inversion of polarization direction well explains the switch of rectification in $J - V$ curves. Using an important PV model [328, 329], we will note that

this is the way in which the surface Schottky barriers are modified by poling.

In the following, we incorporate equations (8.1)-(8.3), (8.5)-(8.23) in a numerical simulator in order to analyze the effects of the modification of contact energetics by polarization. A current-voltage curve for a symmetric ohmic MFM structure with no ferroelectric polarization in the dark is represented in Fig. 8.9(a). As expected, the simulation leads to a linear relation between the current density and the applied voltage. When the ferroelectric layer is polarized, the energy barriers at the contacts are modified accordingly, see Fig. 8.9(b). An effective barrier is developed with a rectifier behavior at the contact on the left when an equivalent volume charge density $\rho_{pol} = P/\delta$ is placed at a distance δ from the interface. A switchable behavior is obtained under the opposite polarization. Although the actual value of V_{bi} is $V_{bi} = 0$, an effective built-in voltage V'_{bi} is created along the MFM structure (compare Fig. 8.9(a) and (b)). The effective V'_{bi} is shifted in the barriers with a value close to the order of $P\delta/\varepsilon_0\varepsilon_r$, as justified by the model of [325]. Fig. 8.9(f) shows the current-voltage curves under illumination. The loop around the origin is created when switching from positive to negative polarization. For the negatively poled samples, the short-circuit current and open-circuit voltage are positive and negative, respectively. After the positive poling, the photocurrent direction is reversed showing the switchable ferroelectric photovoltaic response.

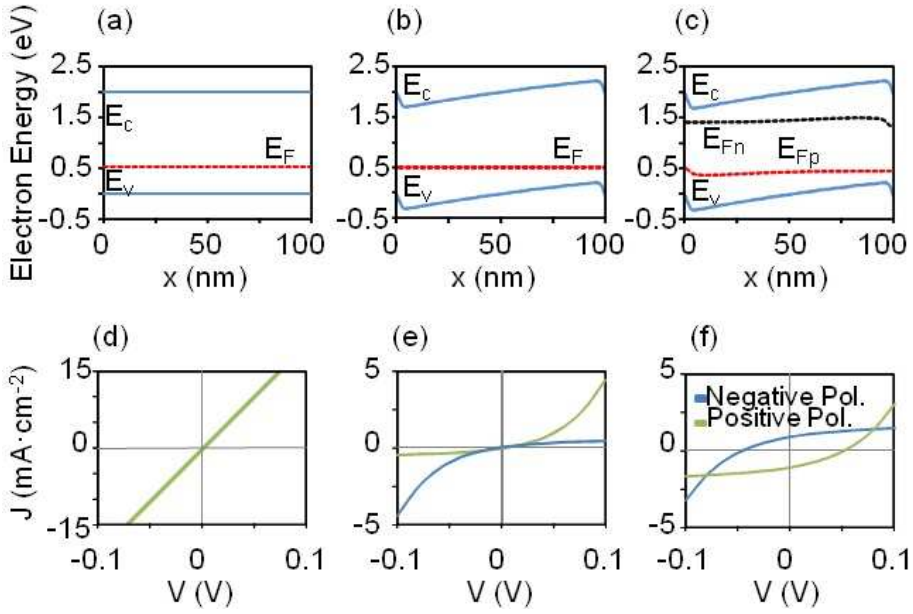

Figure 8.9: Band Diagrams for a symmetric-ohmic MFM structure simulated under (a) no polarization in dark, (b) positive polarization in dark, and (c) positive polarization with illumination. (d)-(f) Corresponding current-voltage characteristics. The MFM is simulated using a doping concentration of $N_A = 10^{17}$ cm^{-3}, and an effective density of states $N_C = 10^{20}$ cm^{-3}, a layer thickness of $d = 100$ nm, $\mu = 1$ cm^2/Vs, $\varepsilon_r = 50$ and $P_r = 6$ μC/cm^2. The ferroelectric effect is modeled with an effective localized charge at the interface related to the bound and screening charges.

As discussed before, the polarization of a ferroelectric layer can be stabilized with compensation charges, i.e. using conducting electrodes as in Fig. 8.7. The bound charge P at the contact with the

electrode, is compensated by the same total charge $-P$ at the electrode surface. The extent to which the charge is spatially distributed at the interface is an important feature for PV properties, as already mentioned in the model of [325]. Another important effect is that the charge in the conducting medium may spread some distance from the interface, according to the screening length of the electrode material, l_s. Then, P is imperfectly screened, leading to a *depolarization field* [330], [331] with value

$$F_{dp} = -\frac{P}{\varepsilon_0 \varepsilon_F} \frac{\varepsilon_F l_s}{\varepsilon_F l_s + \varepsilon_e d/2} = -\frac{P(1-\theta)}{\varepsilon_0 \varepsilon_F} \tag{8.32}$$

where $\varepsilon_e(\varepsilon_F)$ is the relative dielectric constant of the electrode (ferroelectric layer), and θ is the compensation ratio for polarization charge [332]. In the case of metal contacts with different relative dielectric constants ε_{e1} and ε_{e2}, the polarization field is [333] [334]:

$$F_{dp} = \frac{P}{\varepsilon_0 \varepsilon_F} \frac{\varepsilon_F (l_{s1}/\varepsilon_{e1} + l_{s2}/\varepsilon_{e2})}{\varepsilon_F (l_{s1}/\varepsilon_{e1} + l_{s2}/\varepsilon_{e2}) + d} \tag{8.33}$$

where l_{s1} and l_{s2} are the respective screening lengths of the electrodes. Eq.(8.32) reduces to Eq. (8.31) when $\varepsilon_{e1} = \varepsilon_{e2}$ and $l_{s1} = l_{s2}$. The depolarization field always exists in ferroelectrics and is responsible for the instability of the spontaneous polarization. It becomes more important in the case of ultra-thin films (few nm thickness), when these films are fully depleted. This is an important effect in memory applications [335] and many studies indicate that the PV effect in ferroelectric materials is enhanced by the depolarization field which separates charge carriers [336], [337] [338] [339]. [307] showed that for a large dielectric constant material, the screening distance in the electrode material is considerably enhanced which produces larger depolarization field and an increase of PV performance.

8.4.2. Schottky barrier models

It has been widely recognized that the formation of Schottky barriers at the ferroelectric/semiconductor surface has a strong impact on PV properties. The modulation of the depletion width by the ferroelectric polarization was shown by [306]. The state of polarization of the ferroelectric contact layer can control the electronic state of the semiconductor at the surface, from depletion to accumulation [328]. For a polarization parallel to the built-in field, the depletion width is small and the resistance of the diode is low. Many publications have used a PV model based on the modification of the Schottky barriers [340], and demonstrated the control of the depletion regions by altering the polarization conditions [329, 340–342]. The model is also illustrated in Fig. 8.6. For such cases, the current-voltage characteristic deviates from the classical diode like behavior and displays a hysteretic diode like trend, due to the hysteretic nature of the polarization itself, see Fig. 4 in ref. [321]. The large polarization charge detected at the $BiFeO_3$/metal interface significantly modifies the size of the Schottky barrier. Thus, for the upward polarization state, the Pt/$BiFeO_3$ and $BiFeO_3$/$SrRuO_3$ interfaces can have blocking and nearly non-blocking contacts, respectively, as shown in Fig. 8.6a. For downward polarization the role of the barriers is reversed [321].

The characteristics of voltage switching have been amply described in the literature of ferroelectrics.

The polarization of a symmetric Au/BFO/Au sample by [322] produces diode characteristics that are completely switchable under reversal of polarization. The inversion of the diode characteristics depends heavily on the poling temperature. The rectifying characteristics are explained in terms of a reduction of the barrier height by the polarization charge that converts the initial Schottky barrier to an ohmic contact, as mentioned earlier. The migration of positively charged oxygen vacancies is another effect that often plays a dominant role. The migration of vacancies modifies the number of defects in the depletion region and therefore the spatial extent of the depletion, which influences the charge collection effectiveness of the barrier under illumination [323]. It is suggested that migration of oxygen vacancies is a primary mechanism for the switchable PV effect [322, 343].

A series of publications from the 1970's [344, 345] tackled modeling of the effect of ferroelectric polarization on the voltage drop at the ferroelectric/photoconductor barrier. The authors could therefore study the influence of a switch of polarization on the PV performances, usually at short-circuit. Using numerical simulations, we now analyze in more details the Schottky solar cell shown in Fig. 8.3, including the effective polarization charge density at the ferroelectric-metal interface. In the model, we assume an asymmetric MFM structure with an ohmic contact on one side and a rectifier contact on the other side. We solve the Poisson equation in the semiconductor material coupled to the continuity equation that includes drift, diffusion and recombination processes. The polarization charges, including the screening effects, are modelled with fixed effective charges of opposite sign located at a distance δ from both metal-ferroelectric interfaces. They work as an effective dipole.

As shown in Fig. 8.10, the ferroelectric polarization affects the short-circuit current density and the open-circuit voltage in opposite ways. In the case of the negative (positive) poling the effective built-in voltage is higher (lower) than the initial built-in voltage. A higher built-in voltage produces a higher open-circuit voltage. Thus, for negative poling the V_{oc} is higher than the original V_{oc}. The opposite trend is observed with the value of J_{sc}. For negative poling, the injection barrier decreases but the barrier at the extraction electrode increases which hinders the removal of the charge and J_{sc} decreases. In this asymmetric device, no switching behavior is obtained. The positive and negative poling simply modify the degree of asymmetry between the two contacts (a scheme of this idea is displayed in the bottom file of Fig. 8.5 a,b,c). After the modification of the barrier heights with poling, the rectifier and ohmic contacts still play the same role as rectifier and ohmic contacts, respectively.

In order to observe a switching behavior in the $J-V$ curves a symmetric structure must be considered. The band diagram of a symmetric MFM structure with Schottky contacts and no ferroelectric polarization under dark condition at zero applied voltage is represented in Fig. 8.11 a. In this case, the current density both at positive and negative bias voltages is limited by the saturation current of the Schottky diode, Fig. 8.11b. Under positive or negative polarization, the energy barriers are modified, and subsequently, the symmetry of the $J-V$ curve is broken. One contact plays the role of a rectifier contact and the other one acts as ohmic contact (see the top file of Fig. 8.5a,b,c for illustration). The $J-V$ curves for these two poling cases are shown in Fig. 8.11c. When the MFM is illuminated, the $J-V$ curves show a hysteresis loop as depicted in Fig. 8.11d. We conclude here that in a ferroelectric semiconductor device with ideal contacts, the polarization charge would be totally screened and no PV effect at all would exist. However, real materials show a depolarization field, smooth termination

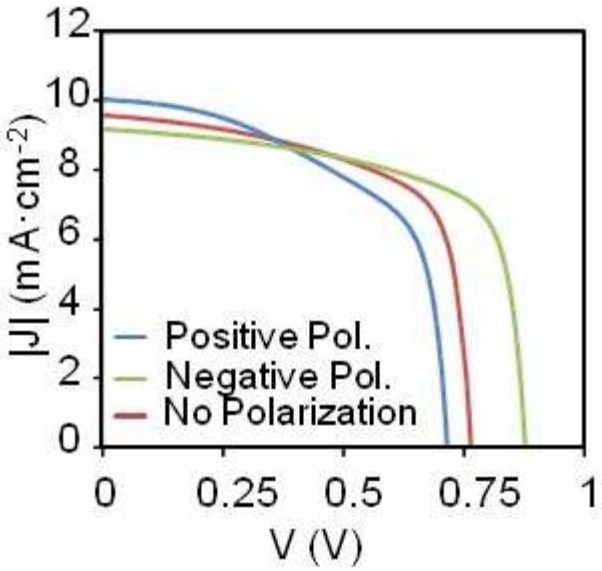

Figure 8.10: Effect of the polarization charge at metal-ferroelectric interface: Current-voltage characteristic in an asymmetric MFM structure under illumination with positive and negative poling and without poling.

of polarization, and other inhomogeneous features as Schottky barriers that do provide the control of interface and bulk electric field by switchable spontaneous polarization.

One should realize that a large part of the reported ferroelectric solar cells have so far been dominated by Schottky barrier effects, while in planar geometry, when the size of the absorber is in the range from several micrometers to much larger (depending on the semiconductor optical absorption coefficient) in order to harvest completely the solar spectrum, then the interfaces cease to play any role in deciding the PV properties. However, in practice to grow micron to more thick film is quite challenging. To the best of our knowledge there is no systematic study on the thickness dependence of the PV effect to discriminate from interface and bulk effects. This seems a potential very interesting research to be done in the future.

8.4.3. Spatially dependent polarization

The effect of considering the hysteresis $P - F$ cycles as the switching between two constant values of the polarization was treated in the previous section. In that case, a constant value of the polarization along the ferroelectric with discontinuities at the contacts was modeled with the effective surface charge at the interfaces. In this section, we analyze the effect of considering the hysteresis $P - F$ cycles as the switching between two polarization states in which $P = P(F) \neq$constant.

The relation between the applied voltage and polarization in a ferroelectric material is obtained by minimizing the total free energy of the system, W, which contains the contributions from the lattice, W_{lat}, and the electronic contribution, W_{el}. There are different approaches to model the polarization-field $(P - F)$ relation. The models based on Landau and Devonshire theories ([346],[347]), make use

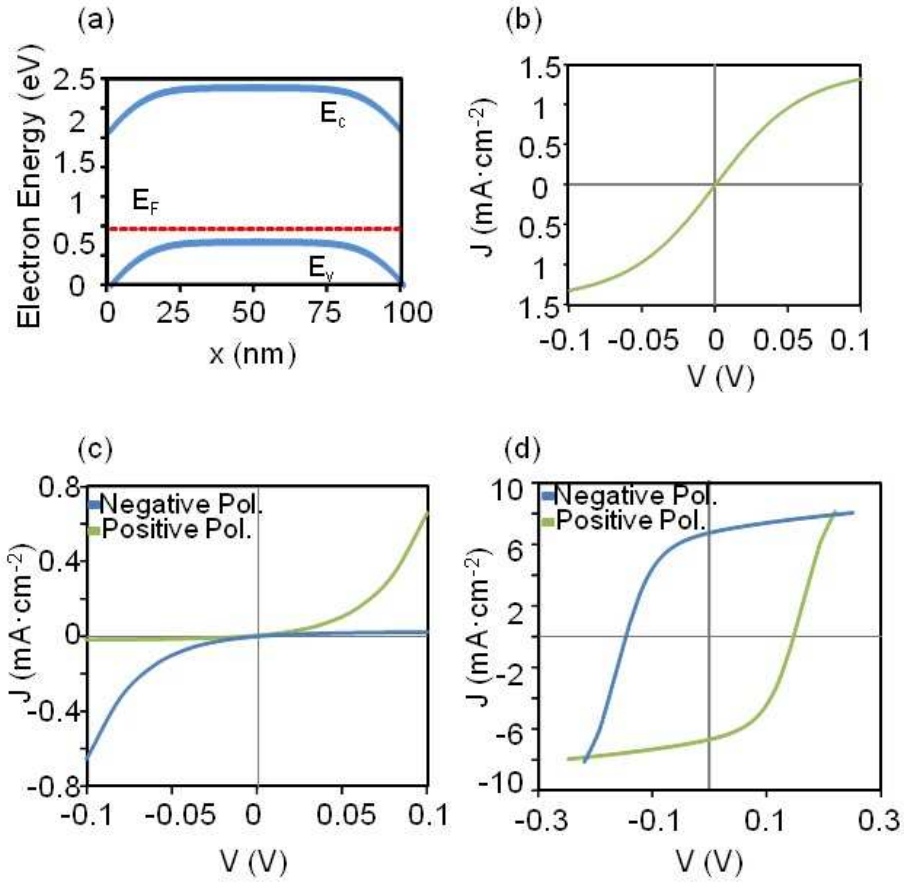

Figure 8.11: (a) Electron energy scheme of a symmetric Schottky MFM structure with the following parameters of the ferroelectric semiconductor: doping concentration of $N_A = 10^{17}\ cm^{-3}$, film thickness of $d = 100$ nm, $\mu = 1\ cm^2/Vs$ and $\varepsilon_r = 10$. The height of the energy barriers at the contacts are considered to be 0.8 eV. (b) Current-voltage characteristic for this MFM structure in dark with no poling effects. The semiconductor is considered ferroelectric (c), (d) Current-voltage characteristics in the MFM structure under positive and negative (c) polarization without and (d) with illumination.

of the relation between the free energy W with the polarization $W(P)$ and relate the electric field and the polarization as $F = dW(P)/dP$ [346], [308]. An approximation of this model is based on the hyperbolic tangent (*tanh*) function [346]. ([348], [349], [350]) also interpreted the device characteristics for ferroelectric devices based on a tanh-function to reproduce the ferroelectric polarization hysteresis. Finally, Preisach's model includes a history-dependent electric field effect [351], [352]. The widely used tanh-function [306], [353] , [350] is given by the expression:

$$P(F) = \varepsilon_0(\varepsilon_{r\infty} - 1)F \pm \tanh\left(\frac{F_c \pm F}{F_c}\right) \tag{8.34}$$

where P_r is the remnant polarization and F_c is the coercive electric field. Eq. (8.34) is an approximation

that considers that the intrinsic polarization in a sample is the superposition of the polarization of all the elementary dipoles [353]. This approach is simple but it models quite accurately the ferroelectric effect on the performance of ferroelectric solar cells. Combining Eqs. (8.14) and (8.34) the relative permittivity is:

$$\varepsilon_r = \varepsilon_{r\infty} \pm \frac{P_r}{\varepsilon_0 F_c} \cosh^{-2}\left(\frac{F_c \pm F}{F_c}\right) \tag{8.35}$$

where the positive sign corresponds to the forward scan and the negative one to the reverse scan. To assess the effect of ferroelectric polarization on the PV performance of solar cells, we apply the previous modeling equations to the Schottky barrier solar cell studied in Fig. 8.3.

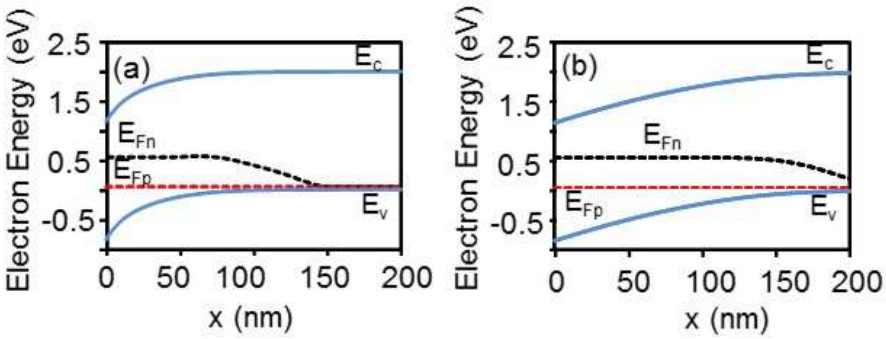

Figure 8.12: Energy diagram along the device of Figure 8.3 and parameters defined in Table 8.1 for an applied voltage of 0.5 V (during the forward scan) and $N_A = 10^{18}$ cm^{-3} (a) without polarization and (b) with polarization. In this example, the device length is $L = 200$ nm and is biased at 0.5 V.

In order to isolate the effect of this phenomenon, the effect of the polarization charges is neglected in a first step, but is incorporated subsequently. Fig. 8.12 represents the energy diagrams along the device without polarization (a) and with polarization in (b), both for a forward scan. The inclusion of the ferroelectric polarization (8.35) in the Poisson equation (8.13) leads to a significant modification in the depletion region of a semiconductor, as shown in Fig. 8.12. In ferroelectric materials, the existence of ferroelectric polarization decreases the total density of charge $\rho_T = \rho/\varepsilon_r$, as inferred from section 8.2, Eqs. (8.9) and (8.13). Thus, the polarization induces a deeper penetration of the electric field within the bulk of the semiconductor and the depletion width increases. According to Eq. (8.14) a large dielectric constant can be obtained at electric fields close to the coercive field F_c, where the slope is very large. Around this value of the electric field, a large depletion region is obtained. The increment of the depletion region with the polarization makes the length and doping of the active layer to play an important role in the device characteristics.

In the last two sections, 8.4.2 and 8.4.3, we have studied separately the contribution of two ferroelectric effects on the performance of MFM solar cells: the polarization charges at the interfaces, which modify the effective injection barriers, and the spatially dependent polarization (or electric field dependent permittivity), which modifies the extension of the effective depletion region in the semiconductor. Now, we study both effects simultaneously in different MFM structures. In an asymmetric MFM solar cell, none of both effects, separately (Fig. 8.10) or simultaneously (Fig. 8.13(a)) allow a switching beha-

vior in the $J-V$ curves. The reason is the initial strong asymmetry of the structure. The existence of negative or positive poling only modifies the value of the effective built-in voltage (high value without polarization), and yet it is not enough to create a switchable behavior (see right column of Fig. 8.5(a,b,c).

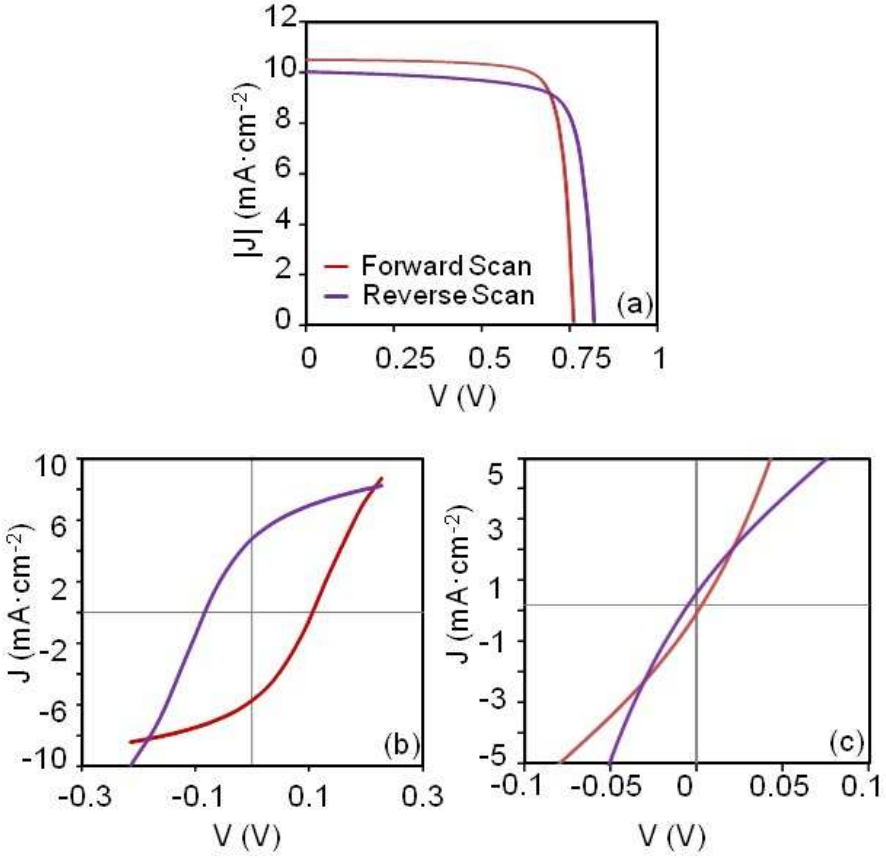

Figure 8.13: Combined effect of the spatially dependent polarization and the polarization charge density at the MF interface on the performance of MFM solar cells, underillumination with positive and negative poling. Current-voltage characteristic in an asymmetric (a) symmetric-Schottky (b) and symmetric-ohmic (c) MFM structure.

In Figs 8.13(b) and (c), we include both effects in the simulation of symmetric-ohmic and symmetric-Schottky MFM diodes. The symmetric-Schottky MFM diode shows a noticeable hysteresis loop in the $J-V$ curves, Fig. 8.13(b), as observed experimentally in the literature. In the case of ohmic-symmetric MFM diodes, surface polarization charges create a small rectifier barrier at one of the contacts. Nevertheless, its effect is diminished by the bulk effects associated to the electric field dependent permittivity in the bulk reducing the hysteresis loop, Fig. 8.13(c).

As a first conclusion, symmetric Schottky MFM structures are thus necessary to obtain a noticeable switchable behavior or a large hysteresis loop in the $J-V$ curves under illumination. A second conclusion

is that both effects associated to the ferroelectric polarization (surface polarization charges or bulk polarization charges) are necessary in order to interpret experimental $J - V$ curves obtained so far.

9

Conclusions

We have developed a model for the charge transport in a symmetric single-carrier metal–organic-metal device that incorporates a mobility model with dependences on the electric field and the temperature. The model describes current-voltage curves that show an ohmic regime and a region controlled by space charge effects. The transition between these regions has not been reproduced previously by using a single physical model. We have described the importance of considering a finite value of the free charge density at the metal–organic interface in the formulation of the model and its results. We have also described a procedure to evaluate the value of this boundary condition at the metal–organic interface.

This model allows for the interpretation of a wide range of experimental data reported in publications from several research groups. We have analyzed experimental data taken in samples of different lengths and measured at different temperatures. From these analyses, we have observed a strong relation between the free charge density at the interface with the current density and the temperature. However, no dependence with the device thickness has been found. We have proposed an empirical expression that relates the charge density at the contact with the current density and the temperature for ITO/CuPc/Al diodes operating in the SCLC regime. This can be a first step towards a compact expression that is valid for other organic material and interfaces.

In addition to the SCLC regime we have studied the ILC regime in a symmetric single-carrier metal–organic-metal device. We have presented a unified procedure to interpret and model current–voltage curves of organic diodes with different barrier heights at the interface and measured under different physical conditions. The procedure is applied to the Ohmic, space-charge and injection limited regimes. The difference between these regimes is the value of the free charge density at the metal–organic interface, which is related to the height of the energy barrier, the organic material, the doping concentration and the temperature. The solution of the transport equations with this proper boundary value for the charge density at the metal–organic interface allows for finding the current–voltage curves of the structure. We have studied the evolution of the free charge density among the Ohmic, ILC and SCLC regimes in different organic materials. This study has led to a compact model between the current density and the free charge-carrier density at the interface. Our procedure can be potentially useful in the characterization of technological aspects and problems that affect the performance of organic diodes and can also be applied to shed light on the contact region of OTFTs.

In this regard, we have provided a simple and fast technique to detect changes in the energy barrier at the interface or the presence of extra generated thermal carriers originating from the modification of the contact region of an organic device. Our method analyzes experimental $J - V$ curves measured in metal–organic contacts, extracts the values of the free charge density at the interface and relates this value with the current density. The evolution of the charge density vs. the current density with the changes of the metal– organic contact allows for detecting the physical origin of these changes. Our procedure has been applied to characterize technological aspects and problems that affect the performance of organic diodes such as the presence of impurities, trapping effects, degradation or surface treatment of the interfaces. We have corroborated our results with more complex experimental techniques and have obtained similar conclusions. In this regard, our procedure provides a quick starting point in the improvement and treatment of the contacts. It defines the initial clues after which more precise and

costly experimental techniques can be employed for further analysis.

In addition to symmetric diodes, we have analyzed asymmetric structures. Analytical and numerical methods have been developed to determine the value of the charge carrier concentration at the charge injecting contacts in both cases as function of the device current density. We have studied the evolution of the free charge density among the Ohmic, ILC and SCLC regimes in different organic materials. This study has led to a compact model between the current density and the free charge-carrier density at the interface. The carrier concentrations at the charge injecting interfaces were extracted from experimental current-density vs. voltage curves, and are power-law functions of the total current density in organic diodes at reverse bias $V < 0$ and at forward bias voltages greater than the built-in voltage $V > V_{bi}$. Under these conditions, the drift charge transport is dominant. The power-law functional relation $p(0) = K_1 J^m$ was verified for symmetric diodes with different injection barriers, and for asymmetric diodes with different built-in voltages and at different temperatures. The exponent in the power law function is around $m \sim 0.75$ for the investigated organic diodes. The proportional constant K_1 in the power law function follows an exponential dependence on the injection barrier.

The carrier-density vs. current-density relation extracted for single-carrier devices has been introduced as boundary condition for the charge at the injecting contacts in the simulation of double-carrier devices, and immediately an excellent agreement has been achieved between the simulated and experimental current-voltage curves of the double-carrier devices. The significance of this characterization-simulation approach is the establishment that the relation between unipolar and bipolar devices is through the charge density at the charge injecting contacts, and the charge density at these interfaces are a power-law function of the total current through the device.

We have completed the study of a metal-organic-metal structure with the incorporation of illumination effects. We have addressed the effect of the boundary values in the simulation of current voltage curves of organic solar cells under illumination. A model for the boundary values of the free charge densities at the anode and cathode interfaces has been proposed. The model is based on the previously developed model for single-carrier and bipolar organic diodes and includes experimental observations made by other authors in OSCs. The model relates the free charge density at the interfaces with the current density flowing through the OSC by means of a power-law function. The power-law function can describe both the injection of charge that occurs at voltages greater than the open circuit voltage as well as the extraction of photogenerated charges at voltages lower than the open circuit voltage. The model includes a set of parameters that take into account the operating conditions and features of the OSCs. The model has been checked in darkness and under illumination conditions. A perfect agreement between experimental data from other authors and our numerical results has been obtained. The model also reproduces anomalous S-shape current-voltage curves, typical behavior of OCSs with blocking contacts and interfaces with low recombination surface-velocities.

To extend the applicability of our study to other devices and physical mechanisms, the work ends with the study of the contact effects in organic thin film transistors (OTFTs) and the study of ferroelectric aspects in solar cells. We have proposed a compact model for the current-voltage characteristics of organic thin-film transistors (OTFTs), which includes the effects of the contact regions.

By carefully inspecting past and current achievements in modeling the contact effects of OTFTs,

we have proposed a model for the current–voltage curves at the contact region that unifies different trends found in experimental data. This model, which is characterized by only one parameter, has been embedded in a generic charge drift model that also includes a gate voltage-dependent mobility. The model is easily reduced to the generic FET model with a constant mobility and no contact effects.

We have proposed a characterization procedure to extract the values of the parameters of the OTFT model, which does not need major reassessment as compared to those for crystalline FETs. We have obtained reliable and good fitting of the TFT generic model to experimental data. We have checked the consistency in the bridge between physical origin of the contact effects and the parameters of the model. The proposed model is a powerful tool to describe the large amount of different structures or fabrication processes the same type organic material in an OTFT can be subjected to. The model captures, in a consistent and relatively simple way, the essential behavior of transistors when temperature, channel length, and width and different energy barriers at the contact region are varied. It also provides information about the free charge density along the transistor channel.

Finally, we have included ferroelectric effects in the physical model of a metal-ferroelectric-metal (MFM) solar cell. Our analyses provide a general picture of the influence of ferroelectric effects on the actual power conversion efficiency of the solar cell device, and we are able to assess whether these effects or their combinations are beneficial or counterproductive. The ferroelectric polarization affects the band bending and the surface barriers. We have analyzed phenomena relevant to device operation: the polarization modulated Schottky barriers at metal-ferroelectric interfaces, depolarization fields, and the switchable rectifying behavior of ferroelectric thin films. From numerical simulation, we concluded that symmetric Schottky MFM structures are necessary to obtain a typical switchable behavior in the current-voltage curves under illumination. Effects associated to both the ferroelectric polarization surface polarization charges and the spatial dependent polarization are necessary in order to interpret experimental current-voltage curves obtained so far.

9.1. Future Work

In this section, suggestions for future work are presented, as a continuation and extension of the research described in this thesis. Some of the applications of this thesis have been recently addressed and even some of them have been published [354].

Modeling Organic Solar Cells under degradation mechanisms as a function of time

Organic solar cells can degrade under illumination as well as in the dark. The degradation of OSCs modifies of the current-voltage $J - V$ characteristics, reducing the efficiency of the solar cell. Many works are devoted to the degradation slowdown of OSCs, testing novel active materials or encapsulation [5]. Other works take advantage from this degradation to make sensors for air, humidity, oxygen, water or other compounds. Different effects have been proposed as degradation mechanisms: the increase of charge trapping in materials and at the contact interfaces, and the change of optical properties. A

simulator that includes these degradation mechanisms would be desired (but not available) to predict the behavior of the solar cell in relation to a wider range of materials and structures. Such a simulator would be very useful in the solar cell design and manufacturing. It should be easy to adapt to new problems and tasks that can arise in the future.

Modeling of Perovskites Solar Cells and Hybrid Solar Cells

The sharply increment of efficiency on perovskite solar cells in these years has captured the attention of the photovoltaic's researchers. To explain the hysteresis of the $J-V$ curves, the experimentally observed giant relative permitivity, and the capacitance measures, new mechanisms have been proposed: the ferroelectricity, the ion migration and trapping and de-trapping of charge. Recently, the ion migration have been proposed as the main mechanism which controls the performance of perovskite solar cells. The ions move while the sweep of the applied voltage takes place to measure a $J-V$ curve. A time dependent simulator of solar cells that explains how the different ions, cations and anions, moves on the semiconductor is essential to understand the experimental hysteresis loops observed in the literature.

Simulation of Multilayer structures

Perovskite solar cells have also emerged as attractive candidates to boost the performance of silicon solar cells in perovskite/silicon multilayer solar cells. Recently, B. Niesen et al. [355] have presented perovskite/silicon tandem cells in the mechanically stacked 4-terminal configuration with efficiencies of up to 25 %. On the other hand, a ferroelectric layer can help to control the performance of solar cells. Thus, the combination of ferroelectric oxide perovskites with conventional (silicon) or emerging (organic, lead halide perovskite) PV technologies would provide a greater performance. This is due to an improved light harvesting, combined with a potentially higher generation yield afforded by the permanent dipole of the ferroelectric material.

10

Resumen en español/Spanish summary

10.1. Resumen

Hoy en día, nuestras necesidades diarias de energía están cubiertas principalmente por los combustibles fósiles. Sin embargo, los combustibles fósiles tienen como hándicap ser un recurso limitado, además de ser la fuente principal de contaminación del medio ambiente. Basándonos en la tendencia de crecimiento de la población mundial junto con un incremento en el uso de los avances tecnológicos, es de esperar que la demanda de energía aumente cada año. Ante este panorama, es necesario buscar fuentes de energía duraderas y renovables.

La energía solar ha sido durante décadas una de las fuentes alternativas de energía más prometedoras. La Tierra recibe aproximadamente 1.74×10^{17} W del Sol, mientras que el actual consumo de energía es de unos 18 TW, es decir, 10.000 veces menos. Esto significa que la Tierra recibe del Sol más energía en una hora que la demanda de energía en un año entero[1]. Entre los diferentes métodos para extraer y convertir la energía solar en eléctrica, las células solares o fotovoltaicas acaparan la atención de muchos investigadores. La intensa investigación en la línea de dispositivos fotovoltaicos ha dado lugar a una extensa variedad de células solares que suelen ser clasificadas por el tipo de capa semiconductora fotoactiva utilizada. Éstas se clasifican en células solares de primera, segunda y tercera generación. Las eficiencias de estas células solares son diferentes y su evolución con el tiempo están recogidas por el Laboratorio Nacional de Energías Renovables (*National Renewable Energy Laboratory* (NREL) [2]). Actualmente, las células solares más eficientes son las de multiunión que alcanzan un 50 por ciento. Las células de la primera generación están constituidas por silicio cristalino (c-Si) o policristalino, (p-Si). La segunda generación está formada por las células solares de lámina delgada, incluyendo las células solares de silicio amorfo (a-Si), de teluro de cadmio (CdTe) y arseniuro de galio (GaAs). Finalmente, la tercera generación engloba a las células solares emergentes. La mayoría de las células de tercera generación no se han comercializado y están en vía de investigación o desarrollo. Esta categoría incluye las células solares orgánicas, de tinta, de puntos cuánticos y de perovskitas. El mercado fotovoltaico está dominado por las células solares de silicio. El silicio es un material abundante en la naturaleza, además presenta unas cualidades eléctricas muy deseables y un amplio espectro de absorción. Sin embargo, el principal problema de las células solares de silicio es el coste de producción debido a importantes requisitos como el uso tanto de salas blancas como de procesos realizados a altas temperaturas. Por esta razón, los precios de la electricidad producida por las células solares son muy altos en comparación con los costes de la energía convencional [3]. Abaratar la electricidad proveniente de células fotovoltaicas es posible a través de un equilibrio entre la eficiencia y los costes requeridos para su fabricación. En este punto, las células solares orgánicas-poliméricas (*organic solar cell*, OSC) son idóneas para el futuro del mercado fotovoltaico ya que pueden alcanzar altas eficiencias de conversión con bajos costes de fabricación [3, 4].

Las células solares orgánicas presentan las ventajas propias de la electrónica orgánica: simplicidad en los procesos de fabricación a bajas temperaturas, la afinidad por alteración química, la flexibilidad, su bajo peso, pueden imprimirse en áreas grandes y su bajo impacto medioambiental. Las células solares orgánicas son compatibles con aplicaciones como la impresión de dispositivos fotovoltaicos en la ropa, su uso en pantallas flexibles o en teléfonos recargables. Esto abre un nuevo abanico de posibilidades que las células solares tradicionales no ofrecen. Sin embargo, los valores actuales de eficiencia están por debajo

de la eficiencia de una célula solar estándar. Otra desventaja es la degradación que sufren las células solares orgánicas debido a la exposición al aire y a la luz, disminuyendo su tiempo de vida media [5]. Para lograr la comercialización de esta tecnología es necesario un esfuerzo conjunto entre desarrollo e investigación para mejorar la eficiencia y el tiempo de vida de estos dispositivos [4, 5].

Una de las regiones más sensibles de una célula solar orgánica es la zona de contacto entre el electrodo metálico y el material orgánico. Por un lado, los contactos controlan el flujo de la corriente. Los portadores que son fotogenerados dentro del semiconductor deben de ser extraídos en la interfaz metal-orgánico. Por otro lado, la región del contacto es altamente sensible a la degradación. La formación de una capa aislante cerca a la interfaz metal-orgánico o el decrecimiento de la velocidad de recombinación en el contacto son efectos desfavorables que reducen la eficiencia de las células solares [6, 7]. Para optimizar el rendimiento de estos dispositivos es requisito indispensable una detallada descripción de los mecanismos físicos que tienen lugar en la estructura metal-orgánico. El modelado y la simulación de estas estructuras son herramientas muy adecuadas para conseguir este objetivo.

El modelado de las células solares orgánicas viene avalado por una extensa experiencia del grupo en el campo de la simulación y el modelado de dispositivos electrónicos orgánicos e inorgánicos. Es de destacar trabajos previos en los que se propuso un modelo unificado para la inyección y el transporte en diodos orgánicos, y son la base del presente trabajo [8–11]. La idea principal de este modelo es que incorpora juntos el arrastre, la difusión, la inyección termoiónica y túnel, y los mecanismos de oxidación y reducción en el estudio de la interfaz metal-orgánico. Este modelo permite relacionar la densidad de carga en la interfaz con el voltaje y la densidad de corriente. Más tarde, este modelo analítico fue incorporado con éxito en un modelo compacto para transistores orgánicos de lámina delgada. El objetivo era caracterizar la regiones de contacto en estos transistores [12–15].

10.2. Objetivos y metodología

El tema central de esta tesis es el modelado y simulación de células solares orgánicas. En general, para modelar la generación y el transporte de carga en células solares orgánicas, la comunidad científica utiliza las ecuaciones de transporte para semiconductores junto con modelos opto-eléctricos. Sin embargo, hay aspectos particulares que difieren entre los investigadores, tales como los modelos utilizados para la generación-recombinación de portadores de carga, para la movilidad, o las condiciones de contorno empleadas para la densidad de carga, siendo este último aspecto el objetivo principal de este trabajo.

La idea fundamental es proponer un modelo que relacione la densidad de carga en la región de contacto con la corriente que circula por dicha región. El objeto del modelo es combinarlo con los modelos eléctricos y ópticos que se emplean en la simulación. Para alcanzar este objetivo se divide el trabajo en retos secundarios con un aumento gradual del nivel de dificultad:

1. Determinación de la condición de contorno para la densidad de carga en la interfaz metal-orgánico. En primer lugar se estudian estructuras metal-orgánico-metal (MOM) donde el transporte de carga es unipolar, para evitar la complejidad del transporte bipolar; los contactos son óhmicos y simétricos para evitar que la corriente esté limitada por el mecanismo de inyección y reducir así el

transporte a procesos de deriva; y en oscuridad para despreciar los fenómenos ópticos.

2. En un segundo paso, se determina el valor de la densidad de contorno para la densidad de carga libre en la interfaz en diodos MOM simétricos con altas barreras. Se analiza cómo afecta la inyección a través de las barreras a los valores de las condiciones de contorno. Se comparan los regímenes de corriente donde la corriente está limitada por inyección (*injection limited current* (ILC)), la corriente está limitada por carga espacial (*space-charge limited current* (SCLC)), o por difusión, y sus efectos en el modelo de la condición de contorno.

3. En tercer lugar, se estudian diodos unipolares asimétricos en oscuridad.

4. Estudio de la conducción bipolar en diodos orgánicos y en células solares orgánicas en oscuridad. Se adapta el modelo para la densidad de carga en la interfaz para esta nueva situación.

5. Finalmente, el modelo se adapta a células solares orgánicas que trabajan bajo iluminación. Se proporciona un procedimiento de caracterización de parámetros del modelo mediante la comparación de datos experimentales con resultados numéricos.

6. El modelo desarrollado para estructuras MOM se aplica en el modelado y simulación de otros dispositivos, en concreto transistores de lámina delgada (*organic thin film transistor*, OTFT). La idea es extender la validez del modelo de la condición de contorno a otros dispositivos orgánicos o afines a estos.

7. Estudio de las células solares ferroeléctricas. Se incorporan al simulador otros materiales y mecanismos físicos, y se comparan los resultados con datos experimentales.

Para llevar a cabo estos objetivos se ha desarrollado en este trabajo un simulador computacional. En este programa se implementan las ecuaciones de transporte junto con los modelos opto-eléctricos y el modelo para las condiciones de contorno. En cada capítulo se detallan los aspectos particulares de cada uno de los pasos mencionados anteriormente.

10.3. Estructura de la Tesis

A lo largo de la memoria, nos centramos en el modelado de los mecanismos físicos en las células solares orgánicas, prestando especial atención al modelado de la región del contacto en estos dispositivos.

Este trabajo se divide en siete capítulos principales a los que da paso esta introducción (Capítulos 2-8). Aunque están escritos en un orden secuencial, cada uno de ellos se puede leer independientemente del resto. Por esta razón la terminología puede cambiar y la notación se define siempre en cada capítulo.

Los primeros cuatro capítulos se centran en el estudio de los mecanismos de inyección y transporte en las estructuras metal-orgánico-metal. Estos capítulos apuntan todos al modelado de las células solares orgánicas, que es el principal objetivo de esta tesis y se trata en el capítulo 6. El capítulo 7 se centra en el modelado compacto de los OTFTs. Aunque el tema puede parecer diferente, el problema de los contactos está presente en ambos dispositivos. El modelo de contacto que desarrollamos en el estudio

de los diodos orgánicos se utiliza dentro de un modelo compacto para TFTs. Finalmente, en el capítulo 8, el simulador numérico se pone a prueba con otro tipo de célula solar: la célula solar ferroelectrica.

En el capítulo 2, se propone un modelo para el transporte de carga en los diodos orgánicos. Este proporciona una explicación física a la región de transición entre los regímenes óhmico y limitado por carga espacial (SCLC). También explica las transiciones internas en el régimen SCLC que tienen lugar cuando se incrementa el campo eléctrico aplicado al dispositivo. El modelo se basa en dos modelos bien asentados: un modelo unificado para la inyección y el transporte de carga en diodos orgánicos, incluyendo una apropiada condición de contorno para la densidad de carga libre en la interfaz metal-orgánico; y un modelo de movilidad dependiente del campo eléctrico y de la temperatura. Se estudian diodos orgánicos con bajas barreras de energía en la interfaz.

Los capítulos 3 y 4 combinan el estudio de las corrientes limitadas por inyección (ILC) y por carga espacial (SCLC). Se analizan diodos que presentan diferentes alturas de barrera de energía. Se propone una unificación de los regímenes de SCLC e ILC a través de un modelo que relaciona la densidad de carga de la interfaz con la corriente que circula a través de ella. A altas densidades de corriente, el modelo de la densidad de carga en la interfaz sigue una función potencial con la densidad de corriente. El modelo unificado permite la caracterización de contactos metal-orgánicos sujetos a diferentes tratamientos tecnológicos controlados o a diferentes procesos de degradación. Este modelo para la condición de contorno es el primer paso para introducir los efectos de contacto en la simulación de dispositivos orgánicos más complejos.

En el capítulo 5 se estudian las condiciones de contorno para la densidad de carga en los contactos metal-orgánico para diodos orgánicos tanto simétricos como asimétricos con conducción unipolar y bipolar. A partir de un análisis de curvas experimentales de corriente-tensión, se propone un modelo analítico que relaciona la densidad de carga en los contactos con la densidad de corriente. Se detalla como el modelo que relaciona la densidad de carga en la interfaz metal-orgánico y la corriente, extraída a partir del análisis de diodos unipolares, puede ser utilizada como condición de contorno para dispositivos bipolares.

En el capítulo 6, se adapta el modelo de la condición de contorno, inicialmente desarrollado para diodos unipolares y bipolares, a las células solares orgánicas. El modelo recoge información sobre los efectos ópticos y eléctricos en las células solares orgánicas. La verificación de este modelo se ha hecho mediante la comparación de datos experimentales con resultados numéricos. El simulador numérico empleado para este fin combina el método de la función de transferencia para el estudio de la propagación óptica, la teoría de Onsager-Braun para describir la disociación del excitón y las ecuaciones de transporte de arrastre y difusión junto con el modelo para la condición de contorno.

En el capítulo 7, se aplica el modelo de corriente-tensión, inicialmente propuesto en diodos unipolares, en el modelado de transistores orgánicos de lámina delgada (OTFT). El modelo que relaciona la corriente en el transistor con el voltaje de caída en los contactos se introduce en un modelo analítico para curvas de corriente-tensión para OTFTs. El modelo compacto resultante permite interpretar anomalías en curvas de corriente-tensión en OTFTs producidas por la región de los contactos.

En el capítulo 8, se incluyen efectos ferroeléctricos en el modelo físico de la célula solar. La idea es extender la validez del simulador a otro tipo de células solares como es el caso de las células solares ferro-

eléctricas. En el simulador se incorporan nuevos materiales y nuevos mecanismos físicos y los resultados se comparan con datos experimentales. En las simulaciones se estudian los efectos ferroeléctricos asociados tanto a las cargas de polarización superficiales como a la dependencia espacial con la polarización. Se verá como ambos efectos son necesarios para interpretar curvas de corriente-tensión experimentales.

Al final de la memoria están las conclusiones y las recomendaciones para trabajos futuros.

10.4. Conceptos generales usados en la tesis

En esta última sección del capítulo introductorio, se presentan una serie de conceptos básicos que se tratan en esta tesis. Están relacionados principalmente con la conducción eléctrica de los semiconductores orgánicos y ayudan a entender los mecanismos de transporte en las células solares orgánicas.

10.4.1. Semiconductor Orgánico

La electrónica orgánica es un complemento muy prometedor a la tecnología del silicio, pues extiende las aplicaciones de la electrónica al campo de las grandes áreas, superficies flexibles y de bajo coste. Todo ello gracias a procesos de fabricación relativamente sencillos realizados a baja temperatura. La principal desventaja de los materiales orgánicos es el bajo valor de la movilidad de los portadores de carga.

Los semiconductores orgánicos están basados en el carbono junto a un cierto número de grupos funcionales que se encuentran adheridos a éste. La conductividad en los semiconductores orgánicos depende de la conjugación, o alternancia de enlaces simples y dobles entre los átomos de carbono. Esto origina la deslocalización de carga dentro de una molécula, permitiendo el movimiento libre de los electrones en la misma. Basándose en la longitud de conjugación, los semiconductores orgánicos pueden ser clasificados en dos grupos: de pequeña molécula, o semiconductores orgánicos y los semiconductores de polímeros. Los semiconductores poliméricos están constituidos por una larga cadena de moléculas pequeñas similares. Estos tienen una gran longitud de conjugación, al contrario que los semiconductores de pequeña molécula, que tienen una longitud pequeña. Ambos tipos presentan unas características eléctricas muy similares, por ello que se estudian juntos.

A pesar de la buena conducción dentro de la molécula, los semiconductores orgánicos (de aquí en adelante, utilizaremos orgánicos para referirnos a orgánicos y a poliméricos) están formados por un sistema de moléculas y la conducción entre diferentes moléculas por todo el material depende no solo del movimiento de la carga dentro de cada molécula sino también de la transferencia de carga entre moléculas. Las moléculas orgánicas están enlazadas por fuerzas débiles de Van der Waals, y por tanto, la transferencia de carga entre moléculas no es tan sencilla como en un cristal covalente.

Transporte en Semiconductores Orgánicos

En general, los semiconductores orgánicos están constituidos por dos grupos de niveles energéticos "bandas de energía" comúnmente caracterizadas por: el orbital molecular de mayor energía (*highest occupied molecular orbital (HOMO)*) y el orbital molecular de menor energía (*lowest unoccupied molecular*

orbital (LUMO)). Por analogía con los semiconductores inorgánicos, el HOMO y el LUMO están asociados respectivamente al máximo de la banda de valencia y al mínimo de la de conducción. El HOMO y el LUMO están separados por una región energética no permitida "bandgap" de anchura típica entre 2 y 3 eV. Se puede conseguir una transición electrónica entre estos dos niveles por la excitación con luz (radiaciones del espectro visible). Esto hace que los semiconductores orgánicos sean apropiados para aplicaciones fotovoltaicas.

La validez de la teoría de bandas (Figura 1.2 (b)) está abierta a debate [16]. Una mejor aproximación para la conducción en los semiconductores orgánicos es el transporte por efecto túnel asistido térmicamente (hopping) sobre las barreras entre moléculas entre diferentes grupos de estados localizados [17] (Figura 10.1 (a)). La teoría de percolación o de hopping se utiliza para describir el comportamiento de estos dispositivos [16]. Una de las evidencias principales de que el transporte es vía hopping es el hecho de que la movilidad depende del campo eléctrico y está activada térmicamente. Este tema se abordará con más profundidad en el Capítulo 2.

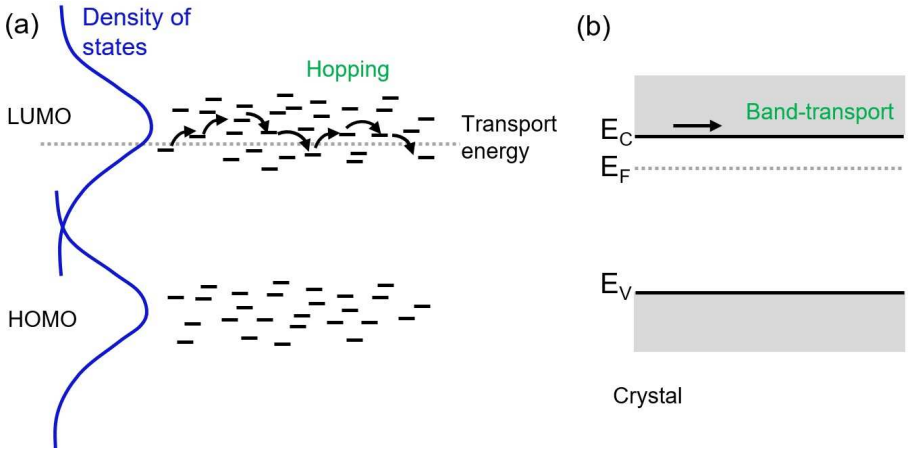

Figure 10.1: (Tipo-n) Modelos de transporte. a) Conducción por hopping/percolación que consiste en saltos (efecto túnel asistido térmicamente) de un estado localizado a otro dentro de una distribución Gaussiana de estados de energía en el LUMO para los electrones y en el HOMO para los huecos. Los portadores de carga inyectados (o fotogenerados) pueden ser generados a altas energías, seguida por una relajación de portadores de carga a la energía de transporte de cuasi-equilibrio. El transporte de la carga en estado estacionario tiene lugar alrededor de la energía efectiva de transporte, que depende principalmente de la temperatura y el desorden. A bajas temperaturas, los portadores de carga se relajan a los estados más profundos y permanecen atrapados. b) Teoría de bandas. En este caso, el transporte tiene lugar en la banda de conducción, E_C, (para los electrones) y en la banda de valencia, E_V, (para los huecos). La línea discontinua es el nivel de Fermi E_F.

Mecanismos de inyección y Extracción de Carga

La inyección y la extracción de carga a través de una interfaz metal-orgánico están presentes en cualquier dispositivo orgánico y en las células solares orgánicas sin excepción. La corriente que fluye a través de esta interfaz es el resultado de diferentes factores tales como la altura de la barrera de inyección, el campo eléctrico, la temperatura, reacciones químicas que dan lugar a dipolos interfaciales, y la curvatura de bandas o el bloqueo (pinning) del nivel de Fermi (Chapter 3). Para pequeñas barreras, los

contactos no imponen restricción al flujo de la corriente. El comportamiento del dispositivo está limitado por el transporte en el volumen del semiconductor orgánico. En este caso, la corriente está limitada por la carga espacial y sigue la típica dependencia cuadrática con el voltaje dada por el modelo de Mott-Gurney [8, 18]. En el caso opuesto, que corresponde a altas de barreras de energía, el comportamiento está principalmente limitado por la inyección a través de la barrera. En este caso se dice que la corriente está limitada por los mecanismos de inyección. Los modelos de inyección tradicionales son el modelo de emisión termiónica empleado para bajas barreras y el modelo de inyección por efecto túnel Fowler-Nordheim para altas barreras.

10.4.2. Células Solares Orgánicas

Una célula solar típica es una estructura multicapa con un electrodo transparente y conductivo (generalmente un ánodo de ITO), un substrato transparente, una capa de transporte por huecos o bloqueador de electrones (tales como PEDOT: PSS), una capa activa orgánica (monocapa, bicapa o una heterounión distribuida (mezcla)) y un cátodo (típicamente de Al o Ca/Al). El comportamiento general de las células solares es el siguiente (Fig. 10.2). La luz (1), entra a través de un sustrato transparente, y se propaga en la estructura de la célula solar orgánica, los electrones absorben la energía y generan excitones (2) (pares electrón hueco excitados ópticamente). El potencial de energía almacenada no es suficiente para disociar inmediatamente los excitones en pares electrón-hueco. Algunos excitones se pierden por recombinación y otros se difunden (3) hasta que encuentran un punto de disociación (generalmente una región con alto campo eléctrico o en la interfaz entre dos materiales diferentes), donde los electrones y los huecos generados se separan (4). Estas cargas separadas son transportadas en direcciones opuestas hacia sus respectivos electrodos (5) donde ellos son extraídos (6).

Arquitecturas de Células Solares Orgánicas

La primera generación de células solares orgánicas se basaba en una capa activa. Este tipo de célula solar está formada por una capa de semiconductor orgánico entre dos metales con diferente función trabajo. La Fig. 10.2 (a) muestra el diagrama de energía con los diferentes mecanismos que tienen lugar en una célula solar mono-capa. En esta configuración, uno de los contactos es óhmico y el otro es un contacto Schottky. El contacto Schottky crea un fuerte campo eléctrico cerca del contacto, que es capaz de disociar excitones. En este dispositivo, la eficiencia de conversión de energía es muy pobre. Este hecho fue subsanado en la segunda generación de células solares orgánicas basadas en una estructura bicapa (Fig. 10.2 (b)).

La idea fundamental que subyace en la bicapa es la de crear una interfaz entre dos materiales (donde uno de ellos es donador y el otro aceptador) donde la disociación del excitón es más eficiente. La eficiencia de la célula solar orgánica bicapa es todavía baja debido a la alta tasa de recombinación del excitón, que se atribuye a la pequeña longitud de difusión del excitón en los semiconductores orgánicos (de aproximadamente 10 nm). La eficiencia fue mejorada con la introducción de las células solares de mezcla (Fig. 10.2 (c)), en la que la fases de donador y aceptador están mezcladas a lo largo de toda la capa fotoactiva. Estas interfaces distribuidas pueden ayudar a que los excitones se disocien antes de que

la recombinación tenga lugar.

La figura 10.2 muestra el diagrama de energía de los principales mecanismos que aparecen en las células solares orgánicas (a) mono-capa, (b) bicapa y (c) de mezcla. Todas estas arquitecturas establecen la base para el diseño de nuevas estructuras, tales con las células solares pseudo-bicapa [19] o el test de diferentes morfologías. Hay trabajos donde se han propuesto diferentes texturas y geometrías para mejorar las propiedades ópticas del dispositivo [20, 21]. En la búsqueda de una óptima célula solar de mezcla, hay investigadores que se centran en diferentes métodos de mezclar los materiales donador y aceptador, evitando la creación de "islas" de un material alrededor del otro. Estas inclusiones pueden actuar como centros de recombinación de trampas de carga que puede influenciar en la densidad de carga local y el transporte de la carga.

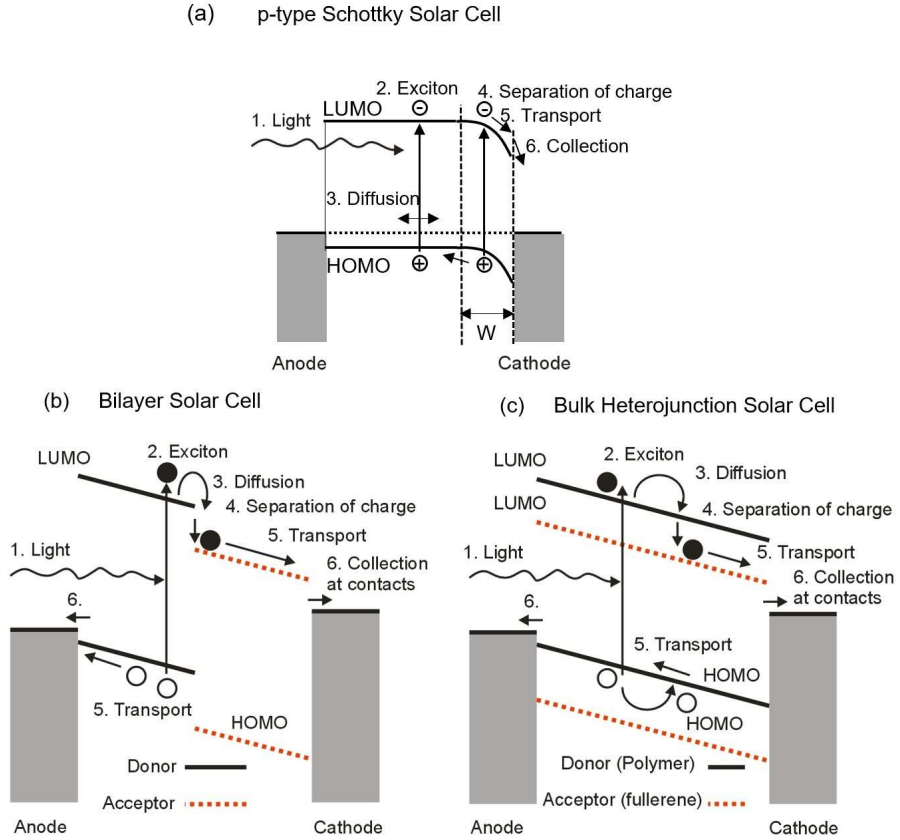

Figure 10.2: Diagrama de energía y los principales mecanismos físicos que tienen lugar en células solares(a) monocapa, (b) bicapa y (c)de mezcla.

Modelos Numéricos

Para comprender y describir el funcionamiento de las células solares orgánicas, en la literatura se encuentran diferentes modelos físicos. Los simuladores numéricos de células solares orgánicas consideran los principales mecanismos físico-químicos que gobiernan el comportamiento del dispositivo. Hay

una gran cantidad de trabajos excelentes que centran su atención en entender cada mecanismo y las interacciones que tienen lugar entre estos. Estos mecanismos pueden clasificarse en tres grupos: ópticos, eléctricos y opto-eléctricos.

Los mecanismos ópticos consideran la luz como una onda electromagnética que sufre reflexiones, refracciones e interferencias en una estructura multicapa. Generalmente, estos mecanismos se modelan a través del uso del método de la matriz de transferencia (*Transfer Matrix Method* (TMM))[22–26], que se caracteriza por su bajo coste computacional y porque sus resultados reproducen con bastante fidelidad los datos experimentales. Otros trabajos utilizan el método de elementos finitos (*finite element method* (FEM))[21, 27] para solucionar las ecuaciones electromagnéticas en la estructura completa. El uso de TMM y FEM, acopladas a las ecuaciones de arrastre-difusión permite, entre otras cosas, estimar los espesores óptimos para la capa activa [21, 24–27]. Los modelos ópticos proporcionan de cómo salida la tasa de generación de excitones, que se usa como parámetro en los modelos opto-eléctricos.

Los modelos opto-eléctricos tienen en cuenta los procesos que tienen lugar desde la creación hasta la disociación de los excitones en la interfaz donadora-aceptadora de las células solares orgánicas [28, 29]. Estos incluyen la formación, recombinación y disociación del excitón. En general, los modelos están basados en la teoría de Onsager-Brown [30], [31], ya que facilita una expresión analítica. Estos modelos determinan el valor de la densidad de carga libre que aparece después de la disociación de excitones que se incorpora después al modelo eléctrico.

Los modelos eléctricos completan el conjunto de modelos necesarios para la simulación de células solares orgánicas. Estos simuladores permiten calcular curvas características de corriente-tensión. En las publicaciones se puede encontrar dos tipos de modelos computacionales: el de deriva-difusión (*drift-diffusion* (DD)) y el modelo de Monte Carlo (MC) [32]. La principal diferencia es que las ecuaciones de DD se centran en las cantidades macroscópicas, mientras que el modelo de MC se centra en el comportamiento de la partícula a nivel microscópico [33], o del estudio realista de las morfologías de mezcla [34].

La técnica de DD se usa de forma generalizada en el modelado de dispositivos semiconductores sobre una geometría genérica de 1, 2 o 3 dimensiones. Muchas publicaciones tratan el transporte de la carga en células solares orgánicas utilizando el modelo de DD. Este método se emplea para simular los dispositivos orgánicos y fotovoltaicos y permite estudiar, entre otros factores, la influencia del nivel de dopado [35, 36], temperatura [37], tipo de recombinación, trampas [38], carga espacial, tiempo de vida y/o movilidad [39, 40] sobre el rendimiento de las células solares orgánicas. También hay modificaciones de las ecuaciones de DD para investigar el impacto de la morfología de la interfaz y de la disociación del excitón sobre la eficiencia del dispositivo [41].

El modelo DD engloba el sistema de ecuaciones diferenciales de Poisson, de deriva-difusión y las ecuaciones de continuidad. En este trabajo, se utilizan ecuaciones de DD. Sus requisitos computacionales son bajos, sus resultados numéricos proporcionan una buena concordancia con los datos experimentales, y además ofrecen estrategias para mejorar la eficiencia del dispositivo. El uso del modelo de DD en células solares orgánicas se combina con una aproximación, comúnmente llamada, enfoque del medio efectivo, en el que la mezcla de materiales donador-aceptor se trata como un material nuevo efectivo [42, 43].

Modelo Compacto

Para acelerar el tiempo de coste computacional se recomienda el uso de modelos compactos. Un modelo compacto se define mediante tres partes importantes: una expresión analítica que describe la característica corriente-tensión, un procedimiento de extracción de parámetros con un intervalo definido de valores de parámetros físicos significativos y una etapa final de verificación del modelo propuesto.

Hay dos tipos de modelos compactos, modelos que son descritos a través de un modelo de circuito equivalente [44], y otros extraídos a partir de la solución analítica de las ecuaciones de DD utilizando aproximaciones específicas [45, 46]. En este último grupo, hay diferentes estudios analíticos que describen las características $J - V$ en células solares de mezcla [42, 47, 48]. Se diferencian por el tipo particular de aproximación empleada, como el perfil espacial de generación [47, 49], el modelo de recombinación [45, 48, 50], el modelo de disociación de pares electrón-huevo, o un modelo particular de atrapamiento de carga. En general, estos modelos son una herramienta muy deseable y útil para el diseño y la optimización de células solares orgánicas sin tener que lidiar con las complejidades computacionales de la simulación numérica [48, 50].

10.5. Conclusiones

A lo largo de esta tesis se han llegado a las siguientes conclusiones recogidas en esta sección:

Se ha desarrollado un modelo para el transporte de carga en diodos metal-orgánico-metal simétrico con conducción unipolar, que incorpora un modelo de movilidad con dependencia con el campo eléctrico y la temperatura. El modelo describe las curvas de corriente-tensión que muestran un régimen óhmico y una región controlada por efectos de carga de espacial. La transición entre estas regiones no se había reproducido anteriormente mediante el uso de un único modelo físico. Se destaca la importancia de considerar un valor finito de la densidad de carga libre en la interfaz metal-orgánico en la formulación del modelo y sus resultados. También hemos descrito un procedimiento para evaluar el valor de esta condición de contorno en la interfaz metal-orgánico.

Este modelo permite la interpretación de una amplia gama de datos experimentales publicados por varios grupos de investigación. Se han analizado datos experimentales tomados en muestras con diferentes longitudes y medidos a diferentes temperaturas. A partir de estos análisis, se ha observado una fuerte relación entre la densidad de carga libre en la interfaz con la densidad de corriente y la temperatura. Se ha propuesto una expresión empírica que relaciona la densidad de carga en el contacto con la densidad de corriente y la temperatura en diodos de ITO/CuPc/Al que operan en el régimen de carga espacial. Esto fue un primer paso hacia una expresión compacta válida para otros materiales orgánicos e interfaces.

Además del régimen de carga espacial se ha estudiado el régimen limitado por corriente en un diodo unipolar simétrico. Se ha presentado un procedimiento unificado para interpretar y modelar las curvas de corriente-voltaje de diodos orgánicos con diferentes alturas de barrera en la interfaz y medidos ante diferentes condiciones físicas. El procedimiento se aplica a distintas regiones: óhmicas y de corriente limitada por carga espacial o por inyección. La diferencia entre estas regiones es el valor de la densidad

de carga libre en la interfaz metal-orgánico, que está relacionada con la altura de la barrera de energía, el tipo de material orgánico, la concentración de dopado y la temperatura. La solución de las ecuaciones de transporte junto con este valor apropiado para la densidad de carga en la interfaz metal-orgánico permite obtener las curvas de corriente-tensión del dispositivo. Se ha estudiado la evolución de la densidad de carga libre en diferentes materiales orgánicos y diferentes tipos de contactos. Este estudio ha dado lugar a un modelo compacto entre la densidad de corriente y la densidad de portadores de carga libres en la interfaz metal-orgánico. Nuestro procedimiento puede ser potencialmente útil en la caracterización de los aspectos tecnológicos y los problemas que afectan el rendimiento de los diodos orgánicos y también se pueden aplicar para comprender la zona de contacto de los transistores orgánicos de lámina delgada OTFTs.

En este sentido, se ha propuesto una técnica simple y rápida para detectar cambios en la barrera de energía en la interfaz o de la presencia de portadores adicionales a los térmicos procedentes de la modificación de la región de contacto de un dispositivo orgánico. Nuestro método de análisis de curvas $J-V$ experimentales medidas en los contactos metal-orgánicos, extrae los valores de la densidad de carga libre en la interfaz para cada valor de densidad de corriente. Las variaciones de la evolución de la densidad de carga frente a la densidad de corriente con los cambios del contacto metal-orgánico permiten detectar el origen físico de estos cambios. Nuestro procedimiento se ha empleado para caracterizar aspectos tecnológicos y problemas que afectan al rendimiento de los diodos orgánicos, tales como la presencia de impurezas, los efectos de atrapamiento, la degradación o el tratamiento de superficie de las interfaces. Se han corroborado nuestros resultados con técnicas experimentales más complejas y se han obtenido conclusiones similares. En este sentido, nuestro procedimiento proporciona un punto de partida rápida en la mejora y el tratamiento de los contactos.

Además de diodos simétricos, se han analizado estructuras asimétricas. Se han desarrollado métodos analíticos y numéricos para determinar el valor de la concentración densidad de carga libre en los contactos, expresado en función de la densidad de corriente del dispositivo. Se ha estudiado la evolución de la densidad de carga libre entre las regiones: óhmicas, dominadas por inyección o por carga espacial para diferentes materiales orgánicos. Este estudio ha dado lugar a un modelo compacto entre la densidad de portadores de carga libres en la interfaz y la densidad de corriente que fluye a través de esta. Las concentraciones de los portadores de carga en las interfaces se extrajeron a partir curvas $J-V$ experimentales, y siguen una función potencial con la densidad de corriente total en diodos orgánicos en polarización inversa $V<0$ y en polarización directa a tensiones superiores al voltaje barrera $V<V_{bi}$. En estas condiciones, el transporte de carga de deriva es dominante. La función potencial $p(0)=K_1J^m$ se verificó para los diodos simétricos con diferentes barreras de inyección, y para los diodos asimétricos con diferentes voltajes aplicados y medidos bajo diferentes temperaturas. El exponente de la función potencial es aproximadamente $m\sim 0.75$ para los diodos orgánicos investigados. La constante proporcional K_1 muestra una dependencia exponencial con la barrera de inyección.

La relación entre la densidad de carga y la densidad de corriente extraída para diodos unipolares se introdujo como condición de contorno para la densidad de carga en los contactos inyectores en la simulación de dispositivos bipolares, consiguiendo reproducir curvas de $J-V$ en estos dispositivos.

Se ha completado el estudio de la estructura metal-orgánico-metal con la incorporación de los efectos

de iluminación. Se ha abordado el efecto de los valores de las condiciones de contorno en la simulación de curvas $J - V$ en las células solares orgánicas bajo iluminación. Se ha propuesto un modelo para los valores de las densidades de carga libres en las interfaces de ánodo y cátodo. El modelo se basa en el modelo desarrollado en las primeras fases de la tesis para los diodos orgánicos de un solo portador y bipolares e incluye observaciones experimentales realizadas por otros autores en las células solares orgánicas. El modelo relaciona la densidad de carga libre en las interfaces con la densidad de corriente que fluye a través de la célula solar por medio de una función potencial. La función potencial puede describir tanto la inyección de carga que se produce con tensiones superiores a la tensión en circuito abierto, como la extracción de los cargas fotogeneradas a tensiones inferiores a la tensión de circuito abierto.

El modelo incluye un conjunto de parámetros que tienen en cuenta las condiciones de funcionamiento y características de las células solares orgánicas. El modelo ha sido comprobado en oscuridad y en iluminación. Se ha obtenido un excelente ajuste entre datos experimentales de otros autores y nuestros resultados numéricos. El modelo también reproduce curvas de corriente-tensión anómalas en forma de 'S', comportamiento típico de las células solares con contactos bloqueantes e interfaces con bajas velocidades de recombinación.

Nuestro modelo de contactos también se ha aplicado otros dispositivos y mecanismos físicos, la tesis finaliza con el estudio de los efectos de contacto en transistores orgánicos de película delgada (OTFTs) y el estudio de los efectos ferroeléctricos en las células solares.

Hemos propuesto un modelo compacto de las características corriente-tensión de transistores orgánicos de película delgada (OTFTs), que incluye los efectos de los contactos. El modelo de contacto unifica diferentes tendencias encontradas en datos experimentales. Este modelo, que se caracteriza por un solo parámetro, se ha incorporado en un modelo genérico de deriva que incluye también una movilidad dependiente de la tensión de puerta. El modelo se reduce fácilmente al modelo FET genérico con una movilidad constante y sin efectos de contacto. Simultáneamente, se ha propuesto un procedimiento de extracción de los valores de los parámetros del modelo para OTFTs. Con el modelo se han reproducido una gran variedad de datos experimentales medidos en OTFTs. Se ha comprobado la consistencia entre el origen físico de los efectos de contacto y los parámetros del modelo. El modelo propuesto es una herramienta muy útil para describir diferentes estructuras en OTFTs. El modelo incorpora efectos de variación de la temperatura, la longitud y el ancho del canal, y contactos con diferentes barreras de energía. El modelo también proporciona información sobre la densidad de carga libre a lo largo del canal del transistor.

Por último, se han incluido efectos ferroeléctricos en el modelo físico de una célula solar metal-ferroeléctrico-metal (MFM). Nuestros análisis proporcionan una visión general de la influencia de los efectos ferroeléctricos sobre la eficiencia de conversión de energía en células solares. Estos análisis permiten evaluar si estos efectos o sus combinaciones son beneficiosas o contraproducentes para el funcionamiento de la célula. La polarización ferroeléctrica afecta a la curvatura de bandas y a las barreras en las interfaces metal-semiconductor. Se han analizado los fenómenos más relevantes en el funcionamiento de estos dispositivos: la modulación de las barreras Schottky por la polarización en la interfaz metal-ferroeléctrico, los campos de despolarización, y el comportamiento conmutable y rectificador de

películas delgadas ferroeléctricas. De la simulación numérica, se concluye que las estructuras Schottky MFM simétricas son las que reproducen el comportamiento conmutable en las curvas de corriente-voltaje bajo iluminación observado de forma experimental. Efectos asociados tanto a las cargas superficiales de polarización, como la polarización dependiente con el campo eléctrico (o lo que es lo mismo con el espacio) son necesarios con el fin de interpretar las curvas experimentales de corriente-tensión.

Bibliografía

[1] Maria-Eleni Ragoussi and Tomás Torres. New generation solar cells: concepts, trends and perspectives. *Chemical Communications*, 51:3957 – 3972, 2015.

[2] *Best Research-Cell Efficiencies NREL http://www.nrel.gov/.*

[3] M.C. Scharber and N.S. Sariciftci. Efficiency of bulk-heterojunction organic solar cells. *Prog. Polym. Sci.*, 38(12):1929–1940, 2013. Topical issue on Conductive Polymers.

[4] C. Deibel and V. Dyakonov. Polymer-fullerene bulk heterojunction solar cells. *Rep. Prog. Phys.*, 73:096401 (39pp), 2010.

[5] M. Jorgensen, K. Norrman, and F. C. Krebs. Stability/degradation of polymer solar cells. *Sol. Energ. Mat. Sol. C.*, 92(7):686–714, 2008.

[6] O. J. Sandberg, M. Nyman, and R. Österbacka. Effect of contacts in organic bulk heterojunction solar cells. *Phys. Rev. Appl.*, 1:024003, 2014.

[7] M. Glatthaar, M. Riede, N. Keeganb, K. Sylvester-Hvid, B. Zimmermann, M. Niggemann, A. Hinsch, and A. Gombert. Efficiency limiting factors of organic bulk heterojunction solar cells identified by electrical impedance spectroscopy. *Sol. Energ. Mat. Sol. C.*, 91:390–393, 2007.

[8] P. Lara Bullejos, J. A. Jiménez Tejada, M. J. Deen, O. Marinov, and W. R. Datars. Unified model for the injection and transport of charge in organic diodes. *J. Appl. Phys.*, 103:064504, 2008.

[9] P. Lara Bullejos, J. A. Jiménez Tejada, F. M. Gómez-Campos, M. J. Deen, and O. Marinov. Evaluation of the charge density in the contact region of organic thin film transistors. *J. Appl. Phys.*, 106:094503, 2009.

[10] P. Lara Bullejos, J. A. Jiménez Tejada, S. Rodríguez Bolívar, M. J. Deen, and O. Marinov. Model for the injection of charge through the contacts of organic transistors. *J. Appl. Phys.*, 105(8):084516, 2009.

[11] Pablo Lara Bullejos. Modelado de mecanísmos físicos y las estructuras constituyentes de un transistor de efecto campo orgánico. Tesis, Universidad de Granada, Granada, junio 2009.

[12] J.A. Jiménez Tejada, K. Awawdeh, J.A. López Villanueva, J.E. Carceller, M. Deen, N. Chaure, T. Basova, and A. Ray. Contact effects in compact models of organic thin film transistors: Application to zinc phthalocyanine-based transistors. *Org. Electron.*, 12(5):832–842, 2011.

[13] K. M. Awawdeh, J. A. Jiménez Tejada, P. López Varo, J. A. López Villanueva, F. M Gómez Campos, and M. J. Deen. Characterization of organic thin film transistors with hysteresis and contact effects. *Org. Electron.*, 14(12):3286 – 3296, 2013.

[14] J. A. Jiménez Tejada, K. M. Awawdeh, P. López Varo, A. K. Ray, and M. J. Deen. Contact effects and hysteresis in organic thin film transistors. In *219th Electrochemical Society Meeting*, Montreal (Canadá), 2011.

[15] K. M. Awawdeh, J. A. Jiménez Tejada, J. A. López Villanueva, J. E. Carceller, M. J. Deen, N. B. Chaure, T. Basova, and A. K. Ray. Compact modeling of the contact effects in organic thin film transistors. In *2011 Spanish Conference on Electron Devices (CDE)*, pages 1–4, Feb. 2011.

[16] P. Stallinga. Electronic transport in organic materials: Comparison of band theory with percolation/(variable range) hopping theory. *Adv. Mater.*, 23:3356–3362, 2011.

[17] V. I. Arkhipov, E. V. Emelianova, and G. J. Adriaenssens. Effective transport energy versus the energy of most probable jumps in disordered hopping systems. *Phys. Rev. B*, 64:125125, 2001.

[18] N. F. Mott and R. W. Gurney. *Electronic Processes in Ionic Crystals*. Clarendon, Oxford, 1940.

[19] Teng Zhang, Erik Birgersson, Krishnamoorthy Ananthanarayanan, Chian Haw Yong, L. N. S. A. Thummalakunta, and Joachim Luther. Analysis of a device model for organic pseudo-bilayer solar cells. *J. Appl. Phys.*, 112(8), 2012.

[20] Marko Topic, Martin Sever, Benjamin Lipovsek, Andrej Campa, and Janez Krc. Approaches and challenges in optical modelling and simulation of thin-film solar cells. *Solar Energy Materials & Solar Cells*, 135:57–66, 2015.

[21] Jiho Yoon, Kyungnam Kang, Sungchul Kim, and Jungho Kim. Effect of oblique incidence angle of sunlight on the optimized folding angle of v-shaped organic solar cells. *Current Applied Physics*, 15:446–451, 2015.

[22] L. Pettersson, L. Roman, and O. Inganas. Modeling photocurrent action spectra of photovoltaic devices based on organic thin films. *J. Appl. Phys.*, 86:487–496, 1999.

[23] N.K. Persson, M. Schubert, and O. Inganäs. Optical modelling of a layered photovoltaic device with a polyfluorene derivative/fullerene as the active layer. *Sol. Energ. Mat. Sol. C.*, 83:169–186, 2004.

[24] Douglas W. Sievers, Vishal Shrotriya, and Yang Yang. Modeling optical effects and thickness dependent current in polymer bulkheterojunction solar cells. *Journal of Applied Physics*, 100:114509, 2006.

[25] J.X. Man, D.Y.Luo, L.M.Yu, D.K.Wang, Z.Liu, and Z.H.Lu. Ultra thin optical design for organic photovoltaic cells. *Optics Communications*, 342:184–188, 2015.

[26] Yue Zang, Xiumin Gao, Xinmiao Lu, Qing Xin, Jun Lin, and Jufeng Zhao. Improved performance of polymer solar cells using PBDTT-F-TT:$PC_{71}BM$ blend film as active layer. *Applied Surface Science*, 376:138–144, 2016.

[27] Viktor Andersson, Kristofer Tvingstedt, and Olle Inganäs. Optical modeling of a folded organic solar cell. *Journal of Applied Physics*, 103(9), 2008.

[28] Feilong Liu, P. Paul Ruden, Ian. H. Campbell, and Darryl L. Smith. Device model for electronic processes at organic/organic interfaces. *Journal of Applied Physics*, 111:094507, 2012.

[29] Robert A. Street. Electronic structure and properties of organic bulk-heterojunction interfaces. *Adv. Mater.*, 28:3814–3830, 2016.

[30] L. Onsager. Initial recombination of ions. *Phys. Rev.*, 15:1, 1938.

[31] C. L. Braun. Electric field assisted dissociation of charge transfer states as a mechanism of photocarrier production. *J. Chem. Phys.*, 80:4157, 1984.

[32] Y Shang, Q. Li, L. Meng, D. Wang, and Z. Shuai. Computational characterization of organic photovoltaic devices. *Theor. Chem. Acc.*, 129:291–301, 2011.

[33] Robin G. E. Kimber, Edward N. Wright, Simon E. J. OKane, Alison B. Walker, and James C. Blakesley. Mesoscopic kinetic monte carlo modeling of organic photovoltaic device characteristics. *Physical Review B*, 86:235206, 2012.

[34] Alessio Gagliardi and Tim Albes. Investigation of the blend morphology in bulk-heterojunction organic solar cells. *Proceedings of the 15th IEEE International Conference on Nanotechnology*, 2015.

[35] Florent Deledalle, Thomas Kirchartz, Michelle S. Vezie, Mariano Campoy-Quiles, Pabitra Shakya Tuladhar, Jenny Nelson, and James R. Durrant. Understanding the effect of unintentional doping on transport optimization and analysis in efficient organic bulk-heterojunction solar cells. *Phyical Review*, 5:011032, 2015.

[36] V. A. Trukhanov, V. V. Bruevich, and D. Yu. Paraschuk. Effect of doping on performance of organic solar cells. *Phyical Review B*, 84:205318, 2011.

[37] Ali Mahmoudloo and Sohrab Ahmadi-Kandjani. Influence of the temperature on the charge transport and recombination profile in organic bulk heterojunction solar cells: a drift-diffusion study. *Appl. Phys. A*, 119:1523–1529, 2015.

[38] S. Nazerdeylami and H. Rezagholipour Dizaji. Influence of exponential tail states on photovoltaic parameters and recombination of bulk heterojunction organic solar cells: an optoelectronic simulation. *Opt Quant Electron*, 48:260, 2016.

[39] Shuai Zhoua and Jiu xun Sun. Charge carrier density dependent transport in disordered organic photovoltaic devices. *Optik*, 126:3678–3682, 2015.

[40] Thomas Kirchartz, Tiziano Agostinell, Mariano Campoy-Quiles, Wei Gong, and Jenny Nelson. Understanding the thickness-dependent performance of organic bulk heterojunction solar cells: The influence of mobility, lifetime, and space charge. *J. Phys. Chem. Lett.*, 3:3470–3475, 2012.

[41] Carlo de Falco, Matteo Porro, Riccardo Sacco, and Maurizio Verri. Multiscale modeling and simulation of organic solar cells. *Comput. Methods Appl. Mech. Engrg.*, 245-246:102–116, 2012.

[42] Pankaj Kumar, S. C. Jain, Vikram Kumar, Suresh Chand, and R. P. Tandon. A model for the J-V characteristics of P3HT:PCBM solar cells. *J. Appl. Phys.*, 105(10):104507, 2009.

[43] L. J. A. Koster, E. C. P. Smits, V. D. Mihailetchi, and P. W. M. Blom. Device model for the operation of polymer/fullerene bulk heterojunction solar cells. *Phys. Rev. B*, 72:085205, 2005.

[44] Adelmo Ortiz-Conde, Francisco J. García-Sánchez, Juan Muci, and Andrea Sucre-González. A review of diode and solar cell equivalent circuit model lumped parameter extraction procedures. *FACTA UNIVERSITATIS Series: Electronics and Energetics*, 27:57 – 102, 2014.

[45] M. L. Inche Ibrahim, Z. Ahmad, and K. Sulaiman. Analytical expression for the current-voltage characteristics of organic bulk heterojunction solar cells. *AIP Advances*, 5:027115, 2015.

[46] Giles Richardson, Colin Please, Jamie Foster, and James Kiripatrick. Asymptotic solution of a model for bilayer organic diodes and solar cells. *Siam J. Appl. Math.*, 72(6):1792–1817, 2012.

[47] Salman M. Arnab and M. Z. Kabir. An analytical model for analyzing the current-voltage characteristics of bulk heterojunction organic solar cells. *Journal of Applied Physics*, 115:034504, 2014.

[48] M.M. Chowdhury and M.K. Alam. A physics-based analytical model for bulk heterojunction organic solar cells incorporating monomolecular recombination mechanism. *Current Applied Physics*, 14(3):340 – 344, 2014.

[49] M.M. Chowdhury and M.K. Alam. An analytical model for bulk heterojunction organic solar cells using a new empirical expression of space dependent photocarrier generation. *Solar Energy*, 126:64 – 72, 2016.

[50] Mesbahus Saleheen, Salman M. Arna, and M. Z. Kabir. Analytical model for voltage-dependent photo and dark currents in bulk heterojunction organic solar cells. *Energies*, 9:412, 2016.

[51] J. J. Kim, M. K. Han, and Y. Y. Noh. Flexible OLEDs and organic electronics. *Semicond. Sci. Technol.*, 26:030301, 2011.

[52] N. Tessler, Y. Preezant, N. Rappaport, and Y Roichman. Charge transport in disordered organic materials and its relevance to thin-film devices: A tutorial review. *Adv. Mater.*, 21:2741–2761, 2009.

[53] Z. Chiguvare, J. Parisi, and V. Dyakonov. Current limiting mechanisms in indium-tin-oxide/poly3-hexylthiophene/aluminum thin film devices. *J. Appl. Phys.*, 94:2440, 2003.

[54] M. Bouhassoune, S.L.M. van Mensfoort, P.A. Bobbert, and R. Coehoorn. Carrier-density and field-dependent charge-carrier mobility in organic semiconductors with correlated gaussian disorder. *Org. Electron.*, 10(3):437–445, 2009.

[55] O. Marinov, M. J. Deen, and B. Iniguez. Charge transport in organic and polymer thin-film transistors: recent issues. *IEE Proc.-Circuits Devices Syst.*, 152(3):189–209, 2005.

[56] M.J. Deen and M.H. Kazemeini. Photosensitive polymer thin-film field-effect transistors based on poly(3-octylthiophene). *Proc. IEEE (Special Issue on Flexible Electronics Technology - Part 1: Systems and Applications)*, 93:1312–1320, 2005.

[57] H. Ishii, K. Sugiyama, E. Ito, and K. Seki. Energy level alignment and interfacial electronic structures at organic/metal and organic/organic interfaces. *Adv. Mater.*, 11(8):605–625, 1999.

[58] S. Narioka, H. Ishii, D. Yoshimura, M. Sei, Y. Ouchi, K. Seki, S. Hasegawa, T. Miyazaki, Y. Harima, and K. Yamashita. The electronic structure and energy level alignment of porphyrin/metal interfaces studied by ultraviolet photoelectron spectroscopy. *Appl. Phys. Lett.*, 67(13):1899–1901, 1995.

[59] T. Shimada, K. Hamaguchi, A. Koma, and F. S. Ohuchi. Electronic structures at the interfaces between copper phthalocyanine and layered materials. *Appl. Phys. Lett.*, 72(15):1869–1871, 1998.

[60] Jayesh M. Bharathan and Yang Yanga. Polymer/metal interfaces and the performance of polymer light-emitting diodes. *J. Appl. Phys.*, 84:3207, 1998.

[61] M. Bokdam, D. Cakir, and G. Brocks. Fermi level pinning by integer charge transfer at electrode-organic semiconductor interfaces. *Appl. Phys. Lett.*, 98(11):113303, 2011.

[62] Ryo Nouchi and Yoshihiro Kubozono. Anomalous hysteresis in organic field-effect transistors with sam-modified electrodes: Structural switching of sams by electric field. *Org. Electron.*, 11:1025–1030, 2010.

[63] P. S. Davids, I. H. Campbell, and D. L. Smith. Device model for single carrier organic diodes. *J. Appl. Phys.*, 82:6319, 1997.

[64] G. G. Malliaras and J. C. Scott. Numerical simulations of the electrical characteristics and the efficiencies of single-layer organic light emitting diodes. *J. Appl. Phys.*, 85(10):7426–7432, 1999.

[65] Ajit Kumar Mahapatro and Subhasis Ghosh. Charge carrier transport in metal phthalocyanine based disordered thin films. *J. Appl. Phys.*, 101(3):034318, 2007.

[66] P. W. M. Blom, C. Tanase, D. M. de Leeuw, and R. Coehoorn. Thickness scaling of the space-charge-limited current in poly(p-phenylene vinylene). *Appl. Phys. Lett.*, 86(9):092105, 2005.

[67] O. Marinov, M. J. Deen, and W. R. Datars. Compact modeling of charge carrier mobility in organic thin-film transistors. *J. Appl. Phys.*, 106:064501, 2009.

[68] Y. Roichman, Y. Preezant, and N. Tessler. Analysis and modeling of organic devices. *Phys. Stat. Sol. (a)*, 201:1246–1262, 2004.

[69] D. Chirvase, Z. Chiguvare, M. Knipper, J. Parisi, V. Dyakonov, and J. C. Hummelen. Temperature dependent characteristics of poly(3 hexylthiophene)-fullerene based heterojunction organic solar cells. *J. Appl. Phys.*, 93(6):3376–3383, 2003.

[70] O. Marinov, M. J. Deen, U. Zschieschang, and H. Klauk. Organic thin-film transistors: Part I-compact DC modeling. *IEEE Trans. Electron Devices*, 56:2952–2961, 2009.

[71] M.J. Deen, O. Marinov, U. Zschieschang, and H. Klauk. Organic Thin-Film Transistors: Part II-Parameter Extraction. *IEEE Trans. Electron Devices*, 56:2962–2968, 2009.

[72] P. W. M. Blom, M. J. M. de Jong, and J. J. M. Vleggaar. Electron and hole transport in poly(p-phenylene vinylene) devices. *Appl. Phys. Lett.*, 68(23):3308–3310, 1996.

[73] M. J. Deen, M.H. Kazemeini, and S. Holdcroft. Contact effects and extraction of intrinsic parameters in poly(3-alkylthiophene) thin-film field-effect transistors. *J. Appl. Phys.*, 103:124509, 2008.

[74] M. J. Deen, M. H. Kazemeini, Y.M. Haddara, J. Yu, G. Vamvounis, S. Holdcroft, and W. Woods. Electrical characterization of polymer-based field-effect transistors fabricated by spin-coating poly(3-alkylthiophene)s. *IEEE Trans. Electron Devices*, 50:1892–1901, 2004.

[75] S. L. M. van Mensfoort and R. Coehoorn. Effect of gaussian disorder on the voltage dependence of the current density in sandwich-type devices based on organic semiconductors. *Phys. Rev. B*, 78(8):085207, Aug 2008.

[76] S. L. M. van Mensfoort, S. I. E. Vulto, R. A. J. Janssen, and R. Coehoorn. Hole transport in polyfluorene-based sandwich-type devices: Quantitative analysis of the role of energetic disorder. *Phys. Rev. B*, 78(8):085208, Aug 2008.

[77] Z. P. Buffett and W. R. Datars. A lattice gas approach to conduction in organic material. *J. Phys.: Cond. Matter*, 17(19):2919, 2005.

[78] P. W. M. Blom, M. J. M. de Jong, and C. T.H.F. Liedenbaum. Device physics of polymer light-emitting diodes. *Polym. Adv. Technol.*, 9:390–401, 1998.

[79] S. Forero, P. H. Nguyen, W. Brütting, and M. Schwoerer. Charge carrier transport in poly(p-phenylenevinylene) light-emitting devices. *Phys. Chem. Chem. Phys.*, 1:1769–1776, 1999.

[80] E. Pinotti, A. Sassella, A. Borghesi, and R. Tubino. Electrical characterization of organic semiconductors by transient current methods. *Synth. Met.*, 122:169–171, 2001.

[81] Salvatore Gambino, A. K. Bansal, and Ifor D.W. Samuel. Comparison of hole mobility in thick and thin films of a conjugated polymer. *Org. Electron.*, 11:467, 2010.

[82] O. Marinov, M. J. Deen, and B. Iniguez. Performance of organic thin-film transistors. *J. Vac. Sci. Technol. B*, B24:1728–1733, 2006.

[83] W. D. Gill. Drift mobilities in amorphous charge-transfer complexes of trinitrofluorenone and poly-n-vinylcarbazole. *J. Appl. Phys.*, 5033:1972, 1972.

[84] Damodar M. Pai. Transient photoconductivity in poly(n-vinylcarbazole). *J. Chem. Phys.*, 52(5):2285, 1970.

[85] R. Agrawal, P. Kumar, S. Ghosh, and A. K. Mahapatro. Thickness dependence of space charge limited current and injection limited current in organic molecular semiconductors. *Appl. Phys. Lett.*, 93(7):073311, 2008.

[86] P. W. M. Blom, M. J. M. de Jong, and M. G. van Munster. Electric-field and temperature dependence of the hole mobility in poly(p-phenylene vinylene). *Phys. Rev. B*, 55(2):R656–R659, Jan 1997.

[87] H. Bässler. Charge transport in disordered organic photoconductors a monte carlo simulation study. *Phys. Stat. Solidi (B)*, 175:15–56, 1993.

[88] Y. N. Garstein and E. M. Conwell. High-field hopping mobility in molecular systems with spatially correlated energetic disorder. *Chem. Phys. Lett.*, 245:351, 1995.

[89] S. V. Novikov, D. H. Dunlap, V. M. Kenkre, P. E. Parris, and A. V. Vannikov. Essential role of correlations in governing charge transport in disordered organic materials. *Phys. Rev. Lett.*, 81(20):4472–4475, Nov 1998.

[90] T. Kreouzis, D. Poplavskyy, S. M. Tuladhar, M. Campoy-Quiles, J. Nelson, A. J. Campbell, and D. D. C. Bradley. Temperature and field dependence of hole mobility in poly(9,9-dioctylfluorene). *Phys. Rev. B*, 73:235201, Jun 2006.

[91] C. Tanase, P. W. M. Blom, and D. M. de Leeuw. Origin of the enhanced space-charge-limited current in poly(p-phenylene vinylene). *Phys. Rev. B*, 70(19):193202, Nov 2004.

[92] Sergei Baranovski. *Charge transport in disordered solids with applications in electronic*. WILEY, 2006.

[93] W. F. Pasveer, J. Cottaar, C. Tanase, R. Coehoorn, P. A. Bobbert, P. W. M. Blom, D. M. de Leeuw, and M. A. J. Michels. Unified description of charge-carrier mobilities in disordered semiconducting polymers. *Phys. Rev. Lett.*, 94(20):206601, May 2005.

[94] C. Schuster, M. Kraus, A. Opitz, W. Brütting, and U. Eckern. Transport properties of copper phthalocyanine based organic electronic devices. *European Physical Journal-special Topics*, 180:117–134, 2010.

[95] R. Coehoorn, W. F. Pasveer, P. A. Bobbert, and M. A. J. Michels. Charge-carrier concentration dependence of the hopping mobility in organic materials with gaussian disorder. *Phys. Rev. B*, 72(15):155206, Oct 2005.

[96] F. Torricelli, D. Zappa, and L. Colalongo. Space-charge-limited current in organic light emitting diodes. *Phys. Rev. Lett.*, 96:113304, 2010.

[97] C. Tanase, E. J. Meijer, P. W. M. Blom, and D. M. de Leeuw. Unification of the hole transport in polymeric field-effect transistors and light-emitting diodes. *Phys. Rev. Lett.*, 91(21):216601, Nov 2003.

[98] Z. B. Wang, M. G. Helander, M. T. Greiner, J. Qiu, and Z. H. Lu. Analysis of charge-injection characteristics at electrode-organic interfaces: Case study of transition-metal oxides. *Phys. Rev. B*, 80:235325, 2009.

[99] A. Nemeth-Buhin, C. Juhasz, V. I. Arkhipov, and H. Bässler. Scaling properties of transport parameters in molecularly doped polymers. *Phil. Mag. Lett.*, 74:295, 1996.

[100] B. Bohnenbuck, E. von Hauff, J. Parisi, C. Deibel, and V. Dyakonov. Current-limiting mechanisms in polymer diodes. *J. Appl. Phys.*, 99(2):024506, 2006.

[101] Noam Rappaport. Research of physical processes of optical excitations and electric conduction in light detection polymeric devices. Tesis, Technion Israel Institute of Technology, 2007.

[102] P. Mark and W. Helfrich. Space-charge limited currents in organic crystals. *J. Appl. Phys.*, 33:205, 1962.

[103] CA. Di, F. Zhang, and D. Zhu. Multi-functional integration of organic field-effect transistors (OFETs): Advances and perspectives. *Adv. Mater.*, 25:313–330, 2013.

[104] P. Sigaud, J. N. Chazalviel, F. Ozanam, and K. Lahlil. Increased hole injection in organic diodes by grafting of dipolar molecules on indium-tin oxide. *Appl. Surf. Sci.*, 218:54–57, 2003.

[105] S. F. J. Appleyard, S. R. Day, R. D. Pickford, and M. R. Willis. Organic electroluminescent devices: enhanced carrier injection using SAM derivatized ITO electrodes. *J. Mater. Chem.*, 10:169–173, 2000.

[106] V. I. Arkhipov, H. von Seggern, and E. V. Emelianova. Charge injection versus space-charge-limited current in organic light-emitting diodes. *Appl. Phys. Lett.*, 83(24):5074–5076., 2003.

[107] L. Yan and Y. Gao. Interfaces in organic semiconductor devices. *Thin Solid Films*, 417(1-b2):101–106, 2002.

[108] S. C. Jain, W. Geens, A. Mehra, V. Kumar, T. Aernouts, J. Poortmans, R. Mertens, and M. Willander. Injection- and space charge limited-currents in doped conducting organic materials. *J. Appl. Phys.*, 89:3804, 2001.

[109] J. Campbell Scott. Metal-organic interface and charge injection in organic electronic devices. *J. Vac. Sci. Technol. A*, 21:521–531, 2003.

[110] V. I. Arkhipov, E. V. Emelianova, Y. H. Tak, and H. Bässler. Charge injection into light-emitting diodes: Theory and experiment. *J. Appl. Phys.*, 84(2):848–856, 1998.

[111] J. K. J. van Duren, V. D. Mihailetchi, P. W. M. Blom, T. van Woudenbergh, J. C. Hummelen, M. T. Rispens, R. A. J. Janssen, and M. M. Wienk. Injection-limited electron current in a methanofullerene. *J. Appl. Phys.*, 94(7):4477–4479, 2003.

[112] P. López Varo, J.A. Jiménez Tejada, J.A. López Villanueva, J.E. Carceller, and M.J. Deen. Modeling the transition from ohmic to space charge limited current in organic semiconductors. *Org. Electron.*, 13(9):1700 – 1709, 2012.

[113] A. L. Alvarez, B. Arredondo, B. Romero, X. Quintana, A. Gutiérrez-Llorente, R. Mallavia, and J. M. Otón. Analytical evaluation of the ratio between injection and space-charge limited currents in single carrier organic diodes. *IEEE Trans. Electron Devices*, 55:674–680, 2008.

[114] Y. N. Garstein and E. M. Conwell. High-field hopping mobility of polarons in disordered molecular solids. a monte carlo study. *Chem. Phys. Lett.*, 217:41–47, 1994.

[115] Roland Schmechel and Heinz von Seggern. Electronic traps in organic transport layers. *Phys. Stat. Solidi (A)*, 201(6):1215–1235, 2004.

[116] S. G. Stevenson, I. D. W. Samuel, S. V. Staton, K. A. Knights, P. L. Burn, J. H. T. Williams, and A. B. Walker. Current-voltage characteristics of dendrimer light-emitting diodes. *J. Phys. D: Appl. Phys.*, 43:385106 (8pp), 2010.

[117] J. P. J. Markham, I. D. W. Samuel, S-C. Lo, P. L. Burn, M. Weiter, and H. Bässler. Charge transport in highly efficient iridium cored electrophosphorescent dendrimers. *J. Appl. Phys.*, 95:438, 2004.

[118] Y.-J. Lin, H.-Y. Tsao, and D.-S. Liu. Hall effect mobility of pentacene films prepared by the thermal temperature. *Appl. Phys. Lett.*, 101:013302, 2012.

[119] W. Warta and N. Karl. Hot holes in naphthalene: High, electric-field-dependent mobilities. *Phys. Rev. B: Condens. Matter Mater. Phys.*, 32:1172–1182, 1985.

[120] T. Sakanoue and H. Sirringhaus. Band-like temperature dependence of mobility in a solution-processed organic semiconductor. *Nature Materials*, 9:736, 2010.

[121] S. Fratini and S. Ciuchi. Bandlike motion and mobility saturation in organic molecular semiconductor. *Phys. Rev. Lett.*, 103:266601, 2009.

[122] Y. J. Lin, C. L. Tsai, Y. C. Su, and D. S. Liu. Carrier transport mechanism of poly(3,4-ethylenedioxythiophene) doped with poly(4-styrenesulfonate) films by incorporating ZnO nanoparticles. *Appl. Phys. Lett.*, 100:253302, 2012.

[123] V. Coropceanu, J. Cornil, D. A. da Silva Filho, Y. Olivier, R. Silbey, and J. L. Brédas. Charge transport in organic semiconductors. *Chem. Rev.*, 107:926–952, 2007.

[124] O. D. Jurchescu, J. Baas, and T. T. M. Palstra. Effect of impurities on the mobility of single crystal pentacene. *Appl. Phys. Lett.*, 84:3061, 2004.

[125] Y. Zheng, A. T. S. Wee, C. Troadec, and N. Chandrasekhar. Temperature-dependent transition from injection-limited to space-charge-limited current in metal-organic diodes. *Appl. Phys. Lett.*, 95:143303, 2009.

[126] A. J. Campbell, D. D. C. Bradley, and D. G. Lidzey. Space-charge limited conduction with traps in poly(phenylene vinylene) light emitting diodes. *J. Appl. Phys.*, 82(12):6326–6342, 1997.

[127] A. J. Campbell, M. S. Weaver, D. G. Lidzey, and D. D. C. Bradley. Bulk limited conduction in electroluminescent polymer devices. *J. Appl. Phys.*, 84(12):6737–6746, 1998.

[128] S. C. Jain, Ashok. K. Kapoor, Wim Geens, J. Poortmans, R. Mertens, and M. Willander. Trap filled limit of conducting organic materials. *J. Appl. Phys.*, 92(7):3752–3754, 2002.

[129] V. R. Nikitenko, H. Heil, and H. von Seggern. Space-charge limited current in regioregular poly-3-hexylthiophene. *J. Appl. Phys.*, 94(4):2480–2485, 2003.

[130] P. Kumar, S. Chand, S. Dwivedi, and M. N. Kamalasanan. Effect of interface layer, curing temperature, and polarization on the hole transport in poly(3-hexylthiophene) thin films. *Appl. Phys. Lett.*, 90(2):023501, 2007.

[131] H. Bednarsky, J. Gasiorowski, M. Domanski, B. Hajduk, J. Jursik, B. Jarzabek, and J. Weszka. Stability of diodes with poly(3-hexylthiophene) and polyazomethines thin organic layer. *Acta Physica Polonica, A*, 122:1083–1086, 2012.

[132] X. Zhang, P. Bäuerle, T. Aida, P. Skabara, and C. Kagan. Electronics for a better tomorrow: Innovation, accessibility, sustainability, a white paper from the chemical sciences and society summit (CS3). Technical report, San Francisco, California, United States, 2012.

[133] J. Laubender, L. Chkoda, M. Sokolowski, and E. Umbach. The influence of oxygen and air on the characteristics of organic light-emitting devices studied by in vacuo measurements. *Synth. Met.*, 111-112:373 – 376, 2000.

[134] I. H. Campbell, J. D. Kress, R. L. Martin, D. L. Smith, N. N. Barashkov, and J. P. Ferraris. Controlling charge injection in organic electronic devices using self-assembled monolayers. *Appl. Phys. Lett.*, 71(24):3528–3530, 1997.

[135] S. Nicht, H. Kleemann, A. Fischer, K. Leo, and B. Lüssem. Functionalized p-dopants as self-assembled monolayers for enhanced charge carrier injection in organic electronic devices. *Org. Electronics*, 15(3):654 – 660, 2014.

[136] A. Abate, D. R. Staff, D. J. Hollman, H. J. Snaith, and A. B. Walker. Influence of ionizing dopants on charge transport in organic semiconductors. *Phys. Chem. Chem. Phys.*, 16:1132–1138, 2014.

[137] R. A. Street, P. P. Khlyabich, and B. C. Thompson. Electrical characterization of organic solar cell contact degradation resulting from ambient exposure. *Org. Electronics*, 14(11):2932 – 2939, 2013.

[138] S.-J. Yoo, J.-H. Lee, J.-H. Lee, and J.-J. Kim. Doping-concentration-dependent hole mobility in a ReO_3 doped organic semiconductor of 4,4,4-tris(n-(2-naphthyl)-n-phenyl-amino)-triphenylamine. *Appl. Phys. Lett.*, 102(18), 2013.

[139] T. Yoshikawa, T. Nagase, T. Kobayashi, S. Murakami, and H. Naito. Analysis of time-of-flight transient photocurrent in organic semiconductors with coplanar-blocking-electrodes configuration. *Thin Solid Films*, 516(9):2595 – 2599, 2008. The 7th International Conference on Nano-Molecular Electronics (ICNME 2006).

[140] J. Lorrmann, B. H. Badada, O. Inganäs, V. Dyakonov, and C. Deibel. Charge carrier extraction by linearly increasing voltage: Analytic framework and ambipolar transients. *J. Appl. Phys.*, 108(11), 2010.

[141] J. Widmer, J. Fischer, W. Tress, K. Leo, and M. Riede. Electric potential mapping by thickness variation: A new method for model-free mobility determination in organic semiconductor thin films. *Org. Electronics*, 14(12):3460 – 3471, 2013.

[142] T. Kirchartz, W. Gong, S. A. Hawks, T. Agostinelli, R. C. I. MacKenzie, Y. Yang, and J. Nelson. Sensitivity of the mott-schttky analysis in organic solar cells. *J. Phys. Chem. C*, 116:7672, 2012.

[143] P. López Varo, J. A. Jiménez Tejada, J. A. López Villanueva, and M. J. Deen. Space-charge and injection limited current in organic diodes: A unified model. *Org. Electron.*, 15(10):2526 – 2535, 2014.

[144] F. Nuësch, K. Kamarás, and L. Zuppiroli. Protonated metal-oxide electrodes for organic light emitting diodes. *Chem. Phys. Lett.*, 283:194–200, 1998.

[145] P. K. H. Ho, J. S. Kim, J. H. Burroughes, H. Becker, S. F. Y. Li, T. M. Brown, F. Cacialli, and R. H. Friend. Molecular-scale interface engineering for polymer light-emitting diodes. *Nature*, 404:481, 2000.

[146] J. Meyer, K. Zilberberg, T. Riedl, and A. Kahn. Electronic structure of vanadium pentoxide: An efficient hole injector for organic electronic materials. *J. Appl. Phys.*, 110(3):033710, 2011.

[147] G. Horowitz, P. Lang, W. Kalb, M. Mottaghi, A. Roumyantseva, and A. Yassar. Organic field effect transistors with self-assembled monolayers. In *Proc. Int. Symp. Super-Funct. Org. Dev. IPAP Conf Ser. 6*, pages 125–129, 2005.

[148] J.C. Love, L.A. Estroff, J.K. Kriebel, R.G. Nuzzo, and G.M. Whitesides. Self-assembled monolayers of thiolates on metals as a form of nanotechnology. *Chemical Reviews*, 105(4):1103–1170, 2005. PMID: 15826011.

[149] B. de Boer, A. Hadipour, M. M. Mandoc, T. van Woudenbergh, and P. W. M. Blom. Tuning of metal work functions with self-assembled monolayers. *Adv. Mater.*, 17(5):621–625, 2005.

[150] S. G. Ray, H. Cohen, R. Naaman, H. Liu, and D. H. Waldeck. Organization-induced charge redistribution in self-assembled organic monolayers on gold. *J. Phys. Chem. B*, 109(29):14064–14073, 2005. PMID: 16852766.

[151] H. B. Akkermann, P. W. M. Blom, D. M. de Leeuw, and B. de Boer. Towards molecular electronics with large-area molecular junctions. *Nature*, 441:69–72, 2006.

[152] H. Bedis. Effect of self-assembled monolayers on the performance of organic photovoltaic cells. *J. Surf. Eng. Mater. Adv. Technol.*, 1:42–50, 2011.

[153] L. Newton, T. Slater, N. Clark, and A. Vijayaraghavan. Self assembled monolayers (sams) on metallic surfaces (gold and graphene) for electronic applications. *J. Mater. Chem. C*, 1:376–393, 2013.

[154] C. Vericat, M. E. Vela, G. Benitez, P. Carro, and R. C. Salvarezza. Self-assembled monolayers of thiols and dithiols on gold: new challenges for a well-known system. *Chem. Soc. Rev.*, 39:1805–1834, 2010.

[155] S. Hong, P. Yeh, J. Dadap, and R. Osgood. Interfacial dipole formation and surface-electron confinement in low-coverage self-assembled thiol layers: thiophenol and p-fluorothiophenol on cu(111). *ACS Nano*, 12:10622, 2012.

[156] X. Cheng, Y.-Y. Noh, J. Wang, M. Tello, J. Frisch, R. P. Blum, A. Vollmer, J. Rabe, N. Koch, and H. Sirringhaus. Controlling electron and hole charge injection in ambipolar organic field-effect transistors by self-assembled monolayers. *Adv. Funct. Mater.*, 19(15):2407–2415, 2009.

[157] F. Gholamrezaie. Self-assembled monolayers in organic electronics. Technical report, Zernike Institute, 2012.

[158] S. Reineke, F. Lindner, G. Schwartz, N. Seidler, K. Walzer, B. Lüssem, and K. Leo. White organic light-emitting diodes with fluorescent tube efficiency. *Nature*, 459:234–238, 2009.

[159] M. Riede, C. Uhrich, J. Widmer, R. Timmreck, D. Wynands, G. Schwartz, W.-M. Gnehr, D. Hildebrandt, A. Weiss, J. Hwang, S. Sundarraj, P. Erk, M. Pfeiffer, and K. Leo. Efficient organic tandem solar cells based on small molecules. *Adv. Funct. Mater.*, 21(16):3019–3028, 2011.

[160] Y. Zhang and P. W. M. Blom. Enhancement of the hole injection into regioregular poly(3-hexylthiopene) by molecular doping. *Appl. Phys. Lett.*, 97:083303, 2010.

[161] X Jiang, Y Harima, K Yamashita, Y Tada, J Ohshita, and A Kunai. Doping-induced change of carrier mobilities in poly(3-hexylthiophene) films with different stacking structures. *Chemical Physics Letters*, 364(5-6):616 – 620, 2002.

[162] A. Mityashin, Y. Olivier, T. Van Regemorter, C. Rolin, S. Verlaak, N. G. Martinelli, D. Beljonne, J. Cornil, J. Genoe, and P. Heremans. Unraveling the mechanism of molecular doping in organic semiconductors. *Adv. Mater.*, 24(12):1535–1539, 2012.

[163] D.B.A. Rep, A.F. Morpurgo, and T.M. Klapwijk. Doping-dependent charge injection into regioregular poly(3-hexylthiophene). *Org. Electronics*, 4(4):201 – 207, 2003.

[164] J. Blochwitz, T. Fritz, M. Pfeiffer, K. Leo, D.M. Alloway, P.A. Lee, and N.R. Armstrong. Interface electronic structure of organic semiconductors with controlled doping levels. *Organic Electronics*, 2(2):97 – 104, 2001.

[165] X. Liu, K.S. Jeong, B.P. Williams, K. Vakhshouri, C. Guo, K. Han, E.D. Gomez, Q. Wang, and J.B. Asbury. Tuning the dielectric properties of organic semiconductors via salt doping. *J. Phys. Chem. B*, 117(49):15866–15874, 2013.

[166] R.D. Pensack, K.M. Banyas, and J.B. Asbury. Charge trapping in organic photovoltaic materials examined with time-resolved vibrational spectroscopy. *J. Phys. Chem. C*, 114:5344–5350, 2010.

[167] P. Anjaneyulu, C. S. Suchand Sangeeth, and Menon R. Carrier density-dependent transport in poly(3-methylthiophene): from injection-limited to space-charge-limited current. *J. Phys. D: Appl. Phys.*, 44:315101, 2011.

[168] K. Kawano, R. Pacios, D. Poplavskyy, J. Nelson, D.D.C. Bradley, and J.R. Durrant. Degradation of organic solar cells due to air exposure. *Sol. Energ. Mat. Sol. C.*, 90(20):3520 – 3530, 2006.

[169] M. Girtan and M. Rusu. Role of ITO and PEDOT:PSS in stability/degradation of polymer:fullerene bulk heterojunctions solar cells. *Sol. Energ. Mat. Sol. C.*, 94(3):446 – 450, 2010.

[170] J. Park, J. E. Royer, C. N. Colesniuc, F. I. Bohrer, A. Sharoni, S. Jin, I. K. Schuller, W. C. Trogler, and A. C. Kummel. Ambient induced degradation and chemically activated recovery in copper phthalocyanine thin film transistors. *J. Appl. Phys.*, 106(3), 2009.

[171] J. A. Jiménez Tejada, J. A. López Villanueva, P. López Varo, K. M. Awawdeh, and M. J. Deen. Compact modeling and contact effects in organic transistors. *IEEE Trans. Electron Devices*, 61(2):266–277, 2014.

[172] P. Sigaud, J.-N. Chazalviel, and F. Ozanam. Barrier lowering and reorientation of dipoles grafted at indium-tin-oxide/polymer interfaces. *J. Appl. Phys.*, 92(2):992–996, 2002.

[173] S. Meskinis, K. Slapikas, R. Gudaitis, S. Tamulevicius, A. Iljinas, A. Gudonyte, J.V. Grazulevicius, V. Getautis, A. Michaleviciute, T. Malinauskas, and R. Lygaitis. Investigation of the electrical characteristics of the metal - organic semiconductor - metal structures with top contact configuration. *Mater. Sci.*, 16:195–201, 2010.

[174] A. Petersen, T. Kirchartz, and T. A. Wagner. Charge extraction and photocurrent in organic bulk heterojunction solar cells. *Phys. Rev. B*, 85:045208, 2012.

[175] D. Bozyigit, W. M. M. Lin, N. Yazdani, O Yarema, and V Wood. A quantitative model for charge carrier transport, trapping and recombination in nanocrystal-based solar cells. *Nat. Commun.*, 6:6180, 2015.

[176] S. Altazin, R. Clerc, R. Gwoziecki, G. Pananakakis, G. Ghibaudo, and C. Serbutoviez. Analytical modeling of organic solar cells and photodiodes. *Appl. Phys. Lett.*, 99:143301, 2011.

[177] J. C. Scott and G. G. Malliaras. Charge injection and recombination at the metal-organic interface. *Chem. Phys. Lett.*, 299:115–119, 1999.

[178] M. Pope and C. E. Swenberg. *Electronic Processes in Organic Crystals and Polymers*. Oxford University Press, 2nd edition, 1999.

[179] L. J. A. Koster, M. Kemerink, M. M. Wienk, K. Maturová, and R. A. J. Janssen. Quantifying bimolecular recombination losses in organic bulk heterojunction solar cells. *Adv. Mater.*, 23(14):1670–1674, 2011.

[180] L. Tzabari and N. Tessler. Shockley-read-hall recombination in P3HT:PCBM solar cells as observed under ultralow light intensities. *J. Appl. Phys.*, 109(6):64501–1–64501–5, 2011.

[181] P. López Varo, J. A. Jiménez Tejada, J. A. López Villanueva, and M. J. Deen. Electrical characterization of controlled and unintentional modified metal-organic contacts. *Org. Electron.*, 15(10):2536–2545, 2014.

[182] P. Langevin. The recombination and mobilities of ions in gases. *Ann. Chim. Phys.*, 28:433, 1903.

[183] C. Deibel, A. Wagenpfahl, and V. Dyakonov. Origin of reduced polaron recombination in organic semiconductor devices. *Phys. Rev. B*, 80:075203, Aug 2009.

[184] P. Bruyn, A. H. P. van Rest, G. A. H. Wetzelaer, D. M. de Leeuw, and P.W. M. Blom. Diffusion-limited current in organic metal-insulator-metal diodes. *Phys. Rev. B*, 111:186801, 2013.

[185] P.H. Nguyen, S. Scheinert, S. Berleb, W. Brütting, and G. Paasch. The influence of deep traps on transient current-voltage characteristics of organic light-emitting diodes. *Org. Electron.*, 2(3–4):105 – 120, 2001.

[186] P. N. Murgatroyd. Theory of space-charge-limited current enhanced by frenkel effect. *J. Phys. D Appl. Phys.*, 3(2):151, 1970.

[187] Prachi Mantri, S.M.H. Rizvi, and B. Mazhari. Estimation of built-in voltage from steady-state current-voltage characteristics of organic diodes. *Org. Electron.*, 14(8):2034 – 2038, 2013.

[188] J.G. Simmons. Theory of metallic contacts on high resistivity solids-I. shallow traps. *J. Phys. Chem. Solids*, 32(8):1987 – 1999, 1971.

[189] Steven A. Hawks, Gang Li, Yang Yang, and Robert A. Street. Band tail recombination in polymer:fullerene organic solar cells. *J. Appl. Phys.*, 116(7):074503, 2014.

[190] A. Foertig, A. Baumann, D. Rauh, V. Dyakonov, and C. Deibel. Charge carrier concentration and temperature dependent recombination in polymer-fullerene solar cells. *Appl. Phys. Lett.*, 95(5):052104, 2009.

[191] Ajit Kumar Mahapatro and Subhasis Ghosh. Schottky energy barrier and charge injection in metal/copper-phthalocyanine/metal structures. *Appl. Phys. Lett.*, 80(25):4840–4842, 2002.

[192] I. D. Parker. Carrier tunneling and device characteristics in polymer light-emitting diodes. *J. Appl. Phys.*, 75(3):1656–1666, 1994.

[193] C.A. Amorim, M.R. Cavallari, G. Santos, F.J. Fonseca, A.M. Andrade, and S. Mergulhão. Determination of carrier mobility in MEH-PPV thin-films by stationary and transient current techniques. *J Nom-Cryst. Solids*, 358(3):484 – 491, 2012.

[194] L. Bozano, S. A. Carter, J. C. Scott, G. G. Malliaras, and P. J. Brock. Temperature- and field-dependent electron and hole mobilities in polymer light-emitting diodes. *Appl. Phys. Lett.*, 74(8):1132–1134, 1999.

[195] T. van Woudenbergh, P. W. M. Blom, and J. N. Huiberts. Electro-optical properties of a polymer light-emitting diode with an injection-limited hole contact. *Appl. Phys. Lett.*, 82:985, 2003.

[196] J. A. Barker, C. M. Ramsdale, and N. C. Greenham. Modeling the current-voltage characteristics of bilayer polymer photovoltaic devices. *Phys. Rev. B*, 67:075205, 2003.

[197] Sungyeop Jung; Kyoung-Youm Kim; Yeon-Il Lee; Jun-Ho Youn; Hie-Tae Moon; Jin Jang; and Jungho Kim. Optical modeling and analysis of organic solar cells with coherent multilayers and incoherent glass substrate using generalized transfer matrix method. *Japanese Journal of Applied Physics*, 50:122301, 2011.

[198] Ali Mahmoudloo; and Sohrab Ahmadi-Kandjani. Influence of the temperature on the charge transport and recombination profile in organic bulk heterojunction solar cells: a drift-diffusion study. *Applied Physics A*, 119:(1523):1523–1529, 2015.

[199] Thomas Kirchartz, Jenny Nelson, and Uwe Rau. Reciprocity between charge injection and extraction and its influence on the interpretation of electroluminescence spectra in organic solar cells. *Phys. Rev. Appl.*, 5:054003, May 2016.

[200] J. Campbell Scott and G. G. Malliaras. Charge injection and recombination at the metal-organic interface. *Chem. Phys. Lett.*, 299(2):115–119, 1999.

[201] V. I. Arkhipov, P. Heremans, E. V. Emelianova, G. J. Adriaenssens, and Bässler H. Charge carrier mobility in doped disordered organic semiconductors. *J. Non-Cryst. Solids*, 338-340:603–606, 2004.

[202] V. I. Arkhipov, E. V. Emelianova, A. Kadashuk, and H. Bässler. Hopping model of thermally stimulated photoluminescence organic materials. *Chem. Phys.*, 266(1), 2001.

[203] P. López-Varo, J.A. Jiménez-Tejada, O. Marinov, C.H. Chen, and M.J. Deen. Charge density at the contacts of symmetric and asymmetric organic diodes. *Org. Electron.*, 35:74 – 86, 2016.

[204] C. G. Shuttle, A. Maurano, R. Hamilton, B. O'Regan, J. C. de Mello, and J. R. Durrant. Charge extraction analysis of charge carrier densities in a polythiophene/fullerene solar cell: Analysis of the origin of the device dark current. *Appl. Phys. Lett.*, 93(18), 2008.

[205] C. G. Shuttle, B. O'Regan, A. M. Ballantyne, J. Nelson, D. D. C. Bradley, J. de Mello, and J. R. Durrant. Experimental determination of the rate law for charge carrier decay in a polythiophene:fullerene solar cell. *Appl. Phys. Lett.*, 92(9), 2008.

[206] G. G. Malliaras, J. R. Salem, P. J. Brock, and J. C. Scott. Photovoltaic measurement of the built-in potential in organic light emitting diodes and photodiodes. *J. Appl. Phys.*, 84(3):1583–1587, 1998.

[207] P. Peumans, A. Yakimov, and S. Forrest. Small molecular weight organic thin-film photodetectors and solar cells. *J. Appl. Phys.*, 93:3693, 2003.

[208] G. Burkhard, E. Hoke, and M. McGehee. Accounting for interference, scattering, and electrode absorption to make accurate internal quantum efficiency measurements in organic and other thin solar cells. *Adv. Mater.*, 22:3293–3297, 2010.

[209] Z. Knittl. *Optics of Thin Films*. Wiley London, 1976.

[210] R. M. A. Azzam and N. M. Bashara. *Ellipsometry and Polarized Light*. North-Holland Amsterdam, 1977.

[211] Maria Hilczer and M. Tachiya. Unified theory of geminate and bulk electron-hole recombination in organic solar cells. *J. Phys. Chem. C*, 114:6808–6813, 2010.

[212] Girish Lakhwani; Akshay Rao; and Richard H. Friend. Bimolecular recombination in organic photovoltaics. *Annu. Rev. Phys. Chem.*, 65(557), 2014.

[213] Sheridan Few; Jarvist M. Frostab; and Jenny Nelson. Models of charge pair generation in organic solar cells. *Physical Chemistry Chemical Physics*, 17:2311–2325, 2015.

[214] Chang Hyun Kim; Omid Yaghmazadeh; Yvan Bonnassieux; and Gilles Horowitz. Modeling the low-voltage regime of organic diodes: Origin of the ideality factor. *Journal Applied of Phisics*, 110(093722), 2011.

[215] Yohai Roichman and Nir Tessler. Generalized einstein relation for disordered semiconductors—implications for device performance. *Appl. Phys. Lett.*, 80(11):1948–1950, 2002.

[216] S. M. Sze. *Physics of semiconductor devices*. WileyInterscience, 1981.

[217] A. Pivrikas, G. Juška, A. J. Mozer, M. Scharber, K. Arlauskas, N. S. Sariciftci, H. Stubb, and R. Österbacka. Bimolecular recombination coefficient as a sensitive testing parameter for low-mobility solar-cell materials. *Phys. Rev. Lett.*, 94:176806, May 2005.

[218] A. Wagenpfahl; D. Rauh; M. Binder; C. Deibel; and V. Dyakonov;. S-shaped current-voltage characteristics of organic solar devices. *Phys. Rev. B.*, 82:115306, 2010.

[219] B. Ruhstaller; S. Carter; S. Barth; H. Riel; W. Riess; and J. C. Scott. Transient and steady state behavior of space charges in multilayer organic light-emitting diodes. *J. Appl. Phys.*, 89(8):4575–4586, 2001.

[220] E. Knapp; and B. Ruhstaller. Numerical analysis of steady-state and transient charge transport in organic semiconductor devices. *Springer Opt. Quant. Electron.*, 2011.

[221] M. Neukom; S. Zufle; adn B. Ruhstaller. Reliable extraction of organic solar cell parameters by combining steady-state and transient techniques. *Organic Electronics*, 13(12):2910–2916, 2012.

[222] B. Ruhstaller E. Knapp. The role of shallow traps in dynamic characterization of organic semiconductor devices. *J. Appl. Phys., 112(2),*, 112(2):024519–1–6, 2012.

[223] R. H́ausermann, E. Knapp, M. Moos, N. A. Reinke, T. Flatz, and B. Ruhstaller. Coupled opto-electronic simulation of organic bulk-heterojunction solar cells: parameter extraction and sensitivity analysis. *J. Appl. Phys.*, 106:104507, 2009.

[224] V. I. Arkhipov, U. Wolf, and H. Bässler. Current injection from a metal to a disordered hopping system. ii. comparison between analytic theory and simulation. *Phys. Rev. B*, 59(11):7514–7520, Mar 1999.

[225] Naveen Elumalai; and Ashraf Uddin. Open circuit voltage of organic solar cells: An in-depth review. *Energy & Environmental Science*, 2015.

[226] D. Credgington; and J. R. Durrant. Insights from transient optoelectronic analyses on the open-circuit voltage of organic solar cells. *The Journal of Physical Chemistry Letters*, 3:1465–1478, 2012.

[227] Wolfgang Brütting, Stefan Berleb, and Anton G. Mükl. Device physics of organic light-emitting diodes based on molecular materials. *Org. Electron.*, 2(1):1 – 36, 2001.

[228] Yutaka Noguchi, Yukimasa Miyazaki, Yuya Tanaka, Naoki Sato, Yasuo Nakayama, Tobias D. Schmidt, Wolfgang Brütting, and Hisao Ishii. Charge accumulation at organic semiconductor interfaces due to a permanent dipole moment and its orientational order in bilayer devices. *J. Appl. Phys.*, 111(11):114508–1–114508–10, 2012.

[229] C. H. Kim, Y. Bonnassieux, and G. Horowitz. Charge distribution and contact resistance model for coplanar organic field-effect transistors. *IEEE Trans. Electron Devices*, 60(1):280–287, 2013.

[230] A. H. Castro Neto, F. Guinea, N. M. R. Peres, K. S. Novoselov, and A. K. Geim. The electronic properties of graphene. *Rev. Mod. Phys.*, 81(1):109–162, Jan.-Mar. 2009.

[231] I. Popov, G. Seifert, and D. Tomanek. Designing electrical contacts to MoS_2 monolayers: A computational study. *Phys. Rev. Lett.*, 108(15):156802–1–156802–5, Apr. 2012.

[232] H. K. Seong, E. K. Jeon, M. H. Kim, H. Oh, J. O. Lee, J. J. Kim, and H. J. Choi. Interface charge induced p-type characteristics of aligned $Si_{1-x}Ge_x$ nanowires. *Nano Lett.*, 8(11):3656–3661, Nov. 2008.

[233] B. Ma, B. J. Kim, L. Deng, D. A. Poulsen, M. E. Thompson, and J. M. J. Fréchet. Bipolar copolymers as host for electroluminescent devices: Effects of molecular structure on film morphology and device performance. *Macromolecules*, 40(23):8156–8161, 2007.

[234] S. Chung, J. Jeong, D. Kim, Y. Park, C. Lee, and Y. Hong. Contact resistance of inkjet-printed silver source-drain electrodes in bottom-contact OTFTs. *J. Disp. Technol.*, 8(1):48–53, 2012.

[235] K. Nagashio and A. Toriumi. Density-of-states limited contact resistance in graphene field-effect transistors. *Jpn. J. Appl. Phys.*, 50(7, Part 1):070108–1–070108–6, Jul. 2011.

[236] M. J. Deen and P. K. Basu. *Silicon Photonics. Fundamentals and Devices*. Wiley, 2012.

[237] N.F. Mott. Note on the contact between a metal and an insulator or semi-conductor. *P. Camb. Philol. Soc.*, 34:568–572, 1938.

[238] W. Schottky. Discrepencies in Ohm's laws in semiconductors. *Phys. Z*, 41:570–573, 1940.

[239] F. Xia, V. Perebeinos, Y. M. Lin, Y. Wu, and P. Avouris. The origins and limits of metal-graphene junction resistance. *Nat. Nanotechnol*, 6(3):179–184, Mar. 2011.

[240] S. M. Song, J. K. Park, O. J. Sul, and B. J. Cho. Determination of work function of graphene under a metal electrode and its role in contact resistance. *Nano Lett.*, 12(8):3887–3892, Aug. 2012.

[241] G. Giovannetti, P. A. Khomyakov, G. Brocks, V. M. Karpan, J. van den Brink, and P. J. Kelly. Doping graphene with metal contacts. *Phys. Rev. Lett.*, 101(2):026803–1–026803–4, Jul. 2008.

[242] T. Wang, B. Yu, Y. Liu, and M. J. Deen. Investigation of electrically induced migration of copper on grapheme surfaces: Theory and experiments. *Appl. Phys. Lett.*, 103:073104–1–073104–3, 2013.

[243] R. T. Tung. Chemical bonding and Fermi level pinning at metal-semiconductor interfaces. *Phys. Rev. Lett.*, 84(26):6078–6081, Jun. 2000.

[244] V. Heine. Theory of Surface States. *Phys. Rev.*, 138(6A):1689–1696, 1965.

[245] J. Tersoff. Schottky-barrier heights and the continuum of gap states. *Phys. Rev. Lett.*, 52(6):465–468, 1984.

[246] Y. He, J. Zhang, S. Hou, Y. Wang, and Z. Yu. Schottky barrier formation at metal electrodes and semiconducting carbon nanotubes. *Appl. Phys. Lett.*, 94(9):093107, 2009.

[247] S. Braun, W. R. Salaneck, and M. Fahlman. Energy-level alignment at organic/metal and organic/organic interfaces. *Adv. Mater.*, 21(14-15):1450–1472, 2009.

[248] Z. Liu, M. Kobayashi, B. C. Paul, Z. Bao, and Y. Nishi. Contact engineering for organic semiconductor devices via Fermi level depinning at the metal-organic interface. *Phys. Rev. B*, 82:035311–1–035311–6, Jul. 2010.

[249] S. Yadav, P. Kumar, and S. Ghosh. Optimization of surface morphology to reduce the effect of grain boundaries and contact resistance in small molecule based thin film transistors. *Appl. Phys. Lett.*, 101(19):193307, 2012.

[250] J. H. Seo, A. Gutacker, B. Walker, S. Cho, A. Garcia, R. Yang, T. Q. Nguyen, A. J. Heeger, and G. C. Bazan. Improved injection in n-type organic transistors with conjugated polyelectrolytes. *J. Am. Chem. Soc.*, 131(51):18220–18221, 2009.

[251] D. Braga, M. Ha, W. Xie, and C. D. Frisbie. Ultralow contact resistance in electrolyte-gated organic thin film transistors. *Appl. Phys. Lett.*, 97(19):193311, 2010.

[252] J. Knoch, Z. Chen, and J. Appenzeller. Properties of metal-graphene contacts. *IEEE NANO*, 11(3):513–519, May. 2012.

[253] L. Yan, C. Punckt, I. A. Aksay, W. Mertin, and G. Bacher. Local voltage drop in a single functionalized graphene sheet characterized by kelvin probe force microscopy. *Nano Lett.*, 11(9):3543–3549, Sep. 2011.

[254] Y. Khatami, H. Li, C. Xu, and K. Banerjee. Metal-to-multilayer-graphene contact-part I: Contact resistance modeling. *IEEE Trans. Electron Devices*, 59(9):2444–2452, Sep. 2012.

[255] S. Das, H. Y. Chen, A. V. Penumatcha, and J. Appenzeller. High Performance Multilayer MoS_2 Transistors with Scandium Contacts. *Nano Lett.*, 13(1):100–105, Jan. 2013.

[256] H. Qiu, L. Pan, Z. Yao, J. Li, Y. Shi, and X. Wang. Electrical characterization of back-gated bi-layer MoS_2 field-effect transistors and the effect of ambient on their performances. *Appl. Phys. Lett.*, 100(12):123104–1–123104–3, Mar. 2012.

[257] B. Liu, Y. Wang, S. Dilts, T. S. Mayer, and S. E. Mohney. Silicidation of silicon nanowires by platinum. *Nano Lett.*, 7(3):818–824, Mar. 2007.

[258] I. Kymissis, C.D. Dimitrakopoulos, and S. Purushothaman. High-performance bottom electrode organic thin-film transistors. *IEEE Trans. Electron Devices*, 48(6):1060 –1064, Jun 2001.

[259] S. Scheinert and G. Paasch. Fabrication and analysis of polymer field effect transistors. *Phys. Stat. Sol. (A)*, 201(6):pp. 1263–1301, 2004.

[260] S. D. Wang, Y. Yan, and K. Tsukagoshi. Understanding contact behavior in organic thin film transistors. *Appl. Phys. Lett.*, 97(6):063307–1–063307–3, 2010.

[261] H. Wang, L. Li, Z. Ji, C. Lu, J. Guo, L. Wang, and M. Liu. Contact-Length-Dependent Contact Resistance of Top-Gate Staggered Organic Thin-Film Transistors. *IEEE Electron Device Lett.*, 34(1):69–71, Jan. 2013.

[262] M.J. Deen and F. Pascal. Electrical characterization of semiconductor materials and devices. review. *J. Mater. Sci.- Mater. El.*, 17(8):549–575, 2006.

[263] G.K. Reeves and H.B. Harrison. Obtaining the specific contact resistance from transmission-line model measurements. *Electron Devic. Lett.*, 3(5):111–113, 1982.

[264] R. Nouchi, T. Saito, and K. Tanigaki. Observation of negative contact resistances in graphene field-effect transistors. *J. Appl. Phys.*, 111(8):084314–1–084314–7, Apr. 2012.

[265] R. Nouchi and K. Tanigaki. Empirical modeling of metal-contact effects on graphene field-effect transistors. *Jpn. J. Appl. Phys.*, 50(7, 1):070109–1–070109–4, Jul. 2011.

[266] S. E. Mohney, Y. Wang, M. A. Cabassi, K. K. Lew, S. Dey, J. M. Redwing, and T. S. Mayer. Measuring the specific contact resistance of contacts to semiconductor nanowires. *Solid-State Electron.*, 49(2):227–232, Feb. 2005.

[267] H. Park, R. Beresford, R. Ha, H. J. Choi, H. Shin, and J. Xu. Evaluation of metal-nanowire electrical contacts by measuring contact end resistance. *Nanotechnology*, 23(24):245201–1–245201–7, Jun. 2012.

[268] J. Hu, Y. Liu, C. Z. Ning, R. Dutton, and S. M. Kang. Fringing field effects on electrical resistivity of semiconductor nanowire-metal contacts. *Appl. Phys. Lett.*, 92(8):083503–1–083503–, Feb. 2008.

[269] T. Mueller, F. Xia, M. Freitag, J. Tsang, and Ph. Avouris. Role of contacts in graphene transistors: A scanning photocurrent study. *Phys. Rev. B*, 79(24):245430–1–245430–6, Jun. 2009.

[270] F. Leonard and A. A. Talin. Electrical contacts to one- and two-dimensional nanomaterials. *Nat. Nanotechnol*, 6(12):773–783, Dec. 2011.

[271] F. Xia, T. Mueller, R. Golizadeh-Mojarad, M. Freitag, J. Lin, Y. M.and Tsang, and P. Perebeinos, V.and Avouris. Photocurrent Imaging and Efficient Photon Detection in a Graphene Transistor. *Nano Lett.*, 9(3):1039–1044, Mar. 2009.

[272] L. Bürgi, T. J. Richards, R. H. Friend, and H. Sirringhaus. Close look at charge carrier injection in polymer field-effect transistors. *J. Appl. Phys.*, 94(9):6129–6137, 2003.

[273] M. Estrada, I. Mejía, A. Cerdeira, J. Pallares, L. F. Marsal, and B. Iñiguez. Mobility model for compact device modeling of OTFTs made with different materials. *Solid-State Electron.*, 52(5):787 – 794, 2008.

[274] D. J. Gundlach, L. Zhou, J. A. Nichols, T. N. Jackson, P. V. Necliudov, and M. S. Shur. An experimental study of contact effects in organic thin film transistors. *J. Appl. Phys.*, 100(2):024509–1–024509–13, 2006.

[275] P. V. Necliudov, M. S. Shur, D. J. Gundlach, and T. N. Jackson. Modeling of organic thin film transistors of different designs. *J. Appl. Phys.*, 88(11):6594–6597, 2000.

[276] S. D. Wang, T. Minari, T. Miyadera, K. Tsukagoshi, and Y. Aoyagi. Contact-metal dependent current injection in pentacene thin-film transistors. *Appl. Phys. Lett.*, 91(20):203508–1–203508–3, 2007.

[277] V. Vinciguerra, M. La Rosa, D. Nicolosi, G. Sicurella, and L. Occhipinti. Modeling the gate bias dependence of contact resistance in staggered polycrystalline organic thin film transistors. *Org. Electron.*, 10(6):1074 – 1081, 2009.

[278] A. Valletta, A. Daami, M. Benwadih, R. Coppard, G. Fortunato, M. Rapisarda, F. Torricelli, and L. Mariucci. Contact effects in high performance fully printed p-channel organic thin film transistors. *Appl. Phys. Lett.*, 99(23):233309–1–233309–4, 2011.

[279] M. J. Deen, M. H. Kazemeini, and S. Holdcroft. Contact effects and extraction of intrinsic parameters in poly(3-alkylthiophene) thin film field-effect transistors. *J. Appl. Phys.*, 103(12):124509–1–124509–7, 2008.

[280] Y. Hong, F. Yan, P. Migliorato, S.H. Han, and J. Jang. Injection-limited contact in bottom-contact pentacene organic thin-film transistors. *Thin Solid Films*, 515(78):4032 – 4035, 2007.

[281] Y. J. Lin and B. C. Huang. Influence of the contact resistance effect on the output characteristics of pentacene-based organic thin film transistors. *Microelectron. Eng.*, 103:76 – 78, 2013.

[282] T. B. Singh, N. Marjanović, G. J. Matt, N. S. Sariciftci, R. Schwödiauer, and S. Bauer. Nonvolatile organic field-effect transistor memory element with a polymeric gate electret. *Appl. Phys. Lett.*, 85(22):5409–5411, 2004.

[283] M. Estrada, A. Cerdeira, J. Puigdollers, L. Reséndiz, J. Pallares, L. F. Marsal, C. Voz, and B. Iñiguez. Accurate modeling and parameter extraction method for organic TFTs. *Solid-State Electron.*, 49:1009–1016, 2005.

[284] M. Shur and M. Hack. Physics of amorphous silicon based alloy field-effect transistors. *J. Appl. Phys.*, 55(10):3831–3842, 1984.

[285] M. C. J. M. Vissenberg and M. Matters. Theory of the field-effect mobility in amorphous organic transistors. *Phys. Rev. B*, 57(20):12964–12967, May 1998.

[286] E. Calvetti, A. Savio, Zs. M. Kovács-Vajna, and L. Colalongo. Analytical model for organic thin-film transistors operating in the subthreshold region. *Appl. Phys. Lett.*, 87(22):223506–1–223506–3, 2005.

[287] L. Mariucci, M. Rapisarda, A. Valletta, S. Jacob, M. Benwadih, and G. Fortunato. Current spreading effects in fully printed p-channel organic thin film transistors with Schottky source and drain contacts. *Org. Electron.*, 14(1):86 – 93, 2013.

[288] M. Rapisarda, A. Valletta, A. Daami, S. Jacob, M. Benwadih, R. Coppard, G. Fortunato, and L. Mariucci. Analysis of contact effects in fully printed p-channel organic thin film transistors. *Org. Electron.*, 13(10):2017 – 2027, 2012.

[289] A. Raychaudhuri, J. Kolk, M. J. Deen, and M. I. H. King. A simple method to extract the asymmetry in parasitic source and drain resistances from measurements on a MOS transistor. *IEEE Trans. Electron Devices*, 42(7):1388–1390, 1995.

[290] L. S. C. Pingree, O. G. Reid, and D. S. Ginger. Electrical scanning probe microscopy on active organic electronic devices. *Adv. Mater.*, 21(1):19–28, 2009.

[291] A. K. Agarwal and B. Mazhari. Simultaneous extraction of source and drain resistances in top contact organic thin film transistors from a single test structure. *Org. Electron.*, 13(11):2659–2666, 2012.

[292] S. D. Wang, T. Minari, T. Miyadera, K. Tsukagoshi, and J. X. Tang. Contact resistance instability in pentacene thin film transistors induced by ambient gases. *Appl. Phys. Lett.*, 94(8):083309–1–083309–3, 2009.

[293] Y. Ishikawa, Y. Wada, and T. Toyabe. Origin of characteristics differences between top and bottom contact organic thin film transistors. *J. Appl. Phys.*, 107(5):053709–1–053709–7, 2010.

[294] B. G. Streetman. *Solid State Electronic Devices*. Prentice-Hall, Englewood Cliffs, NJ, 1980.

[295] O. Marinov, M. J. Deen, J. Yu, G. Vamvounis, S. Holdcroft, and W. Woods. Variable current transport in polymer thin film transistors. *J. Vac. Sci. Technol. A*, 22(3):755–759, 2004.

[296] K. M. Awawdeh, J. A. Jiménez Tejada, P. López Varo, J. A. López Villanueva, and M. J. Deen. Influence of the contact effects on the variation of the trapped charge in the intrinsic channel of organic thin film transistors. In *2013 Spanish Conference on Electron Devices (CDE)*, pages 71–74, 2013.

[297] A. Cerdeira, M. Estrada, R. García, A. Ortiz Conde, and F.J. García Sánchez. New procedure for the extraction of basic a-Si:H TFT model parameters in the linear and saturation regions. *Solid-State Electron.*, 45(7):1077 – 1080, 2001.

[298] C. W. Sohn, T. U. Rim, G. B. Choi, and Y. H. Jeong. Analysis of contact effects in inverted-staggered organic thin-film transistors based on anisotropic conduction. *IEEE Trans. Electron Devices*, 57(5):986–994, 2010.

[299] M. Egginger. *Electrical Characterisation of Poly(vinyl alcohol) based Organic Field Effect Transistors*. PhD thesis, Ph.D. dissertation, Johannes Kepler University of Linz, Johannes Kepler University Linz, Altenbergerstraße, Linz, Austria, 2009.

[300] M. Estrada, A. Cerdeira, I. Mejia, M. Avila, R. Picos, L. F. Marsal, J. Pallares, and B. Iñiguez. Modeling the behavior of charge carrier mobility with temperature in thin-film polymeric transistors. *Microelectron. Eng.*, 87:2565–2570, 2010.

[301] D. A. Bernards, D. J. Macaya, M. Nikolou, J. A. DeFranco, S. Takamatsu, and G. G. Malliaras. Enzymatic sensing with organic electrochemical transistors. *J. Mater. Chem.*, 18:116–120, 2008.

[302] L. Torsi, F. Marinelli, M. D. Angione, A. Dell'Aquila, N. Cioffi, E. De Giglio, and L. Sabbatini. Contact effects in organic thin-film transistor sensors. *Org. Electron.*, 10(2):233 – 239, 2009.

[303] L. C. Teague, O. D. Jurchescu, C. A. Richter, S. Subramanian, J. E. Anthony, T. N. Jackson, D. J. Gundlach, and J. G. Kushmerick. Probing stress effects in single crystal organic transistors by scanning Kelvin probe microscopy. *Appl. Phys. Lett.*, 96(20):203305–1–203305–3, 2010.

[304] Pilar Lopez-Varo, Luca Bertoluzzi, Juan Bisquert, Marin Alexe, Mariona Coll, Jinsong Huang, Juan Antonio Jimenez-Tejada, Thomas Kirchartz, Riad Nechache, Federico Rosei, and Yongbo Yuan. Physical aspects of ferroelectric semiconductors for photovoltaic solar energy conversion. *Physics Reports*, 653:1 – 40, 2016. Physical aspects of ferroelectric semiconductors for photovoltaic solar energy conversion.

[305] R. Nechache, C. Harnagea, S. Li, L. Cardenas, W. Huang, J. Chakrabartty, and F. Rosei. Bandgap tuning of multiferroic oxide solar cells. *Nature Photonics*, 9:61 – 67, 2015.

[306] P. W. M. Blom, R. M. Wolf, J. F. M. Cillessen, and M. P. C. M. Krijn. Ferroelectric schottky diode. *Phys. Rev. Lett.*, 73:2107–2110, Oct 1994.

[307] Meng Qin, Kui Yao, and Yung C. Liang. Photovoltaic mechanisms in ferroelectric thin films with the effects of the electrodes and interfaces. *Applied Physics Letters*, 95(2), 2009.

[308] Phanish Suryanarayana and Kaushik Bhattacharya. Evolution of polarization and space charges in semiconducting ferroelectrics. *Journal of Applied Physics*, 111(3), 2012.

[309] Chen Ge, Kui-Juan Jin, Can Wang, Hui-Bin Lu, Cong Wang, and Guo-Zhen Yang. Numerical investigation into the switchable diode effect in metal-ferroelectric-metal structures. *Applied Physics Letters*, 99(6), 2011.

[310] Can Wang, Kui-juan Jin, Zhong-tang Xu, Le Wang, Chen Ge, Hui-bin Lu, Hai-zhong Guo, Meng He, and Guo-zhen Yang. Switchable diode effect and ferroelectric resistive switching in epitaxial $BiFeO_3$ thin films. *Applied Physics Letters*, 98(19), 2011.

[311] H. T. Yi, T. Choi, S. G. Choi, Y. S. Oh, and S.-W. Cheong. Mechanism of the switchable photovoltaic effect in ferroelectric $BiFeO_3$. *Advanced Materials*, 23(30):3403–3407, 2011.

[312] W. Ruppel, R. Von Baltz, and P. Wurfel. The origin of the photo-emf in ferroelectric and non-ferroelectric materials. *Ferroelectrics*, 43(1):109–123, 1982.

[313] Juan Bisquert, David Cahen, Gary Hodes, Sven Ruhle, and Arie Zaban. Physical chemical principles of photovoltaic conversion with nanoparticulate, mesoporous dye-sensitized solar cells. *The Journal of Physical Chemistry B*, 108(24):8106 – 8118, 2004.

[314] P. Würfel. *Physics of Solar Cells. From Principles to New Concepts*. Wiley, 2005.

[315] T. Kirchartz, J. Bisquert, I. Mora-Sero, and G. Garcia-Belmonte. Classification of solar cells according to mechanisms of charge separation and charge collection. *Physical Chemistry Chemical Physics*, 17:4007 – 4014, 2015.

[316] Juan Bisquert. *Nanostructured Energy Devices: Equilibrium Concepts and Kinetics*. CRC Press: Boca Raton, 2014.

[317] Hui Liu, Jun Chen, Yang Ren, Linxing Zhang, Zhao Pan, Longlong Fan, and Xianran Xing. Large photovoltage and controllable photovoltaic effect in $PbTiO_3$-Bi(Ni2/3+xNb1/3ax)O_3 δ ferroelectrics. *Advanced Electronic Materials*, 1(4):1400051, 2015. 1400051.

[318] P. T. Landsberg and C. Klimpke. Theory of the Schottky barrier solar cell. *Proceedings Royal Society (London) A*, 354:101 – 118, 1977.

[319] W Gärtner. Depletion-layer photoeffects in semiconductors. *Physical Review*, 116:84–87, 1959.

[320] Wei Ji, Kui Yao, and Yung C. Liang. Bulk photovoltaic effect at visible wavelength in epitaxial ferroelectric $BiFeO_3$ thin films. *Advanced Materials*, 22(15):1763–1766, 2010.

[321] D. Lee, S. H. Baek, T. H. Kim, J.-G. Yoon, C. M. Folkman, C. B. Eom, and T. W. Noh. Polarity control of carrier injection at ferroelectric/metal interfaces for electrically switchable diode and photovoltaic effects. *Phys. Rev. B*, 84:125305, Sep 2011.

[322] H. T. Yi, T. Choi, S. G. Choi, Y. S. Oh, and S.-W. Cheong. Mechanism of the switchable photovoltaic effect in ferroelectric $BiFeO_3$. *Advanced Materials*, 23(30):3403–3407, 2011.

[323] Yuxi Yang, Wenting Xu, Xijun Xu, Yaojin Wang, Guoliang Yuan, Yiping Wang, and Zhiguo Liu. The enhanced photocurrent of epitaxial $BiFeO_3$ film at 130 c. *Journal of Applied Physics*, 119(4), 2016.

[324] M. Alexe, C. Harnagea, D. Hesse, and U. Gösele. Polarization imprint and size effects in mesoscopic ferroelectric structures. *Applied Physics Letters*, 79(2):242–244, 2001.

[325] L. Pintilie and M. Alexe. Metal-ferroelectric-metal heterostructures with schottky contacts. i. influence of the ferroelectric properties. *Journal of Applied Physics*, 98(12), 2005.

[326] I. B. Misirlioglu and M. Yildiz. Carrier accumulation near electrodes in ferroelectric films due to polarization boundary conditions. *Journal of Applied Physics*, 116(2), 2014.

[327] Bo Bo Tian, Yang Liu, Liu Fang Chen, Jian Lu Wanga, Shuo Sun, Hong Shen, Jing Lan Sun, Guo Liang Yuan, Stephane Fusil, Vincent Garcia, Brahim Dkhil, Xiang Jian Meng, and Jun Hao Chu. Space-charge effect on electroresistance in metal-ferroelectric-metal capacitors. *Scientific Reports*, 5(18297), 2015.

[328] Xiaohui Liu, Yong Wang, J. D. Burton, and Evgeny Y. Tsymbal. Polarization-controlled ohmic to schottky transition at a metal/ferroelectric interface. *Phys. Rev. B*, 88:165139, Oct 2013.

[329] Liang Fang, Lu You, Yang Zhou, Peng Ren, Zhi Shiuh Lim, and Junling Wang. Switchable photovoltaic response from polarization modulated interfaces in $BiFeO_3$ thin films. *Applied Physics Letters*, 104(14), 2014.

[330] I. P. Batra, P. Wurfel, and B. D. Silverman. Phase transition, stability, and depolarization field in ferroelectric thin films. *Phys. Rev. B*, 8:3257–3265, Oct 1973.

[331] R. R. Mehta, B. D. Silverman, and J. T. Jacobs. Depolarization fields in thin ferroelectric films. *Journal of Applied Physics*, 44(8):3379–3385, 1973.

[332] J. Y. Jo, Y. S. Kim, T. W. Noh, Jong-Gul Yoon, and T. K. Song. Coercive fields in ultrathin batio3 capacitors. *Applied Physics Letters*, 89(23), 2006.

[333] M. Ye. Zhuravlev, R. F. Sabirianov, S. S. Jaswal, and E. Y. Tsymbal. Giant electroresistance in ferroelectric tunnel junctions. *Phys. Rev. Lett.*, 94:246802, Jun 2005.

[334] D. Pantel and M. Alexe. Electroresistance effects in ferroelectric tunnel barriers. *Phys. Rev. B*, 82:134105, Oct 2010.

[335] Ronald C. G. Naber, Kamal Asadi, Paul W. M. Blom, Dago M. de Leeuw, and Bert de Boer. Organic nonvolatile memory devices based on ferroelectricity. *Advanced Materials*, 22(9):933–945, 2010.

[336] P.S. Brody. High voltage photovoltaic effect in barium titanate and lead titanate-lead zirconate ceramics. *Journal of Solid State Chemistry*, 12(3):193 – 200, 1975.

[337] Masaaki Ichiki, Yasushi Morikawa, and Takeshi Nakada. Electrical properties of ferroelectric lead lanthanum zirconate titanate as an energy transducer for application to electrostatic-optical motor. *Japanese Journal of Applied Physics*, 41(11S):6993, 2002.

[338] M. Ichiki, H. Furue, T. Kobayashi, R. Maeda, Y. Morikawa, T. Nakada, and K. Nonaka. Photovoltaic properties of (pb,la)(zr,ti)o3 films with different crystallographic orientations. *Applied Physics Letters*, 87(22), 2005.

[339] Meng Qin, Kui Yao, Yung C. Liang, and Santiranjan Shannigrahi. Thickness effects on photoinduced current in ferroelectric $(Pb_{0.97}La_{0.03})(Zr_{0.52}Ti_{0.48})O_3$ thin films. *Journal of Applied Physics*, 101(1), 2007.

[340] Y. S. Yang, S. J. Lee, S. Yi, B. G. Chae, S. H. Lee, H. J. Joo, and M. S. Jang. Schottky barrier effects in the photocurrent of sol–gel derived lead zirconate titanate thin film capacitors. *Applied Physics Letters*, 76(6):774–776, 2000.

[341] Guo-Liang Yuan and Junling Wang. Evidences for the depletion region induced by the polarization of ferroelectric semiconductors. *Applied Physics Letters*, 95(25), 2009.

[342] Rui Guo, Lu You, Yang Zhou, Zhi Shiuh Lim, Xi Zou, Lang Chen, R. Ramesh, and Junling Wang. Non-volatile memory based on the ferroelectric photovoltaic effect. *Nat Commun*, 4, 2013.

[343] Y. Cao, J. Shen, C. A. Randall, and L. Q. Chen. Phase-field modeling of switchable diode-like current-voltage characteristics in ferroelectric batio3. *Applied Physics Letters*, 104(18), 2014.

[344] Gertrude F. Neumark. Theory of the anomalous photovoltaic effect of zns. *Phys. Rev.*, 125:838–845, Feb 1962.

[345] R. R. Mehta. Some theoretical considerations relating to switching and remanence in ferroelectric/photoconductor memory devices. *Ferroelectrics*, 4:5–18, 1972.

[346] Ralph Smith and Jordan E. Massad. A unified, methodology for modeling hysteresis in ferroelectric, ferromagnetic and ferroelastic materials. *North Carolina State University,Center for Research in Scientific Computation,Raleigh*, 2001.

[347] P. Chandra and P.B. Littlewood. A Landau Primer for Ferroelectrics. *Condensed Matter Physics*, 105:69 – 116, 2006.

[348] S. L. Miller, R. D. Nasby, J. R. Schwank, M. S. Rodgers, and P. V. Dressendorfer. Device modeling of ferroelectric capacitors. *Journal of Applied Physics*, 68(12):6463–6471, 1990.

[349] S. L. Miller, J. R. Schwank, R. D. Nasby, and M. S. Rodgers. Modeling ferroelectric capacitor switching with asymmetric nonperiodic input signals and arbitrary initial conditions. *Journal of Applied Physics*, 70(5):2849–2860, 1991.

[350] Timothy J. Reece and Stephen Ducharme. Modeling of metal-ferroelectric-insulator-semiconductor structures based on Langmuir Blodgett copolymer films. *Journal of Applied Physics*, 106(12), 2009.

[351] F. Preisach. Über die magnetische nachwirkung. *Zeitschrift für Physik*, 94:277 – 302, 1935.

[352] Feng Yang, Y. C. Zhou, M. H. Tang, and Fen Liu. Simulation of electric displacement hysteresis and strain butterfly loops in perovskite ferroelectric films. *Journal of Applied Physics*, 106(1), 2009.

[353] Jingsong Liu, Shuren Zhang, Fugui Chen, Chengtao Yang, and Xiaohua Zhou. Measurements and simulation of hysteresis loops of donor-doped strontium bismuth tantalate ceramics. *Physics Letters A*, 321(3):199 – 204, 2004.

[354] J. Bisquert; R. Gottesman; P. Lopez-Varo; L. Gouda; J. A. Jimenez-Tejada; J. Hu; S. Tirosh; A. Zaban. Dynamic phenomena at perovskite/electron-selective contact interface as interpreted from photovoltage decays. *Chem*, 2016.

[355] Bjoern Niesen, Jérémie Werner, Loris Barraud, Florent Sahli, Matthias Bräuninger, Arnaud Walter, Raphaël Monnard, Bertrand Paviet-Salomon, 2 Davide Sacchetto Christophe Allebé, Matthieu Despeisse, Soo-Jin Moon, Sylvain Nicolay, Stefaan De Wolf, Stéphane Altazin, Lidia Stepanova, Kevin Lapagna, Beat Ruhstaller, and Christophe Ballif. Perovskite/crystalline silicon tandem solar cells. In *SimOEP16*, 2016.

[356] P.H. Nguyen, S. Scheinert, S. Berleb, W. Brütting, and G. Paasch. The influence of deep traps on transient current-voltage characteristics of organic light-emitting diodes. *Organic Electronics*, 2(3-4):105 – 120, 2001.

Appendix I

I.1. Analytical model for single-carrier organic diodes

The model considers drift-diffusion and known values for the hole densities at the interfaces, $p(x = 0) = p_A$ and $p(x = L) = p_C$. It also assumes a constant value for the mobility and a linear evolution of the potential along the organic material [42, 184, 356] given by,

$$V(x) = (V_{bi} - V_{AC})x/L \tag{A.1}$$

where V_{AC} is the anode-cathode voltage applied across the diode. Both sides of eq. (5.2) can be multiplied by $\exp(qV(x)/k_BT)$ and integrated between $x = 0$ and $x = L$. Assuming a constant mobility, the Einstein relation $D_p/\mu = V_T$, and since the current is also constant in the device, then

$$J_{AC}\int_0^L \exp(V/V_T)dx = -q\mu\int_{V(0)}^{V(L)} p\exp(V/V_T)dV \tag{A.2}$$

$$-\mu q V_T\int_{p_A}^{p_C}\exp(V/V_T)dp$$

We substitute (A.1) in the integral of the left-hand expression of (A.2) and integrate the right-hand expression by parts by defining $u \equiv p$ and $v \equiv \exp(V/V_T)$. The result after integrations is

$$\frac{J_{AC}V_TL}{(V_{bi} - V_{AC})}\{\exp[(V_{bi} - V_{AC})/V_T] - 1\} = \tag{A.3}$$

$$q\mu V_T\{p_A - p_C\exp[(V_{bi} - V_{AC})/V_T]\}$$

where $V(0) = 0$ and $V(L) = V_{bi} - V_{AC}$ were used for the anode and cathode potentials, respectively. Canceling V_T and multiplying by $\exp(V_{AC}/V_T)$ and $-q(V_{AC} - V_{bi})/L$ both sides of the equality, J_{AC} can be expressed as

$$J_{AC} = \frac{q\mu(V_{AC} - V_{bi})}{L}\frac{p_A\exp(V_{AC}/V_T) - p_C\exp(V_{bi}/V_T)}{\exp(V_{AC}/V_T) - \exp(V_{bi}/V_T)} \tag{A.4}$$

Equation (A.4) is an analytical relation between the current density J_{AC} and the applied voltage V_{AC} between the anode and the cathode of the diode.

Since in darkness $J_{AC} = 0$ at zero applied voltage $V_{AC} = 0$, then a relation between p_A and p_C is established, as

$$p_C = p_A \exp(-V_{bi}/V_T) \tag{A.5}$$

With this relation, eq. (A.4) can be written as function of interface charge at the anode:

$$J_{AC} = \frac{q\mu(V_{AC} - V_{bi})}{L} \frac{p_A[\exp(V_{AC}/V_T) - 1]}{\exp(V_{AC}/V_T) - \exp(V_{bi}/V_T)} \tag{A.6}$$

This model was used in [184] to reproduce experimental $J - V$ curves at low voltages.

If we assume known values for the mobility and built-in voltage in the last equation, then the value of p_A can be related to experimental values of the current density $J_{AC} = J_{exp}$ and the applied voltage $V_{AC} = V_{exp}$ as

$$p_A = \frac{J_{exp}L}{q\mu(V_{exp} - V_{bi})} \frac{\exp(V_{exp}/V_T) - \exp(V_{bi}/V_T)}{\exp(V_{exp}/V_T) - 1} \tag{A.7}$$

I.2. Extraction of the interface charge density in symmetric MOM diodes

For zero built-in voltage, eq. (A.7) reduces to

$$p_A = \frac{J_{exp}}{q\mu F_{AVG}} \approx \frac{J_{exp}}{q\mu F_0}, \text{ with } F_{AVG} = V_{exp}/L \tag{A.8}$$

where F_o is the electric field at the charge injecting interface, and F_o is approximately equal to the average electric field F_{AVG}, when space charge effects are negligible. The relation between F_o and F_{AVG} is given in II.1.

I.3. Extraction of the interface charge density in non-symmetric MOM diodes ($V_{AC} < 0$ and $V_{AC} > V_{bi}$ cases)

From the analytical expression (A.4) at positive-bias voltages higher than the built-in voltage $V_{AC} > V_{bi}$, the following asymptotical equation can be obtained

$$J_{AC} = q\mu(V_{AC} - V_{bi})p_A/L \tag{A.9}$$

The derivative of the current in eq. (A.9) as a function of the voltage is

$$\frac{dJ_{AC}}{dV_{AC}} = q\mu p_A/L \tag{A.10}$$

In similar way, from the analytical expression (A.4) at negative-bias voltages lower than zero $V_{AC} < 0$, the following asymptotical equation can be obtained

$$J_{AC} = q\mu(V_{AC} - V_{bi})p_C/L \tag{A.11}$$

The derivative of the current in eq. (A.11) as a function of the voltage is

$$\frac{dJ_{AC}}{dV_{AC}} = q\mu p_C/L \tag{A.12}$$

Thus, eqs. (A.10) and (A.12) allow for extracting the values of p_A and p_C from experimental data directly without knowing the value of the built-in voltage.

Appendix II

II.1. Relation between average, interface and space-charge electric fields

In a semiconductor with constant mobility, assuming drift-only charge transport in eq. (5.2), the current density is $J_{AC} = q\mu pF$; thus, $p = J_{AC}/(q\mu pF)$. Substituting in Poisson's eq. (5.4), the electric field in presence of space charge qp is given by [10, 186]

$$\frac{dF}{dx} = \frac{qp}{\varepsilon_r\varepsilon_0} = \frac{q}{\varepsilon_r\varepsilon_0}\frac{J_{AC}}{q\mu F} \Rightarrow F\frac{dF}{dx} = \frac{J_{AC}}{\varepsilon_r\varepsilon_0\mu} \Rightarrow$$

$$\frac{dF^2}{dx} = \frac{2J_{AC}}{\varepsilon_r\varepsilon_0\mu} \tag{B.1}$$

Taking the anode contact at $x = 0$ and denoting the electric field at the anode contact with $F_o \equiv F(0)$, then

$$F^2(x) - F_0^2 = \frac{2J_{AC}x}{\varepsilon_r\varepsilon_0\mu} \Rightarrow F(x) = \sqrt{F_0^2 + \frac{2J_{AC}x}{\varepsilon_r\varepsilon_0\mu}} \tag{B.2}$$

Substituting eq. (B.2) in eq. (5.5) and integrating from the anode $x = 0$ to a position x in the device, we obtain

$$-\Delta V = -(V(x) - V_A) = \int_0^x \sqrt{F_0^2 + \frac{2J_{AC}x}{\varepsilon_r\varepsilon_0\mu}}dx \tag{B.3}$$

where V_A is the potential at the anode. Defining a new integration variable $y \equiv F_o^2 + 2J_{AC}x/(\varepsilon_r\varepsilon_0\mu)$, and integrating, then

$$-\Delta V = \frac{\varepsilon_r\varepsilon_0\mu}{3J_{AC}}\left[\left(\sqrt{F_0^2 + \frac{2J_{AC}x}{\varepsilon_r\varepsilon_0\mu}}\right)^3 - \left(\sqrt{F_0^2}\right)^3\right] \tag{B.4}$$

Rewriting eq. (B.4) for $x = L$ (entire device), where $-(V(L) - V_A) = V_{AC}$, and dividing by L, one gets

$$F_{AVG} = \frac{V_{AC}}{L} = \frac{2}{3F_{SCLC}^2}\left[\left(\sqrt{F_0^2 + F_{SCLC}^2}\right)^3 - \left(\sqrt{F_0^2}\right)^3\right] \tag{B.5}$$

where we have defined the electric field F_{SCLC} due to space charge limited conduction (SCLC) as

$$F_{SCLC}^2 = 2J_{AC}L/(\varepsilon_r\varepsilon_0\mu) \tag{B.6}$$

The relation (B.5) between the average electric field $F_{AVG} = V_{AC}/L$, the electric field at anode F_o and the field F_{SCLC} can be transformed into

$$\frac{3F_{AVG}F_{SCLC}^2}{2} + F_0^2 = \left(\sqrt{F_0^2 + F_{SCLC}^2}\right)^3 \tag{B.7}$$

We have verified that this relation is correct for a symmetric MOM device, even when substituting data from numerical simulations with the drift-diffusion model. This is expected since the drift charge transport is dominant. The SCLC electric field is positive $F_{SCLC} > 0$, although it might be very small; in this case, $F_{AVG} \approx F_o$.

Appendix III

IIIA. Publicaciones.

Publicaciones a fecha de entrega en la Escuela de Posgrado de la Universidad de Granada:

Journal publications derived from to the Thesis

1) Modeling the ohmic-SCLC transition in organic semiconductor. P. López Varo, J. A. Jiménez Tejada, J. A. López Villanueva, J. E. Carceller, M. J. Deen. *Organic Electronics* **2012**.

2) **Invited paper.** Compact modeling and contact effects in thin film transistors. J. A. Jiménez Tejada, J. A. López Villanueva, P. López Varo, K. M. Awawdeh, M. J. Deen. *IEEE Transactions on Electron Devices* **2014**.

3) Space-charge and injection limited current in organic diodes: A unified model. P. López Varo, J. A. Jiménez Tejada, J. A. López Villanueva, M. J. Deen. *Organic Electronics* **2014**.

4) Electrical characterization of controlled and unintentional modified metal–organic contacts. P. López Varo, J. A. Jiménez Tejada, J. A. López Villanueva, M. J. Deen. *Organic Electronics* **2014**.

5) Charge density at the contacts of symmetric and asymmetric organic diodes. P. López Varo, J. A. Jiménez Tejada, O. Marinov, C. H. Chen, M. J. Deen. *Organic Electronics* **2016**.

6) Physical aspects of ferroelectric semiconductors for photovoltaic solar energy conversion. P. López Varo, L. Bertoluzzi, J. Bisquert, M. Alexe, M. Coll, J. Huang, J. A. Jiménez Tejada, T. Kirchartz, R. Nechache, F. Rosei, Y. Yuan *Physics Reports* **2016**.

Other journal publications

7) Characterization of organic thin film transistors with hysteresis and contact effects. K. M. Awawdeh, J. A. Jiménez Tejada, P. López Varo, J. A. López Villanueva, F. M. Gómez Campos, and M. J. Deen. *Organic Electronics* **2013**.

8) Charge transfer processes at the semiconductor/electrolyte interface for solar fuel production: insight from impedance spectroscopy. L. Bertoluzzi, P. López Varo, J. A. Jiménez Tejada, J. Bisquert. *Journal of Materials Chemistry A* **2016**.

9) Combinatorial Investigation and Modelling of MoO3 Hole-Selective Contact in TiO2—Co3O4—MoO3 All-Oxide Solar Cells K. Majhi, L. Bertoluzzi, K. J. Rietwyk, A. Ginsburg, D. A. Keller, P. López-Varo, A. Y. Anderson, J. Bisquert, A. Zaban *Advanced Materials Interfaces* **2016**.

10) Understanding the Synergistic Effect of WO3-BiVO4 Heterostructures by Impedance Spectroscopy X. Shi, I. Herraiz-Cardona, L. Bertoluzzi, P. Lopez Varo, J. Bisquert, J. Hyeok Park, S. Gimenez. *Journal of Physical Chemistry C* **2016**.

11) Co3O4 based All-oxide-PV: A Numerical Simulation Analyzed Combinatorial Material Science Study K. Majhi, L. Bertoluzzi, D. A. Keller, H. Barad, A. Ginsburg, A. Y. Anderson, R. Vidal, P. López-Varo, I. Mora-Sero, J. Bisquert, A. Zaban. *Journal of Physical Chemistry C* **2016**.

12) Dynamic phenomena at perovskite/electron-selective contact interface as interpreted from photovoltage decays. R. Gottesman, P. López Varo, L. Gouda, J. A. Jiménez Tejada, J. Hu, S. Tirosh, A. Zaban and J. Bisquert *Chem* **2016**.

Conference publications

1) **Invited paper.** Contact effects and hysteresis in organic thin film transistors J. A. Jiménez Tejada, K. M. Awawdeh, P. López Varo, A. K.Ray, M. J. Deen. *ECS-219th Electrochemical Society, Meeting Abstracts*, **2011**.

2) Study of electrical phenomena in organic devices: solar cells, diodes, thin film transistors P. López Varo, K. M. Awawdeh, J. A. Jiménez Tejada. *4th EMUNI Research Souk the Euro-Mediterranean Student Research Multi-Conference, Meeting Abstracts*, **2012**.

3) Method of extraction of mobility model parameters in organic diodes P. López Varo, J. A. Jiménez Tejada, J. A. López Villanueva, K. M. Awawdeh, M. J. Deen. *ICOE 2012-8th International Conference on Organic Electronics, Meeting Abstracts*, **2012**.

4) Influence of the contact effects on the variation of the trapped charge in the intrinsic channel of organic thin film transistors. K. M. Awawdeh, J. A. Jiménez Tejada, P. López Varo, J. A. López Villanueva, M. J. Deen. *IEEE Proceedings of the 9th Spanish Conference on Electron Devices, CDE'2013*, **2013**.

5) **Invited paper.** Modeling of charge injection in organic/polymeric diodes J. A. Jiménez Tejada, P. López Varo, K. M. Awawdeh, M. J. Deen. *ECS-223th Electrochemical Society, Meeting Abstracts*, **2013**.

6) Monitoring the introduction of impurities in organic/polymeric diodes by the analysis of current voltage curves P. López Varo, J. A. Jiménez Tejada, K. M. Awawdeh, M. J. Deen. *ICOE 2013-9th International Conference on Organic Electronics, Meeting Abstracts*, **2013**.

7) Modeling of organic or polymeric thin-film transistors with contact and instability effects P. López Varo, J. A. Jiménez Tejada, K. M. Awawdeh, M. J. Deen. *5th International Workshop on Compact Thin-Film Transistor (TFT) Modeling for Circuit Simulation (CTFT), Meeting Abstracts*, **2013**.

8) Characterization of Metal/Organic Interfaces in Organic Solar Cells degraded with Oxygen and Ambient Atmosphere P. López Varo, J. A. Jiménez Tejada, M. J. Deen. *DURSOL Conference 2014, Meeting Abstracts*, **2014**.

9) Importance of boundary condition in the modeling of organic solar cells P. López Varo, J. A. Jiménez Tejada, O. Marinov, M. J. Deen. *International Conference on Simulation of Organic Electronics and Photovoltaics, SimOEP14, Meeting Abstracts*, **2014**.

10) Role of the Metal-Organic Interfaces in Current-Voltage Characteristics of Bulk Heterojunction Organic Solar Cells J. A. Jiménez Tejada, P. López Varo, O. Marinov, M. J. Deen. *227th ECS -227th Electrochemical Society Meeting- The Electrochemical Society, Meeting Abstracts*, **2015**.

11) Effect of the metal-organic interfaces in the modeling of organic solar cells P. López Varo, J. A. Jiménez Tejada, J. A. López Villanueva, O.Marinov, M. J. Deen. *EURO TMCS I -Theory, Modelling and Computational methods for semiconductors-, Meeting Abstracts*, **2015**.

12) Role of the Metal-Organic Interfaces in Current-Voltage Characteristics of Bulk Heterojunction Organic Solar Cells P. López Varo, J. A. Jiménez Tejada, A. Mañas Martínez, A. B.Sancho Pareja, O. Marinov and M. J. Deen. *HOPV15 -Hybrid and Organic Photovoltaics Conference-, Meeting Abstracts*, **2015**.

13) Modeling Capacitive Effects on the Hysteresis of Perovskite Solar Cells P. López Varo, L. Bertoluzzi, J. A. Jiménez Tejada, J. Bisquert. *ABXPV, International Conference on Perovskite Thin Film Photovoltaics, Meeting Abstracts*, **2016**.

14) Role of the Metal-Organic Interfaces in the Modeling of Organic Solar Cells J. A. Jiménez Tejada, P. López Varo, O. Marinov, C. H. Chen, M. J. Deen. *International Workshop on Flexible Electronics (WFE), Meeting Abstracts*, **2016**.

15) Ferroelectric mechanisms in solar cells P. López Varo, L. Bertoluzzi, J. A. Jiménez Tejada, J. Bisquert. *International Conference on Semiconductor Ferroelectrics and Photoferroelectrics (SEFERR16)*, **2016**.

16) Boundary Value for the free Charge Density in the Modeling of Organic Photovoltaic Device P. López Varo, J. A. Jiménez Tejada, J. E. Carceller, J. A. López Villanueva,

O. Marinov and M. J. Deen. *Simulation of Organic Electronics and Photovoltaics, SimOEP 2016, Meeting Abstracts*, **2016**.